This project has received funding from the European Union's Horizon 2020 research and innovation programme under grant agreement No 637268

Project no.: **637268**

Project full title: **Robust Internal Thermal Insulation of Historic Buildings**

Project Acronym: **RIBuild**

Deliverable no.: **D3.1**

Title of the deliverable: **Closed Technology Loop of Laboratory Experiments and Simulation Models in the Field of Internal Insulation Testing**

Contractual Date of Delivery to the CEC:	**31.12.2017**
Actual Date of Delivery to the CEC:	**29.01.2018**
Organisation name of lead contractor for this deliverable:	**TUD**
Author(s):	**P. Freudenberg, U. Ruisinger, E. Stöcker, S. Roels, N. F. Jensen, T. Odgaard, P. Otiv**
Participants(s):	**Carl-Magnus Capener, Lukas Lång, Ruut Peuhkuri, Ernst Jan de Place Hansen**
Work package contributing to the deliverable:	**WP3**
Nature:	**R**
Version:	**2.0**
Total number of pages:	**123**
Start date of project:	**01.01.2015**
Duration of project:	**31.12.2019**

Abstract

This report comprises laboratory tests of internally insulated wall samples with embedded joist end constructions of three typical constellations (Denmark, Belgium, Germany). These tests aim to derive general conclusions about the performance of different insulation systems in comparison with each other with a focus on the joist end behaviour. Furthermore, these tests offer valuable data sets for the validation of software tools, which are used by engineers and researchers to predict the hygrothermal performance. This allows a demonstration of the reliability and the limitations of the applied software.

Abbreviations

DTU	Technical University of Denmark
KUL	Katholieke Universiteit Leuven
TUD	Technische Universität Dresden
IBK	Institute of Building Climatology | Institut für Bauklimatik
HAMT	(Combined) heat air and moisture transfer
WP	Work package

Table of Contents

1 Introduction

The project RIBuild aims to develop a practitioner's guideline for the application of internal insulation in historic buildings. From a building physics point of view, the failure of constructions due to high moisture levels is the most critical aspect of internal insulation. This risk can be evaluated by simplified calculations or advanced hygrothermal models (simulation tools). The last is seen controversial by practitioners, because of its complexity in the specification of the input (weather data, material data sets etc.), the model complexity itself (vapour transport, liquid water transport, convection etc.) and the interpretation of results (e.g. mould index, freezing-thawing cycles). Therefore, an application of hygrothermal simulation tools in a practical guideline assumes proof of results accuracy for these complex methods. The most appropriate way is a validation of the simulation results with measurements. It offers furthermore the opportunity to demonstrate the performance of materials, constructions, buildings and derive practical conclusions. An overview of this approach in the context of involved work packages within RIBuild is given in the graph below (figure 1).

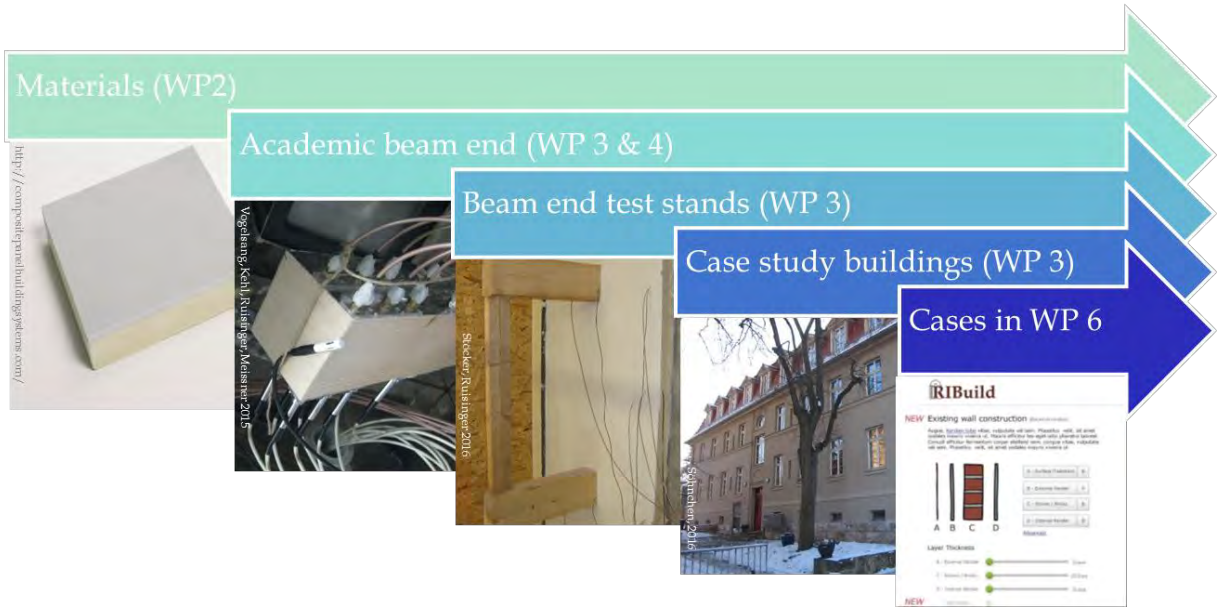

Fig. 1.: Integration of work package 3 into the RIBuild-project

WP3 activities rely on a proper material description; each material in WP3 has previously been characterized with a selection of measurements reported in D2.1. These characteristics provide essential information about the thermal and hygric storage and transport properties of these materials. This allowed principally different functionalities in the selection of different insulation products applied in the test stands of WP3. Supplementary, typical basic materials (bricks, mortar, wood etc.) were chosen for the testing. Based on this product variety, different levels of complexity for the validation and performance demonstration were implemented. The starting level is a single wood material sample in form of an academic wooden beam end under defined boundary conditions in the lab. This task was reported in WP4 (D4.1) as it officiates also as validation case for the three-dimensional extension of the hygrothermal software tool (DELPHIN 6). A further complexity grade is achieved with lab studies of wall samples with embedded joist ends under controlled boundary conditions. This is the core task of the laboratory activities in WP3. Three test stands were designed, erected and analysed within this work package at TUD (section 4), DTU (section 5), KUL (section 6). Each of these focused on a particular research question and investigated particular constructive details, boundary conditions and interior insulation products. Not all test stands were already used to validate the software tools. However, all

cases offered valuable findings about the performance of internally insulated walls. TUD test stand was furthermore adduced for the validation of hygrothermal simulations and for the development of an inverse modelling approach (section 6) which allows a systematic calibration of simulation results. The validation and calibration cases (sections 4.8 and 6) convey the confidence in the application of hygrothermal simulation models for practical cases. They represent an important requirement for the simulation studies in WP 6 as they prove the reliability of the simulation results.

2 Executive Summary

The test stands described in this report are realized by thee partners, TUD, DTU and KUL. Each test stand covers a certain aspect with regard to the tested materials (A), beam end constructions (B) and research focus (C).

Tested materials (A)
Test stands at TUD involved three different insulation materials: calcium silicate (100 mm) mineralic boards (100 mm) and composite boards (80 mm) with conduction resistances about 2.2 to 3.1 m²K/W. A similar resistance was given in the outdoor test unit of DTU for the analysed Xella-container with mineralic board insulation in the same thickness as in the TUD test stand (100 mm). Test stands at KUL included three different insulation systems (EPS, mineral wool and calcium silicate) with resistance of about 3.0 to 3.5 m²K/W.

Tested beam end constructions (B)
Tested beam end constructions ranged from uncovered beam ends with different sealing techniques in TUD and KUL test stands to OSB-covered beam ends with uniform sealing technique in the DTU test stand. Test stands differed furthermore in the decoupling of beam wood and wall construction. TUD test stand prevented capillary contact in this level with a foil, DTU and KUL kept the capillary contact. Critical conditions were recorded for the uncovered and open beam end in both test stands at KUL and TUD. KUL found that especially the combination of capillary active interior insulation (calcium silicate) with open joist end constructions is not recommendable. TUD found that the performance of the open joist end depends strongly on the length of drying periods as these are more efficient in open beam end constructions. DTU concluded a beneficial effect of hydrophobized exterior masonry surface but at the same time a necessity for additional measures in order to reach uncritical conditions in the masonry and joist end (e.g. reduction of indoor relative humidity level) for the evaluated location in Denmark.

Research foci (C)
TUD test stand was kept as a simplified constellation in order to allow a validation and a further calibration of the derived experiments with the DELPHIN simulation results (C, validation in section 4.8, calibration in section 7). Accuracy of the simulation model and its 3D-extension was proved in validation cases selected from the measurements and reported in section 4.8. The accordance of simulation results and measurements is sufficient, although the short-time reaction of materials and components shows higher discrepancies. A proved model accuracy allowed the development of a new calibration procedure (inverse modelling). The term calibration addresses the identification of unknown input parameters of the simulation model, e.g. those parameters, which cannot be measured directly. This calibration approach in section 7 enabled finally the systematic adjustment of the hygrothermal results to achieve the maximum accordance between simulated and measured outcomes.

3 Laboratory Experiments

Facilities for the analysis of hygrothermal building envelope characteristics can be distinguished concerning their spacial scale into test buildings, outdoor full-scale test facilities, outdoor test units and laboratory test stands. Outdoor test buildings and full-scale test facilities are usually fully occupied buildings, which are exposed to unmodified weather conditions. Outdoor test units are at least providing controlled indoor boundary conditions and include furthermore modified or unmodified weather loads. Lab test facilities fix both, indoor and outdoor boundary conditions. (Cattarin, Causone, Kindinis, & Pagliano, 2016).

Both, indoor and outdoor test facilities offer certain advantages. Outdoor test buildings and facilities allow a realistic evaluation of a given construction under lifelike indoor and outdoor conditions. Unfortunately, a monitoring embracing all influential factors is hardly realizable and this implies a multitude of uncertainties. In addition, all findings derived from suchlike measurements are of limited assignability for other locations, building properties, occupancy patterns etc. Laboratory facilities, on the other hand, provide the advantage of selected and self-defined boundary conditions and are therefore able to exclude certain effects or uncertainties arising from diverse boundary conditions and they are able to generate repeatable results. On the other hand, they are not suitable for the evaluation of a practical risk.

Both, test buildings and -outdoor and indoor- test units, are included in work package 3. This deliverable D3.1 is focused on the lab tests. It covers both an outdoor test units (DTU: section 5) and two lab test stands (TUD: section 4, KUL: section 6,).

3.1 Internal Insulation Laboratory Experiments

A number of test stands resp. outdoor test units in the field of internal insulation were described in the literature, evaluating new measurement techniques, e.g. X-Ray technology in (Vereecken & Roels, 2014),boundary conditions, e.g. experimental simulation of wind-driven rain in (Guizzardi, Derome, Vonbank, & Carmeliet, 2015) or the validation of the hygrothermal model, e.g. (Marincioni, Altamirano-Midina, & Ridley, 2014). Further, wooden constructions in combination with internal insulation was studied, e.g. (Sedlbauer & Krus, 2003), (Alev, Uus, Teder, Miljan, & Kalamees, 2014). Another focus was the combination of vacuum insulation panels, e.g. in (Bichlmair, Krus, & Kilian, 2014), (Kopecky, Kamil, Bures, & Tywoniak, 2017).

3.2 Laboratory Experiments within RIBuild

Nevertheless, some research questions remained unsolved. One of them is the experimental performance of critical constructive details (wooden beam ends) in buildings, which were retrofitted with internal insulation. Especially the comparison of basically different insulation systems (one focus of the TUD test stand): vapour-tight systems, vapour-permeable and capillary inactive systems and vapour-permeable and capillary active systems, is not known. Another question is the strengthening effect of adverse boundary conditions, resulting from wind-driven rain in combination with surface treatments (focus of the DTU test stand) or resulting from wind conditions (focus of KUL test stand: pressure differences), on the moisture accumulation risk in these beam end details.

TUD: DTU: KUL:

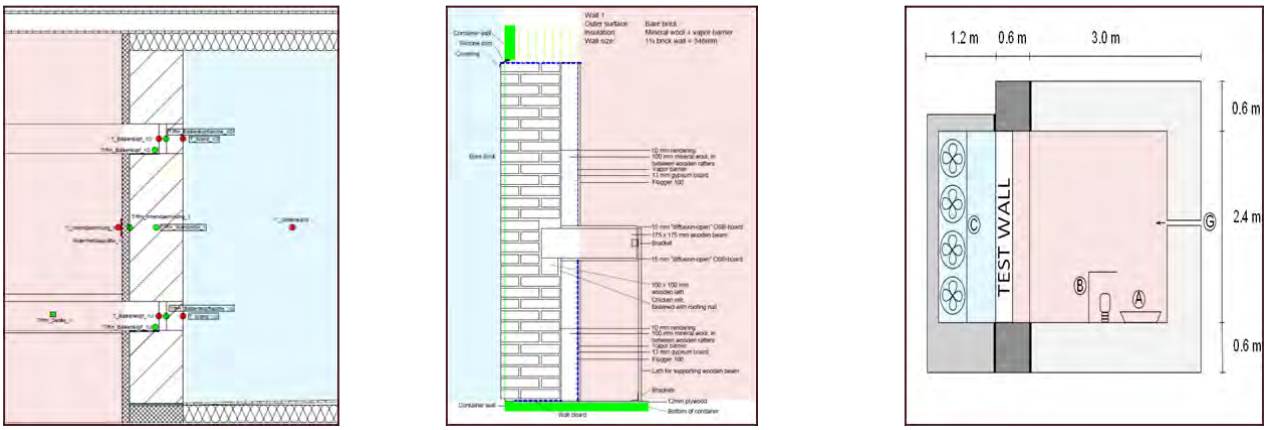

Fig. 2.: Overview of test facilities. Red area implies warm-side (indoor climate) conditions, blue area implies cold-side (outdoor climate) conditions

Tab. 1.: Overview laboratory test stands with beam ends in internally-insulated walls within RIBuild

	TUD (section 4)	**DTU (section 5)**	**KUL (section 6)**
Test facility/unit	Hot side – cold side chamber with 6 fields	Heated test buildings with 24 fields	Hot side – cold side chamber with 8 fields
Test purpose	All test stands: evaluate different interior insulation systems in combination with joist ends / wooden beam ends		
	Impact of connection technology (air tightness) joist end-wall	Combination with partition and different surface treatments	Impact of air gap between finishing and beam end
Conditions	Inside: 19-36°C, 14-75% Outside: -14-30°C, 22-96%	Inside 20°C, 60-70% Outside climate Lyngby	Inside: 20°C, 54% Outside: 3°C, 86%
Basic Construction	Brick, ca. 36 cm with levelling plaster (R~0.4 m²K/W)	Brick, ca. 36 cm with levelling plaster (R~0.6 m²K/W)	Brick, ca. 30 cm, bare (R~0.8 m²K/W)
Insulation products	Composite boards (8 cm) , calcium silicate and mineralic insulation boards (10 cm) (R~2.2-3.2 m²K/W)	Mineralic insulation boards, foam concrete, composite boards, lime mortar, etc. (R~2.4-3.4 m²K/W)	Calcium silicate and EPS (10 cm), mineral wool (12 cm) (R~3.0-3.5 m²K/W)

3.3 Transfer of Laboratory Experiment Results into Practice

Laboratory tests are always confined to a number of simplifications. These simplifications are necessary to comprehend the involved processes in an isolated manner. On the other hand, these simplifications results in a limited generalizability of the results. The explained tests stands aimed to provide comparisons between selected insulation systems and joist end detail variants concerning selected processes like:

- Heat- and moisture transport through the construction under varying temperature conditions in a face-brick wall and in embedded joist end details with different sealing techniques of brick wall sections with three different insulation systems (TUD)

- Heat-, moisture and air transfer through the construction under varying temperature and air pressure conditions in joist end details (brick wall) with different sealing techniques and in brick walls with three different internal insulation systems (KUL)

- Heat- and moisture transport through the construction under realistic weather conditions (temperature, relative humidity, wind-driven rain, wind, solar radiation, longwave radiant exchange) in variants of bricks walls (different insulation systems, surface coatings/paintings) and embedded joist end details with a consistent sealing technique (DTU)

The achieved laboratory tests do not result in conclusions for practice in form of engineering or workmanship recommendations because of the following reasons:

1. Initial conditions do not match the practical case. The masonry and the levelling mortar of the test stands at TUD and DTU were erected less than one year prior measurement start. This results in a high built-in moisture content of the masonry, which was still at 100%-level for the TUD and at 85-100% level in the DTU test stand during the explained measurement phases. An increased moisture level in the entire test constructions is resulting from that. In real buildings, the masonry was able to dry out over several years and would be much lower.

2. Indoor boundary conditions are not realistic. The chosen relative humidities in the warm chamber of the TUD test stand equalled the level of a passive, ventilated building in winter (no vapour emission by people) with a level of 20-40%. This level is lower than usual. On the opposite, relative humidity in the DTU test stand was kept at 60-70%, which is much higher than usual.

3. Outside boundary conditions are strongly simplified. Cold-side boundary conditions cover only temperature and relative humidity conditions in the TUD test stand and temperature, relative humidity and air pressure conditions in the KUL test stand. Realistic boundary conditions would comprise all relevant weather elements: temperature, relative humidity, wind velocity and direction, wind-driven rain, solar radiation.

4. Constructions are simplified. Both, TUD and KUL beam end details are open. Joist ends are usually covered by flooring on top, filled with heavy materials between the timber work and covered at the ceiling side to provide basic functionalities like the required sound insulation between upper and lower floor. This would result in a basic isolation of the beams (and beam ends) from the indoor climate. In the test stands, this level is open and the short joist ends on the opposite side of the masonry are furthermore in direct contact with the indoor air. Due to the higher transfer properties of wood in longitudinal direction, the wood response might be

affected. Additionally, the masonry of the test stands is realized in an accurate way, there are no joint cracks, no renewed jointing and no material irregularities as given in historical buildings.

5. Materials are no original historical ones. Brick, mortar and levelling mortar (interior plaster) are created with new materials in all test stands. This difference is less important for the TUD and KUL test stands, as those are not exposed to wind driven rain and the thermal conductivity and vapour diffusion resistance of the chosen materials lies within the range of historic materials.

On the other hand, some comparative conclusion can be made based on the performed laboratory tests. These are:

- Vapour-tight and capillary inactive insulation systems are not recommended for a raised built-in moisture levels in historic constructions as the drying potential is excessively reduced compared to vapour-open and capillary active systems. (TUD)

- A tight connection between the beam end masonry pocket and the room air, e.g. via tapes, collars etc. provides more stable conditions in the beam end compared to open constructions. (TUD, KUL)

- An open integration of the beam ends results in higher fluctuations of the temperature and moisture content in the beam end timber compared to the closed construction. If this results in an increased damage risk or not must be evaluated under realistic boundary conditions in case study buildings. This assumes also a more realistic evaluation of the mass-related moisture content threshold for wood, as these are only given in form of fixed values, e.g. 20 m% (DIN 68800-1: 2011) in the literature. (TUD, KUL)

- Hydrophobization of the facing brickwork reduces the liquid water load due to wind-driven rain but on the other hand the drying potential of the wall. It could lead to critical conditions compared to non-hydrophobized constructions. This depends on the hydrophobizing agent as well as the indoor and outdoor boundary conditions. A realistic investigation of this effect should be evaluated in case study buildings. (DTU)

4 Test Stand at TUD

4.1 Introduction

The test stand at IBK, TU Dresden enabled simultaneous evaluation of solid walls with three different insulation systems combined with embedded beam end constructions. Tested insulation systems were (1) Polyurethane hybrid boards, (2) calcium silicate boards and (3) mineral boards. Each insulation system comprised three different test fields, an undisturbed field in the middle of the test wall strip as well as an upper and a lower joist end involving different sealing techniques. Each of these nine test fields was equipped with a measurement track that involved temperature, relative humidity, wood moisture content and air velocity sensors. These sensors record the reaction of the test construction on the test conditions provided on both sides of the test wall.

Two aims are targeted with the test facility. Firstly, the measurement results allow an evaluation of the insulation system performance in comparison with each other. This addresses the drying-out of build-in moisture, the distribution of condensate, the thermal performance of wet building materials, the resulting airflow in the different joist end cavities and other aspects. The second aim is the provision of reference cases for the software (DELPHIN) validation in form of measured states and fluxes in the construction for controlled boundary conditions.

4.2 Setup and Equipment of the Test Stand

The test facility consists of mainly three parts, a cold-side chamber, the test wall (with nine test fields) and the warm-side chamber. Both chambers are accessible through a door and equipped with air-conditioning technology. The test facility itself is placed in a separate basement room in the laboratory test building of the ZfBau[1] at TUD. This provides stable boundary conditions and thus a minimum energetic effort for the warm-side boundary conditions.

Each chamber shows different wall mounting due to the required insulation level of provided boundary conditions. Insulation level is higher for the cold-side chamber (12 cm of PUR with λ=0,024 W/mK) due to the aimed temperature level of down to -10°C. No insulation was necessary for the warm-side chamber walls because the temperature conditions in the basement room matched the desired temperature conditions in the warm-side chamber very well. The panelling of the walls was made with OSB-boards that provide high vapour tightness due to the contained binding agents in the OSB boards. This was supplemented with sealing tapes at the edges and corners of the chambers to achieve a satisfying vapour and air-tightness of the cold chamber in particular.

The test wall has a dimension of 3 m in width and 2.5 m in height. It was placed on a socket made of foam glass insulation of 10 cm in height. Foam glass shows a high compressive strength and serves furthermore as thermal and hygric decoupling measure due to its low thermal conductivity, its vapour tightness and its non-liquid-water conducting property. Within the test wall, vertical and horizontal subdivisions are incorporated to prevent mutual interaction of the nine test fields.

[1] This acronym represents an association of several institute laboratories at TUD. The association was founded in January 2016 under the auspices of Prof. John Grunewald and four other professors in the civil engineering sector.

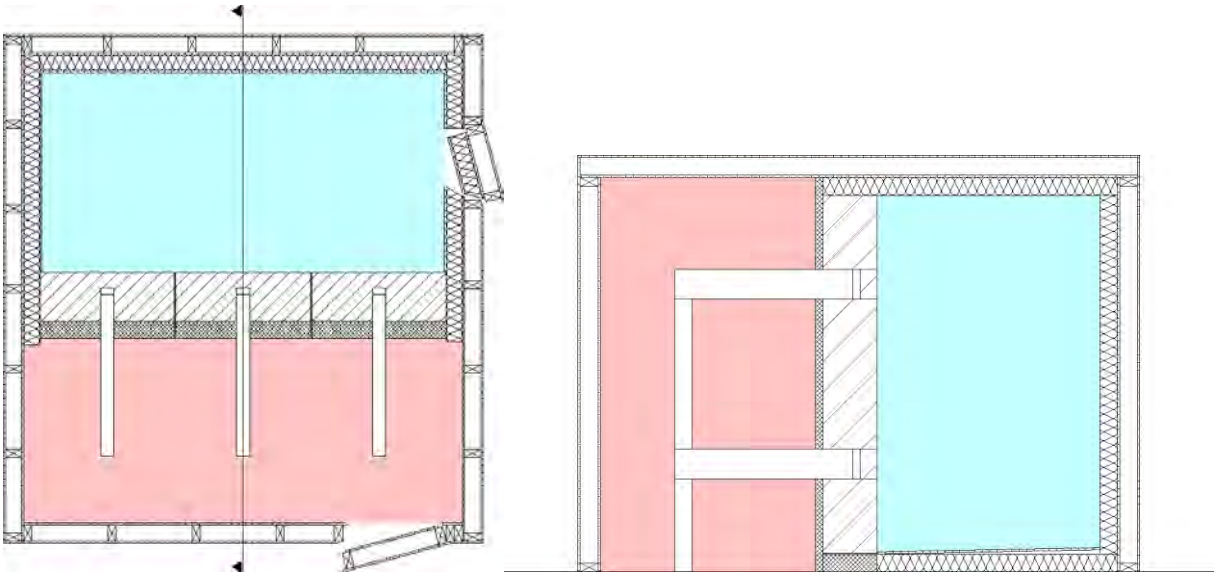

Fig. 3.: Floor plan (left) and vertical section (right) of the test stand with warm-side chamber (red) and cold-side chamber (blue).

The warm-side chamber is equipped with a radiant heater and a humidifier, which are temporarily put into operation. The heater was mainly used to accelerate the drying-out of build-in moisture at the beginning of the test phase and furthermore to provide hot and humid warm-side conditions during the regular operation of the test stand. The cold side chamber was equipped with a heating and cooling unit of 2.0 kW heating power and 2.2 kW cooling power, a humidifying unit, a dehumidifying unit and a number of vents for homogeneous air mixing. Achievable air temperatures range between -10°C and 25°C, relative humidity between 20% and 90%.

Fig. 4.: Cold-side chamber (left) with de-humidifier (dark grey device), air inlet (behind vents) and heating unit (white device). Warm-side chamber showing wires of the measurement equipment in the wall and with the beam ends supported by a wooden auxiliary construction.

Three test strips with different insulation systems adjoin within the test wall. Tested insulation systems are PUR-hybrid insulation boards (iQ-Therm), calcium silicate boards (Calsitherm) and mineral

insulation boards (Multipor). Each insulation systems was mounted on the basic test wall, which was sealed with a levelling plaster at the warm side. The cold-side surface of the masonry remained bare. The term insulation system comprises, in this case, a combination of an adhesive mortar, the insulation boards and a finishing plaster, which was reinforced with a synthetic gauge. A vapour barrier and an insulation strip were used to separate the three insulation system test strips.

4.3 Basic Construction

The basic construction is the same for all test fields resp. test strips. It consists of the brick masonry with one and a half bricks in thickness in cross bracing. German standard format for these bricks is 240 mm (length), 115 mm (height), 71 mm (depth). Vertical and horizontal joints are realized with a lime cement plaster in varying thickness of about 5 to 10 mm. In this regard, the masonry is a typical German construction as it was realized in historical buildings before 1922 when the first German brick standard was spread. Common brick thermal conductivities ranged from 0.6 to 1.1 W/mK at that time. (Arbeitsgemeinschaft Mauerziegel im Bundesverband der Deutschen Ziegelindustrie e.V., 2005).

To ensure plain warm-side surfaces for an ideal contact between insulation board and wall, a levelling mortar was added on the warm side of the masonry. The bare cold side of the masonry was, in contrast to construction site practice where imperfections are usual, full-face jointed in order to reduce irregularities[2]. It is therefore called “academic masonry”.

Tab. 2.: Material specification for the basic construction based on lab measurements at IBK, TUD.

Material Name	ρ Density [kg/m³]	λ Thermal Conductivity [W/mK]	μ Vapour Diffusion Resistance Factor [-]	A_W Water Uptake Coefficient [kg/m²s^{0,5}]	θ_{80} Water Content at 80 % r. h. [m³/m³]	θ_{eff} Effective Pore Vol. [m³/m³]
Brick	1843	0,938	15	0,2189	0,001	0,288
Mortar	1878	0,803	37	0,0361	0,060	0,223
Levelling Plaster	995	0,220	11	0,0212	0,078	0,331

Because effective saturation of the mortar is lower (0.223 m³/m³) than for brick (0.288 m³/m³), it can be stated that moisture storage potential is higher for the brick although the difference is not large. Furthermore the moisturizing process starts earlier in the mortar, already at air relative humidity of about 24% while brick is only starting in the overhygroscopic range of more than 95%.

The brick shows both, a higher transport potential for liquid water and a higher storage potential than the mortar. In case of interstitial condensation and built-in moisture, a drying process towards warm side depends mainly on the properties of the insulation process. The drying process towards cold side, if possible, will be ruled by the base construction. The expected build-in moisture in the masonry is initially present in the horizontal and vertical jointing. It can be expected that this water is distributed relatively quickly within the brick-mortar pattern but takes a relatively long period to dry out due to the

[2] These irregularities might cause uncontrolled airflow through the masonry and thus impede the analysis of measurement results.

limited vapour and liquid water transport potential of the selected mortar. From this built-in moisture-point of view, the mortar is not an ideal material. However, in practice, where liquid water is mainly expected from the outside in form of driving rain and should not be absorbed quickly by the construction, this mortar property would show its warranty.

Tab. 3.: Material specification for the beam wood (spruce) based on lab measurements at IBK, TUD

Material Name and grain direction		ρ [kg/m³]	λ [W/mK]	μ_{dry} [-]	A_w [kg/m^2·s^{0,5}]	θ_{80} [Vol.-%]	θ_{por} [Vol.-%]	K_l [s]
Spruce	longitudinal	394	0.122	4,6	0,012	6,6	72,8	2,0e-10
	radial			186,1	0,012			1,8e-10
	tangential			487,7	0,005			9,2e-10

The wooden beams made of spruce show differing material properties depending on the grain direction of the wood. Measured values are listed in table Tab. 3.: Especially the liquid water and vapour transport properties are much higher for longitudinal than for tangential direction.

4.4 Tested Interior Insulation Products resp. Systems

Each of the three test strips shown in the previous chapter includes three measurement test fields: two joist end fields and one field in between. These fields are equipped with measurement tracks that are specified in the next chapter. The selected insulation materials are representing three completely different types on interior insulation. One type is highly capillary active and vapour permeable with a high thermal conductivity (Calsitherm), one type is slightly capillary active with high vapour permeability (Multipor) and one material shows a low capillary activity and low vapour permeability (iQ-Therm). Main material properties are listed in the following table.

Tab. 4.: Material specification for the three insulation boards (test strips) based on lab measurements at IBK, TUD.

Material Name	ρ Density [kg/m³]	λ Thermal Conductivity [W/mK]	μ Vapour Diffusion Resistance Factor [-]	A_W Water Uptake Coefficient [kg/m²s^{0,5}]	θ_{80} Water Content at 80 % r. h. [m³/m³]	θ_{eff} Effective Pore Vol. [m³/m³]
PUR-hybrid board (iQ-Therm)	55	0.031	63	0.003	<0.001	0.093
Calcium silicate board (Calsitherm)	190	0.059	3.6	0.766	0.007	0.916
Mineral Board (Multipor)	100	0.039	3	0.006	0.005	0.128

This overview shows a relatively high density for one material (Calsitherm) linked to a higher thermal storage capacity and a relatively high thermal conductivity. It shows a high vapour diffusion resistance

for one material (iQ-Therm) and a high water uptake coefficient for one material (Calsitherm). All materials show low equilibrium moisture content at 80% relative humidity of the adjacent air. The effective pore volume, which is accessible for liquid water, differs among the materials and corresponds with the θ_{80}-values order but not with the A_W-values

Another aspect in the comparison of all three systems in terms of energetic efficiency is the dependency of thermal conductivity on the water content of the material. If steady-state conditions are assumed, then the material moisture content would be a consequence of the conditions in the surrounding air. This dependency is measured in form of the sorption isotherms of a material. The resulting, increasing water content of any porous material increases the thermal conductivity due to the fact that embraced air in the pores of the insulation system is replaced by water with an immanently higher thermal conductivity (air: ca. 0.026 W/mK, water: 0.556 W/mK). The volume of replaceable air depends on the pore volume, which is open for water penetration (θ_{eff}). The highest value for θ_{eff} is given for Calsitherm with 0.916 m^3/m^3. Consequently, this product shows the highest potential rise in thermal conductivity for an increasing relative humidity of the surrounding air. Multipor shows a lower θ_{eff} – value of 0.128 m^3/m^3, iQ-Therm the lowest with 0.093 m^3/m^3. The thermal conductivity functions (depending of water content) show that this increase of thermal conductivity is mainly relevant for a very high relative humidity in the overhygroscopic range (>90%). Under these wet conditions, U-values could be estimated with 0.34 W/m²K for iQ-Therm (instead of 0.31 W/m²K), 0.56 W/m²k for calcium silicate (instead of 0.43 W/m²K) and 0.36 W/m²K for Multipor (instead of 0.31 W/m²K).

It can be expected that an increasing moisture content in the construction, e.g. caused by built-in moisture from the levelling and finishing plaster, would primarily affect the thermal insulation of Calsitherm and cause a remarkable loss of thermal insulation function for this product. Especially iQ-Therm is not supposed to show a relevant performance loss due to moisture content. On the other hand, the drying potential of the basic construction in the test strips with iQ-Therm and Multipor is very low compared to Calsitherm. This implies a higher risk of moisture accumulation in the base construction.

4.4.1 Test Strip 1 – PUR-Hybrid Boards (iQ-Therm)

Test construction in strip 1 is iQ-Therm system including composite boards made of PUR, which are supplemented with holes that are filled with calcium silicate cores. Holes show a diameter of 4 mm and are placed at a distance of about 40 mm. This material is therefore highly insulating and slightly capillary active. PUR itself would feature a thermal conductivity of 0.02 to 0.03 W/mK and calcium silicate of about 0.05 to 0.07 W/mK. The product specification defines a design thermal conductivity of 0.033 and a dry value of about 0.031 W/mK. This is only slightly above the PUR value, which implies that the material fraction of PUR is very high in relation to the calcium silicate part and is thus governing the material properties. Vapour diffusion resistance is given by the producer with 27 [-] (PUR: 30 to 150, calcium silicate: 2-20), the water uptake coefficient with 0.774 $kg/m^2h^{0.5}$ (calcium silicate: about 70 $kg/m^2h^{0.5}$, PUR: no suction).

Tab. 5.: Layer specification for the iQ-Therm construction (test strip 1) for dry materials

Layer Name	Thickness [m]	Thermal conductivity [W/mK]	Thermal resistance [m²K/W]
Surface warm side			0,130
Finishing plaster: IQTop	0,005	0,478	0,010
Insulation: iQ-Therm	0,080	0,031	2,581
Adhesive mortar: IQFix	0,005	0,497	0,010
Levelling plaster: Remmers GP	0,010	0,220	0,045
Brick: Schlagmann	0,365	0,938	0,389
Surface cold side			0,04
		Entire resistance	3.21 m²K/W
		U-value	0.31 W/m²K

4.4.2 Test Strip 2 – Calcium Silicate Boards (Calsitherm)

The second insulation system, calcium silicate boards, is a homogeneous mineral material produced with natural raw materials like sand and lime. The boards are inherently stable and show a high liquid water conductivity resp. capillary activity. Thermal conductivity of the product used in the test stand is given by the producer with 0.059 (dry value). This system requires therefore the highest thickness to achieve the same thermal resistance as the other materials. Unfortunately, production thickness is limited to 10 cm and the resulting U-value of this system is thus higher than for the other two insulation systems resp. test strips. Vapour diffusion resistance factor for the mounted product is about 3-6 [-] which is very low and implies a high drying potential. Water uptake coefficient is given with about 45 $kg/m^2h^{0.5}$ for this particular product.

Tab. 6.: Layer specification for the Calsitherm construction (test strip 2) for dry materials

Layer Name	Thickness [m]	Thermal conductivity [W/mK]	Thermal resistance [m²K/W]
Surface warm side			0.130
Finishing plaster: Calsitherm	0.005	0.600	0.008
Insulation: Calsitherm boards	0.100	0.059	1.695
Adhesive mortar: Calsitherm	0.010	0.600	0.017
Levelling plaster: Remmers GP	0.010	0.220	0.045
Brick: Schlagmann	0.365	0.938	0.389
Surface cold side			0.004
		Entire resistance	2.32 m²K/W
		U-value	0.43 W/m²K

4.4.3 Test Strip 3 – Mineral Boards (Multipor)

Test strip 3 has another mineral insulation material available, Mulitpor. These insulation boards show a moderate thermal conductivity (0.042 to 0.047 W/mK) and a low vapour diffusion resistance factor (2 to 3 [-]). In contrast to Calsitherm calcium silicate boards, the water uptake coefficient of this system is much smaller (0.36 $kg/m^2h^{0.5}$). The thickness of this system (10 cm) was chosen in order to have a similar thermal resistance resp. U-value of the entire construction as in test strip 1 (iQ-Therm).

Tab. 7.: Layer specification for the Multipor construction (test strip 3) for dry materials

Layer Name	Thickness [m]	Thermal conductivity [W/mK]	Thermal resistance [m²K/W]
Surface warm side			0,130
Finishing plaster: Multipor	0,005	0,180	0,028
Insulation: Multipor boards	0,100	0,039	2,564
Adhesive mortar: Multipor	0,010	0,180	0,056
Levelling plaster: Remmers GP	0,010	0,220	0,045
Brick: Schlagmann	0,365	0,938	0,389
Surface cold side			0,04
		Entire resistance	3.25 m²K/W
		U-value	0.31 W/m²K

4.4.4 Moisture-Sensitivity of the U-Value

The U-values listed above are not realistic values and should only provide a basis for the comparison. They underlay two major simplifications. First, they are based on the thermal conductivities of the dry materials. As shown in the previous material dependencies, thermal conductivity depending on the material moisture content, an increasing water content would cause a rising thermal conductivity. If the dry thermal conductivities listed above would be replaced by the thermal conductivities which would result from the sorption isotherms at 95% relative humidity, then the U-values would be 0.34 instead of 0.31 W/m²K (dry value) for iQ-Therm, 0.56 instead of 0.43 W/m²K (dry value) for Calsitherm and 0.36 instead of 0.31W/m²K (dry value) for Multipor.

4.5 Measurement Tracks

The test wall and the adjacent chambers (warm-side chamber and cold-side chamber) were equipped with a number of sensors by the producer Ahlborn Mess-und Regelungstechnik GmbH. Each sensor aimed to record a defined physical quantity in a defined temporal resolution (5 minutes) at a defined location within the test construction resp. the chamber. Selected sensor type depends on the required physical quantity, the required measurement range and precision. An overview of all sensors is given in table 21 in the appendix.

Besides the three measurement tracks in each test strip (upper joist end, middle part and lower joist end), each chamber was provided with a set of sensors to record the warm and cold side boundary conditions. Measurements in the cold side chamber embrace air conditions in three different heights and surface temperatures of the ceiling, the sidewall and the back wall of the chamber. A list of the sensor IDs and the corresponding sensor type is given in table 22 in the appendix.

4.5.1 Measurement Tracks in Test Strip 1 (iQ-Therm)

Test strip 1 with hybrid PUR insulation boards (iQ-Therm) provides the basic set of sensors for each of the three measurement tracks. The middle part includes a heat flux board (WFP1) at the inner surface (covered with 2 mm of finishing plaster) and an inner surface temperature sensor (TIDO1). The interface between masonry and insulation, precisely within the adhesive mortar layer, is equipped with a combined sensor that registers temperature and relative humidity (TIDE1, HIDE1). The same type of sensor is used for recording the situation in the middle of the masonry, precisely within the bed joint of the masonry (TWM1, HWM1). This type of sensor is shown in graph Fig. 5.: for the middle of the

masonry (left) and for the near-surface situation (right). The casing around the sensor is a protective measure and made of a diffusion-open tissue.

Fig. 5.: Combined temperature and relative humidity sensors in the masonry: sensor with protective casing in the middle of the masonry (left) and near-surface sensor (right)

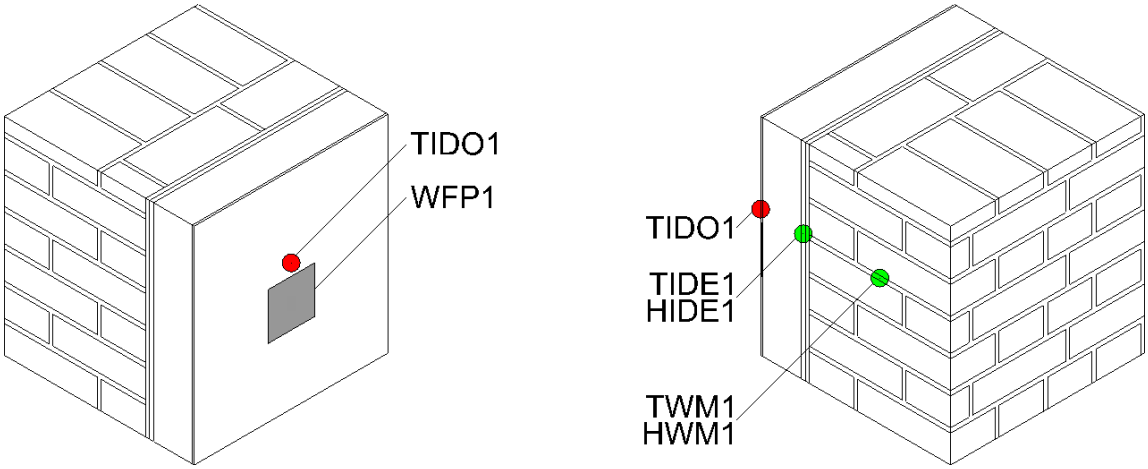

Fig. 6.: Measurement track in the middle of test strip 1 (iQ-Therm) with the location of sensors within the wall.

Measurement tracks in the upper and lower joist end field cover a wider spectrum of positions and measured quantities. One sensor is placed some millimetres behind the front face of the beam and records temperature and relative humidity in the wood (TBKSH1, HBKSH1). This sensor was inserted with a directional drill hole entering from the upper side face of the beam. The resulting hole was filled with silicone mass afterwards to avoid infiltration of warm-side air. Another sensor was directly placed at the surface of the beam-end front face and measured the temperature (TBK1U). Furthermore the joist end fields include measurements in the masonry, a cavity-directed surface sensor (temperature and relative humidity TBKT1, HBKT1) and one cold-side-directed surface sensor (temperature: TWA1). Both sensors are in line with the surface sensor of the joist end. All explained sensor types are installed in both, the upper (sensor key is supplemented with the character “O”) and the lower (sensor key ending with “U”) joist end field.

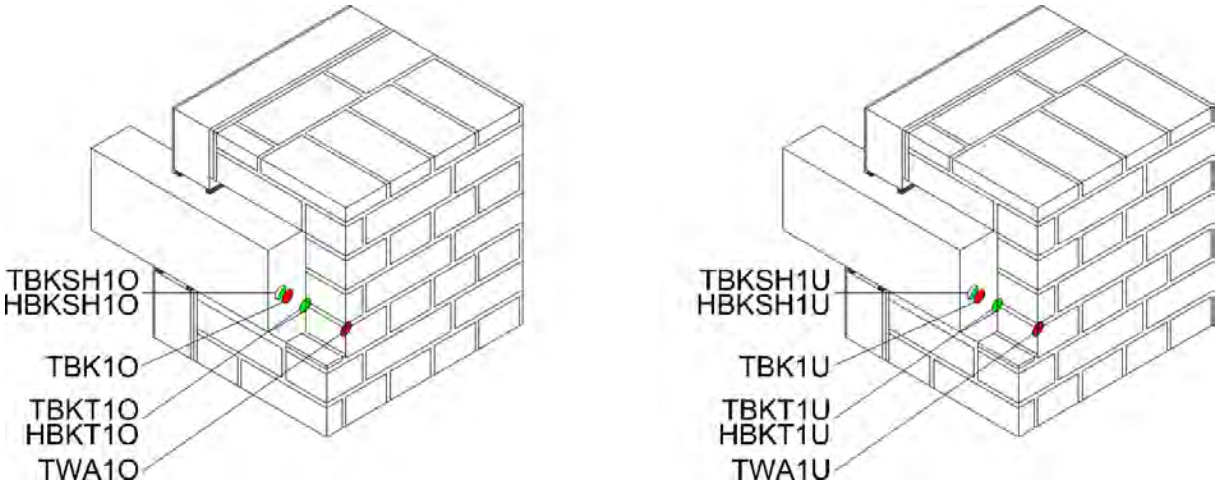

Fig. 7.: Measurement track in the upper and lower joist end test fields of test strip 1 (iQ-Therm) with the location of sensors within the wall.

The beam-ends in the first test strip were tightened with a double layer of pre-compressed joint sealing tape in the gap between masonry and joist end as shown in the subsequent picture. In practice, usually a single layer of sealing tape would be realized. Below the joist end, a PE-foil is applied to avoid hygric contact at the contact face between wood and masonry mortar. The same decoupling technique was used for the other joist end contact faces as well.

Fig. 8.: Double layer of pre-compressed sealing tape around the joist end prior mounting of the insulation boards (left) and PE-foil in the masonry block-out for the joist end (right), both in the first test strip of the test wall (iQ-Therm).

4.5.2 Measurement Tracks in Test Strip 2 (Calsitherm)

Test strip 2 (Calsitherm) covers the same sensor types as test strip 1. It comprises furthermore additional positions and quantities to register the wood moisture content (mass-related wood moisture content) and the situation around the beam end.

Supplemented sensors are a combined temperature and relative humidity sensor in the middle field on the cold chamber-directed surface of the masonry (TWA2, HWA2), a mass-related moisture content sensor in the front end of the beam (HFBK2O, HFBK2U), a combined sensor (temperature, relative humidity) 5 cm below the upper joist end field within the adhesive mortar layer (TIDEBU2O, HIDEBU2O) and a surface temperature sensor on the finishing plaster layer within the same height

(TIDOBU2O). In addition, the lower joist end detail was supplemented with sensors, a combined sensor in the adhesive mortar layer about 7 cm above the joist end (TIDEBO2U, HIDEBO2U) and a temperature sensor (TIDOBO2U) on the finishing plaster in the same levelling as the previous one.

Mass-related wood moisture content measurement relies on the conductance method due to the change of electrical conductance in accordance with the change of moisture content in the material. This measurement technique requires an insertion of two stainless steel screws perpendicular to the grain direction in a depth of 4 cm and a distance of 2.5 cm. It is also necessary to measure the temperature at the same position to correct the temperature dependency of the electrical conductance.

The joist ends in test strip 2 are tightened in a different way than in test strip 1. A single layer of the pre-compressed sealing tape and a plaster junction tape (on the levelling mortar) was applied in the upper field. In the lower field, the plaster junction tape was set aside and solely the sealing tape was mounted.

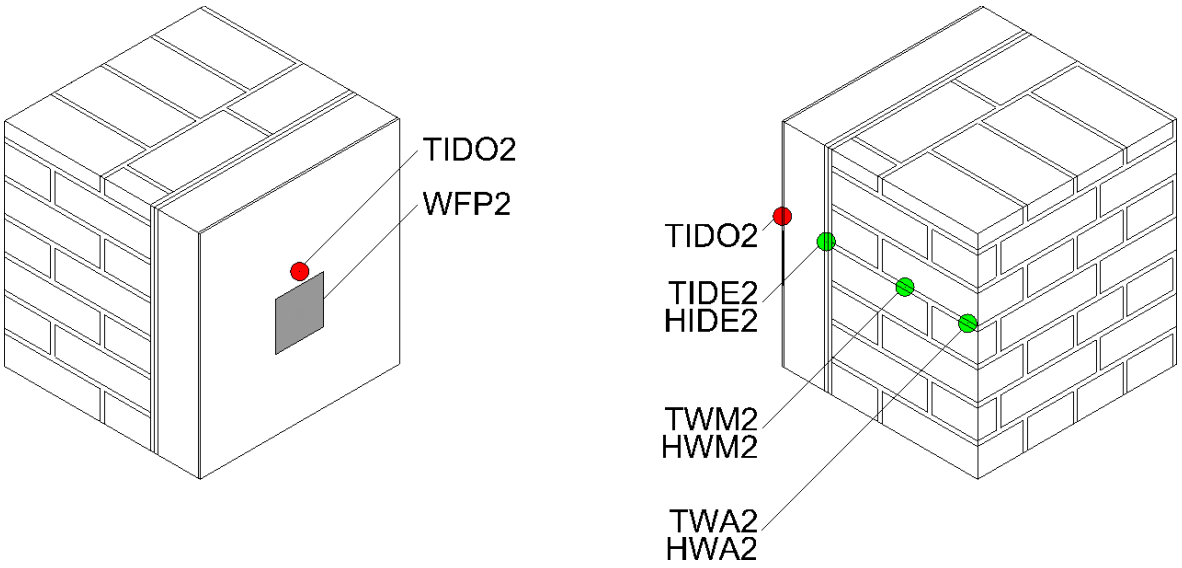

Fig. 9.: Measurement track in the middle of test strip 2 (Calsitherm).

Fig. 10.: Mass-related wood moisture content measurement in the front end of the beam (left) and preparation of the combined sensors behind the front face of the beam (right).

Fig. 11.: Sealing variants in test strip 2 (Calsitherm) for the lower joist end (left) and for the upper joist end (right).

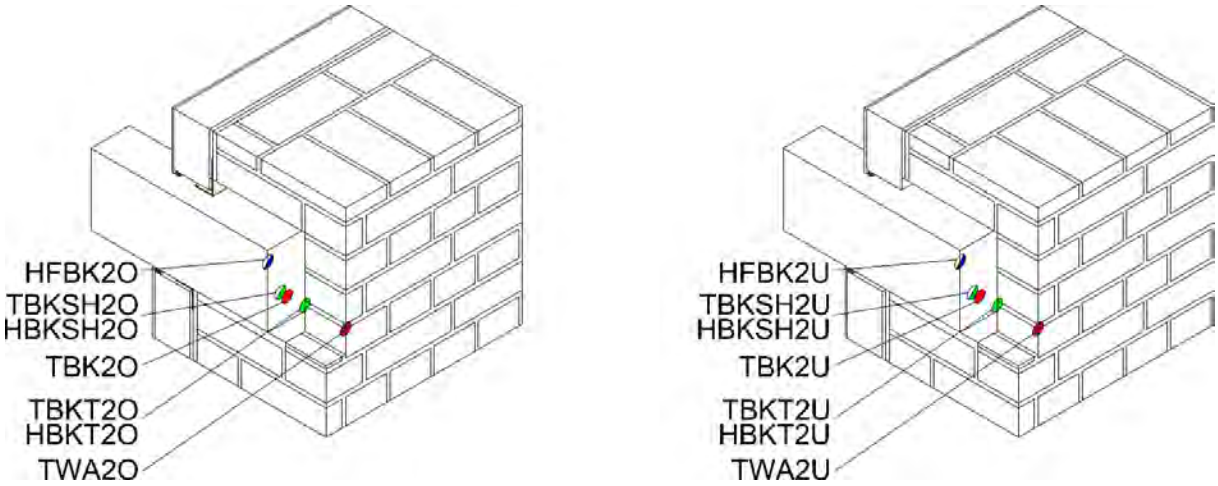

Fig. 12.: Measurement track (sensors) in the upper (sensor ids ending with "O": left figure) and lower (sensor ids ending with "U": right figure) joist-end test fields of test strip 2 (Calsitherm).

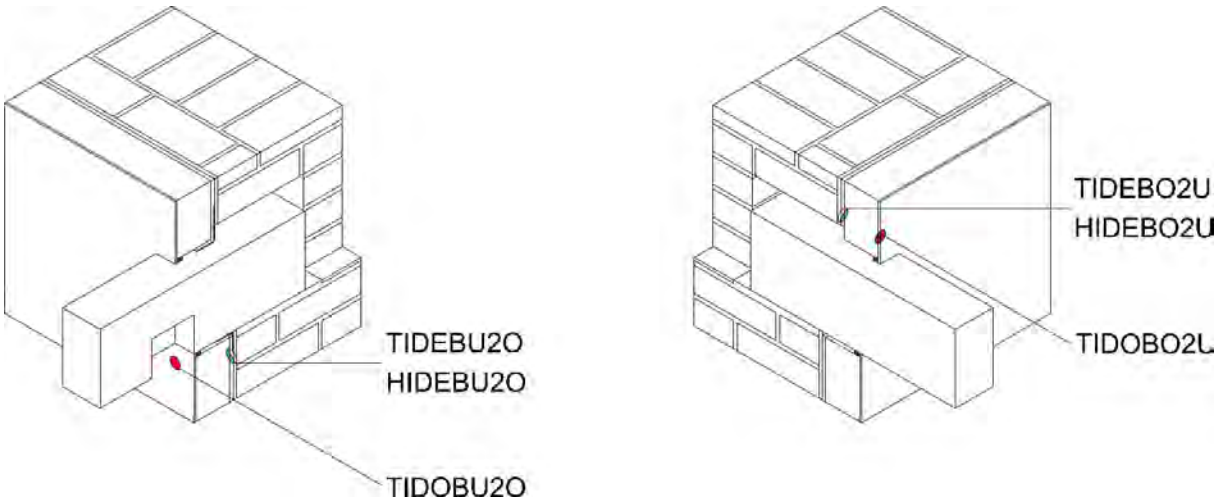

Fig. 13.: Supplemented sensors in the upper (left) and lower (right) joist end field.

4.5.3 Measurement Tracks in Test Strip 3 (Multipor)

Test field 3 extends the measurements for some more quantities and positions. A special interest was set into the airflow though the construction. Especially weak areas of the exterior wall, like pervasions via joist ends or other constructive parts, underlay a risk of unwanted airflow through the construction. This risk was evaluated in test strip 3, where defined cracks are inserted into the beam end (crack measures are a thickness of 3 mm and a depth of 40 mm) and defined holes were inserted into the masonry joints (diameter of the holes is 2 and 5 mm). Both can be closed down variably. The impact of these leakages were measured with additional temperature and relative humidity sensors sidelong the joist end (TLS3O/U, HLS3O/U) and in the contact face between masonry and joist end (TMB3O/U, HMB3O/U, TBO3O/U, HBO3O/U), furthermore with air velocity sensors in the upper part of the cavity (VAMLS3O/U, TAMLS3O/U).

The treatment of the upper and the lower joist end in this test field is much more permeable than in the previous test fields. An open, unsealed variant was chosen for the upper joist end and a hemp band was used for the lower joist end.

Fig. 14.: Inserted holes with test tubes in the bed joint of the masonry as seen from the cold side (left) and sawed cut in the joist end as seen from the war side (right).

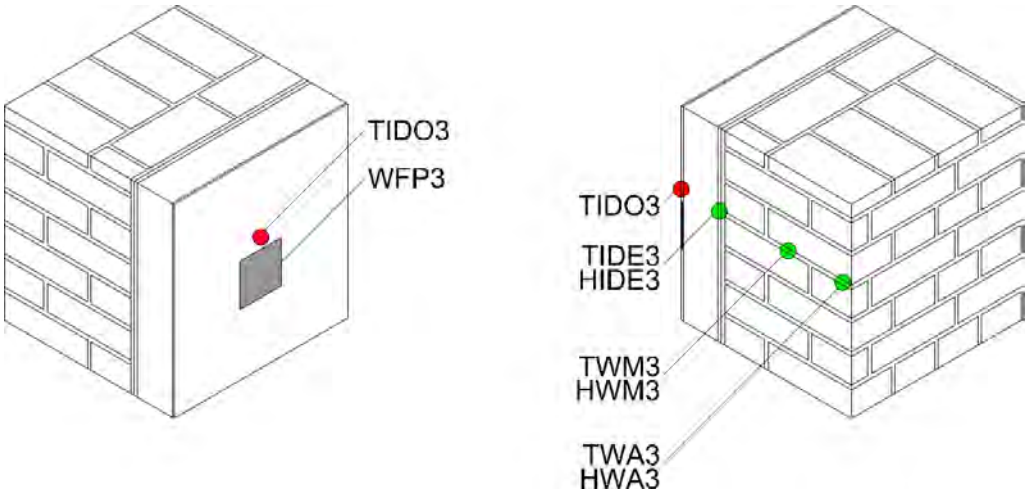

Fig. 15.: Measurement track in the middle of test strip 3 (Multipor).

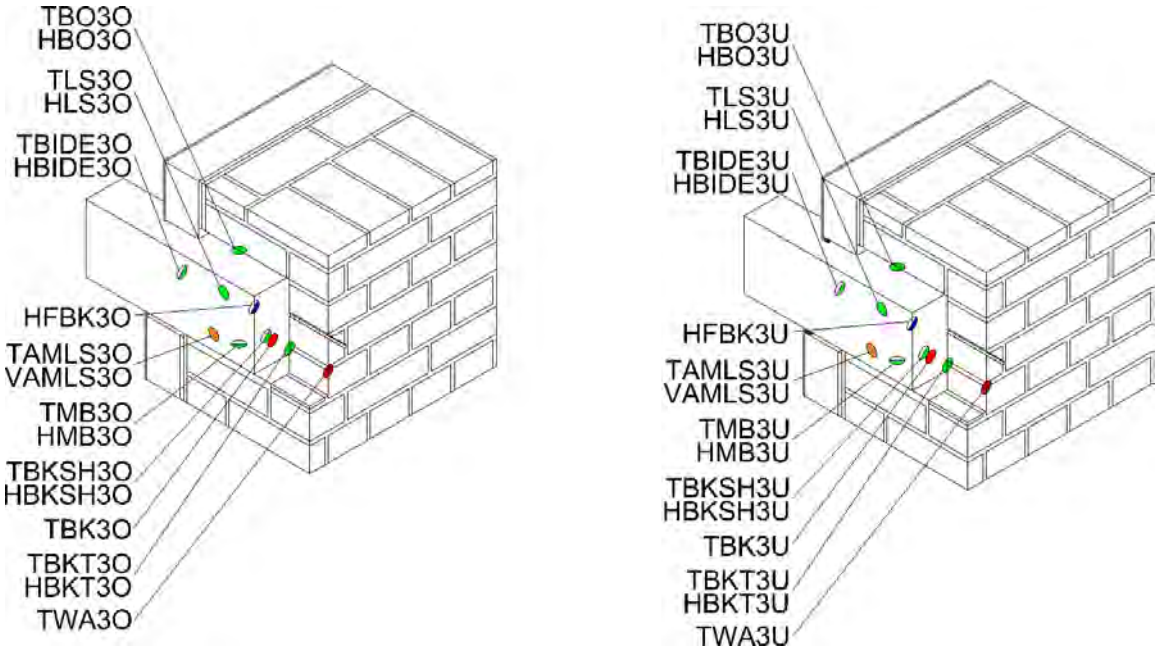

Fig. 16.: Measurement track (sensors) in the upper (sensor ids ending with "O": left figure) and lower (sensor ids ending with "U": right figure) joist end test field of test strip 3 (Multipor)

4.6 Test Scenario Boundary Conditions

Boundary conditions include different scenarios for the temperature and relative humidity with different purposes. A preparation period (pre-conditioning phase) aimed to dry the construction and reduce the high built-in moisture level, which has initially at saturation level in the plaster and mortar layers. Due to the mounting time schedule of the three different insulation products, different drying periods were realized for each test field resp. product field. The drying phase for test strip 1 (iQ-Therm) was the shortest as the system was mounted in August 2015. Around November and December in 2015, the other two test strips were completed (strip 2: Calsitherm, strip 3: Multipor). Consequently, three different starting levels are reached for each of these products. These differences have to be taken into account in the analysis of insulation product performance.

Besides this, three different types of boundary conditions scenarios were executed and considered for the performance study. First scenario type is called steady state period (StSt) in this report. It aims to keep boundary conditions constant in order to compare the fluxes through the constructive details and thus exclude storage effects. The second scenario type is referred to as oscillating period (Osc). Conditions are changed in regular intervals until a balanced state in the construction is reached. This scenario was realized in order to provide quasi-steady state conditions. The third scenario is paraphrased step period in this report. Conditions were changed in a step-wise manner, each condition maintained until the conditions within the construction stayed constant. An overview on the realized conditions in all three selected phases is given in table 8.

Tab. 8.: List of test scenarios which are chosen for the analysis

Phase	Phase Start	Phase end	Temperature (cold chamber)	Rel. humidity (cold chamber)
1) Steady state January 2016	18.01.2016 17:00	20.01.2016 17:00	19 °C (±1,5 K)	55 % (±7 %)
	20.01.2016 17:00	26.01.2016 09:30	-10 °C (±1 K)	45 % (±5 %)
	26.01.2016 09:30	02.02.2016 16:00	19 °C (±1,5 K)	55 % (±7 %)
2) Oscillating February 2016	08.02.2016 17:00	09.02.2016 07:00	5 °C (±1,5 K)	55-65 % (±5 %)
	09.02.2016 07:00	10.02.2016 17:00	19 °C (±1,5 K)	50-55 % (±5 %)
	Repeated for eight days (last day: 16.02.2016)			
3) Step change June 2016	17.06.2016 09:00	21.06.2016 17:00	20 °C (±1,5 K)	70 % (±5 %)
	21.06.2016 17:00	28.06.2016 19:00	5 °C (±1,5 K)	60-80 % (±10 %)
	28.06.2016 19:00	03.07.2016 19:00	0 °C (±1,5 K)	60-80 % (±5 %)

4.6.1 Steady State Phase

The steady-state period took place in January 2016 over five days (constant conditions). Starting conditions were about 19°C and 55% relative humidity at the cold side, 20°C and 20% relative humidity at the warm side. Conditions were changed on the cold side to -10°C. Warm side was not modified via air conditioning systems during this period. The consistent rise of air relative humidity could be a consequence of two influencing factors, the air exchange with the hall climate and the test construction (built-in moisture). A remarkable influence of moisture release from the construction to the room side is possible because of the mounting time point, one month prior test phase. The surrounding climate of the test stand was not recorded and remains therefore an open issue.

The HVAC-system of the test chamber was not able to hold fully constant condition because it was operating in an intermittent way. Fluctuations of the air temperature on the cold side of the chamber are about 2K, variation of air relative humidity is about 10%. Relative humidity control (dehumidification, humidification) was furthermore only operating properly above 5°C, whereby the values vary around 45% with a subtle increase. Instabilities for both quantities are also supposed to be a consequence of the high moisture content of the construction in combination with the difficulties of the HVAC system control. These fluctuations might be problematic for the graph and results analysis. To improve the visual and numeric interpretation, all following graphs are provided in two versions, in their original form as 5-Minute average values and in a modified form of 50-value rolling mean as smoothing function. This allows especially a better distinction between the combined temperature and relative humidity sensors at different heights (top: “O”, centre: “M”, bottom: “U”) on the cold side of the test stand. It eliminates furthermore some peaks, which result from the automated HVAC-system processes (e.g. de-icing of cooling coils).

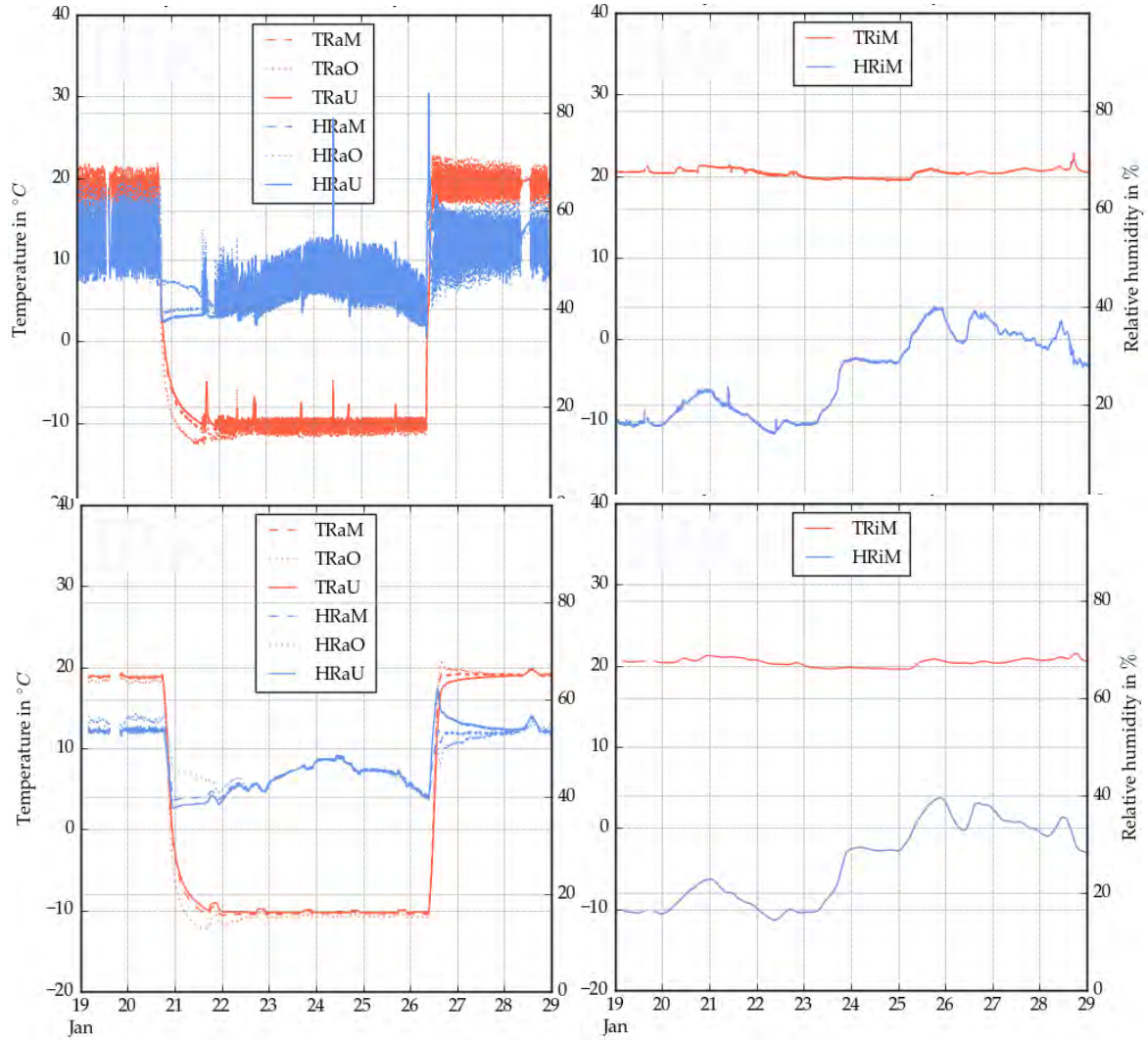

Fig. 17.: (Air) temperature (T) and (air) relative humidity (H) in the cold (left; Ra) and warm side (right; Ri) chamber during the steady-state period in January 2016, at top (O), middle (M) and bottom (U) position. The upper graphs show 5-Minute averages, the lower graphs show the rolling mean over 50 values.

The cold side graphs show the difference between the sensors at three height levels in the chamber. It ranges from below 0.5 K (<1% rel. hum.) during constant phase up to 2 K (8-9% rel. hum.) during the conversion period. The differences are the highest for the uppermost sensor and the lowest for the bottom sensor.

4.6.2 Oscillating Phase

Cold side conditions were changed from a level of 19°C down to 3°C (top sensor), resp. 5°C (bottom sensor) with a simultaneous relative humidity change from 50 to 65%. This temperature fall/rise required a strong dehumidification and humidification effort. The temperature variations are the greatest for the sensor located on top of the chamber. Resulting humidify fluctuations are the stronger, the higher the sensor is located in the chamber. Conditions in the warm-side chamber are nearly constant with an air temperature of around 22°C and relative humidity of around 30%.

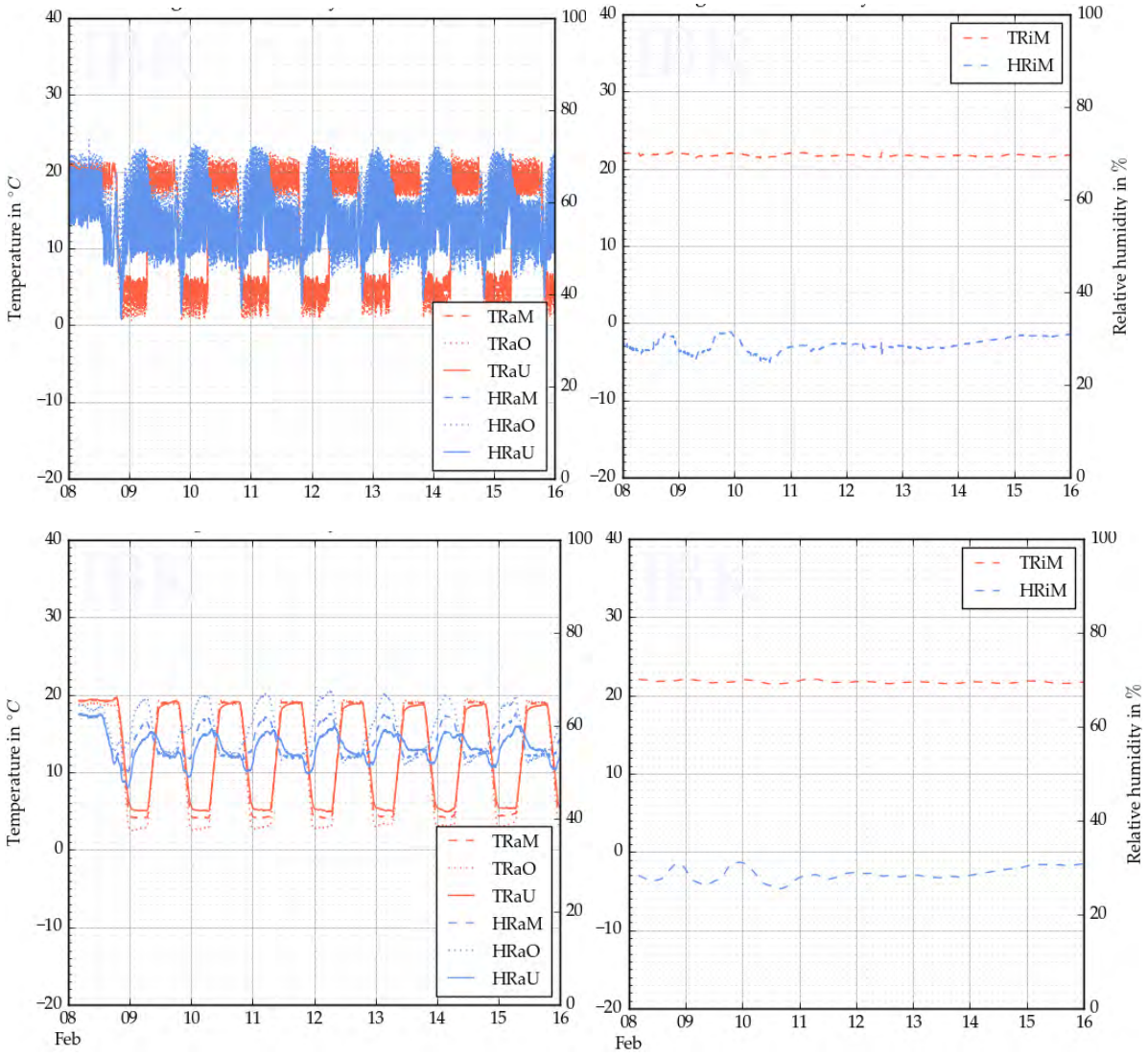

Fig. 18.: (Air) temperature (T) and (air) relative humidity (H) in the cold (left; Ra) and warm side (right; Ri) chamber during the oscillating period in February 2016, at top (O), middle (M) and bottom (U) position. The upper graphs show 5-Minute averages, the lower graphs show the rolling mean over 50 values.

4.6.3 Step Change Phase

This period was provided in June/July 2016 over four days at 20°C, 70%, seven days at 5°C, 60% and four days at 0°C, 60%. The actual target values differ from the measured values due to the particularities (intermittent operation) of the HVAC equipment. In contrast to the previous periods, where relative humidity in the warm chamber was relatively low, warm side is supplemented with a humidifier aiming to provide 60% relative humidity. Humidifying device causes the same effect of strongly fluctuating conditions if the present values are close to the target value. Warm-side conditions started furthermore from a drying period at a high temperature level of about 35°C.

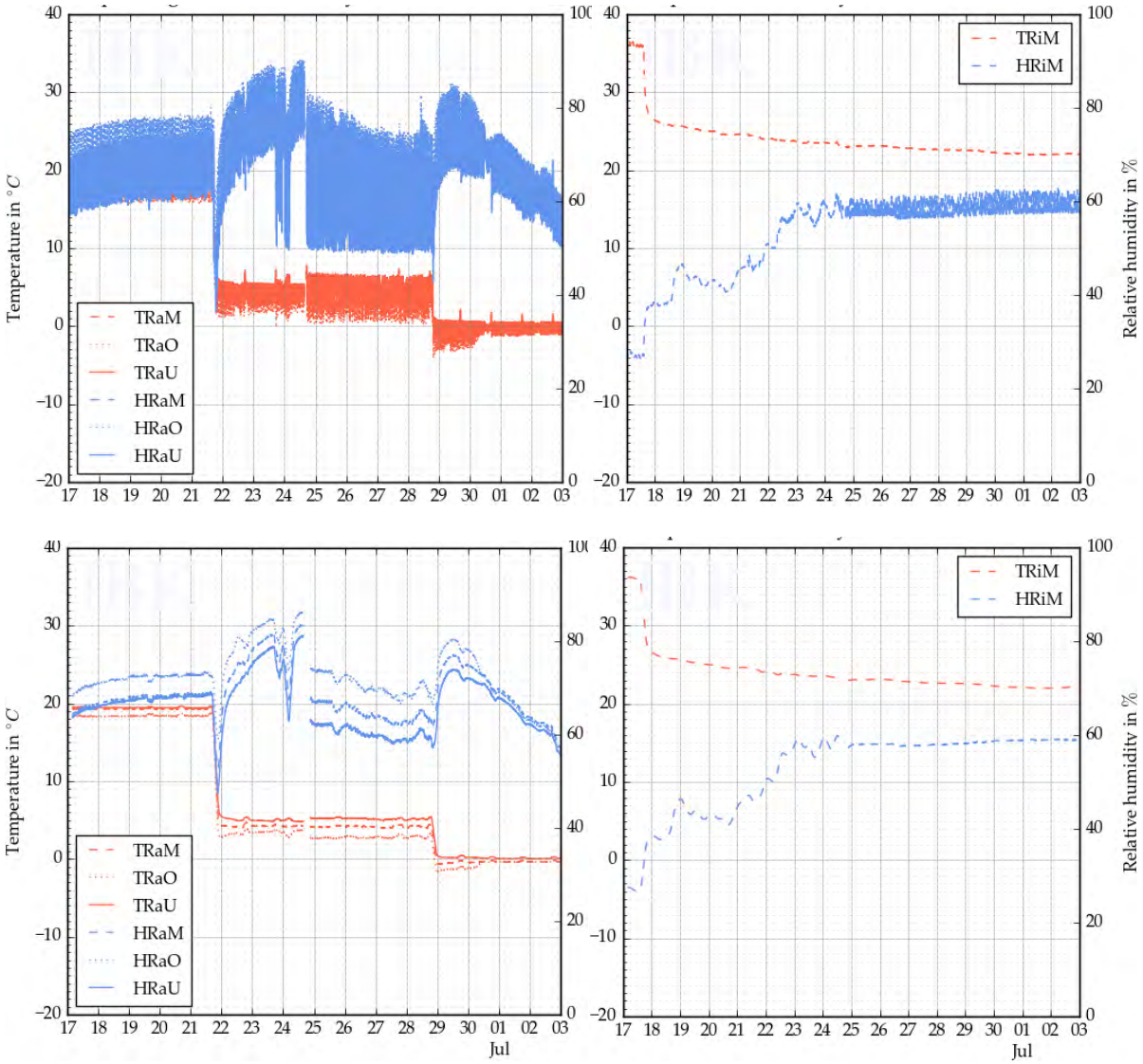

Fig. 19.: (Air) temperature (T) and (air) relative humidity (H) in the cold (left; Ra) and warm side (right; Ri) chamber during the step period in June/July 2016, at top (O), middle (M) and bottom (U) position. The upper graphs show 5-Minute averages, the lower graphs show the rolling mean over 50 values.

4.7 Analysis of Measurement Results

Initial conditions are representing the worst case, which should not be expected in practice. Due to the fact that masonry was built immediately before the mounting of the insulation products, there is a high built-in moisture level in the masonry. As interior insulation is predominantly applied in historic buildings and producers of insulation systems exclude explicitly a moisture-loaded wall as a risk factor that must be eliminated before the construction works start. The main workflow steps for the construction works of the test stand are as follows:

Tab. 9.: Overview construction works for the TUD joist end test stand

Construction work step	Time
Erection of the masonry	April 2015
Installation of the HVAC system (cold side)	June 2015
Mounting of levelling mortar (warm side)	August 2015
Insulation system in test strip 1 (iQ-Therm)	August 2015
Insulation system in test strip 2 (Calsitherm)	November 2015
Insulation system in test strip 3 (Multipor)	December 2015

Besides the water content in the masonry, the insulation system itself humidifies the wall through its system components. All insulation systems used in this test stand require a levelling mortar, an adhesive mortar on the masonry and a finishing plaster inside. The levelling mortar could be abdicated in some cases while the other two layers cannot.

4.7.1 Response of the Masonry

The following graph shows the temperature and relative humidity conditions of the masonry during the steady state period. Sensors were located in the bed joint in the centre of the brick wall in each test strip (middle fields). Measurements within the bricks were not derived. Relative humidity in the jointing is lasting on a very high level of nearly 100% for all sensors. Despite previous drying periods, it was not possible to reduce this high moisture level in the middle of the masonry. A side effect of this condition is an increased risk of sensor damage or sensor drift.

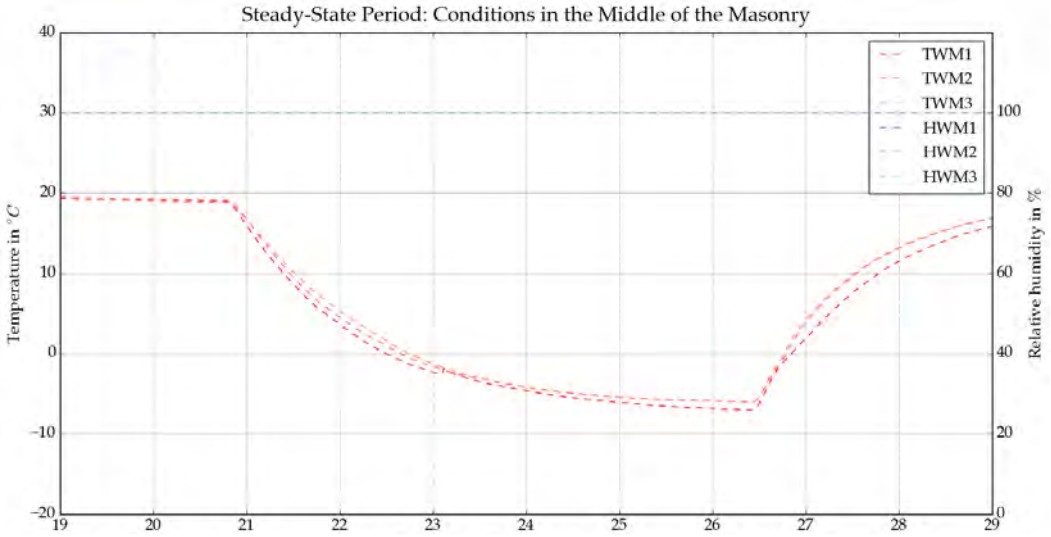

Fig. 20.: Conditions of the brick masonry during the steads-state test period in January 2016.

Conditions in the masonry during the oscillating period and the step change period are displayed in the following graphs. It can be seen that finally in July one of three sensors (field 3: Multipor) is recording values below 100%. This can be traced back to the longer drying period of this test strip and its highly vapour permeable insulation material.

Temperature conditions are starting at a constant level of 19.0 to 19.2°C for the steady state period, 19.5 to 19.7°C for the oscillating period and 20.7 to 21.5°C for the step period. Differences within the measurement uncertainty (± 0.1K) are not interpreted here and temperature can therefore be seen as equal for all sensors in periods 1 and 2. The last period shows slightly larger differences, which is a

consequence of the different thermal resistances in the three test fields. Therefore field 1 (iQ-Therm) with the lowest U-value shows the lowest temperatures in the middle of the masonry.

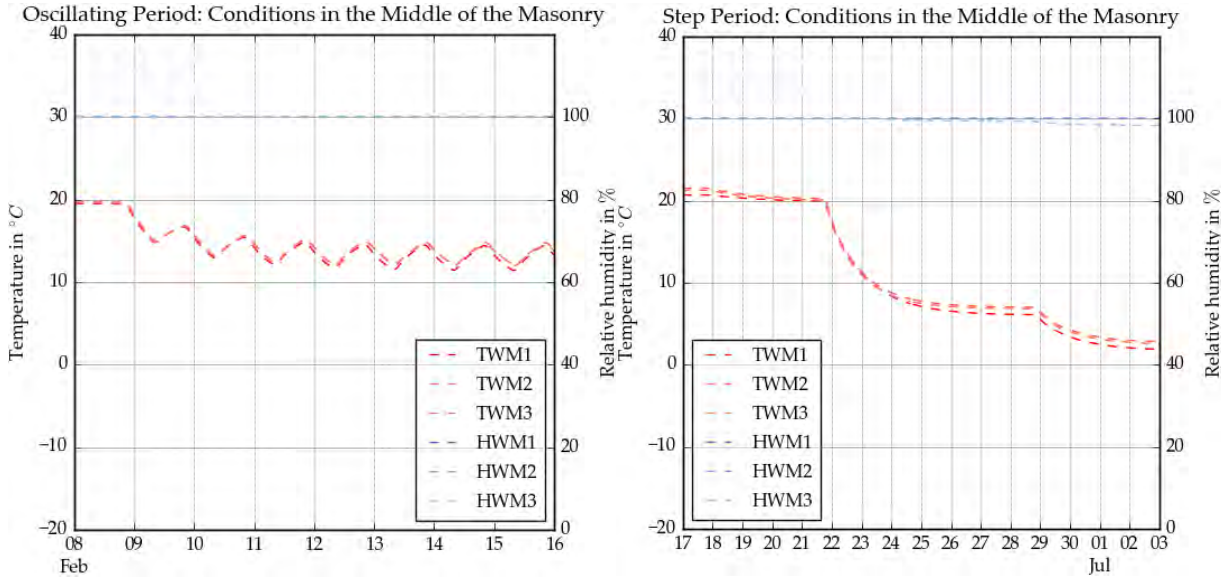

Fig. 21.: Masonry conditions during oscillating and step period 2016: red curves show temperature conditions in each of the three test fields in the middle of the wall, blue curves show relative humidity.

4.7.2 Response of the Interface Masonry – Insulation System

In each test strip the middle field was equipped with sensors between insulation boards and masonry or more precise between the adhesive mortar and the levelling plaster layer. This is supposed to be the most critical interface of the construction because of two factors. Firstly, this is the expected layer for interstitial condensation for an internally insulated wall as the temperature level decreased strongly behind the insulation layer and the vapour pressure level is still high, as all insulation systems are diffusion permeable. Secondly, this area shows a high built-in moisture content from the adhesive mortar used to mount the boards at the wall resp. on the levelling mortar.

Accumulated condensate or built-in moisture can potentially escape towards both sides based on two different mechanisms, vapour diffusion and liquid water distribution. Both mechanisms assume a certain pressure difference (capillary pressure, vapour pressure) and depend furthermore on the vapour diffusivity and the liquid water conductivity of the insulation material. Vapour diffusivity of the insulation systems is moderate for iQ-Therm in test field 1 ($\mu_{iQ\text{-}Therm}$ = 27 [-]) and relatively low for the test fields 2 (Calsitherm) and 3 (Multipor) ($\mu_{Calsitherm}$ = 3-6 [-],$\mu_{Multipor}$ = 2-3 [-]). The consequence is a reduced drying potential for vapour diffusion for iQ-Therm and a high drying potential for the other two systems.

The order of the mounting process, in particular the mounting of the iQ-Therm system in advance of all other systems, cause a strengthening of this effect because the drying period for the iQ-Therm test field was shorter than for the others.

A drying process to the cold side through the masonry is possible if the masonry is not constraining. As explained in the previous paragraph, masonry is constantly carrying liquid water from the construction phase. Release of built-in moisture from installing the insulation system should therefore mainly be given towards the warm chamber side.

Another relaxation potential for the built-in moisture is the distribution of liquid water within the connected pore system of the test walls. Due to the applied construction technology in form of a full-faced connection of all wall layers with capillary active mortars resp. plasters, liquid water transferability is given over the whole wall profile. An indicator for the liquid water conductivity of a material is the water uptake coefficient A_W. The highest value was measured for the calcium silicate boards with 1.11 kg/m²s$^{0.5}$, second range position is given by iQ-Therm with 0.013 kg/m²s$^{0.5}$ and the lowest value by Multipor with 0.006 kg/m²s$^{0.5}$. Subsequently Calsitherm shows the highest overall drying potential due to high liquid water conductivity and a low diffusion resistance factor. Multipor has also a small resistance to vapour diffusion but only a small potential for liquid water distribution. The lowest relaxation potential for captured liquid water among the tested insulation products is finally given for iQ-Therm with relatively high vapour diffusion resistance and a small water uptake coefficient.

The graphs below show the temperature and moisture conditions between insulation system and base construction for all three test fields. The recorded temperature conditions in the materials start at the same level of initial air temperature level of about 20°C in this test period. Decreasing temperature at the cold side causes the most rapid fall of temperature level in the iQ-Therm field, followed by Multipor and latest by Calsitherm. The order of temperature levels at the coldest point is not equivalent to the order of dry U-values of these constructions. It matches rather the order of U-values of the moisturized materials.

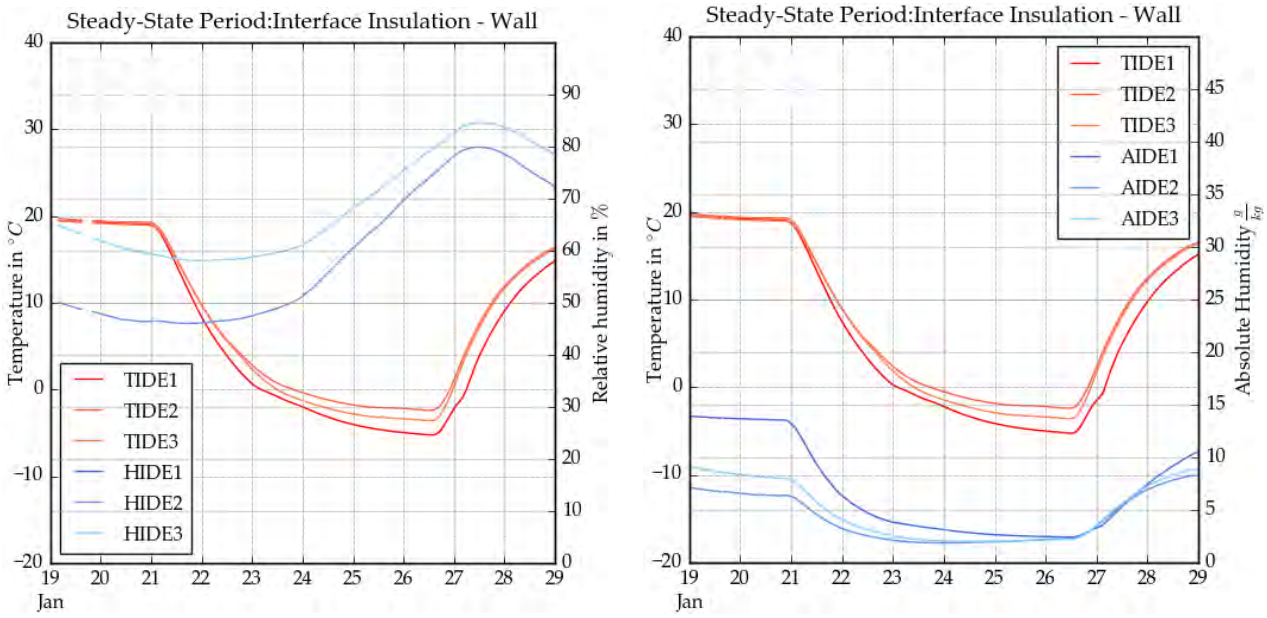

Fig. 22.: Conditions in the interface between masonry and insulation system for all three test strips in the steady-state period. AIDE is the sensor key for absolute water content, TIDE for the temperature.

Relative humidity of iQ-Therm (sensor HIDE1) is congruent with the Multipor (sensor HIDE3) curve. Relative humidity curve shows a relatively low level in the Calsitherm wall section (HIDE2) which should be, on the one hand, attributed to the higher temperature level in the base construction due to the lower thermal resistance of this insulation system. The curve of the absolute humidity shows on the other hand, that this wall section is furthermore at the lowest absolute water content level of all three test fields. This is supposed to be a consequence of the beneficial drying conditions of this vapour open and capillary active system. The highest absolute humidity level is given for the vapour and liquid water-obstructive iQ-Therm system. The difference is about 5 g/kg between this system and the two vapour-open test strips with Calsitherm and Multipor.

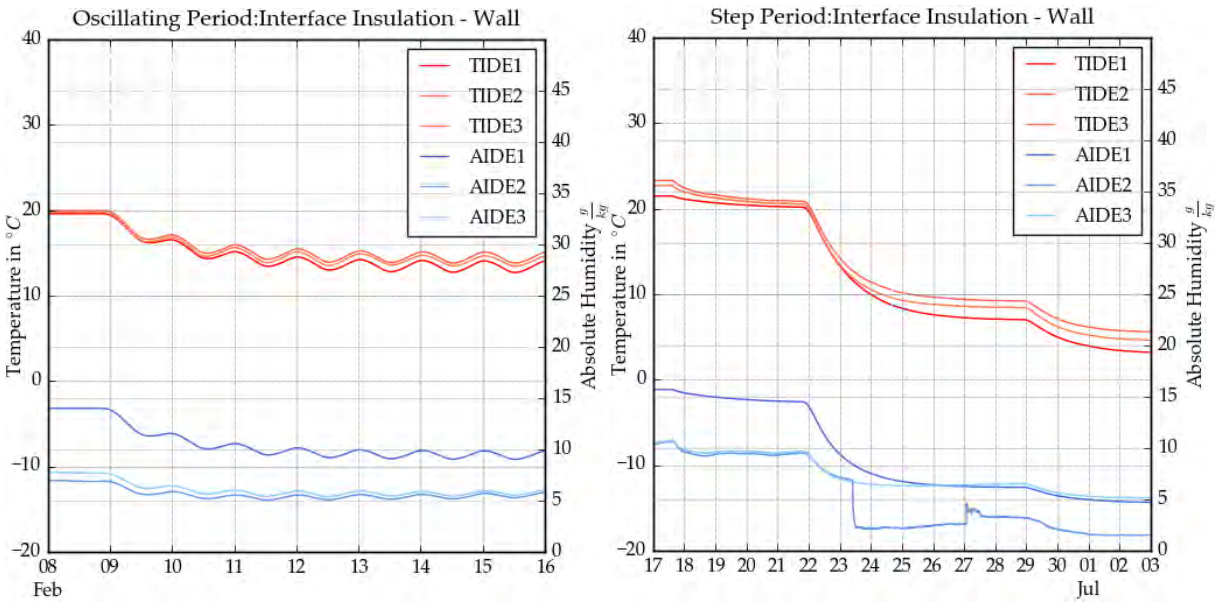

Fig. 23.: Conditions in the interface between masonry and insulation system for all three test strips in the oscillating period (left figure) and step period (right figure). AIDE is the sensor key for absolute water content, TIDE for the temperature.

The difference is still obvious in the latest test period (step period) in June 2016 and still at a difference of about 5 g/kg. This difference becomes smaller when the temperature level at the cold side decreases due to the strengthened vapour transfer process resulting from the rapidly decreasing partial pressure in the cold-side air. It converges towards saturation level with relative humidity values above 95% at the end of this test period where saturation level equals a water content of about 5 to 6 g/kg.

4.7.3 Response of the Cold Surface (Masonry Surface)

Surface measurements at the cold side of the test stand in the middle field were only installed in system 2 (Calsitherm) and system 3 (Multipor). Sensors were integrated into the bed joint of the masonry in a depth of about 2.5 cm behind the masonry surface.

Temperature conditions in system 2 and 3 differ marginally and show the expected case of higher temperature level for Calsitherm (TWA2) due to the lower thermal resistance of this insulation system. The greatest differences are displayed for the phase of rapidly decreasing temperature of the adjacent cold-side air and reach 1 to 2 K. This temperature difference is supposed to be a consequence of the higher storage capacity of the Calsitherm wall strip, causing a delay in the temperature drop. Cold-side moisture conditions are compared in form of the relative and the absolute humidity of the air. The absolute moisture level is higher for Calsitherm (AWA2) than for Multipor during warm periods and corresponds stronger in the cold periods. A slightly higher moisture level for the calcium silicate test strip compared to the mineral board strip in obvious in all phases. This should be a consequence of the slightly higher temperature level in the calcium silicate test-strip due to the lower thermal resistance. Furthermore, a lower cold-side temperature causes a very low partial pressure level and consequently a higher vapour pressure difference. This promotes the vapour transport from the warm-climate chamber resp. from the interface insulation-masonry towards cold side.

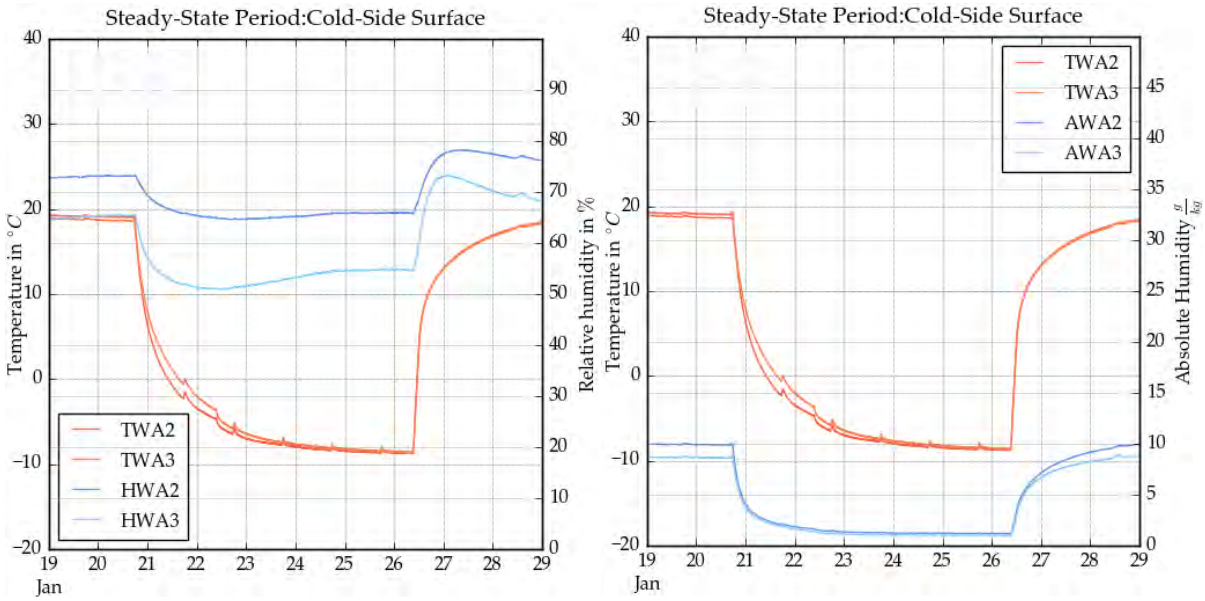

Fig. 24.: Cold-side conditions for the steady-state period in test strip 2 and 3 in January 2016. Left figure: temperature (TWA) and relative humidity (HWA). Right figure: temperature (TWA) and absolute humidity (AWA)

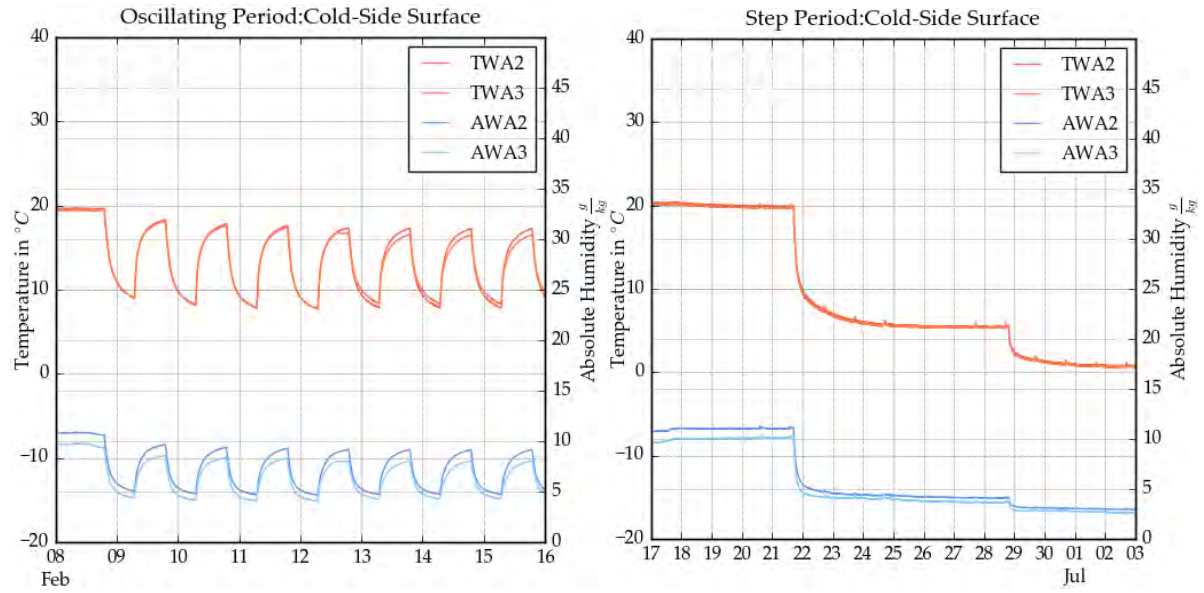

Fig. 25.: Cold-side temperature (TWA) and absolute humidity (AWA) conditions for the oscillating (left figure) and the step period (right figure): in test strip 2 and 3 in January 2016.

4.7.4 Response of the Warm Surface (Insulation System Surface)

The warm-side surface was equipped with temperature sensors and heat flux boards on each of the three test strips. Heat flux boards enable a comparison of the effective heat transfer coefficient of the walls (U-value) with the calculated, idealized U-values. The heat flux sensors are embedded into the finishing plaster layer, about 1-2 mm below the surface. Surface temperature sensors are directly placed on the warm-side surface.

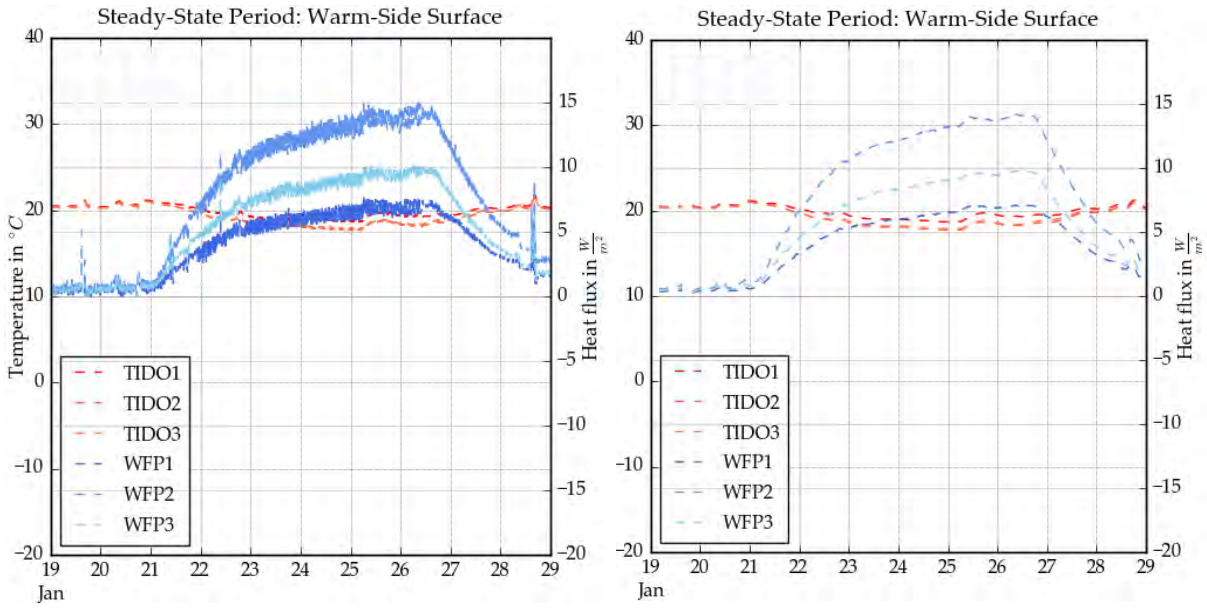

Fig. 26.: Warm-side conditions for the test period 1 (steady-state). Left figure: original curve. Right figure: smoothed curve with rolling mean over 50 values.

Assuming an idealized case of steady-state conditions in the wall for January, 25th would result in the following values for the resulting U-values. The table contains the average heat flux over this day calculated from the boundary conditions of -10.73 °C at the cold side (medium height sensor) and 19.65°C at the warm side. Both values are averages over the day 25.

Tab. 10.: Comparison of calculated and measured U-values for the first test phase (steady-state)

Construction	U-Value calc. [W/m²K]	Heat flux meas. W/m²	U-value meas. W/m²K
Test strip 1: iQ-Therm	0.31	6.31	0.21
Test strip 2: Calsitherm	0.43	12.80	0.42
Test strip 3: Multipor	0.31	8.76	0.29

The relationship between calculated U-values from this period equals the order calculated U-values for completely wet insulation materials (see section 4.4.4) , although this is not the case. Other sources for deviations are the surface transfer coefficients and storage effects. Calsitherm (test strip 2) shows the highest heat fluxes, as it is the material with the lowest thermal resistance. Multipor (test strip 3) is on the second position and iQ-Therm shows the lowest measured U-value. Besides the differences in the absolute values, there is also a difference in the slope of the heat flux curves. The highest slope is given for the Calsitherm test field, the lowest for the iQ-Therm test field. This is equivalent to the order of thermal resistances of the systems.

Nevertheless, all values are below the calculated U-values. One reason might be that steady-state conditions are not yet given in the experiment. This option is supported by the heat-flux curve shape, which is still rising on January 26th, when cold-side temperature is set back to 20°C. Hence, the calculated U-value includes the storage effect of the constructions, which leads to smaller values during cool-down phases and higher values during heat-up phases. The first phase is therefore not the best choice to compare real and idealized U-values. A more promising phase would be the oscillating period with harmonically fluctuating conditions of sinusoidal changing temperatures (and humidities). Heat-up and cool-down phases are represented in equivalent time fractions. The curves are given in the following graph (left). Boundary conditions as an average over February 12th to 14th are a cold-side air

temperature of 11.8°C and a warm-side air temperature of 21.7°C. The resulting heat transmission coefficients are listed in the table below, together with the results of the third period (step period).

Tab. 11.: Comparison of measured U-values for the second (oscillating) and third (step-change) test phase

Phase	Oscillating Phase		Step-Change Phase	
Construction	Heat flux meas. W/m²	U-value meas. W/m²K	Heat flux meas. W/m²	U-value meas. W/m²K
Test strip 1: iQ-Therm	2,19	0,22	4,25	0,23
Test strip 2: Calsitherm	4,31	0,44	8,23	0,44
Test strip 3: Multipor	2,88	0,29	5,74	0,31

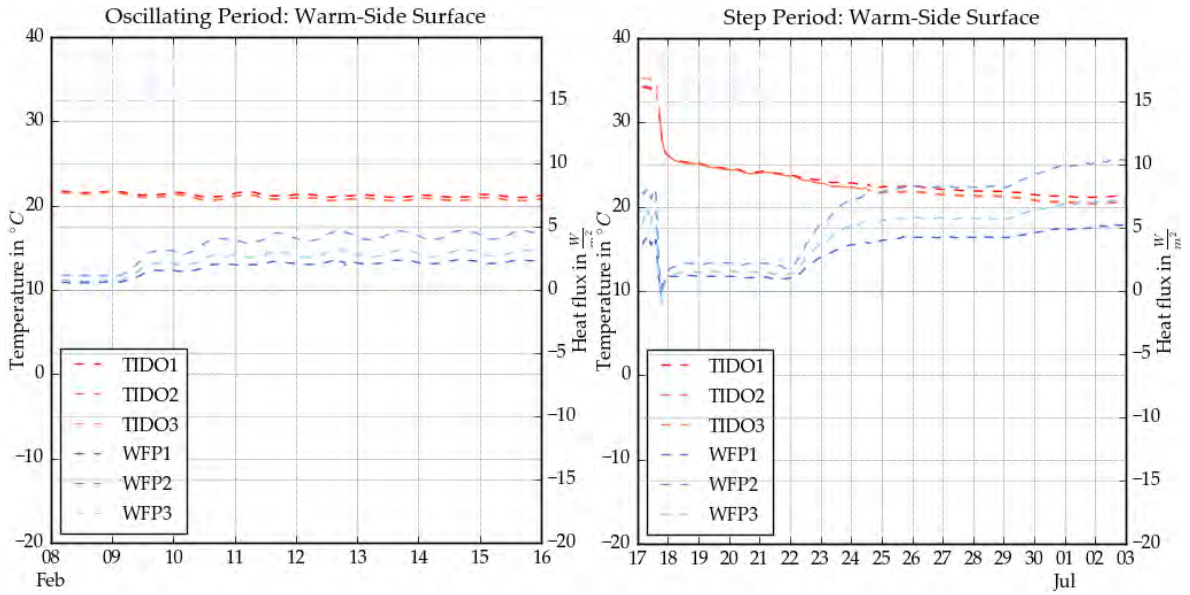

Fig. 27.: Warm-side conditions for the test period 2 (left) and 3 (right) as smoothed curves

The U-values show a good accordance between measured and calculated values for the mineral insulation board and the calcium silicate boards with differences below 0.01 W/m²K for the step change period. A huge deviation is given for the hybrid PU-insulation board (iQ-Therm) with a difference of 0.08 W/m²K between steady-state calculation and measurement. The reason for this deviation is not clear. Strongly reduced surface heat transfer coefficients might be one reason, inhomogeneous temperature conditions on the cold side and on the warm side might be another reason.

4.7.5 Response of the Joist Ends

As mentioned in the first paragraphs, each test strip in the test stand includes three different test fields, a middle field (2D-case) and two joist ends (upper and lower joist end test field). The overall six joist ends are treated in different ways in order to derive conclusions about the best-practice sealing variant. An overview of these variants is given in the following table.

Tab. 12.: Overview of the applied sealing variants in the six joist end fields

Construction	Upper joist end test field	Lower joist end test field
Test strip 1: iQ-Therm	Double layer of pre-compressed joint sealing tape and plaster connection collar	Double layer of pre-compressed joint sealing tape and plaster connection collar
Test strip 2: Calsitherm	Single layer of pre-compressed joint sealing tape and plaster connection collar	No joint sealing tape, plaster connection collar
Test strip 3: Multipor	No treatment (No joint sealing type and no plaster connection collar), open joint	Single layer of hemp joint tape and no plaster connection collar

Some joist ends are highly decoupled from the indoor climate (test strip 1) others are typically decoupled and one joist end was left completely open. Especially the reaction of the joist end timber on changes of the indoor and outdoor climate in dependency on this sealing variant is of interest because timber is sensitive to degradation processes, e.g. rot. This is evaluated with two types of sensors in the material, one type that records combined temperature, relative humidity and one type that records volumetric wood moisture content.

The first type of sensors measures the state of air in the small cavity around the sensor and does actually not return the material water content but the relative humidity in this small air cavity. Although this measurement is supposed to correlate with the measured wood moisture content, there is no direct reliable method to calculate the wood moisture content from these data series. Results of this sensor type are shown below for the upper ("O") and the lower ("U") joist end test fields in the first test period.

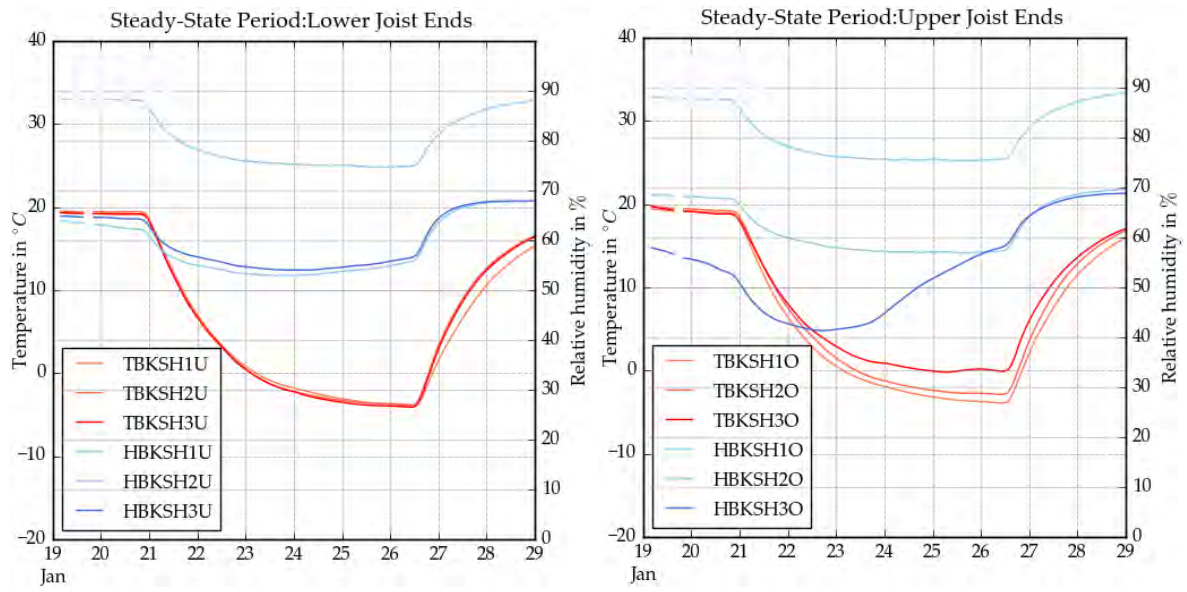

Fig. 28.: Temperature and relative humidity at the joist end front end. Left figure: lower joist ends in the test strips 1 to 3. Right figure: upper joist ends in the test strips 1 to 3.

Temperature curves show a high accordance for the lower joist ends among the three test strips. The temperature level difference, which was shown in the previous paragraph for the undisturbed wall section, is not visible in the joist ends. Otherwise, the lowest temperature level would be present in test strip 1 (iQ-Therm) and the highest temperature level in test strip 2 (Calsitherm). In contrast to the lower test fields, the variety of realized beam end tightness is larger for the upper joist ends. Test strip 3 (Multipor) was left unsealed while the Calsitherm (test strip 2) joist end was slightly sealed and the iQ-Therm joist end was as tight as in the lower field. The temperature level is therefore equal between upper and lower test field for the first test strip (iQ-Therm) and higher for the other two upper joist end

test fields and the sealed one in test field 3 (Multipor). Moreover, it is obvious that the temperature condition at the joist end is primarily influenced by the sealing variant and less by the selected insulation system.

In contrast to the temperature, which is nearly equal for all sealing variants, the relative humidity differs a lot between the sealed joist end fields. The first test strip (iQ-Therm) shows the highest relative humidity for both, the upper and the lower test field. Values touch the 90% limit at the end of the first test period and are thus critical. A further comparison is done with the absolute water content. Again, iQ-Therm shows the highest level. The higher built-in water content (shorter drying period), respectively the reduced drying potential of this construction, might be the reasons. In contrast to iQ-Therm, the other test fields are not that critical, especially the performance of the open joist end in test strip 3 (upper field) is not that critical as expected.

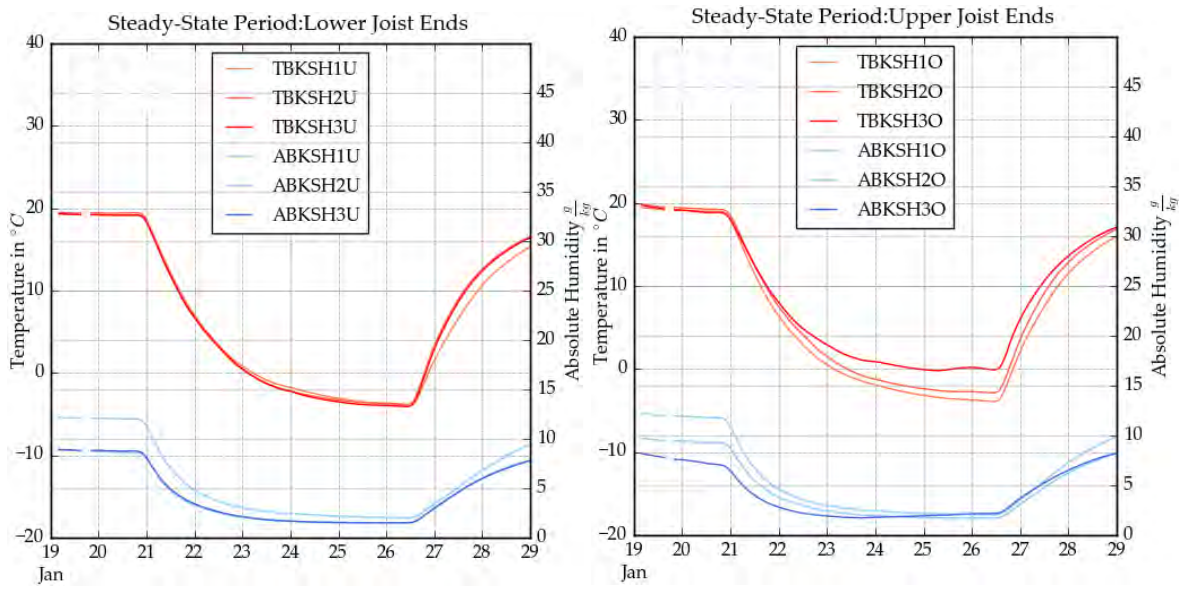

Fig. 29.: Temperature and absolute humidity at the joist end front end. Left figure: lower joist ends in the test strips 1 to 3. Right figure: upper joist ends in the test strips 1 to 3.

The same is true for the other phases where the open joist-end shows again the lowest moisture level among all joist-end fields. A change of order for very low temperatures is a consequence of the temperature levels in the joist end cavities. Due to the lower saturation level of colder air, the order of absolute moisture contents equals the order of temperature levels for the range close to saturation.

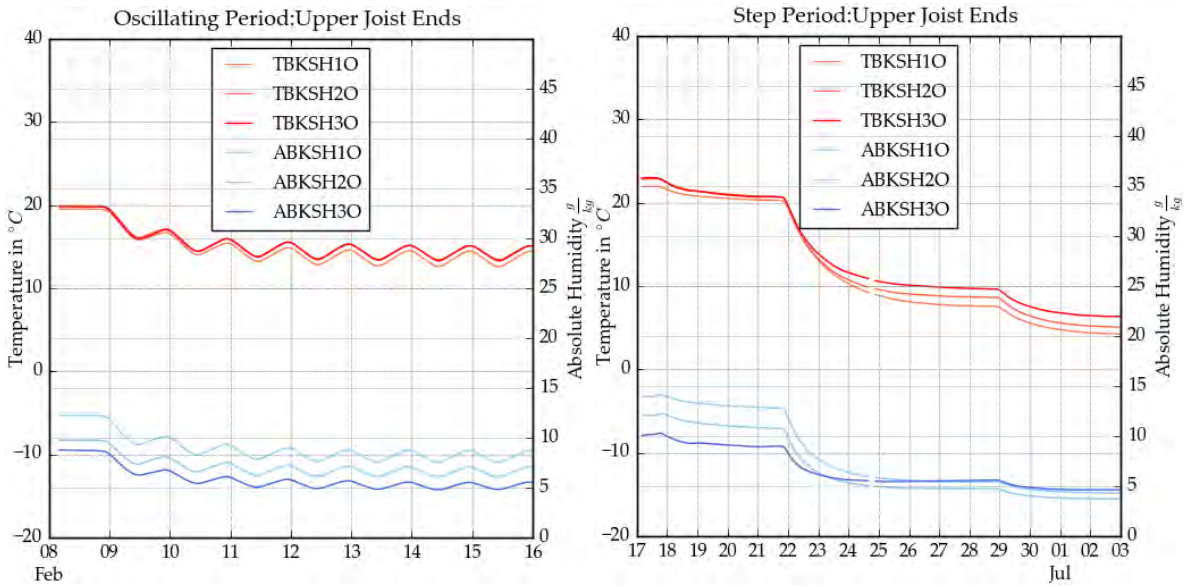

Fig. 30.: Temperature and absolute humidity at the joist end front end for the upper joist ends. Left figure: test period 2 (oscillating period). Right figure: test period 3 (step period).

Another measurement performed in the joist ends is the wood moisture content in a depth of some cm behind the joist front end. Wood moisture content measurements give the mass of water in relationship to the mass of dry wood. Recorded values are expected to range between 5 and 30%. Wood with values below 5-6 % is classified as dry timber, values above 30-35% characterize a wet material. Values around 6 to 17 mass percent should be expected for wood that is used in buildings.

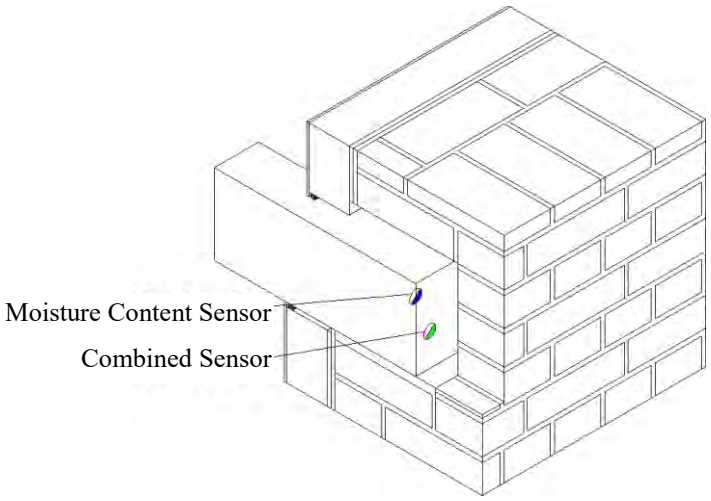

Fig. 31.: Location of mass-related wood moisture content sensor (blue/white) and location of combined temperature/ relative humidity sensor in the joist end fields.

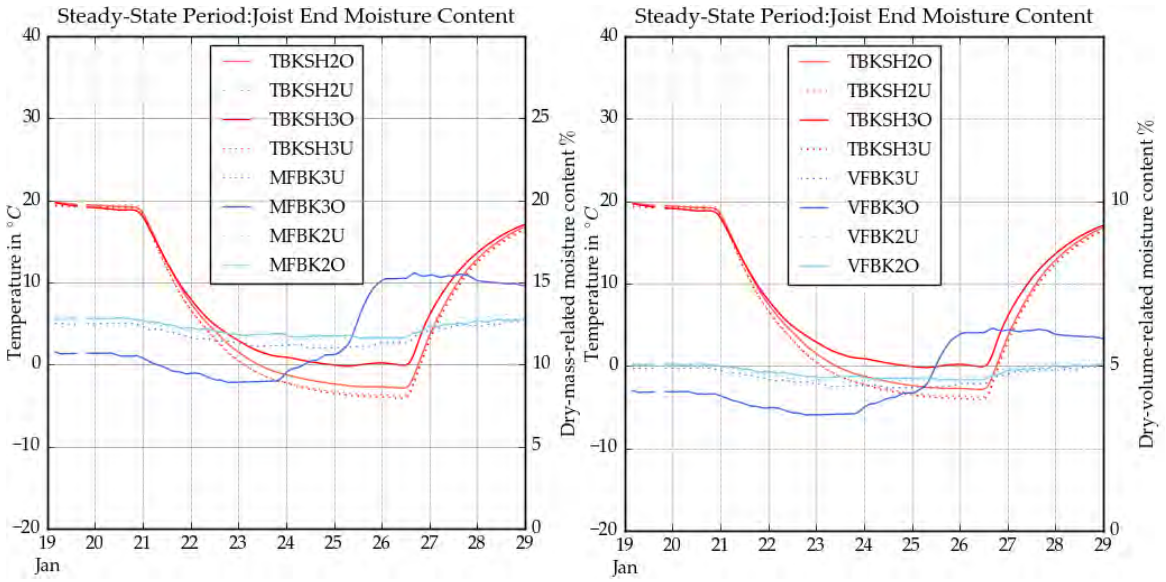

***Fig. 32.:** Measured wood moisture content (blue curves) and joist end temperature (red curves) for the steady-state period in field 2 and 3 (upper and lower test field) as smoothed curves. Left figure: mass-related water content. Right figure: volume-related water content*

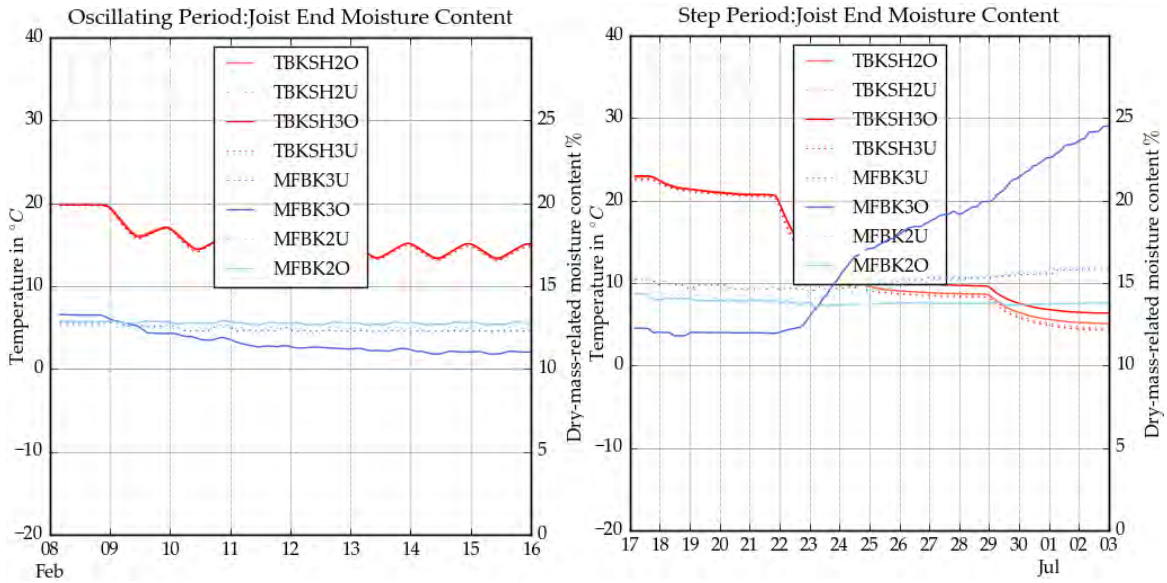

***Fig. 33.:** Measured wood moisture content (blue curves) and joist end temperature (red curves) for test period 2 (oscillating period) and test period 3 (step period)*

The first two graphs show two versions of the measured wood moisture content. Left graph shows the originally measured values of the mass-related moisture content. The second value shows the volume-related moisture content of the wood, based on the dry density of the material. In reality, an increasing wood moisture content would also cause a swelling and shrinking process, which is associated to a volume expansion of up to 10 %, depending on the wood grain direction and type. The more realistic volumetric moisture content would consequently underrun the dry values, which are displayed in the graph.

In practice, mass-related wood moisture is analysed in order to evaluate damage risks for the wooden construction. Different threshold values between 20 and 25% are recommended. Test period three (step period) shows values which are reaching the 25% level for the unsealed joist end (upper joist end) in

test field 3 (Multipor) and consequently a critical level. The derived conclusion for practice would be a necessity for a tighter connection around the joist end. On the other hand, this joist end starts at a remarkably lower moisture level, which implies that the open construction is also promoting the drying process. Consequently, the damage risk is not coercively higher for this sealing variant. However, the treatment should be decided against the background of indoor and outdoor climate conditions. If indoor conditions are expected to be uncritical (low vapour pressure) and outdoor climate will not show long cold periods, an open construction could show a sufficient performance. Otherwise, a tight construction would be a conservative solution.

One finding from the diagrams above is the non-existing correlation between relative humidity sensor measurements and wood moisture content measurement. In contrast to the results of the combined sensors (TBKSH, HBKSH), relative humidity seemed uncritical for the upper joist end in test field 3 in comparison to test field 2 for the steady-state test period. The same conclusion was true for the comparison of calculated absolute humidity. Indeed, wood moisture content is much more critical for test field 3 in comparison to test field 2 for the upper joist end in the steady-state phase. On the other hand, oscillating phase with changing drying and wetting conditions shows a beneficial behaviour of the open joist end in both measurement types, the combined sensor (relative humidity/ absolute humidity) and the wood moisture content sensor.

Conditions at the joist ends are essentially influenced by the presence of joist end sealing and furthermore affected by the applied insulation system. In this regard, it is less important how the sealing is realized. Joist ends in the test stands covered several sealing techniques, which did not show a remarkable difference under changing temperature conditions in the test chambers. Only the completely open joist end showed a quick reaction on drying and wetting conditions and reached in short-term the critical level of 20-25 mass-%.

The type of sealing could be more influential if pressure differences, e.g. caused by wind, are present. These tests are subject of the KUL laboratory research in chapter 6 starting on page 95.

4.8 HAMT Simulation

Hygrothermal simulations are performed with DELPHIN (Nicolai, Grunewald, & Zhang, 2007; Grunewald J. , 1996). DELPHIN is an engineering and research simulation software for the coupled heat, moisture, and mass transfer (HAMT) in porous building materials. It was developed in the 1990th, based on the theoretical work of Grunewald and has continuously been enhanced in several research projects so far.

Setting up the hygrothermal model in DELPHIN requires on the one hand suitable material characterizations resp. functions, arising from laboratory measurements (Grunewald, Häupl, & Bomberg, 2003) (Scheffler, Grunewald, & Häupl, 2004). Another requirement is the definition of the hygrothermal model project itself, which includes specifications of the geometry, boundary conditions, numerical settings etc. A general description of hygrothermal performance simulation is addressed by standards (EN 15026-2007) (WTA 6-5-1, 2014). These documents cover either the practical application than the specific evaluation of hygrothermal experiments.

The main hygrothermal model parameters, which have to be specified for the experiment at TUD are summarized in the list below with some corresponding estimation approaches for both, operators from practice (standard values) and advanced users. This list is not exhaustive.

Tab. 13.: List of hygrothermal simulation model parameters and a selection of estimation approaches.

Category	Parameter	Symbol	Unit	Estimation Approaches
Surface Transfer	Combined (radiative, convective)	$h_{Conv\&Rad}$	W/m²K	- Via measurement of heat flux and surface temperature - Standard values in ISO 6946-2015 (Tab. 1)
	Convective transfer coefficient	$h_{Conv\&Rad}$	W/m²K	For free convection (buoyancy-driven) - Literature: (Baehr, 2016) (VDI, 2016) - Standard values: EN 15026-2007 (Tab. 2) For forced convection - Literature: (Baehr, 2016) (VDI, 2016) - Standard values: EN 15026-2007 (Equ. 20), ISO 6946-2015 (App. A) - Measurement via θ, ε (view factors resp. geometry)
	Radiative transfer coefficient	$h_{Conv\&Rad}$	W/m²K	- Literature: (Baehr, 2016) (VDI, 2016) - Standard values: EN 15026-2013 (Tab. 2, Equ. 21), ISO 6946-2015 (App. A)
	Vapour transfer coefficient	β_{Vap}		- Literature: (Baehr, 2016) (VDI, 2016) - Standard values: EN 15026-2007 (Equ. 22)
Material Parameters	Density	ρ_S	Kg/m³	- Standard values in EN 10456
	Specific heat capacity	c_S	J/kgK	- Standard values in EN 10456
	Thermal conductivity	λ	W/mK	- Measurement acc. to EN 12939, EN 12664, EN 12677 - Standard values in EN 10456
	Moisture storage function	w (φ)	m³/m³	- Measurement acc. to EN 12571, ISO 11274, ISO 17313
	Vapour diffusion resistance f.	μ	-	- Measurement acc. to EN 12572 - Standard values in EN 10456
	others explained in Del. 2.1			
Boundary Conditions	Air temperatures	θ_{air}	°C	- Measurement acc. to ISO 7726-2001 (indoor) - Measurement acc. to ISO 17741, VDI 3786 (outdoor)
	Air relative humidity	φ_{air}	%	- Measurement acc. to ISO 7726-2001 (indoor) - Measurement acc. to ISO 17741, VDI 3786 (outdoor)
	others not included in TUD experiment			
Initial Conditions	Material temperature	θ_{air}	°C	- Measurement in WTA 4-11-02
	Material relative humidity	φ_{air}	%	- Measurement in WTA 4-11-02

others not included in TUD experiment

This chapter brings up some aspects in the definition of the HAMT project definition, which should be concerned. It starts with the explanation of some input parameters and their underlying simplifications. Furthermore, aspects of the geometric constellation and the output specification are broached.

4.8.1 Input Data: Surface Transfer Conditions

Inner and outer surface transfer conditions describe the heat transfer from the material surface to the surrounding air. Two transfer processes are included, radiative exchange and convective exchange. The consideration in form of constant coefficients, e.g. h_{Conv} & h_{Rad} $[W/m^2K]$ or the reciprocal values R_{Conv} & R_{Rad} $[m^2K/W]$, is a strongly simplified approach, which is mainly constructive for engineering assessments. For this case, standard ISO 6946:2015 recommends a constant value of $R_{Rad\&Conv} = 0.04$ $[m^2K/W]$ for exterior surfaces and $R_{rad\&conv} = 0.10$ *(upwards heat flow) … 0.17(heat flow downwards)* $[m^2K/W]$ for interior surfaces.

For laboratory tests, where detailed quantities are measured, different approaches are possible. The first, most simple, approach comprises measurements of the surface heat flux q_{Meas} $[W/m^2]$, the temperatures of the surrounding air $\theta_{Air,Meas}$ $[K]$ and the temperature of the construction surface $\theta_{Surf,Meas}$ $[K]$. This allows a computation of the combined (convective and radiative) surface heat transfer resistance $R_{Rad\&Conv}$ based on the relationship:

$$\theta_{Air,Meas} - \theta_{Surf,Meas} = R_{Rad\&Conv} \cdot q_{Meas} \rightarrow R_{Rad\&Conv} = \frac{\theta_{Air,Meas} - \theta_{Surf,Meas}}{q_{Meas}} \; [m^2K/W] \qquad \text{Equ. 1}$$

The disadvantage of this approach is the inability to distinguish between radiative and convective heat transfer. This would be problematic if surface vapour transfer coefficients are to be identified, as this cannot be done directly from the convective part. Additional measurements would be required to supplement this.

Separate measurement for the identification of both parts is the alternative. Radiative heat transfer could be identified based on the knowledge of the test room geometries (view factors), the surface materials emission coefficients and measurements of the test wall and test chamber surface temperatures. The quantification of convective heat transfer depends on the test constellation. In case of forced convection (fans), knowledge of relative air velocities is essential. In case of free convection, temperature conditions (surface and air temperature) are required.

The measurements in the joist end test facility comprise two different approaches. On the warm-side of the test wall, where free convection is assumed, measurements of surface heat flux and temperatures are recorded. Surface temperature sensors and heat flux boards were placed in each middle part of the three test wall strips. The same height was chosen for the air temperature sensor in the warm chamber. On the test wall surface towards cold-side chamber, measurements of the chamber and wall surface temperatures are available for the computation of radiative transfer. Convective transfer is estimated based on temporal air velocity measurements.

An extract of the heat flux and temperature difference measurement is displayed in the following graph. It is obvious from the dot clouds around the linear approximation function that a constant value for the combined heat transfer is not given. This could be a consequence of varying convective conditions as well as varying radiative conditions. A distinction is not possible bases on the available measurement results.

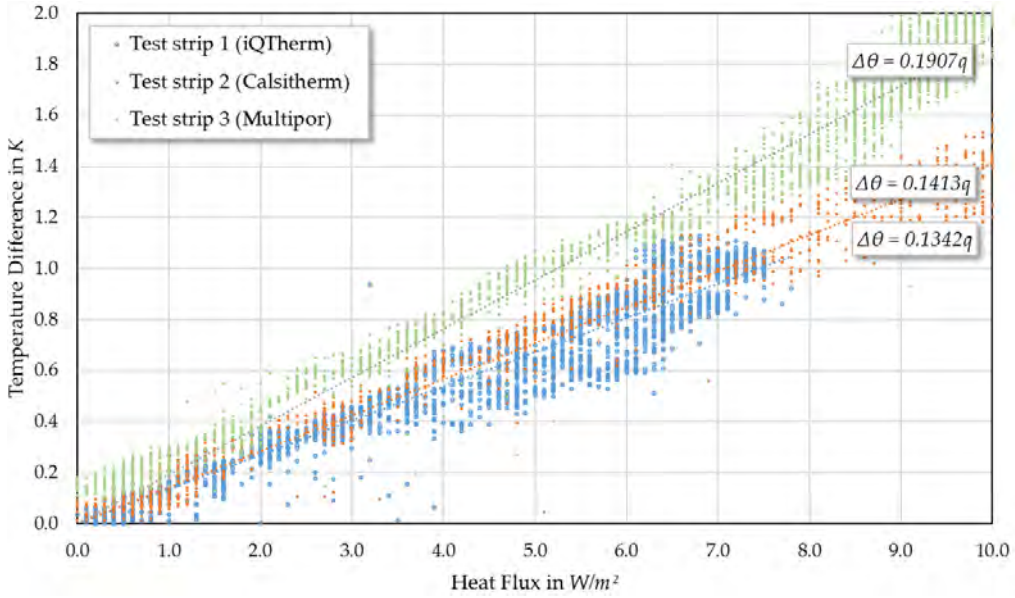

Fig. 34.: Approximation of the measured values with the linear function ending in the root point (f(0)=0) in order to identify the function slope resp. surface thermal resistance for the test period 1 (steady-state period in January 2016)

An even higher variation of surface transfer coefficients is visible in the comparison of the three test periods (steady state period (SS), oscillating period (O) and step period (S)). The highest resistance is given for the harmonically fluctuating conditions in the second test period (O). Lowest values of *0.11 to 0.19 [m²K/W]* and thus close to standard ISO 6946- values of *0.10 to 0.17 [m²K/W]* were computed for the steady-state period (SS). There is furthermore a difference between the test strips. This can partially be attributed to the differing temperature conditions (heat transfer resistances) in the test strips. This leads to a tendency of lower values of the convective transfer coefficients for the Calsitherm test strip with the lowest heat transfer resistance and higher surface resistances for the other test strips in the average of all test periods. Latter are characterized by a smaller temperature difference between surface and surrounding air (iQ-Therm, Multipor). Consequently, the driving force for the buoyancy flow is lower for these test fields and the convective surface heat transfer coefficient is higher resp. resistance lower.

Tab. 14.: Results from the surface and air temperature measurements on the warm side of the test stand for three different periods of nearly stable conditions (SS), fluctuating conditions (O) and stepwise changed conditions (S) on the cold side.

Test period	Test field	$\Delta\theta_{Surf\text{-}Air}$ [K]	q_{Surf} [W/m²]	$R_{C+R,Inside,meas}$	$R_{C+R,Inside,measLinear}$
SS: Jan 2016	iQTherm	0.530	4.030	0.115	0.134
	Calsitherm	1.119	7.908	0.148	0.141
	Multipor	1.047	5.423	0.377	0.191
O: Feb 2016	iQTherm	0.458	1.809	0.287	0.239
	Calsitherm	0.773	3.570	0.235	0.210
	Multipor	0.808	2.394	0.377	0.324
S: Jun 2016	iQTherm	0.717	3.265	0.267	0.196
	Calsitherm	1.170	6.401	0.204	0.174
	Multipor	1.075	4.480	0.276	0.226

Cold-side heat transfer coefficients are identified from the measurement of surface temperatures (right figure blow) and the measurement of air velocity (left). As already mentioned in the previous paragraph, surface temperature difference is strongly time and location dependent.

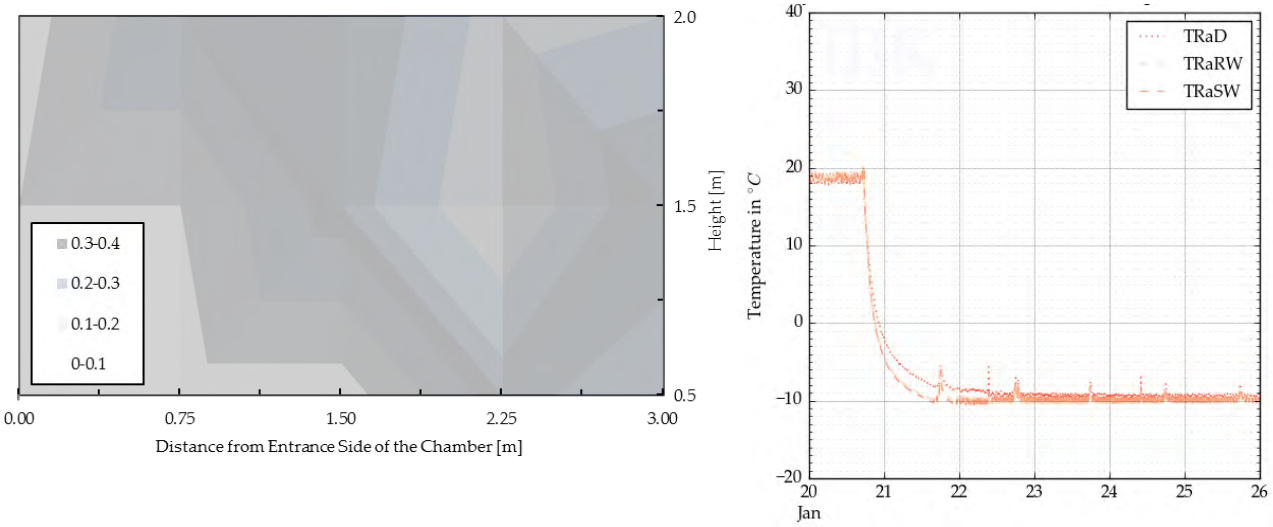

Fig. 35.: Measurements for the approximation of thermal transfer coefficients for the cold side: left figure: in-situ air velocity measurements (ranges in the legend given in m/sec). Right figure: Surface temperature measurements at three different points in the chamber (TRaD: ceiling, TRaRW: backside wall, TRaSW: side wall)

The net exchanged heat flux is computed based on the geometrical situation and the emission coefficients ε of the surfaces. Assumed ε-values are 0.93 for the wall surface (masonry) and 0.80 for the OSB-board surfaces at the inside of the cold chamber. The net heat flux between wall and surrounding chamber envelope is calculated based on the view factors for the middle point of the wall towards ceiling, side walls and back wall of the chamber. The view factors are computed as fractions of the solid angle taken by each exchange surface for the middle point of the wall (no distinction of measurement points) via trigonometric functions. They are 0.47 for the back wall, 0.14 for the ceiling/floor and 0.25 for both side walls (0.125 each). Radiant fluxes from the test wall surface to the environment are summarized below for the three different test periods.

Tab. 15.: Computed heat fluxes and derived surface radiative transfer resistance due to measured surface temperatures at the test wall and at the cold-side chamber surfaces of ceiling, sidewalls and back wall for all three test periods.

Test period	Test field	$q_{Wall\text{-}Ceiling}$ [W/m²]	$q_{Wall\text{-}SideWall}$ [W/m²]	$q_{Wall\text{-}BackWall}$ [W/m²]	$q_{Sum,Rad}$ [W/m²]	$R_{Sum,Rad}$ [m²K/W]
SS: Jan 2016	iQTherm	0.81	3.97	3.82	8.59	0.38
	Calsitherm	1.14	5.09	4.74	10.96	0.48
	Multipor	1.71	7.13	6.70	15.54	0.68
O: Feb 2016	iQTherm	1.62	5.79	5.31	12.72	0.56
	Calsitherm	1.85	6.63	6.10	14.57	0.64
	Multipor	2.07	7.43	6.85	16.35	0.72
S: Jun 2016	iQTherm	1.49	4.53	4.11	10.12	0.45
	Calsitherm	1.24	3.65	3.29	8.17	0.36
	Multipor	1.64	5.10	4.64	11.38	0.50

The derived surface radiative heat transfer resistance is related to the average air temperature difference between cold and warm side chamber for each test period (Phase SS: 22.7 K, Phase O: 10.2 K, Phase S: 12.7 K). It is obvious that all values are widely below the standard values for radiative heat transfer of about $h_{rad} \approx 4$ to 5 W/m²K (according to EN 15026 and EN 6946) and respectively above the

corresponding heat transfer resistance $R_{rad} = 1/ h_{rad}$ of about 0.2 to 0.25 m²K/W. This traces back to the small temperature difference between test wall surface and climate chamber walls. In a real building neighbourhood with long-wave exchange towards sky dome and other objects, much higher radiant heat transfer coefficients are to be expected.

Convective heat exchange due to air velocity at the surface is a tricky issue for the climate chamber. In general, the thickness of the fluid boundary layer at the wall is proportional to the convective heat transfer resistance; an increasing R-value means a thicker boundary layer. Hence, the corresponding temperature field at the surface of the test wall is a consequence of the air velocity field. There are solution approaches for idealized cases, assuming for instance laminar boundary layer for an airflow, which was longitudinally streamed along the wall. This is not the case for the given wall where we have neither an impingement flow nor a parallel stream. Empiric models are also available to cover realistic conditions inside of the buildings. Some approaches for the convective coefficients due to volumetric flow rates based on experiments are given in (Spitler, Pedersen, & Fisher, 1991) (Fisher & Pedersen, 1997). They suggest the following relationship for a room with an inlet at the side wall to compute the resulting convective heat transfer coefficient for the vertical wall (Spitler, Pedersen, & Fisher, 1991, S. 509):

$$h_{conv} = 1.6 + 92.7 \cdot \sqrt{\frac{V_{Flow} \cdot U_0}{g \cdot V_{Room}}}$$

The volume flow rate V_{Flow} the can be estimated with 0.6 m³/sec in the experiment, the velocity of the supply air U_0 was measured directly behind the air outlets of the vents and varies between 2.3 – 2.5 m/sec for the two smaller vents (diameter about 25 cm) and 4.5 m/sec for the bigger vent (diameter about 40 cm). The volume of the chamber V_{Room} is about 10.3 m³ and the gravitational acceleration is 9.81 m/sec². This leads to a resulting convective heat transfer coefficient of about 12 to 17 W/m²K.

The finding from this investigation is the quantification of the overall heat resistance on both sides of the test stand. It's stated from the heat flux and temperature measurements on the warm side of the chamber that the combined heat transfer resistance varies between 0.13 and 0.32 m²K/W ($h_{con+rad}$ = 3.1 to 7.7 W/m²K) with the highest average values in the Multipor test strip and the lowest ones in the Calsitherm test strip. Identified heat transfer resistances on the cold surface of the test wall are amounted to a radiative resistance of 0.38 to 0.72 m²K/W (h_{rad} = 1.3 to 2.6 W/m²K) and a convective resistance of 0.06 to 0.08 W/m²K (h_{con} = 12 to 17 W/m²K). Both parts sum up to an overall cold-side transfer coefficient of $h_{con+rad}$ = 13.3 to 19.6 W/m²K and corresponding resistance of 0.05 to 0.075 W/m²K.

The relationship between (convective) heat and mass transfer is assumed to equal the Lewis relation of $\beta_m = \alpha_m/(\rho \cdot c_P) \cdot Le^{m-1}$ (Baehr, 2016, S. 94). The dimensionless Lewis number Le is assumed to be 0.87 [-] for vapour in air according to (Baehr, 2016, S. 95, Tab. 1.5), m is assumed to be 1/3, density of water at 10°C is 999.7 kg/m³, specific heat capacity 4195 J/kgK. The equation can hence be simplified for the application of vapour transfer coefficient as $\beta_{vap} = \alpha_{conv} \cdot 2.6 \cdot 10^{-7}$. According to this approach, vapour transfer coefficients are for the cold side are around $3 \; to \; 5 \cdot 10^{-6}$ m/sec and under substraction of an estimated radiative part of 2 W/m²K for the warm side $2 \; to \; 13 \cdot 10^{-7}$ m/sec.

4.8.2 Input Data: Material Properties and Functions

Material parameters are not explained in detail here as this is addressed by work package 2 of the RIBuild project. This paragraph should just illustrate one aspect of uncertainty, which is caused by material data sets in a HAMT simulation tool. Material properties are measured in the laboratory in form time series or single values. Each measurement of a single sample of a building material includes uncertainties in the execution of experiments, the uncertainty range of the measurement devices and sensors, possible faults in the data transfer from the sensors to the final analysis tool etc. Furthermore, building materials themselves are irregular and one sample could produce other results than the next sample. These random sources of error should be minimized by the multiple repetition of each experiment. Therefore, each material is measured in form of numerous samples for each lab test. Results for these series are given below for two selected materials of the test stand.

Tab. 16.: Uncertainty range of material properties (equation parameters) due to laboratory measurements results variation for two exemplary materials of the test stand at TUD.

Material	Parameter	symbol	unit	Measured values		
				minimum	average	maximum
Insulation	Vapour diffusion resistance factor	μ	[-]	6.4	6.7	7.2
	Thermal conductivity (dry material)	λ	W/mK	0.043	0.044	0.045
	Water uptake coefficient	A_w	$kg/m^2s^{0.5}$	0.0052	0.006	0.0068
	Bulk density (dry material)	ρ	kg/m^3	92.9	98.5	106.7
Masonry	Vapour diffusion resistance factor	μ	[-]	13.7	14.2	14.7
	Thermal conductivity (dry material)	λ	W/mK	0.82	0.87	0.91
	Water uptake coefficient	A_w	$kg/m^2s^{0.5}$	0.20	0.23	0.26
	Bulk density (dry material)	ρ	kg/m^3	1710	1780	1850

Random errors will solely be centered if extreme runway value errors are excluded. This is partially given with the manual check of lab data by an experienced laboratory assistant resp. researcher, e.g. via comparison of given scatter and idealized (e.g. Gauss) distribution. In addition to random errors, there is a risk of systematic errors, which arise for example from the measurement technique itself, inappropriate calibration procedures, sensor drifts or scaling errors. Given the example of thermal conductivity measurement, standard deviations are to be quantified with ± 10% and can rise up to 30% and more depending on the measurement technique, selected boundary conditions, nature of the material (e.g. anisotropic materials), sample preparation etc. (Wulf, 2009).

4.8.3 Simulation Results

Another period than those explained in the previous paragraphs, was chosen for the analysis of simulation outcomes. This phase in March 2016 is characterized by a sudden temperature reduction from 20°C down to -10°C for several days and afterwards a temperature increase back to 20°C. The following simulation results are focused on the middle test field (calcium silicate).

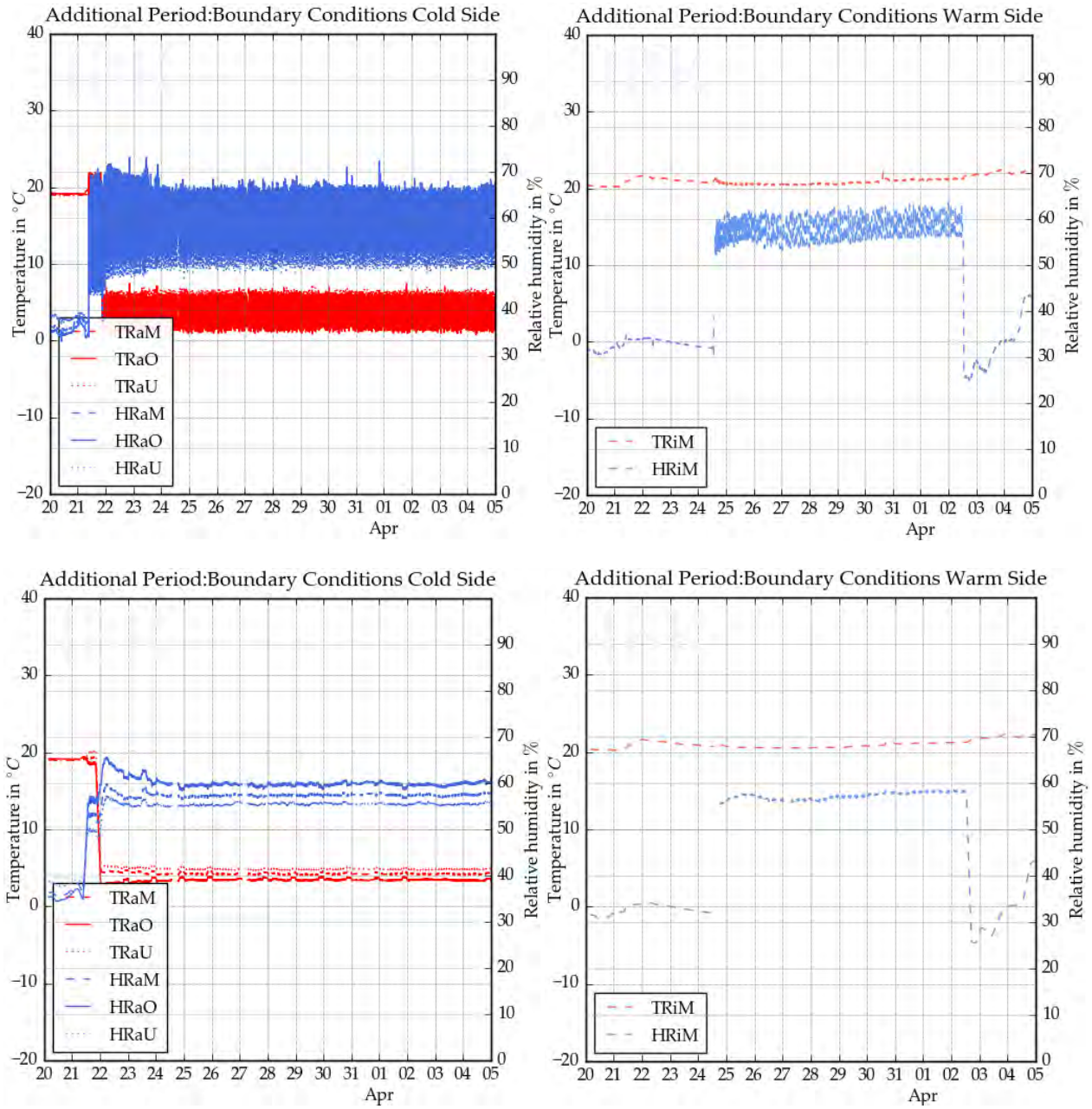

Fig. 36.: Boundary conditions for the phase which was chosen for hygrothermal simulation of test strip 2 (calcium silicate). Left graphs show the original measurement results (upper left: cold side original, lower left: cold side original), right figures show the 50-value (5-Minute interval) running mean (upper right: cold side smoothed, lower right: warm side smoothed)

Initial simulations were provided for the evaluation of the undisturbed middle-field of the test wall (1D resp. 2D wall section). An identification of uncertain simulation parameters like the surface heat and moisture transfer coefficients was done via GenOpt as explained in paragraph 6 resp. published in (Freudenberg, Ruisinger, & Stöcker, 2017). The hygrothermal model is therefore presumed to be calibrated. The identified parameters are adopted by the following hygrothermal simulations.

A preliminary evaluation was addressing the exactness of the revised DELPHIN model. This was already proved on a basic level by a number of validation cases (Sonntag, Nicolai, & Vogelsang, 2013). Nevertheless, these cases are not covering all dimensions (hygric, 2D). Therefore, they are complemented with cases that are more complex. The comparison between DELPHIN 5 und 6 was

carried out for the lower joist end detail in the test stand. A vertical section with simplified masonry structure modelling is displayed in the following graph.

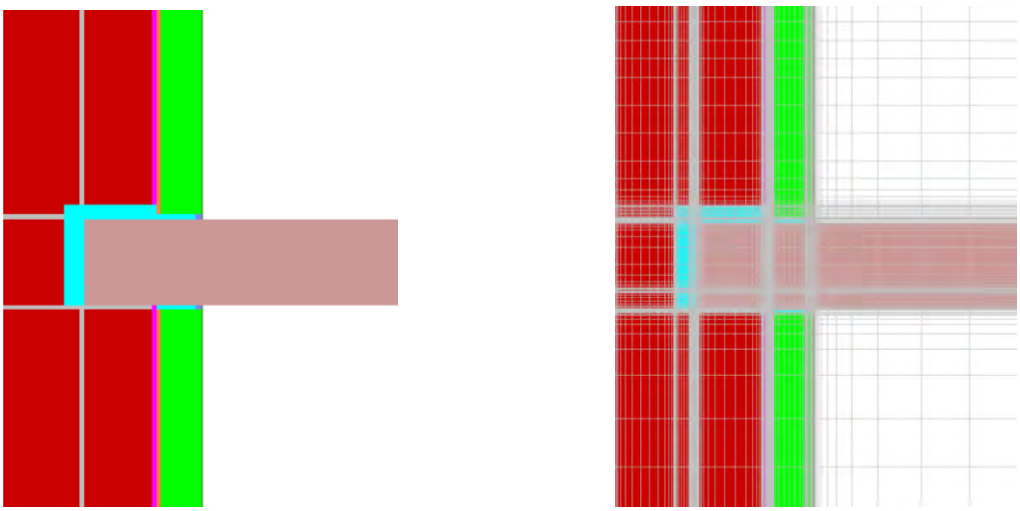

Fig. 37.: Screenshot of the DELPHIN 5 model view: vertical section through the lower joist end in test strip 2. Left figure: geometry model. Right figure: discretized model (about 8000 grid elements).

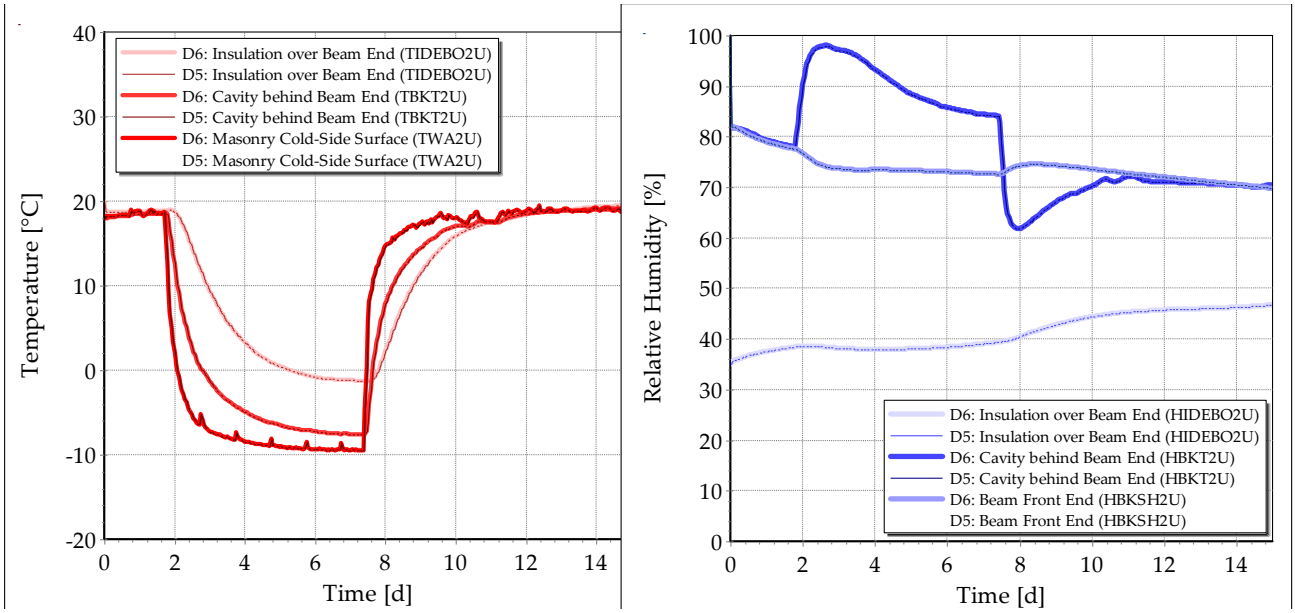

Fig. 38.: Validation test for DELPHIN 6 with DELPHIN 5 simulation results for different sensor positions in test strip 2. Lower joist end field. Left figure: three temperature positions. Right figure: three relative humidity positions.

The diagrams above show well-matching curves and thus very small differences between the simulation outcomes of DELPHIN 5 and 6. The maximum difference mounts up to 0,5 K and 0,12 % relative humidity and is therefore neglectable.

Further simulations with DELPHIN included a variation of different parameters, which are partially combined. Other parameters like the surface transfer coefficients were adopted from the optimization procedure result. Furthermore varied parameters are:

- Application of longitudinal, radial and tangential material data sets for spruce
- Variation of hygric and thermal surface transfer coefficients in the beam end cavity
- Consideration of long-wave radiation exchange in the cavity (field condition)

- Computation of (cavity-) air thermal conductivity via temperatures of the cavity-directed surfaces and the beam support geometry
- Variation of the spruce thermal conductivity

These parameter studies are mainly conducted with DELPHIN 5, due to the fact, that most of the field conditions were not implemented at that time in DELPHIN 6.

The following figure shows the comparison of the two-dimensional temperature (left) and the moisture field (relative humidity, right figure) after the seventh day of the simulation phase. It shows a spacially very limited impact of the beam end itself on the surrounding masonry. The disturbance of temperature and humidity field penetrates only about 30 cm into the adjacent construction and shows its strongest impact in the middle of the detail cross sections, its lowest impact at the surface of the involved constructions. Because the beam is thinner in horizontal section than in the vertical section and the transport characteristics of the material functions are reduced in tangential resp. radial grain direction compared to longitudinal direction, the impact in the absent third dimension (horizontal section) is supposed to be even smaller there compared to the vertical section.

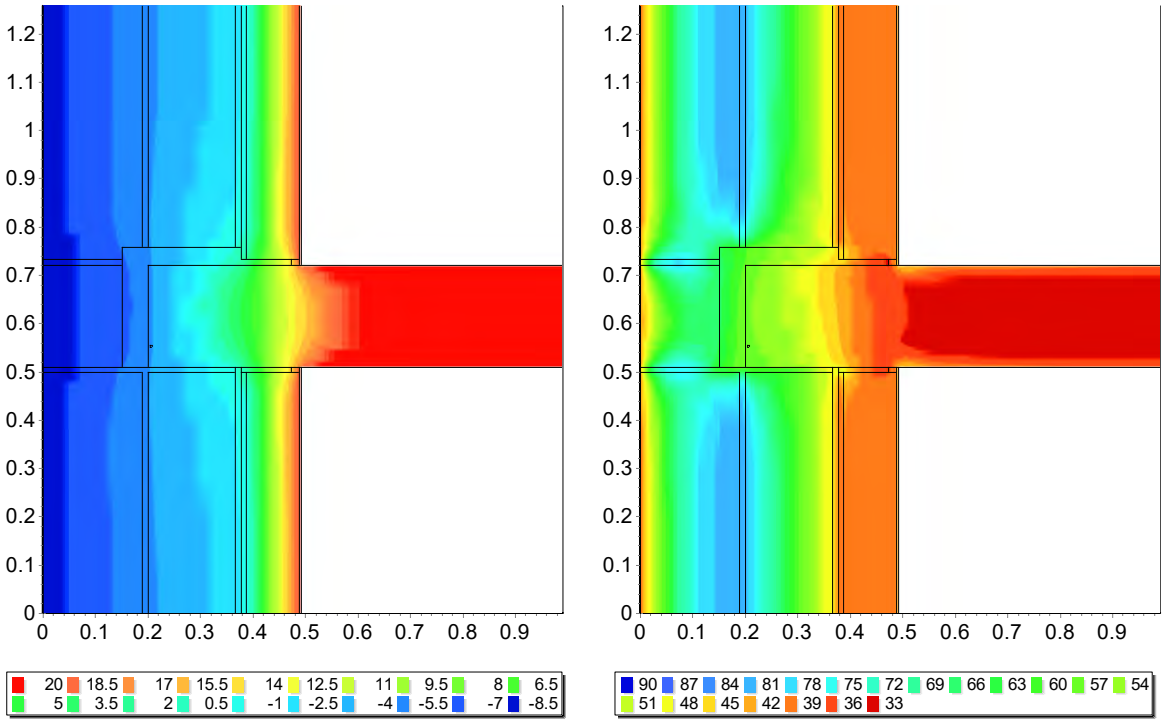

Fig. 39.: 2D-Color map plot of the temperature field (left) and the relative humidity field (right) on the seventh day of the simulation period gained with DELPHIN 5. Assumed material file data set for the spruce was those for the longitudinal grain direction.

The general impact of the beam end on the temperature field is a decreased temperature level at the exterior surface and an increased temperature level towards room side compared to the surrounding construction. Despite the reduced temperatures in the beam-external masonry, the relative humidity level is smaller in this area compared to the undisturbed masonry.

The following paragraph includes an evaluation of the beam-end material data set on the results. Material data sets are varied in regard to the grain direction of the wood. A general description of the

data set differences is given in a previous paragraph (4.3). The versions with the radial data set are not included in this overview as they yield only a marginal difference to the tangential results.

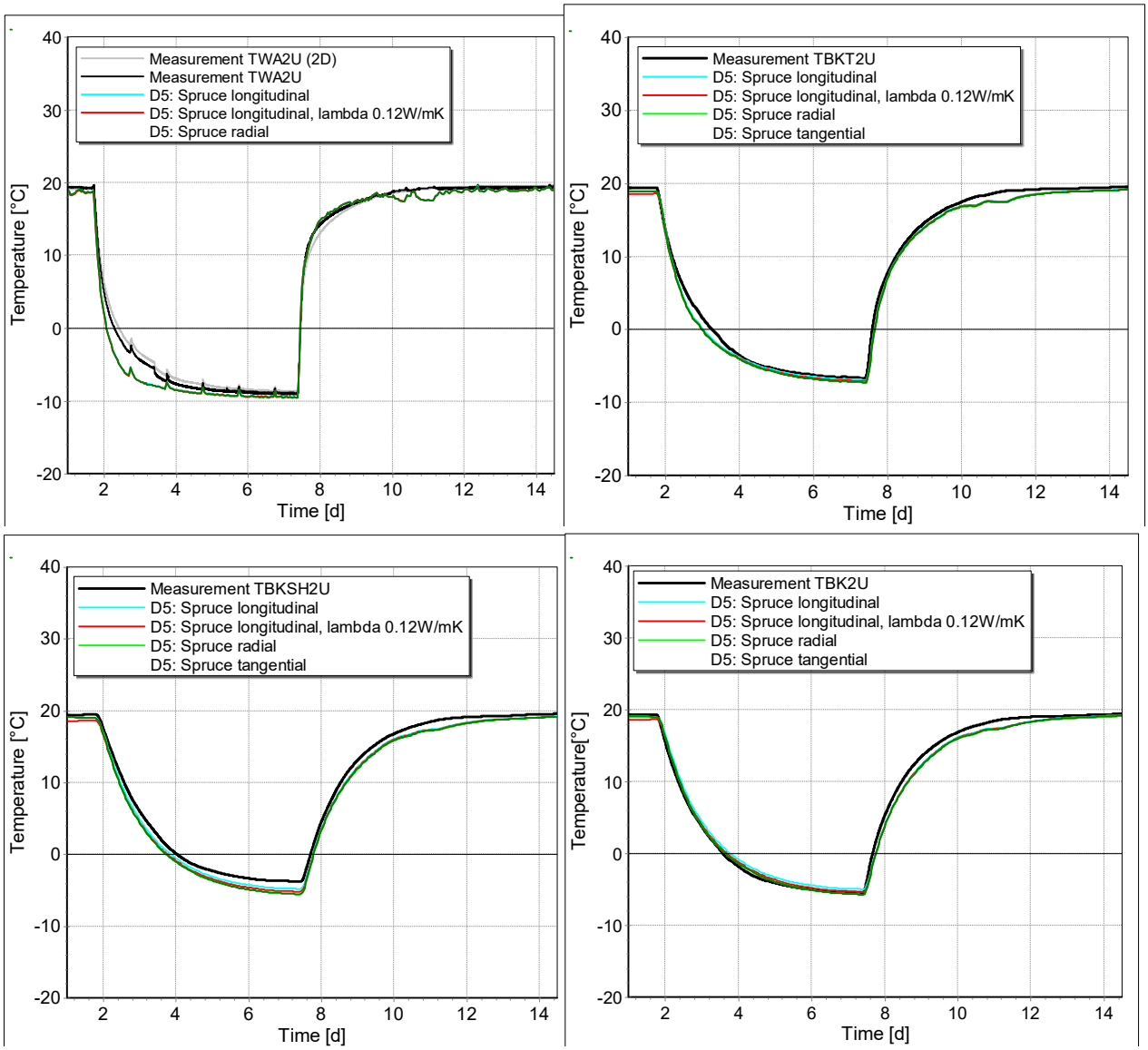

Fig. 40.: Comparison between measured and simulated temperature for different positions in the joist end test field (test strip 2. lower joist-end). Upper left figure: surface-near temperature in the masonry. Lower left figure: temperature in the beam front end. Upper right figure: at the masonry surface towards beam end cavity. Lower right: surface temperature at the beam front end surface.

Some millimetres behind the cold-side surface (sensor TW2U), the temperature difference between measurement and simulation rises to about 3K, which is the highest difference in the measurement period. During the rest of the phase, especially at the end, temperature differences reduce to a level of 0.5 K. At that time point, the grain-dependence of material properties are not relevant any more. At the vertical surface (front end of the beam, sensor TBKT2U), the difference is even smaller. After six days, the differences between measurement and simulated curves are about 0.5 K (tangential material data set) resp. 0.2 K (longitudinal material data set). For these curves, the difference between measured and simulated curve is also smaller in the cool-down phase.

Within the construction, highest temperature differences were noticed for the sensor in the beam front end (sensor TBKSH2U). They amount to 1 K for the simulation with longitudinal material data set and

about 2 K for radial resp. tangential data set. Surface measurements at the joist end show a slightly better accordance with measurement results with about 0.5 K deviance. Again, the cool-down process is not reflected in a comparable quality and shows a retarded reaction. An improvement was hereby achieved with a modification (reduction) of the thermal conductivity of spruce for the longitudinal material characteristics.

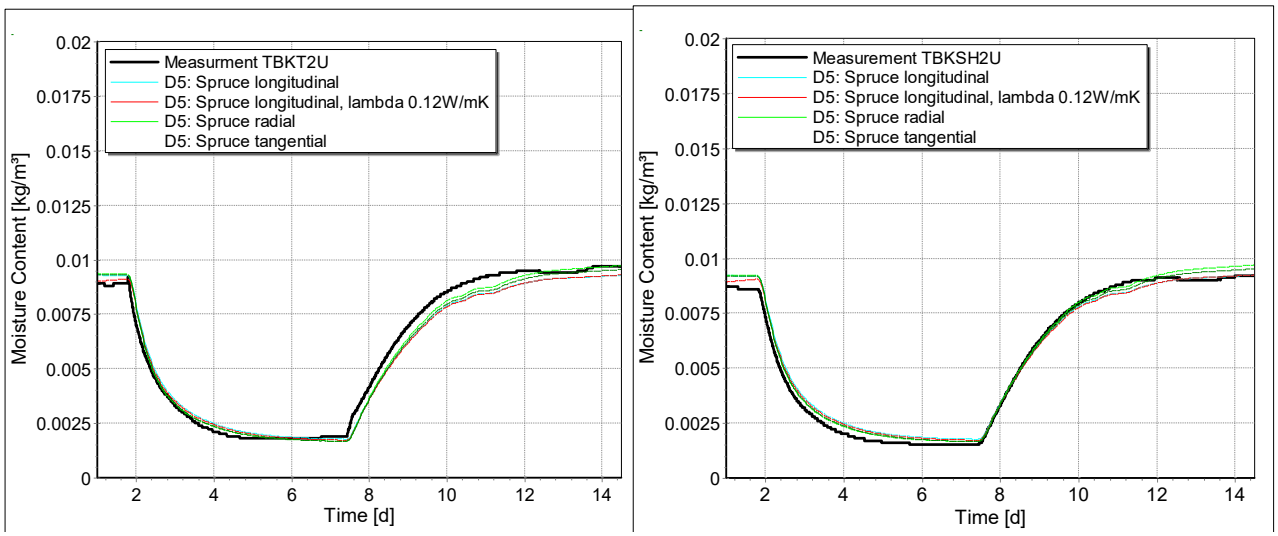

Fig. 41.: Comparison between measurements results and simulation model results for different points at the end of the beam front end and for the volume-related moisture content. Left figure: end of the joist end cavity. Right figure: in the wood of the joist end. Both graphs show results of the lower joist end detail in test strip 2 (calcium silicate).

Measurements in test strip 2 included also the moisture content in the wood of the beam close to the font end face. The accordance between simulated and measured curves is pleasing for both sensors with differences of less than 0.5 g/kg. The simulated variants differ marginally and are therefore not deeper analysed.

In accordance to the findings from the simulation study with different material directions of the wood, versions with different field models achieve a good accordance for the moisture content of the beam end. A rather small improvement was given with an exclusive increase of surface transfer resistances between the cavity-directed surfaces and the cavity-enclosed air. A higher improvement was achieved with a combination of these variants, namely the implementation of long-wave exchange model for the cavity with adjusted thermal conductivity of the cavity air and increased surface resistances at the cavity-directed areas. These results are shown in the following graphs.

The graphs show very small differences at the vertical surface of the beam front end with about 0.2 resp. 0.5 g/m³ after six resp. nine days for the version with an adjusted thermal conductivity of the cavity air. A reduction of accordance is reached with the combination of this approach with increased cavity surface resistances. The curves are nearly perfectly matching if both approaches are combined with the computation of long-wave heat exchange in the cavity. The deviations between measurement and simulation results are in all cases very small at the end of the simulation period. They vary between 0.2 g/kg for the first version over 0.4 for version two and 0.1 for the last version with combined approaches.

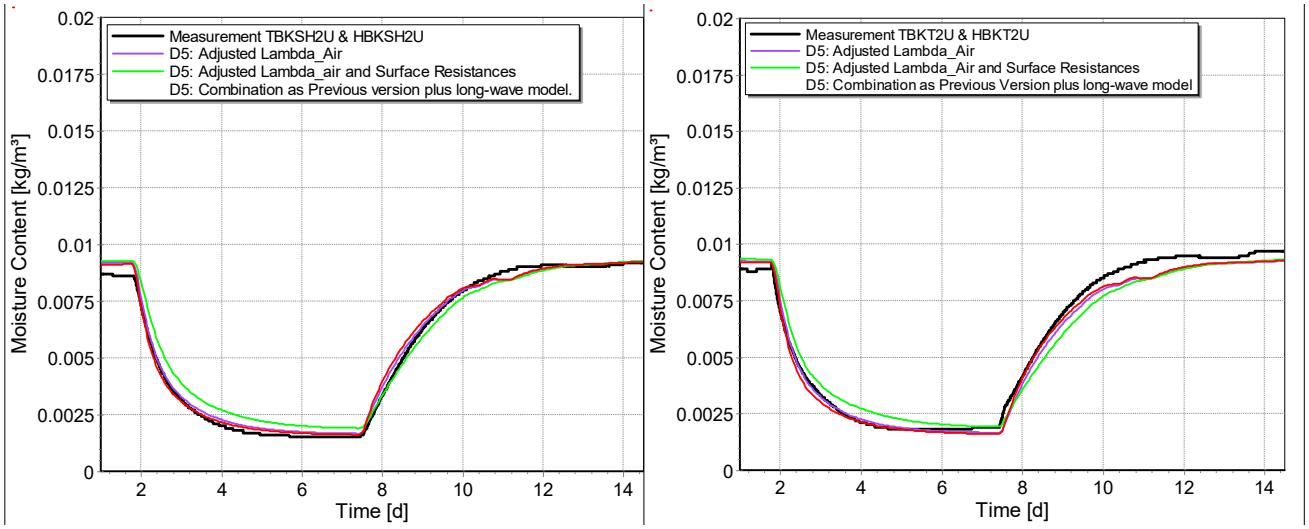

Fig. 42.: Comparison between measurement and simulation variants with different field models for sensor points at the beam front end. Left figure: front face of the beam end. Right figure: sensor in the beam end. Both graphs display the situation in the lower test field of test strip 2 (calcium silicate).

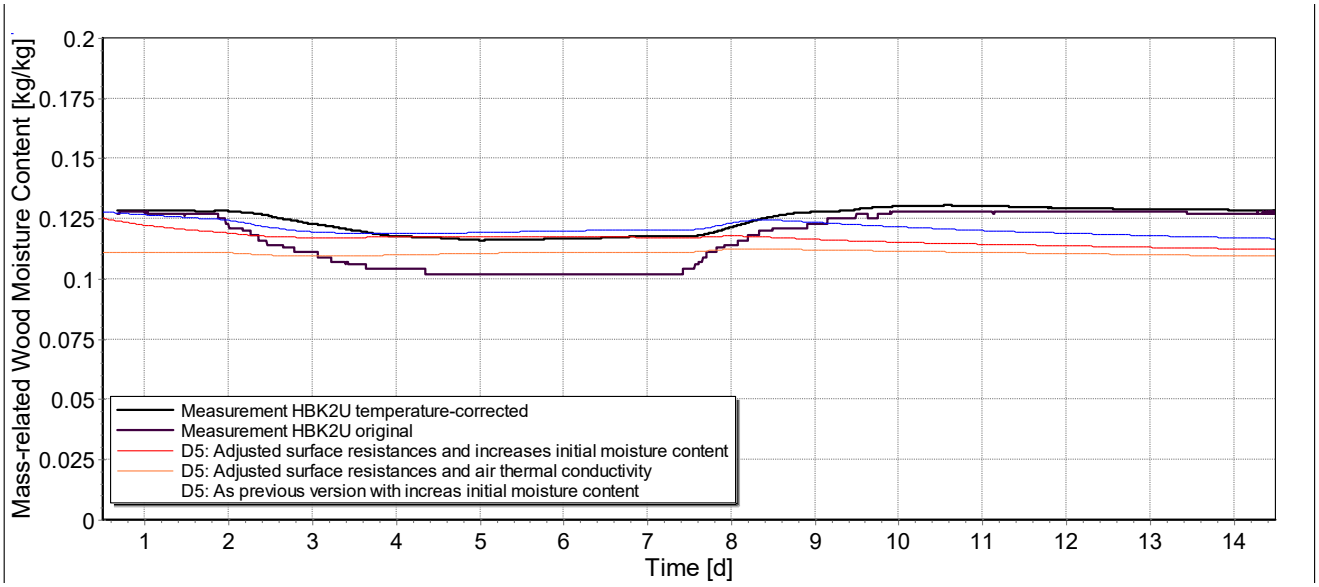

Fig. 43.: Comparison between measured and simulated wood moisture content with different field models and initial conditions for test strip 2 (calcium silicate), lower joist end detail.

The comparison between wood moisture content measurement and simulation shows the high impact of inappropriate initial conditions. The induced underestimation in the previous graph amounts to 2 Mass-% for the second simulation version in the legend list. The correction of wood moisture content was necessary, as the supplementing temperature sensor for the resistance sticks was not placed directly in the adjacent area. Therefore, another sensor series was used to compute the corrected moisture content measurement. A remaining error source is nevertheless expected because of the fact that this type of sensor is calibrated for specific wood materials and sorption characteristics.

All previous comparisons between measurement and simulation show a sufficient accordance between the 2D-simulation results and the measured curves in the test stand. Especially the risk-guiding moisture content (wood moisture content and combined sensor measurements) yielded realistic results. It was furthermore shown that a multitude of input parameters and specific models is available and suitable to improve the accordance additionally. From the comparison of different material data sets for

the wood, the general recommendation is the application of longitudinal material characteristics as they represent the real behaviour of the joist end in a sufficient way. The assumed thermal resistance at the cavity-directed surfaces has also a noticeable impact and should not exceed a level of 0.5 m²K/W for the derived simulations. A computation of thermal conductivity of the air around the joist end in order to consider the convective processes there, was also partially improving the agreement.

In completion to the two-dimensional simulation with DELPHIN 5, further investigations with three-dimensional simulations (DELPHIN 6 extension) are summarized in the following paragraph. Setting up the three-dimensional model starts with a reduction of the computation grid elements. For the joist end detail, the section level through the vertical symmetry axis of the beam end appeared most promising. The initial number of elements (about 600,000) was thereby reduced by 50%. Further grid reduction was achieved with a smart discretization towards adiabatic boundary levels.

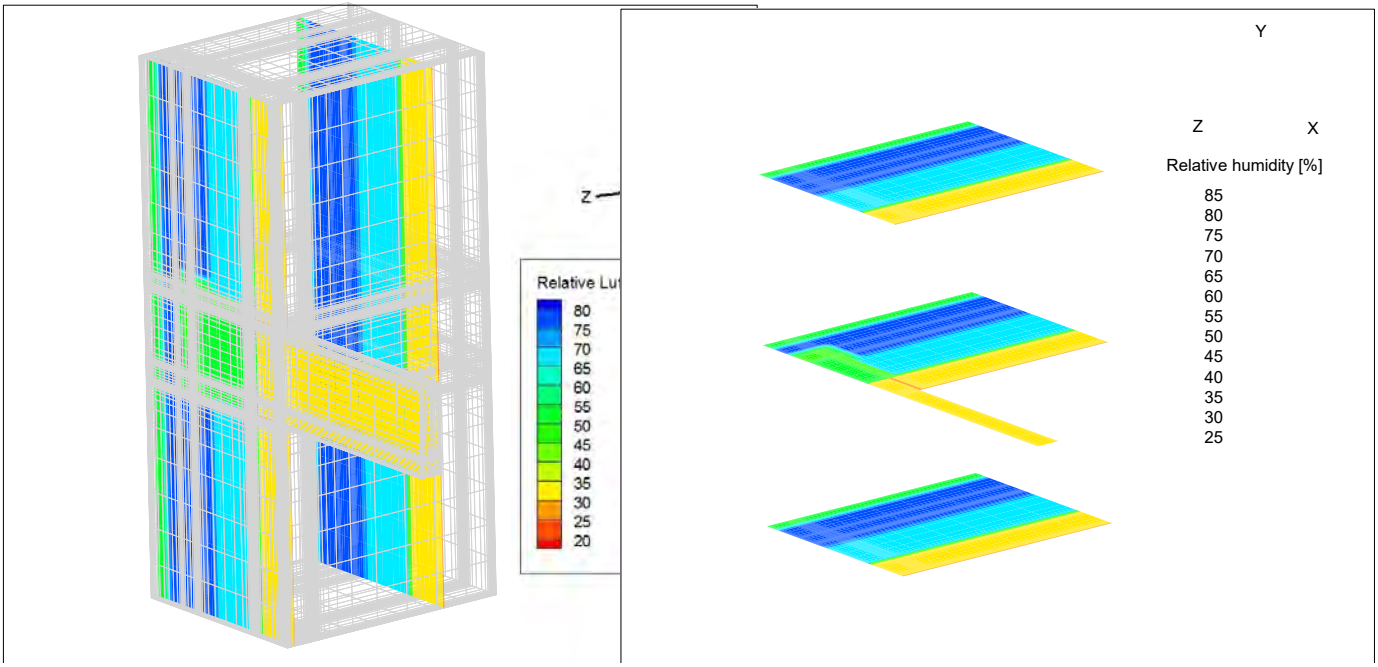

Fig. 44.: Initial conditions for the relative humidity in the 3D-DELPHIN model for the lower joist end detail in test strip 2 (calcium silicate). Left figure: isometric view with implemented vertical sections at two positions. Right figure: Horizontal sections at different heights.

The initial conditions in this graph were defined in accordance to the measurements in the test stand. Different temperature and sensor positions allowed a detailed identification of initial conditions. The previous figure shows only the relative humidity. This ranged from a minimum level of 35% in the insulation layer, over 55% around the joist end, up to 82% in the middle of the masonry. Temperature conditions ranged from about 19.5°C to 20°C and were quite homogeneous. They are therefore not displayed in a separate graph.

The following figure shows the resulting temperature conditions in the construction after a simulation period of about six days. Again, the left figure shows vertical sections at two positions, one section through the beam end and one section through the wall in the boundary area. The right-hand figure shows horizontal sections through the detail, one above the beam end, one section through the middle of the beam end and one below.

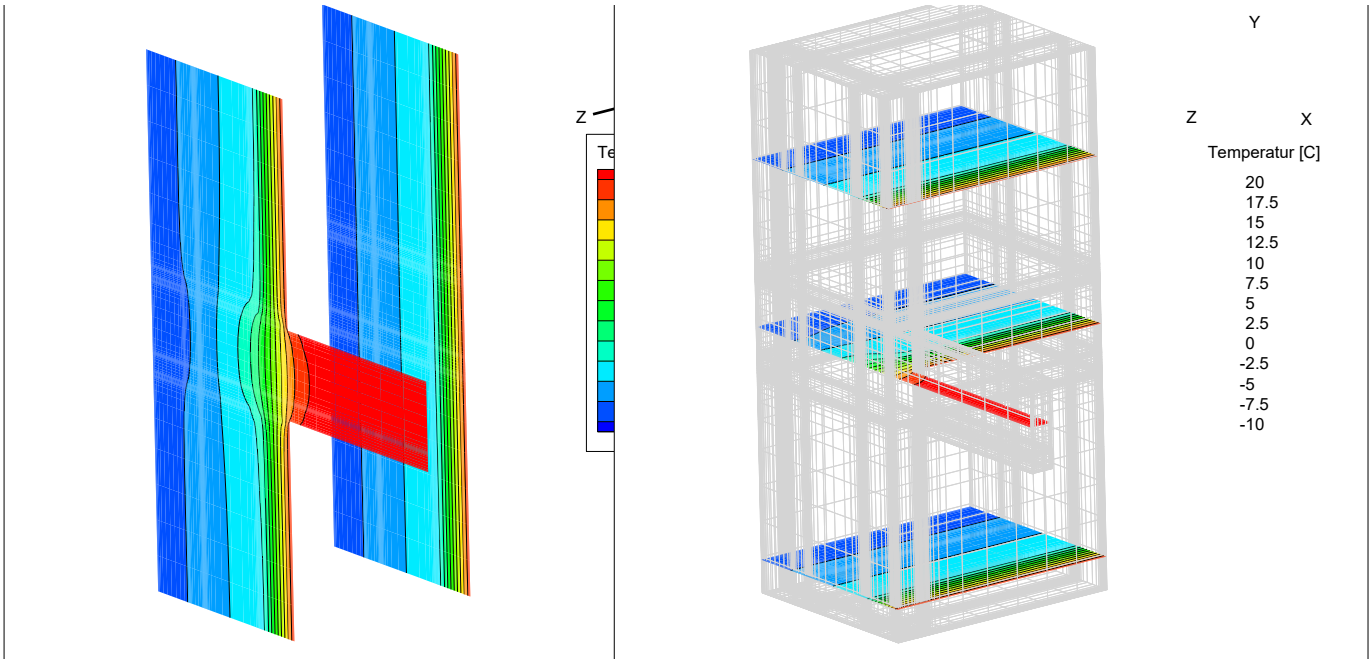

Fig. 45.: Simulated temperature field in the beam end after six days for test strip 2 (calcium silicate), lower joist end detail. Left figure: vertical sections. Right figure: Horizontal sections with discretization grid.

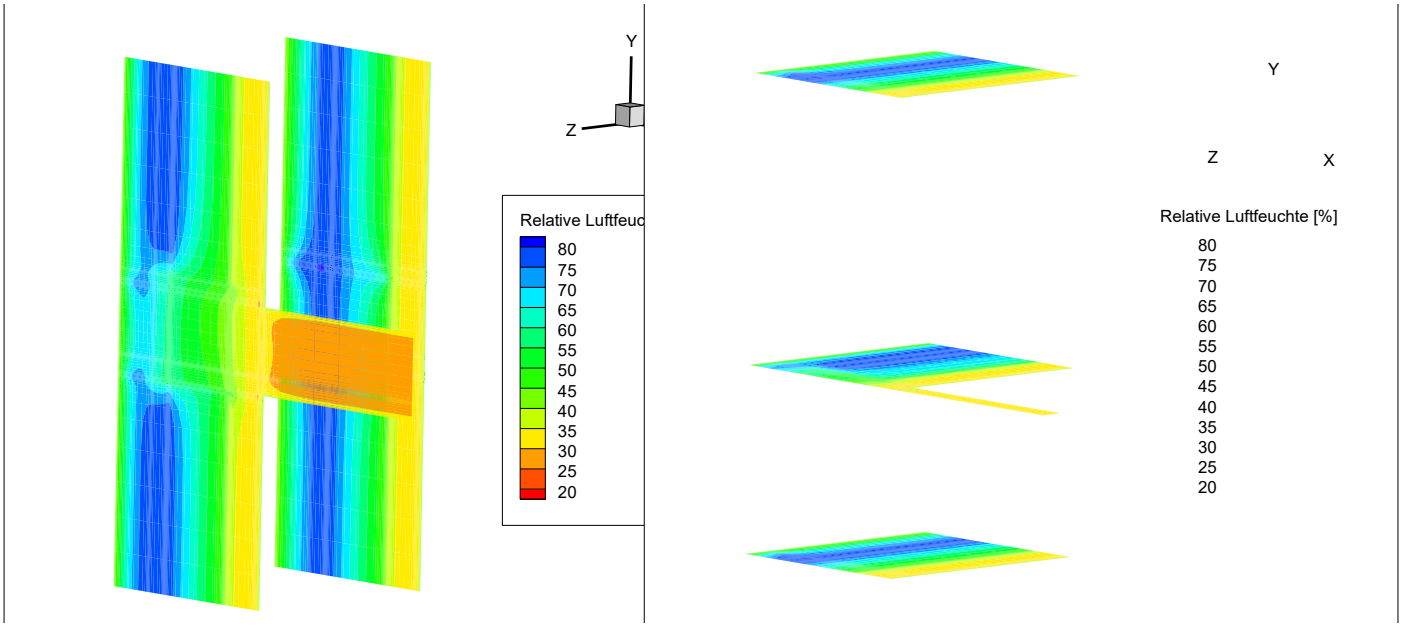

Fig. 46.: Simulated relative humidity field in the beam end after six days for test strip 2 (calcium silicate), lower joist end detail. Left figure: vertical sections. Right figure: Horizontal sections.

The 3D-computed temperature distribution shows a high accordance with the 2D-results. The beam end causes a heat-conducting effect into the cavity behind it. At the opposite side (cold-side) the cavity functions as an insulation layer and causes a reduced temperature level in the masonry behind. A rather small difference between 3D and 2D results is also given for the relative humidity outcomes. This is displayed in the following diagrams for the temperature values in order to allow a better comparison between both courses.

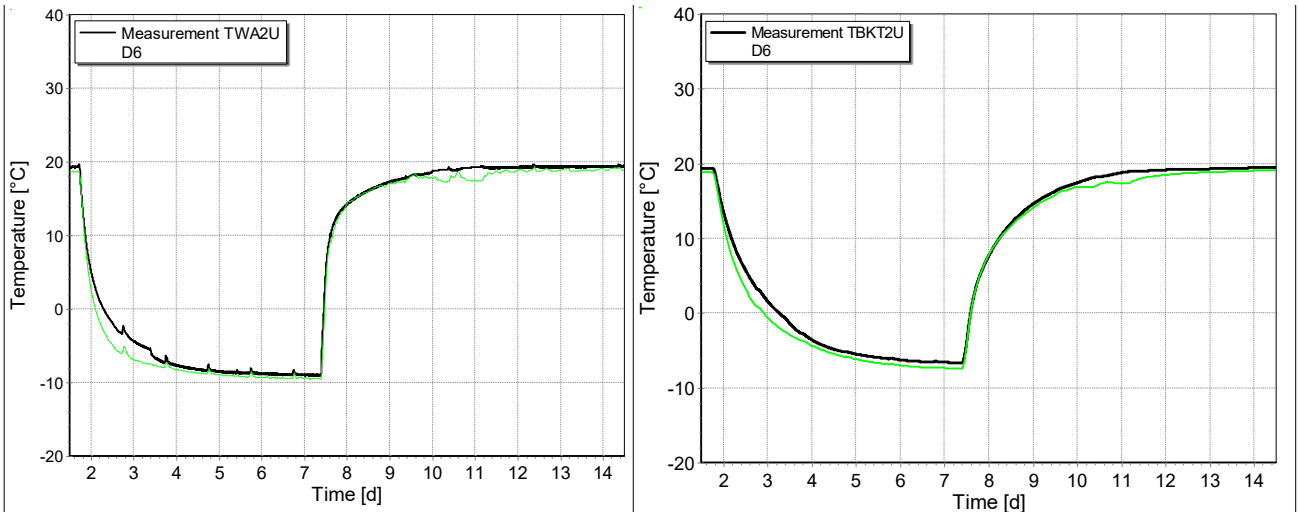

Fig. 47.: Comparison between measurement results and 3D-DELPHIN simulations for one sensor close to the exterior (cold-side) surface of the masonry (left) and one sensor at the end of the joist end (right) for test strip 2, lower joist end detail.

The comparison of measured and simulated curve for the sensor close to the exterior surface (TWA2U) amounts to less than 0.4 K at the end of the seventh day. In the following days, the accordance between both curves is nearly perfect until, approximately after the 10th day, a fluctuation of simulation results starts to develop. This effect was already given in the 2D simulation results and is not fathomed. The maximum difference during the cool-down phase is still appearing in the same extend as in the 2D simulations. The difference at the vertical layer of the beam end (TBKT2U) is again smaller than the previous one and amounts to less than 0.6 K after six days and less than 0.7 K after ten days.

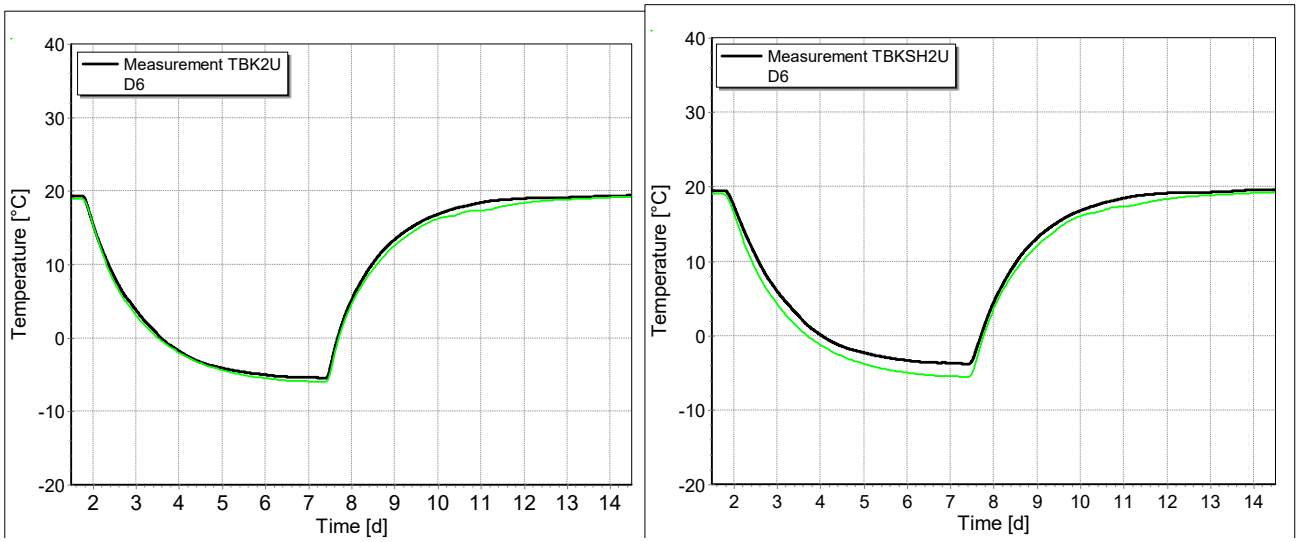

Fig. 48.: Comparison between measurement results and 3D-DELPHIN simulations for one sensor at the front end face of the beam (left) and one sensor in the beam end (right) for test strip 2, lower joist end detail.

The temperature conditions in the front end of the beam (TBK2U) show a very well congruence with the simulated curves. Deviations are less than 0.6 K after ten days. In contrast to this, the accordance is worse for the results of the material-measurement in the joist end (TBKSH2U). The same tendency was given for the 2D simulation results. Maximum difference after seven days amounts to about 2 K and is finally, after ten days) reduced to below 1 K. This difference could be a consequence of the sensor installation, which was not realized in parallel to the isotherms for practical reasons. Therefore, the wires of the sensor could induce heat from the warm-side chamber into the joist end as it is covered with a thin metal coating that connects both positions.

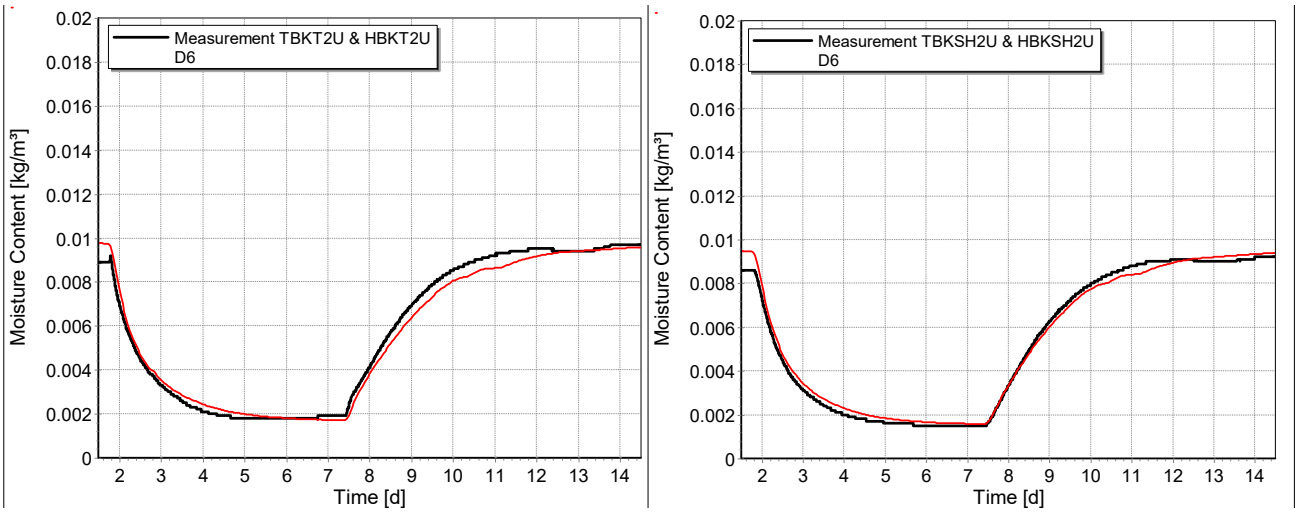

Fig. 49.: Comparison between measured and 3D-simulated curves of moisture content in the cavity of the beam end (left) and in the beam end (right) for test strip 2 (calcium silicate), lower beam end.

Although the temperature differences are relatively high in the wood of the beam end (TBKSH2U), the computed moisture content in the beam end shows very small deviations from the measurement results. It amounts to a maximum of around 0.1 g/kg after seven days although even the initial conditions were different. A similar conclusion can be derived for the situation in the cavity at the beam end. Again measured and simulated moisture content at the front end face show a sufficient accordance with differences below 0.5 g/kg.

Finally, the achieved improvement of the DELPHIN 6- 3D simulation compared to the 2D-version of DELPHIN 5 is not substantial. One reason is surely the lack of field models (e.g. long-wave heat exchange model) and other add-ons, which are only available in DELPHIN 5 yet and achieved partially improvements in the previous simulation studies.

4.9 Summary and Conclusions

The lab tests in three differently insulated test fields provided general findings about the particular behaviour of the chosen insulation systems on varying temperature conditions in the adjacent test chambers. It could be clearly shown that:

- The higher the thermal resistance of the insulation system, the lower the temperature fluctuations at the interior and exterior surfaces and the lower the temperature level of the existing construction. [see chapters 4.7.3 and 4.7.4] This impact depends in particular on the local weather conditions and the properties of the existing masonry. A sound engineering assessment of a suitable thermal resistance of the insulation system to be added is essential for any building.
- Applying insulation materials, which are not capillary active and which show an elevated vapour ratarding property, should be avoided in cases of built-in moisture. It causes a huge delay of the drying process and therefore an increased damage risk for both, the wall (e.g. frost damage) and the beam end (e.g. rot). [see chapter 4.7.2 starting on page 30]
- Vapour-open (and capillary active) insulation systems show a high drying potential, which causes a lower humidity level in the interstitial condensation plane. They could be used if built-in moisture level is raised to preserve the drying potential towards room side. This is explicitly recommended for reduced drying potential towards outdoor air, e.g. due to hydrophobziation or painting coatings, tight bricks etc. [see chapter 4.7.2 starting on page 30]

Another outcome of the lab tests is the impact of joist end sealing techniques on the hygrothermal behaviour of the timber in the masonry pocket. A small impact of the sealing technique itself was detected in contrast to the impact of the applied insulation system. But the presence of a sealing around the beam end was stated to be very high. The open joist end caused a very quick response on changing climate conditions and reached critical values of the mass-related wood moisture content and the relative humidity [see chapter 4.7.5 starting on page 35]. In contrast to this open construction, the sealed beam end showed an either constant level of moisture content, which was less dependent on the boundary conditions and less fluctuating but on a higher but uncritical long-time level. The sealed beam end should therefore be the preferred solution. The open joist end could be chosen for locations with less-severe winter conditions and low indoor moisture level.

It must be mentioned here that the practical behaviour of joist ends in internally insulated walls is more complex than suggested by the explained TUD test stand. Some aspects, e.g. solar radiation, wind-driven rain and wind are not yet included in the test scenarios. Other factors like the chosen materials (new wood, new bricks and mortar) and the construction simplifications (uncovered joists) differ as well. The materials are typical ones and lie within the huge range of historical building materials for bricks, timber and mortar. The impact of the joist end construction is expected to be more important. In In real buildings, additional floor and ceiling coverage around the beams is the normal situation. There are high requirements regarding the sound insulation and fire protection of these constructions, additionally valuable space for pipes and wires. Consequently, realized floor slab constructions are often closed and filled. This causes inherently a decoupling of the joist end masonry pocket from the indoor climate.

5 Test stand at DTU

5.1 Introduction

At the Department of Civil Engineering at the Technical University of Denmark (DTU), a large scale experimental set-up was constructed to investigate the application of several interior insulation systems. Applied to single leaf masonry assemblies with embedded wooden wall plate and beam ends, designed to resemble those built in Danish historic multi storey building from the period 1850-1950. A total of 24 masonry assemblies were constructed, of which 16 where oriented towards west-southwest and 8 towards east-northeast. The investigated insulation systems included: 1) traditional mineral wool system, 2) Polyurethane foam boards with calcium silicate channels, 3) calcium silicate boards, 4) foam concrete boards, 5) insulation mortar, 6) hygrowick and vapour retarder encapsulated mineral wool batts, and 7) lightweight mineral insulation boards. Each insulation system was installed on one to six masonry assemblies, leaving four empty as reference assemblies. Several of the insulation systems were combined with different exterior and/or interior surface treatments. Each of the 24 masonry assemblies were fitted with measurement equipment for logging the temperature and relative humidity development of up to 10 locations within the individual masonry assemblies.

Focus of this study is on the evaluation of the hygrothermal performance of identical masonry assemblies with embedded wooden parts, fitted with a range of different diffusion-open, capillary active, interior insulation systems. In addition, evaluate the interaction between the individual insulation systems and different exterior surface treatments. The study addresses issues such as wind-driven rain, interstitial condensation, and reduced drying potential, in order to tackle the changed moisture conditions caused by the interior thermal insulation.

The experimental set-up at DTU is led by Søren Peter Bjarløv, associate professor at DTU, while industrial Ph.D. student at DTU, Tommy Riviere Odgaard, has made his Ph.D. work about the experimental set-up. Ph.D. student at DTU, Nickolaj Feldt Jensen, is taking over the work and maintenance of the test site from Tommy, and is currently doing his Ph.D. work about the experimental set-up.

Photos and illustrations in the following sections by Søren Peter Bjarløv, Tommy Riviere Odgaard and Nickolaj Feldt Jensen.

5.2 Test Stand Description

The experimental set-up was designed around the use of two 40 feet insulated reefer containers, placed at the test site of the Department of Civil Engineering at the Technical University of Denmark in Kongens Lyngby, Denmark (55.79°N, 12.53°E). The insulated reefer containers have the external measurements of approximately 12.2 m in length, 2.4 m in width and 2.9 m in height, with an internal volume of 67.6 m^3. For the experiment, holes of 1 m in width and 2 m in height were cut into the facades of the containers, which would accommodate the single leaf masonry assemblies. The holes were cut with a spacing distance of 0.4 m between the holes. In the first container, denoted as the GI container, 16 holes were cut, 8 facing towards west-southwest and 8 facing towards east-northeast. In the second container, denoted as the Xella container, 8 holes were cut, all facing towards west-southwest.

Fig. 50.: External view of the GI container.

The test containers were constructed so that masonry assemblies would be sealed off to limit heat and moisture transport through the container walls, in order to emulate adiabatic conditions surrounding the assemblies. The reefer containers are of type H0, which commonly have an average R-value of 2.5 $K \cdot m^2/W$. The sealing process was carried out by installing a vapour retarder between the masonry assembly and the container walls, floor and ceiling, to limit air and moisture movement to occur only through the masonry assembly, as shown in figure 51 To further increase the airtightness of the test containers, the joints between the masonry assemblies and the container walls, were sealed on the exterior side using mastic sealant, which would also serve as prevention against rain entering the container through the joints. For the heat losses and to prevent the sides of the walls to be affected by the indoor climate, structures consisting of 400 mm mineral wool (λ = 0.037 W/m·K) and wooden rafters were constructed in the spacings between the masonry assemblies, and 150 mm mineral wool (λ = 0.037 W/m·K) was installed above the masonry assemblies. The floor construction of the reefer containers was however not insulated further than the above-mentioned R-value of the reefer container, thus no thermal decoupling was carried out between the container floor and the test walls. However, thermal decoupling was not considered as an issue, as the closest sensors are located approximately 800mm above floor level. The roof construction constructed on top of the containers were designed so rain water run-off from the roof would not affect the masonry assemblies, which was carried out by installing rain gutters at the edges of the roof. In addition to the gutters, flashings were installed directly above the masonry assemblies, thus creating an overhang of a few centimetres, shown as covering in figure 51. The purpose of the overhang was to avoid rain entering the assembly through the horizontal section of masonry assemblies sticking out through the container walls. Furthermore, the reefer containers were raised up using steel beams, creating a distance of +350 mm between the ground level outside the containers and the lower part of the test walls. This measure was carried out in order to avoid rain from splashing up from the ground and striking the lower part of the test walls.

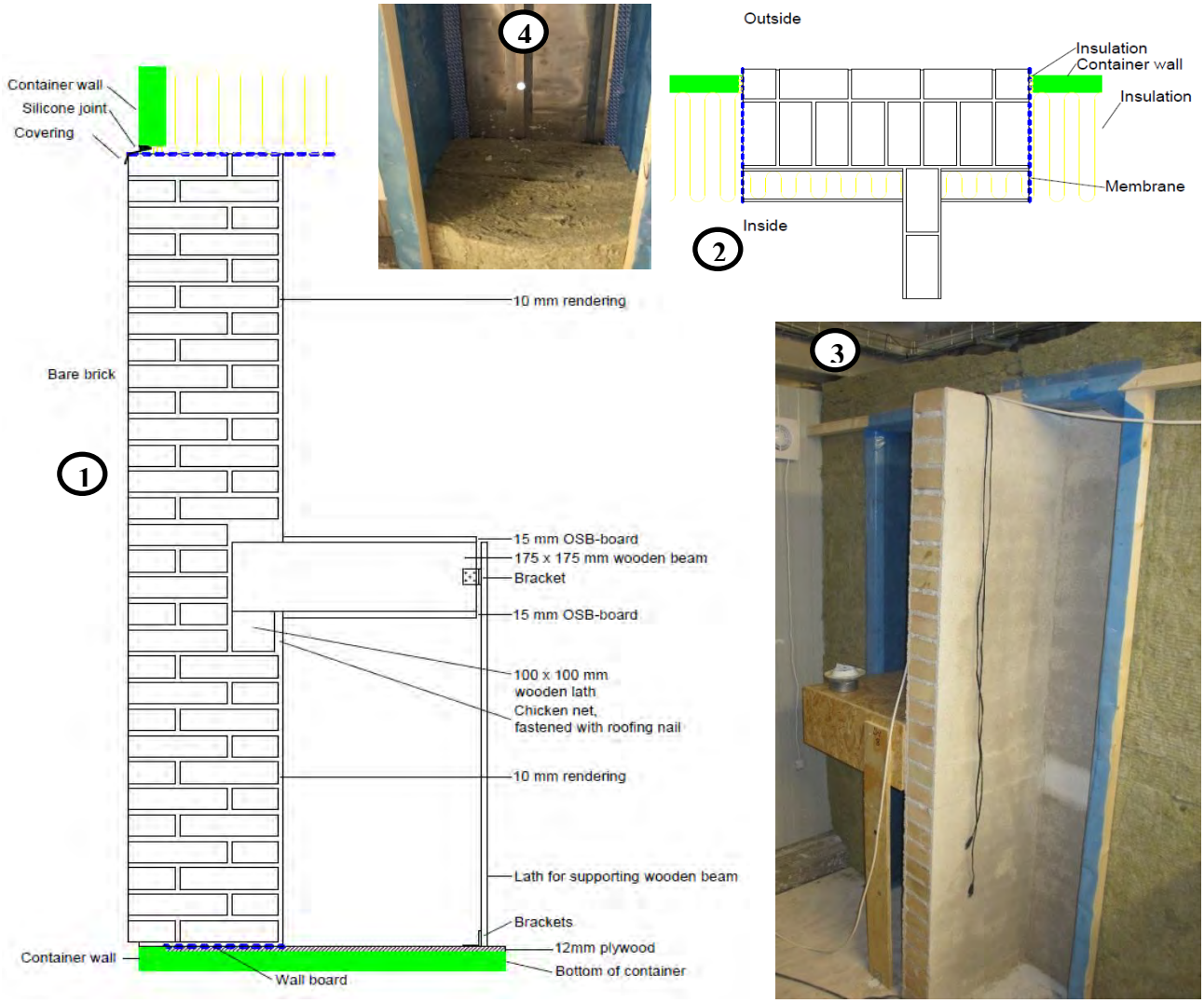

Fig. 51.: Container test set-up. 1) Vertical section through a masonry assembly with the intermediate floor structure. 2) Horizontal section through a masonry assembly with the adjacent internal wall. 3) Masonry assembly shown with surrounding vapour retarder and separating insulation. 4) Vapour retarder and insulation in the spacing between masonry assemblies.

Over the course of the experiment, the temperature and relative humidity of the indoor climate were maintained throughout the year using convectors and/or heating fans, and humidifiers, supplied with demineralized water. In the GI container three 2000 W heating fans are used, while in the Xella container two 1000W electrical convectors and one 2000 W heating fans are used. In addition, an exhaust fan and a fresh-air value were installed in each of the reefer containers, in order to create an air change rate of approximately 0.5 times per hour, a commonly used value in Danish residential buildings (Hansen, et al., 2010). The exhaust fan was installed in the south-eastern end of the container, while the fresh-air valve was installed in the north-western end. It should be noted that dehumidifier or cooling units were not installed as a part of the experimental set-up, and fluctuation due to high humidity or temperature could occur over the course of the experiment.

Measurements of the outdoor climate were carried out using a small local weather station mounted approximately 1.5 m above the GI container as well as the DTU weather station located on top of DTU

building 119, 150-200 m west-southwest of the test containers, at an altitude 16 m above the experimental test set-up. In addition to the two weather stations, three RG3-M HOBO rain gauges with built-in loggers from Onset were installed. One rain gauge located on each side of the GI container, and one on the south side of the Xella container. The rain gauges were fitted with a custom-build frame and acrylic glass structure, for measuring the amount of wind driven-rain striking the masonry assemblies. The custom-build frame and acrylic glass structure was designed by Ph.D. students at DTU, Tessa Kvist Hansen and Tommy Riviere Odgaard in collaboration with LINATEX A/S. The acrylic glass structure would serve as a vertical collection area, from where the rain would run into the RG3-M HOBO rain gauge containing a tipping bucket. The RG3-M HOBO rain gauge was designed to log the time of tipping and the amount of tips. All three rain gauges were installed and functioning from early June 2016. As the experiment had been in operation 13 months prior to the installation of the RG3-M HOBO rain gauges, the wind-driving rain data for these months were determined using wind-driven rain modelling (Straube, 2010).

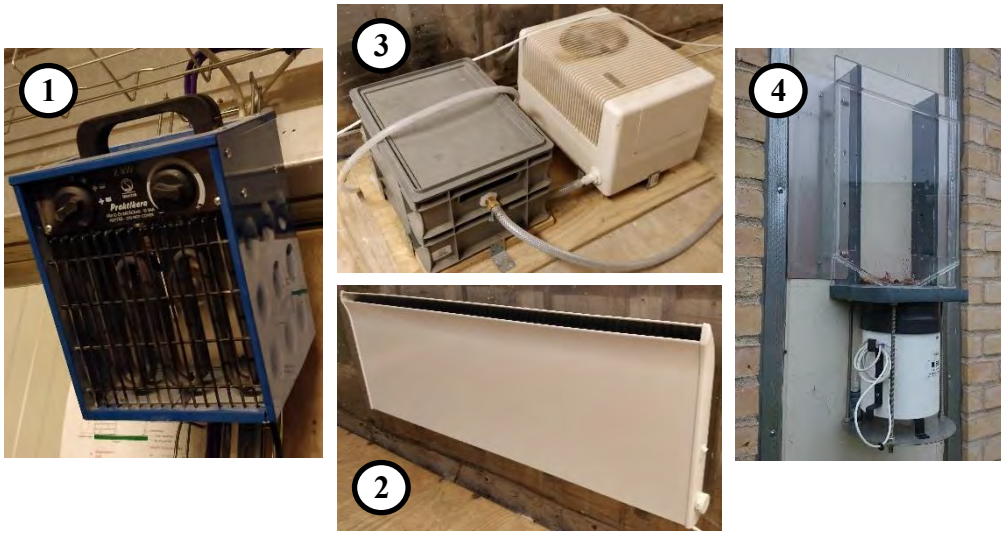

Fig. 52.: Container test set-up. 1) 2000W Malmbargs heating and circulation fan. 2) 1000W Adax electrical convector. 3) Brune B125 humidifier. 4) Onset rain gauge.

Prior to the installation of the insulation systems, the masonry assemblies were after their completion on September 18th 2014 subjected to a forced dry-out period, both internally and externally. The internal forced dry-out was carried out using two 2000W calorifere, which would heat up the indoor climate to 40-50°C with a relative humidity of 10-30%. The external forced dry-out was carried out by erecting a text around the masonry assemblies and heat up the space using one 9000W calorifere. The extermal forced dry-out was carried out from primo December 2014 to mid-April 2015. The insulation systems were installed in ultimo February 2015, and the experiment started logging data from May 1st 2015.

5.3 Wall configurations

A total of 24 single leaf masonry assemblies were constructed, with the dimensions 198.7 cm high, 94.8 cm wide, and 35.8 cm thick. Thickness corresponding to 1½ stones, with a 10 mm layer of rendering on the interior side. The masonry assemblies were designed to replicate a typical Danish masonry wall built between 1850 to 1930. For the construction of the masonry assemblies, yellow soft-moulded masonry brick, from Helligsø Teglværk, and 7.7% lime adjusted mortar with a grain size of 0-4 mm, from Wewers A/S. The lime adjusted mortar was designed to bear a resemblance to the mortar used in historic buildings, and it was used both for the mortar joints as well as for the rendering on the interior side.

The masonry assemblies were constructed as a 3-dimensional set-up including a wooden floor structure as well as a ½-stone adjacent internal masonry wall, rendered on both sides. This was carried out in order to emulate potential problems which could occur at the joints between the exterior wall and the floor structure or the adjacent internal walls. Due to the thermal bridging effect created by insulating the exterior wall sections adjacent to these construction parts. The wooden floor structure was constructed using a 100 x 100 mm wooden wall plate embedded into the masonry wall (picture 1 of figure 53), which would serve to carry the 175 x 175 mm embedded wooden beam end resting on top of it. Note that during the installation of the wooden wall plate, no foil was placed between the masonry wall and the wooden wall plate in order to prevent capillary contact. Both the wall plate and beams were of Pomeranian pine wood. The wooden beam was installed up against the rendered surface of the adjacent internal masonry walls, and embedded into the masonry assembly by a distance of approximately 100 mm. The cavity for the wooden beam end and the installed wooden beam are shown in picture 2 and 3 of figure 53.After embedding the end of the wooden beam into the masonry wall, it was been estimated that an air cavity of approximately 10 mm would occur surrounding the beam end. Finally, after installation of the wooden beam and the final rendering works, a wooden box was construction using 15 mm OSB boards on all the sides with the exceptions towards the adjacent internal masonry wall and towards the interior surface of the exterior wall (picture 4 of figure 53. To emulate the pugging layer traditionally created between the wooden beams, 100 mm mineral wool batts were installed inside the OSB board box. As it can be seen from the picture in figure 53, the wooden floor construction was constructed to the left of the interior wall, while the wall area to the right was kept empty for the purpose other types of small scale experiments.

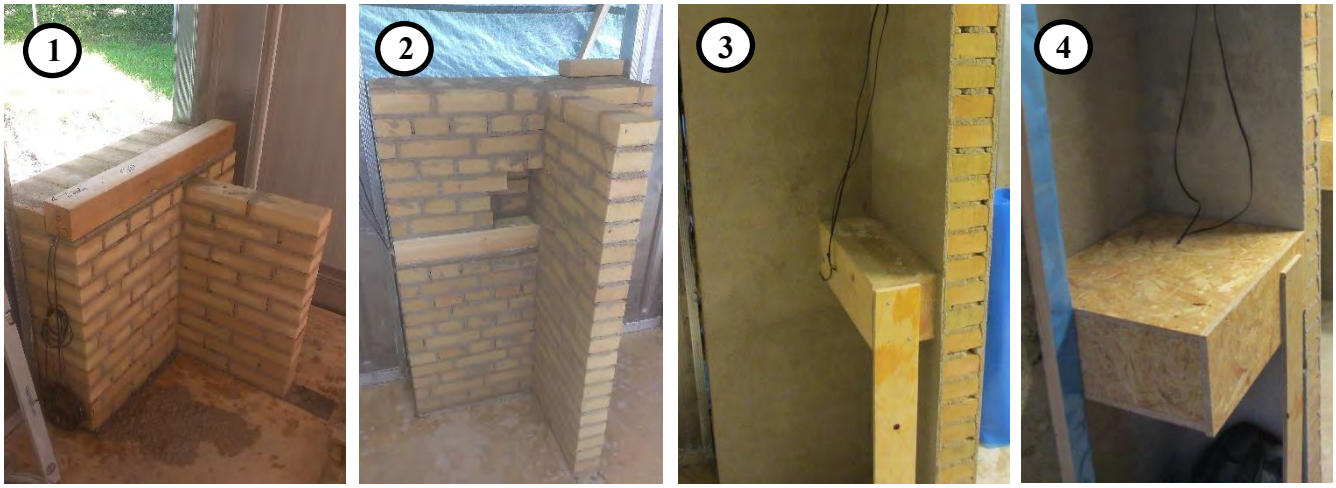

Fig. 53.: Masonry assembly build-up. 1) Installation of embedded wooden wall plate. 2) Bare masonry wall with hole for the embedded part of the wooden beam. 3) Rendered masonry wall with embedded wooden beam. 4) Finished wooden floor structure with OSB boards on top, bottom and sides.

The exterior surfaces of the masonry assemblies were treated differently in order to emulate different possible scenarios, thus a number of the assemblies have been left as bare brick (picture 2, figure 54), while a number of the assemblies have been treated with Remmers Funcosil FC hydrophobization (Concentration = ~40% w/w) (picture 3 of figure 53). Lastly, the exterior surface of the assembly X1 in the Xella container was rendered with the same lime adjusted mortar as used for rendering of the interior surfaces and the mortar joints (picture 1 of figure 53). The treatments were carried out following the forced dry-out period described above, to avoid construction moisture getting trapped within the masonry assemblies.

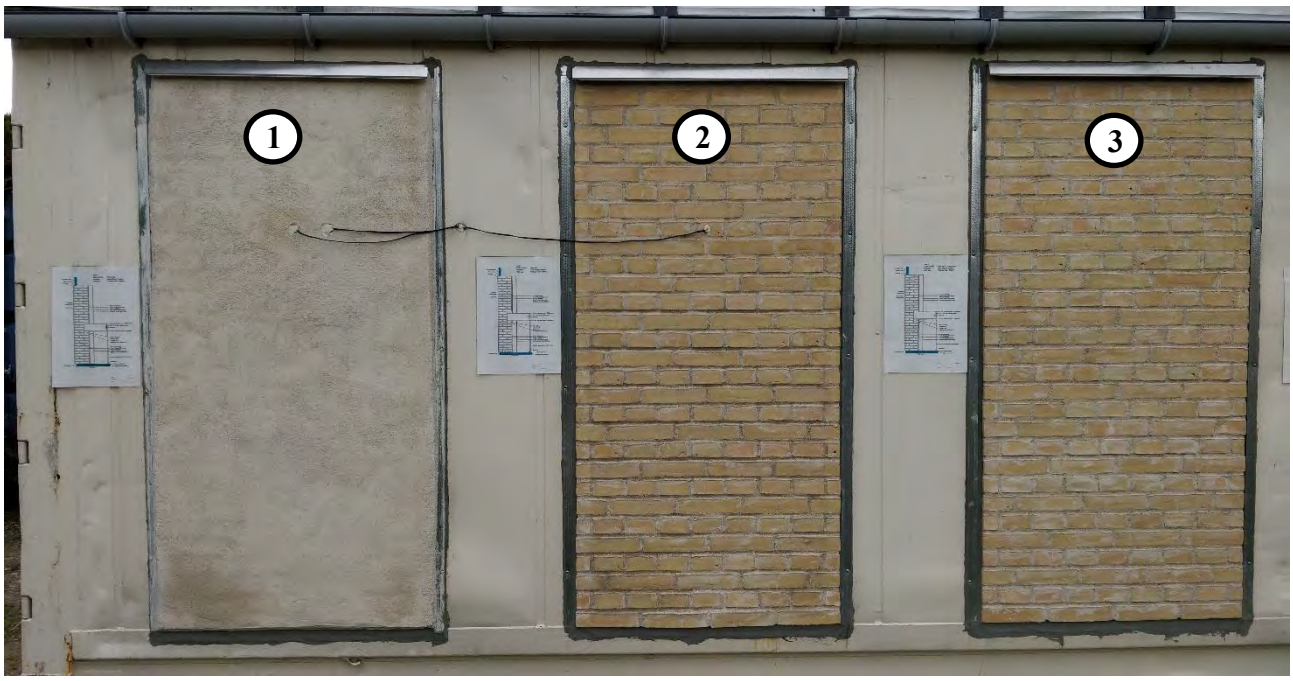

Fig. 54.: The exterior wall treatments. 1) Rendered. 2) Bare brick. 3) Bare brick with hydrophobization.

The insulation systems applied to the masonry assemblies were installed according to the manufacturer's recommendations, by people dispatched from the respective companies, thus ensuring correct installation of the individual products. With the exceptions of foam concrete, TI-mortar, HygInsu, and the traditional mineral wool system, which were installed by local masons and carpenters.

The mineral wool system was constructed using wooden rafters with 100 mm mineral wool in between, installed directly against the interior render layer of the masonry assembly. Vapour retarder and gypsum boards were installed as interior finishing layers. The TI-mortar was installed by first applying a thin scratch coat layer, followed by the insulation mortar, and finally the interior rendering finishing. The HygInsu system is a systems designed by DTU and Rockwool Group. The system was constructed using 100 mm mineral wool partly encapsulated in a vapour retarder, and at the same time, fully encapsulated in a Hygrowick layers with capillary transport properties. The encapsulated mineral wool was installed using steel profiles, and two layers of gypsum boards were used as interior finishing layers. The IQ-Therm, Skamoplus, foam concrete and Ytong Multipor insulation boards were all fully adhedered to the interior render layer of the masonry assemblies, using a thin layer of adhesive light mortar. Finally, the insulation systems were closed off with their respective finishing layers. The exception to this were the walls 6 and 7 in the Xella container. Where Autoclaved Aerated Concrete (AAC) blocks with the dimension 100 by 200 mm and a density of 350 kg/m^3 were installed in front of the wooden wall plate, below the wooden floor partition. The AAC blocks were installed at this location in order to create a deliberate thermal bridge near the wooden wall plate. The increased heat loss would allow for higher temperatures in the wooden wall plate and the embedded wooden beam end, thus protecting the wall plate and beam end (picture 1 and 2 of figure 55).

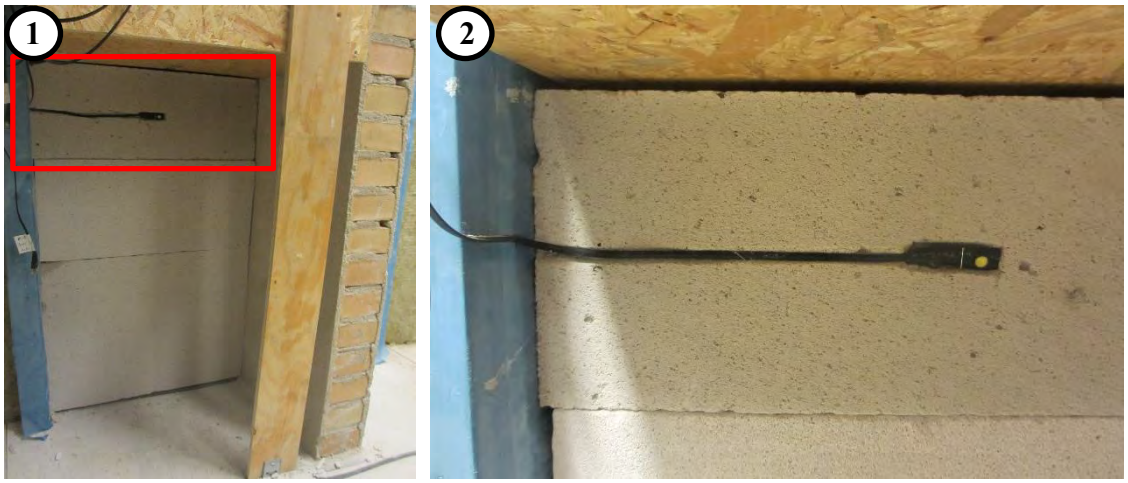

Fig. 55.: Installation of the AAC blocks in front of the wooden wall plate, below the wooden floor partition. 1) Lower part of the masonry assembly with Ytong Multipor in the lower part of the wall area, and AAC in the upper part. 2) Close-up of the sensor installed in the AAC block.

The following provides an overview of the insulation systems applied to the masonry assemblies in the two test containers:

The GI container

- G1:100 mm mineral wool in between wooden rafters, vapour retarder, 13 mm gypsum board, Diffusion-tight paint (Flügger 100). Exterior surface: Bare brick.
- G2: 10 mm IQ-Fix, 80 mm IQ-Therm, 10 mm IQ-Top, 3 mm IQ-Fill, Diffusion-open paint (IQ-Paint). Exterior surface: Bare brick with hydrophobization.
- G3: Reference wall, no insulation system. Exterior surface: Bare brick.
- G4: 10 mm Weber Multi 292, 100 mm Skamoplus Indeklimaplade (Calsium Silicate), 8 mm Weber Multi 292. Diffusion-open paint (Ytong Multipor Silicate Interior Paint.). Exterior surface: Bare brick.
- G5: 8mm Ytong Light-mortar, 100 mm foam Concrete from the Technical University of Denmark, 8mm Ytong Light-mortar, Diffusion-open paint (Ytong Multipor Silicate Interior Paint.). Exterior surface: Bare brick.
- G6: 8mm Ytong Light-mortar, 100 mm foam Concrete from the Technical University of Denmark, 8mm Ytong Light-mortar, Diffusion-open paint (Ytong Multipor Silicate Interior Paint.). Exterior surface: Bare brick with hydrophobization.
- G7: 10 mm IQ-Fix, 80 mm IQ-Therm, 10 mm IQ-Top, 3 mm IQ-Fill, Diffusion-open paint (IQ-Paint). Exterior surface: Bare brick.
- G8: ~5 mm scratch coat, 40 mm insulation mortar from the Danish Technological Institude, ~5mm airlime rendering mortar (0-1 mm gain size). Exterior surface: Bare brick.
- G9: ~5 mm scratch coat, 40 mm insulation mortar from the Danish Technological Institude, ~5mm airlime rendering mortar (0-1 mm gain size). Exterior surface: Bare brick.
- G10: 10 mm IQ-Fix, 80 mm IQ-Therm, 10 mm IQ-Top, 3 mm IQ-Fill, Diffusion-open paint (IQ-Paint). Exterior surface: Bare brick.

- G11: 8mm Ytong Light-mortar, 100 mm foam Concrete from the Technical University of Denmark, 8mm Ytong Light-mortar, Diffusion-open paint (Ytong Multipor Silicate Interior Paint.). Exterior surface: Bare brick with hydrophobization.
- G12: 8mm Ytong Light-mortar, 100 mm foam Concrete from the Technical University of Denmark, 8mm Ytong Light-mortar, Diffusion-open paint (Ytong Multipor Silicate Interior Paint.). Exterior surface: Bare brick.
- G13: 10 mm Weber Multi 292, 100 mm Skamoplus Indeklimaplade (Calsium Silicate), 8 mm Weber Multi 292. Diffusion-open paint (Ytong Multipor Silicate Interior Paint.). Exterior surface: Bare brick.
- G14: Reference wall, no insulation system. Exterior surface: Bare brick.
- G15: 10 mm IQ-Fix, 80 mm IQ-Therm, 10 mm IQ-Top, 3 mm IQ-Fill, Diffusion-open paint (IQ-Paint). Exterior surface: Bare brick with hydrophobization.
- G16: 100 mm mineral wool partly encapsulated in a vapour retarder, and fully encapsulated in a Hygrowick layer, 2 x 13 mm gypsum boards. No interior paint was applied. Exterior surface: Bare brick.

The Xella container

- X1: 8mm Ytong Light-mortar, 100 mm Ytong Multipor, 8mm Ytong Light-mortar, Diffusion-open paint (Ytong Multipor Silicate Interior Paint.). Exterior surface: Rendered.
- X2: 8mm Ytong Light-mortar, 100 mm Ytong Multipor, 8mm Ytong Light-mortar, Diffusion-open paint (Ytong Multipor Silicate Interior Paint.). Exterior surface: Bare brick.
- X3: 8mm Ytong Light-mortar, 100 mm Ytong Multipor, 8mm Ytong Light-mortar, Diffusion-open paint (Ytong Multipor Silicate Interior Paint.). Exterior surface: Bare brick with hydrophobization.
- X4: Reference wall, no insulation system. Exterior surface: Bare brick with hydrophobization.
- X5: Reference wall, no insulation system. Exterior surface: Bare brick.
- X6: 8mm Ytong Light-mortar, 100 mm Ytong Multipor, 8mm Ytong Light-mortar, Diffusion-open paint (Ytong Multipor Silicate Interior Paint.). Exterior surface: Bare brick. 100 by 200 mm AAC blocks below the wooden floor partition.
- X7: 8mm Ytong Light-mortar, 100 mm Ytong Multipor, 8mm Ytong Light-mortar, Diffusion-open paint (Ytong Multipor Silicate Interior Paint.). Exterior surface: Bare brick. 100 by 200 mm AAC blocks below the wooden floor partition.
- X8: 8mm Ytong Light-mortar, 100 mm Ytong Multipor, 8mm Ytong Light-mortar, Diffusion-tight paint (Flütex 5). Exterior surface: Bare brick.

Note that the material properties for the materials used in the above-described wall assemblies are described below in table 17.

Tab. 17.: Material properties. The text colour indicates the material data origin: green is a measured data set for the particular material in the test stand, blue is a material data set from a similar material as used in the test stand from the DELPHIN data base, purple indicates values, which are adopted from material producer.

Density [kg/m³]	Specific heat capacity [J/kgK]	Open porosity [m³/m³]	Effective saturation (long term process) [m³/m³]	Capillary saturation content (short term process) [m³/m³]	Hygroscopic sorption value at RH=80% [m³/m³]	Thermal conductivity [W/mK]	Water uptake coeficient [kg/m² s$^{1/2}$]	Water vapour diffusion resistance factor [-]	Liquid water conductivity at effective saturation [s]
1643	942	0.3850	0.3850	0.2750	0.0036	0.6000	0.2782	16.9000	1.4000E-09
392	850	0.8707	0.8000	0.6000	0.0182	0.0946	0.0434	7.3787	5.9557E-09
554	2673	0.6535	0.6532	0.6150	0.0712	0.1858	0.0161	348.0200	9.9961E-10
554	2575	0.6535	0.6532	0.6250	0.0712	0.1881	0.0096	222.8830	9.8456E-10
554	2775	0.6535	0.6532	0.6250	0.0712	0.2084	0.0167	4.5411	7.4264E-10
-	-	-	-	-	-	-	-	-	-
630	1880	0.4000	0.3500	0.2700	0.0368	0.1300	0.0019	280.0000	8.2794E-11
37	840	0.9200	0.9000	0.9000	0.0002	0.0400	0.0000	1.0000	0.0000E+00
49	1400	0.9815	0.0933	0.0700	0.0004	0.0370	0.0129	27.0127	1.2011E-09
225	1129	0.9136	0.9040	0.7122	0.0130	0.0611	0.7261	4.2300	6.3100E-10
262	1212	0.9010	0.8190	0.3120	0.0190	0.0680	0.0970	8.6400	3.1620E-08
1243	998	0.5310	0.4280	0.2070	0.0170	0.0780	0.3900	22.4300	6.3100E-06
99	1331	0.9628	0.8092	0.0870	0.0056	0.0381	0.0060	6.7300	3.1620E-08
161	1036	0.9390	0.4710	0.2790	0.0090	0.4400	0.8800	18.7500	4.4670E-07
830	815	0.6855	0.5400	0.3200	0.0522	0.1550	0.0031	13	1.8480e-09
1655	866	0.3750	0.3090	0.3000	0.0100	0.5000	0.6000	6.6000	1.4130E-05
1313	863	0.5044	0.2770	0.2000	0.0725	0.4968	0.0051	18.7486	5.5634E-12
725	1042	0.7265	0.3745	0.2407	0.0061	0.1471	0.1070	11.7335	2.2538E-09
1270	900	0.5200	0.5200	-	0.0166	0.479	0.222	14	0
-	-	-	-	-	-	-	-	-	-
850	850	0.6500	0.5510	0.4000	0.0072	0.2000	0.2770	10.0000	6.2600E-09
-	-	-	-	-	-	-	-	28500	-
-	1000	-	-	-	-	1 / 1.1630	-	-	-
1450	-	-	-	-	-	-	-	1440	-
-	-	-	-	-	-	-	-	-	-
-	-	-	-	-	-	-	-	-	-
1480	-	-	-	-	-	-	-	80	-

Material/product
Masonry Brick: Yellow, soft-moulded brick
Ytong AAC blocks 350 kg/m3
Pine Radial (core), for wall plate and beam
Pine Tangential (core), for wall plate and beam
Pine wood (sapwood), for wooden battens
OSB board
Mineral wool
IQ-Therm
Skamoplus Indeklimaplade (Calsium Silicate)
Foam Concrete (DTU)
TI-mortar
Ytong Multipor
7.7% lime adjusted wet mortar, grain size 1-4 mm (Air lime)
Ytong Light-mortar
Weber Multi 292
IQ-Fix
IQ-Top
IQ-Fill
Scratch coat, air-lime rendering mortar, grain size 0-1 mm
Gypsum boards
Vapour retarder (DAFA Profoil)
Isover Hygrowick
Diffusion-tight paint (Flütex 5)
Diffusion-tight paint (Flügger 100)
Diffusion-open paint (Ytong Multipor Silicate Interior Paint)
Diffusion-open paint (IQ-Paint)

5.4 Measurement techniques

Two measurement methods were used over the course of the experiment: 1) Digital HYT221 sensors by Innovative Sensor Technology IST AG, logging temperature and relative humidity every 10 minutes. 2) Manual measurement of electrical resistance of wooden- and gypsum dowel sensors. The manual measurements were carried out every 2 weeks, using a COW T301 measurement equipment, by BMT Instruments. The accuracy of the digital HYT221 sensors from IST is for relative humidity measurements ±1.8% at 23°C, between 0% to 90% relative humidity, while for temperature measurements ±0.2K between 0°C to 60°C. The sensors have a measurement range of 0% to 100% relative humidity, and temperatures from -40°C to 125°C (IST, 2014).

For the experiment, the digital HYT221 sensors were prior to installation in masonry assemblies, protected using adhesive shrink tubing which would cover the entire sensor (picture 1-3 of figure 56). After installation of the adhesive shrink tubing, a small piece of the tubing would be removed at the sensing area of HTY221 sensors (picture 4 of figure 56).

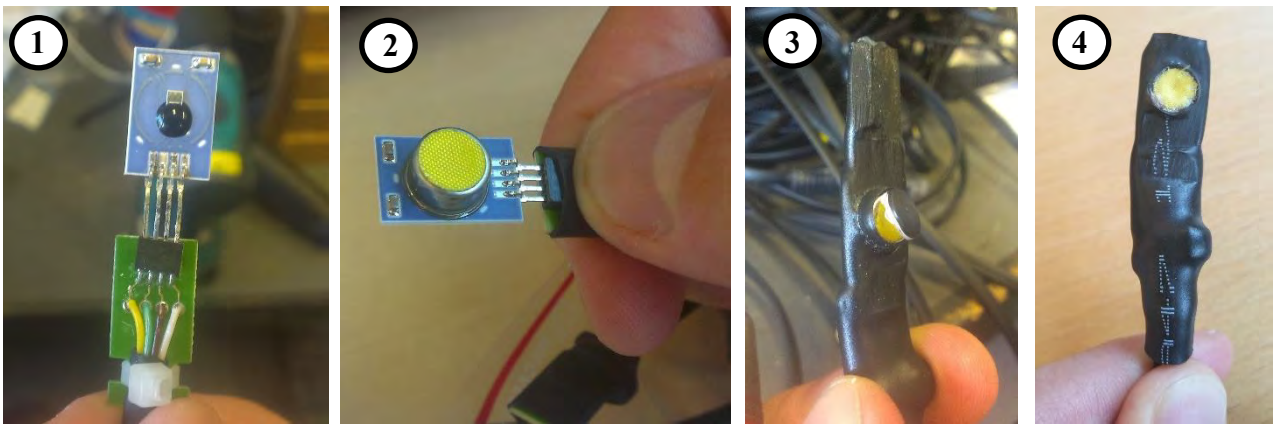

Fig. 56.: Sensor production. 1) Before adhesive shrink tubing 1. 2) Before adhesive shrink tubing 2. 3) After adhesive shrink tubing. 4) After adhesive shrink tubing, with tubing removed at the sensing area.

After application of the protective shrink tubing, the sensors were calibrated using four different saturated salt solutions for adsorption and desorption measurements. The saturated salt solutions used for the calibration are listed below as bullet points:

- Potassium Carbonate K2CO3 (44%)
- Sodium Chloride NaCl (75%)
- Potassium Nitrate KNO3 (93%)
- Potassium Sulfate K2SO4 (97%).

The calibration was carried out using a vapour tight box, with sealed inlets for the sensors and internal fan, which would ensure uniformity of the air within the box (picture 1 of figure 57). The sensors would be exposed to a certain salt solution until steady conditions occurred, then the next salt solution would be introduced, and so forth. Over the course of the calibration process, the measurements were validated using a Rotronic Hygrometer A2 measurement tool (picture 2 of figure 57), calibrated prior to calibration of the HYT221 sensors. Based on the measured (by the HYT221 sensors) and validated relative humidities, a linear trend line was created using Matlab for each of the sensors, providing the equations required for converting the measured relative humidities into real relative humidities. The linear trend lines were created with focus on the relative humidity measured from 75% and up, as these values were relevant in the experimental set-up in relation to the growing conditions for mould as well as wood decay. Finally, the equations were applied to the measured relative humidities, and the results were truncated to be in the range 0.00 to 99.99%.

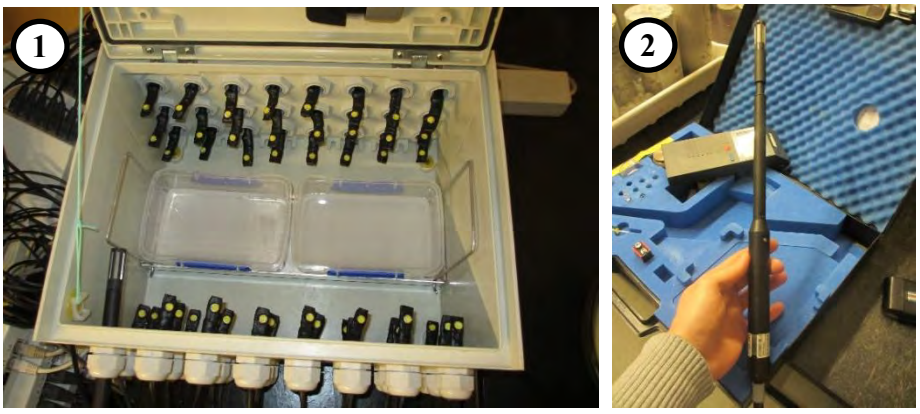

Fig. 57.: Sensor calibration. 1) Sensors and saturated salt solutions placed within the vapour tight box. 2) Rotronic Hygrometer A2 measurement tool.

The digital logging system used in the experiment was based on the use of Arduino boards, which would read measurements from the sensors and log the data to a computer through the software LabVIEW. Further data treatment would be carried out using Matlab.

The location of the digital HYT221 sensors, as well as the wooden- and gypsum dowel sensors are described below and their locations are also shown in figure 57.

- Sensor location 1: Digital HYT221, wooden- and gypsum dowel sensors installed in the masonry bricks, 54 mm from the exterior surface, in the horizontal centre of the wall area to the left of the adjacent internal masonry walls, 325 mm above the floor structure.

- Sensor location 2: Digital HYT221 sensor installed in the masonry bricks, 177 mm from the exterior surface (approximately at the centre of the masonry wall), in the horizontal centre of the wall area to the left of the adjacent internal masonry walls, 325 mm above the floor structure.
- Sensor location 3: Digital HYT221 sensor installed in a 10 mm recess in the masonry bricks behind the interior rendering layer, in the horizontal centre of the wall area to the left of the adjacent internal masonry walls, 325 mm above the floor structure.
- Sensor location 4: Digital HYT221 sensor installed behind the interior finishing layer of the respective insulation system (not valid for the reference assemblies without interior insulation), in the horizontal centre of the wall area to the left of the adjacent internal masonry walls, 325 mm above the floor structure.
- Sensor location 5: Digital HYT221 and wooden dowel sensors installed in the wooden wall plate, 40 mm below the wooden beam. The HYT221 sensor placed approximately in the centre of the wall area to the left of the adjacent internal masonry walls, while the wooden dowel sensor was placed 135 mm from the adiabatic surface on the left side.
- Sensor location 6: Digital HYT221 sensor installed 20 mm from the end of the wooden beam end embedded in the masonry wall, placed approximately in the middle of the beam (at half height and half width of the beam).
- Sensor location 7: Digital HYT221 sensor installed approximately in the centre of the wooden beam (at half height, half-length and half width of the beam) .
- Sensor location 8: Digital HYT221 sensor installed in a 10 mm recess in the masonry bricks behind the interior rendering layer, 20 mm to the left of the adjacent internal masonry walls, 325 mm above the floor structure..
- Sensor location 9: Digital HYT221 sensor installed behind the interior finishing layer of the respective insulation system (not valid for the reference assemblies without interior insulation), 20 mm to the left of the adjacent internal masonry walls, 325 mm above the floor structure.
- Sensor location 10: Digital HYT221 sensor installed in a 10 mm recess in the AAC blocks 100 mm below the floor structure, behind the interior finishing layer, in the horizontal centre of the wall area to the left of the adjacent internal masonry walls. A sensor was only installed at this location in walls 6 and 7 in the Xella container.

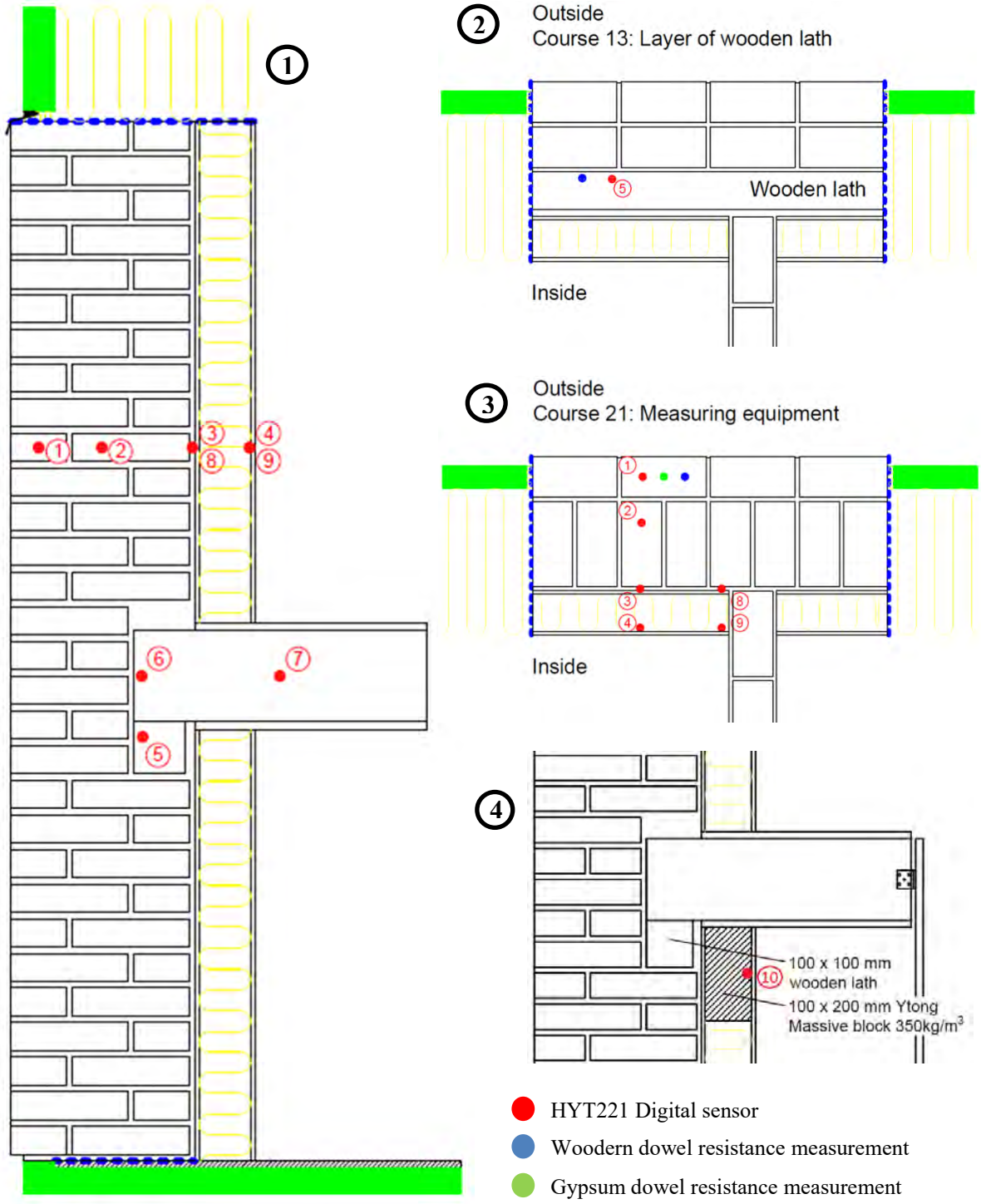

Fig. 58.: Sensor placement. 1) Vertical section showing sensor placement. 2) Horizontal section at masonry course 13 showing sensor placement. 3) Horizontal section at masonry course 21 showing sensor placement. 4) Vertical section showing sensor placement in AAC block below the floor structure.

Installation of the sensors within the masonry bricks were carried out by drilling holes into the bricks, and fitting the sensor into the hole (picture 1 of figure 59). Silicone would then be filled into the cavity around the sensor cable, thus leaving a small cavity just around the sensor (picture 2 of figure 59). Similar process was used for the installation of sensors within the wooden beams and the wooden wall

plate (picture 4 of figure 59). For the insulated masonry assemblies, the sensors were as mentioned above, placed in 10 mm recesses cut into the insulation material, just behind the interior finishing layers (picture 6 of figure 59). After installation, the sensors would then be covered by finishing layers for the respective insulation system (picture 7 of figure 59).

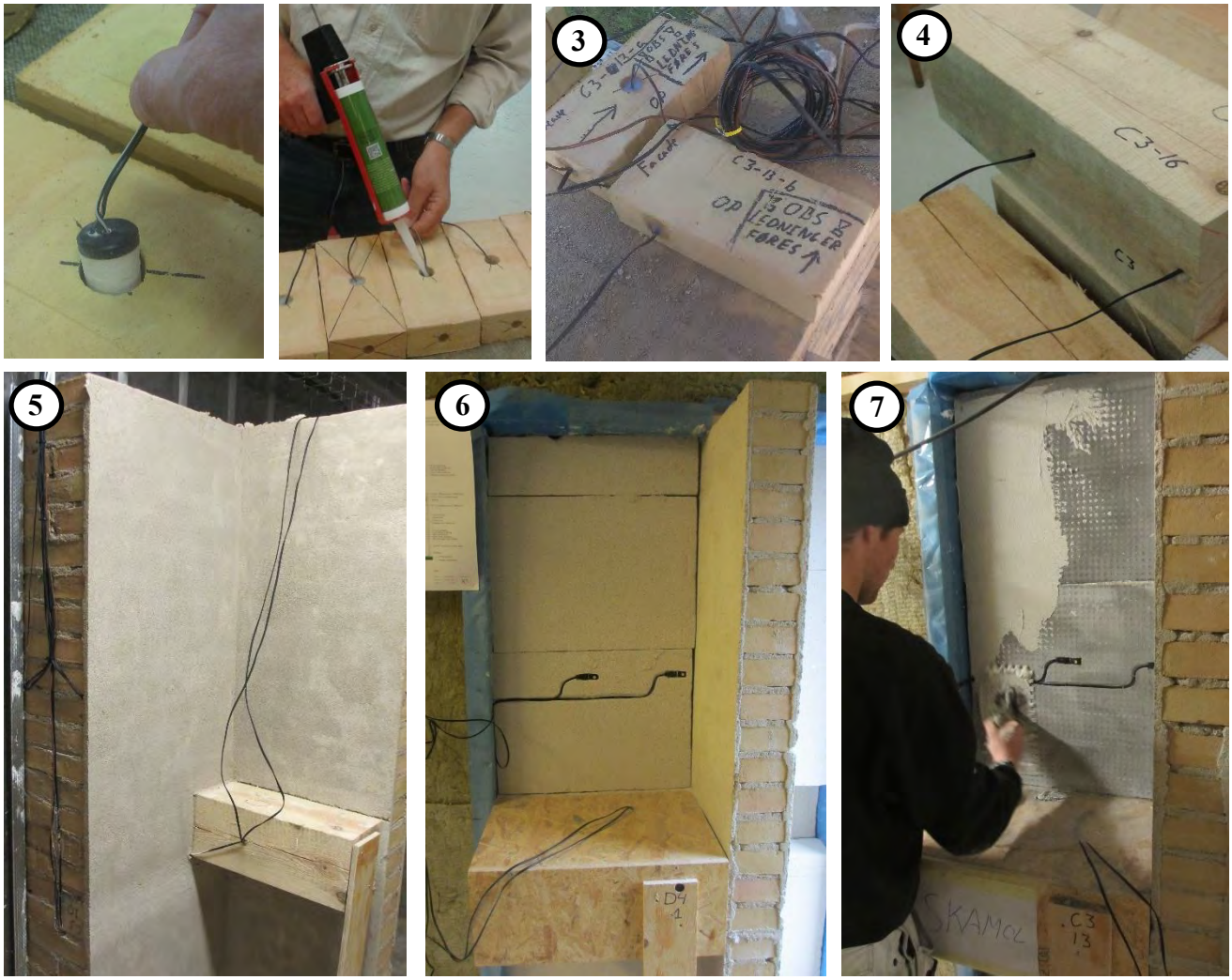

Fig. 59.: Sensor installation. 1) Sensors installation in masonry brick. 2) Filling cavity around the sensors with silicone. 3) Sensors at location 1 and 2 being installed in the masonry assembly. 4) Sensors at location 6 and 7 in the wooden beam. 5) Reference wall with all the sensors installed. 6) Installation of sensors 4 and 9 in recesses in the Xella Multipor boards. 7) Covering up sensors 4 and 9 in Skamoplus boards with the interior finishing.

Besides the sensor locations shown in figure 59 two sensors were also installed within each of the containers for measuring the indoor temperature and relative humidity, hanging 200 mm below the container ceiling and 2 m from the front and back end of the container (picture 1 of figure 60). The results from the two indoor sensors were average for the data analysis. The outdoor temperature and relative humidity measured using a sensor installed behind wooden cladding boards, under the rain gutter (picture 2 of figure 60).

Additional sensors were also placed on interior surface of a few masonry assemblies, behind leather patches or acrylic glass boards (picture 3 and 4 of figure 60). The leather patches or acrylic glass boards served to emulate leather furniture and picture frames respectively. Suspected to create a microclimate with higher risk of mould growth, between these elements and the interior surface of the masonry

assemblies. The acrylic glass boards were installed on walls no. 2, 4, and 7 in the GI container, as well as walls 1-5 in the Xella container. The leather patches were only installed on walls 2 and 3 in the Xella container.

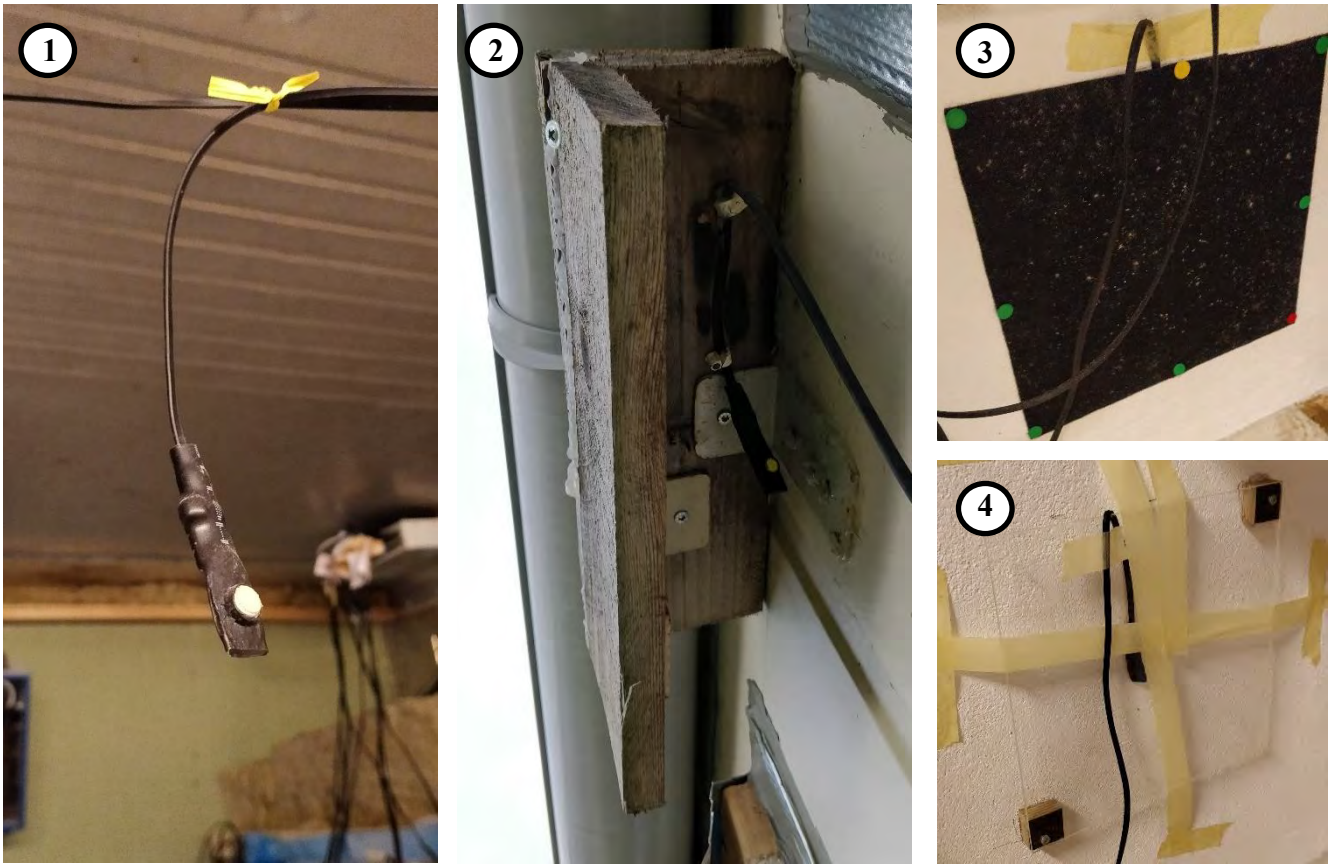

Fig. 60.: Additional HYT221 sensors. 1) Indoor ceiling hanging sensors. 2) Outdoor sensors below the rain gutters. 3) Sensors behind leather patches. 4) Sensors behind acrylic glass boards.

5.5 Boundary Conditions

In the initial period (May to August 2015), the temperature and relative humidity of the indoor climate were set to 20°C and 70%, to stress the experiment. Subsequently, the relative humidity was adjusted to 60%, corresponding to the upper boundary of indoor climate class 3, the highest climate class for dwellings in Denmark (Brand, et al., 2013).

The reefer containers were oriented so the GI walls 1-8 and Xella walls 1-8 were facing west-southwest, with a compass angle of 237°, while the GI walls 9-16 were facing east-northeast, with a compass angle of 57°. In Denmark, southwest is the prevailing wind direction and it is therefore considered the most critical orientation for wind-driven rain. Combined with the high amounts of solar radiation from south, there is a potential for moisture transport from the exterior surface towards the indoor environment. The north facing masonry assemblies were considered as this orientation experiences considerably lower amount wind-driven rain, but at the same time, also considerably lower amount solar radiation.

5.6 Measurement Results

At the time of writing the present report, only results from the Xella container have been analysed and documented. This work was carried out by Ph.D. students at DTU, Nickolaj Feldt Jensen and Tommy Riviere Odgaard in (Jensen, Bjarløv, Rode, & Odgaard, 2018). Results regarding the tests wall from the GI container are schedules to be analysed and documented during autumn of 2018; and will be included as a part of the WP7 deliverable.

The study investigated the combination of several measures to cope with the changed hygrothermal conditions as a consequence of the application of internal thermal insulation. This included hydrophobization of the exterior masonry surface; as well as the implementation of a deliberate thermal bridge in front of the embedded wooden wall plate, below the wooden floor structure. The thermal bridge was created by installing a 100 by 200 mm AAC block with a higher thermal conductivity than the Multipor mineral insulation boards. The study also included a small simulation study presented in section 5.7.2.

The following masonry assemblies were assessed: X2, X3, X5 and X6, see section 5.7.2 for more information. The results presented in the following sections are from two years of monitored data from 2015.05.01 until 2017.05.01; and the data is based on smoothened 96-h running average values for temperature graphs and hourly average values for the relative humidity graphs. It was observed that the conditions in the test walls did not stabilized until around May 2016, and thus the period prior to May 1st 2016 has been denoted as the stabilization period. Damage models for mould growth and wood decay were used for evaluation of the measured hygrothermal conditions in the test walls, and were used only for the datasets after the stabilization period. As the hygrothermal conditions during the stabilization period were considered to be affected by the initial conditions, and thus not representative for the operating conditions of the test walls.

5.6.1 Hygrothermal conditions near the interior surface

Fig. 61 shows the measured relative humidity and theorical predicted risk of mould growth near the interior surface, in point 3 for the reference wall 5 and point 4 for the insulated walls 2, 3, and 6. In addition point 10 for wall 6 is included, showing the hygrothermal conditions near the interior surface for the deliberate thermal bridge (AAC block) installed in front of the embedded wooden wall plate.

The relative humidity near the interior surface was observed to generally follow the indoor climate in the test container, however with surplus resulting from differences in the moisture content and material properties of the surface material, surface temperature between the wall configurations as well as the use or not of a hydrophobization agent. During the observed period after stabilization two important effects were noticed (Fig. 61), the effect of 1) exterior façade hydrophobization, and 2) interior thermal insulation. It was observed that during the summer period lowering the rain intrusion, by hydrophobization of the exterior surface, was crucial for reducing the relative humidity near the interior surface. The relative humidity near the interior surface of the hydrophobized Walls 3 and 6 were seen to be 5-10% lower compared to the interior surface of the reference Wall 5. Meanwhile, the un-hydrophobized insulated Wall 2, showed relative humidity levels in between the hydrophobized walls and the reference wall. During following winter and spring however, the interior thermal insulation was observed to be crucial in reducing the relative humidity near the interior surface. During winter, the highest relative humidity of approximately 85% was observed for the reference Wall 5, closely followed by the sensor located near the interior surface in front of the deliberate thermal bridge by approximately 83%. Meanwhile, the insulated Walls 2, 3 and 6 were seen to experience relative

humidity levels 10-15% below those of the reference wall. Despite the rather large difference observed between the unhydrophobized insulated Wall 2 and the hydrophobized insulated Walls 3 and 6 during the summer, a mere 1-2% difference was observed between these walls during winter and spring.

No mould growth was predicted by the mathematical model for the interior surface on any of the four test walls during the observed period.

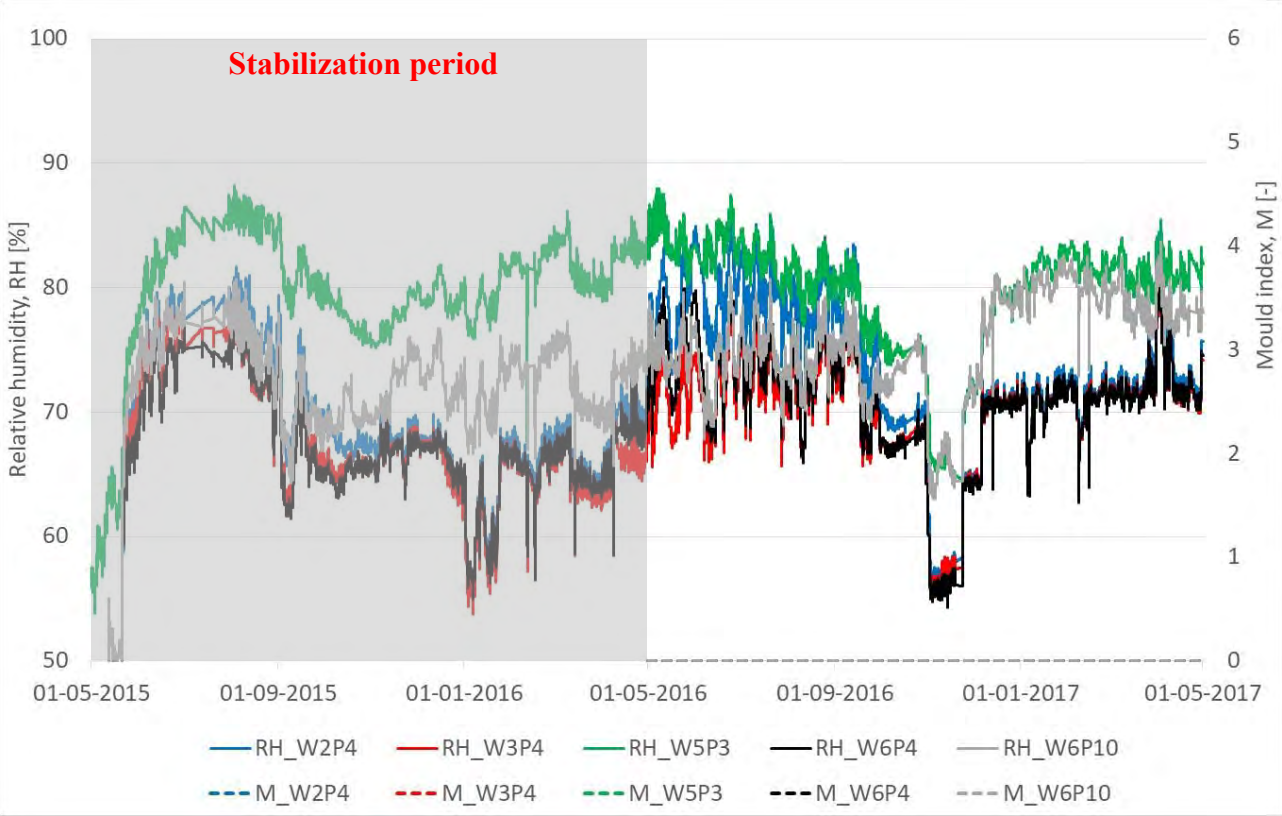

***Fig. 61.:** Measured relative humidity, RH, and calculated mould index, M, for the sensor at the interior surface: Point 3 for the reference wall 5, Point 4 for the insulated walls 2, 3 and 6 as well as Point 10 for wall 6 with the deliberate thermal bridge.*

5.6.2 Hygrothermal conditions at the interface

Fig. 62 shows the measured relative humidity and theorical predicted risk of mould growth at the interface between the existing masonry wall and the new insulation system (behind the insulation), point 3 for the insulated walls 2, 3, and 6.

The interface between the existing masonry wall and the new insulation system is of particular interest when dealing with diffusion open thermal insulation systems for internal application. As internal insulation reduces the heat flow to the existing masonry wall, thus lowering the temperature of the wall and its drying potential. This in turn increases the risk of interstitial condensation in case of warm moisture air from the indoor climate reaching the cold internal surface of the existing masonry wall at the interface. Thus, a combination of reduced heat flow to the existing masonry wall with diffusion open thermal insulation, allowing moisture diffusion from the indoor climate, could result in condensation and/or moisture induced damages. Despite the fact that insulation system is designed to allow moisture within the construction to dry out to the indoor climate, this phenomena was still

observed at the interface for all insulated walls 2, 3, and 6, see Fig. 62. With condensation occurring for several months during the winter period. The un-hydrophobized Wall 2 remained rather stable at 100% relative humidity throughout most the period after stabilization, with only a minor drop during summer to around 92%. For Walls 3 and 6 on the other hand, the hydrophobization of the exterior surface is clearly seen to have a positive effect during summer, as rain intrusion is reduced. Resulting in relative humidity levels at the interface down to around 70-75%. However, the relative humidity in the hydrophobized walls at the interface is seen to experience a rapid increase during winter. These findings correlate with previous simulation studies by DTU (Finken, Bjarløv, & Peuhkuri, 2016) (Otiv, 2016).

The mathematical mould model predicted worsened conditions for all insulation walls, with the un-hydrophobized Wall 2 reaching a mould index of M = 2.6. Meanwhile the hydrophobized Walls 3 and 6 reached M = 0.8 and 0.9 respectively. It should be noted that these results were reached with only one year of experimental data following the stabilization period, and that all insulated walls showed increasing tendency during winter. Threshold values for predicted mould growth was defined by Viitanen et al. (Viitanen, Krus, Ojanen, Eitner, & Zirkelback, 2015), in which M > 3.0 is considered as unacceptable for surfaces not in direct contact with the indoor air. With the increasing tendency of the insulated walls it is expected that the threshold will be surpassed with longer datasets.

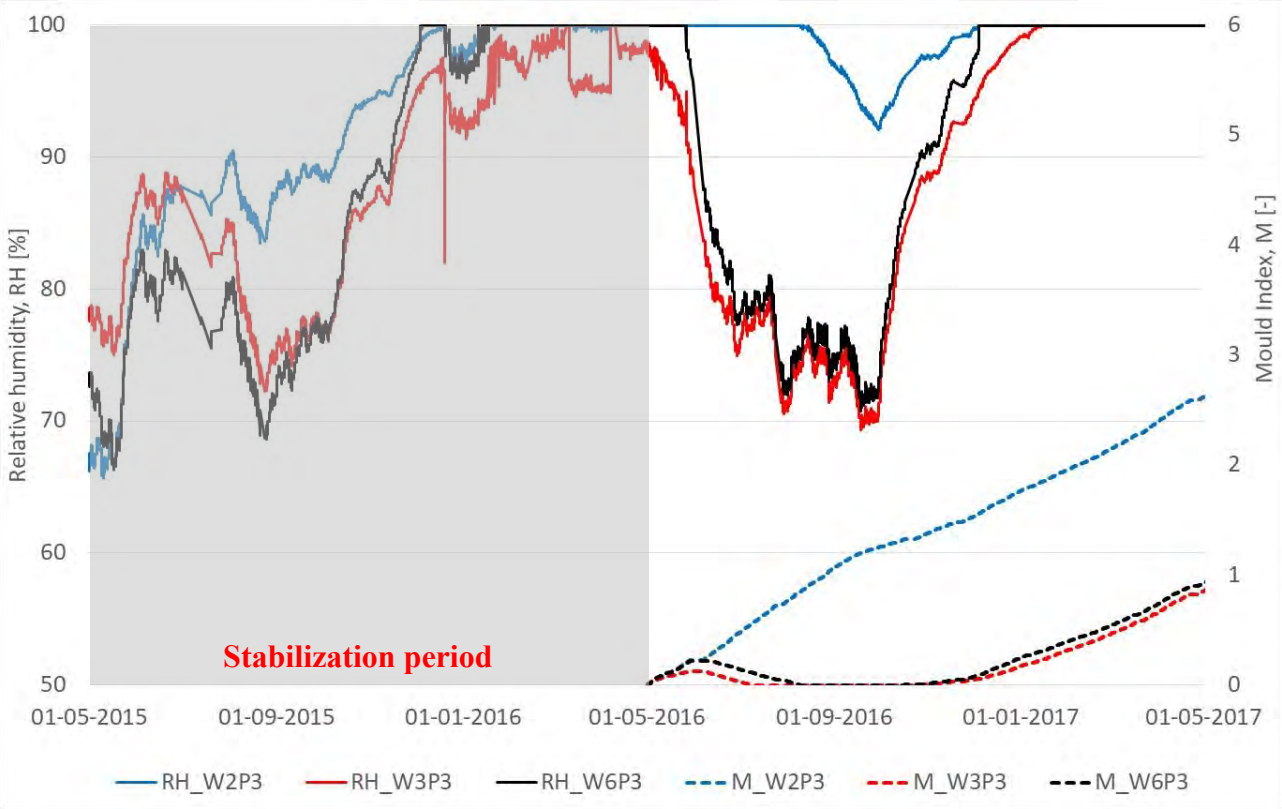

Fig. 62.: Measured relative humidity, RH and calculated mould index, M, for the sensor at the interface between existing mansonry wall and new insulation system, Point 3, in the insulated walls 2, 3, and 6.

5.6.3 Hygrothermal conditions in the embedded wooden wall plate

Fig. 63 shows the measured relative humidity and theorical predicted risk of wood decay in the embedded wooden wall plate, point 5. Traditionally, internal insulation is installed covering the entire

surface from floor to ceiling. However, installing thermal insulation in front of the embedded wooden wall plate supporting the floor structure may pose a potential risk. In Fig. 63 it is seen that reference Wall 5 experienced relative humidity levels exceeding 90-95% during the winter period, while a small decrease was observed during summer. The mathematical model predicted a risk of wood decay in the embedded wooden wall plate during the period May to July. The application of internal insulation in Wall 2 was seen to lower the temperature (see Fig. 64) especially during winter, and increase the relative humidity in the wall plate compared to the reference wall. This in turn increased the risk of wood decay in the wall plate, where the wood decay is seen to occur one month earlier in the spring of 2017 compared to the reference wall. Hydrophobization of the exterior surface (Wall 3) was on the other hand seen to reduce the relative humidity in the wall plate to levels below that of the reference wall throughout the experimental period; thus lowering the risk of wood decay. Lastly, the implementation of the deliberate thermal bridge in front of the wall plate was seen increase the temperature in the wall plate (see Fig. 64) and further reduce the relative humidity, thus also the risk of wood decay. Note that no wood decay was predicted for the embedded wooden wall plate in the hydrophobized Wall 3 and 6. Furthermore, the high relative humidity levels observed for the embedded wooden wall plate in reference Wall 5 indicate a need to control the indoor humidity already prior to application of the internal insulation system. However as earlier mentioned, the indoor humidity set point for the experiment was a rather high; which may not be representative for conditions within historic buildings in Denmark during the winter period.

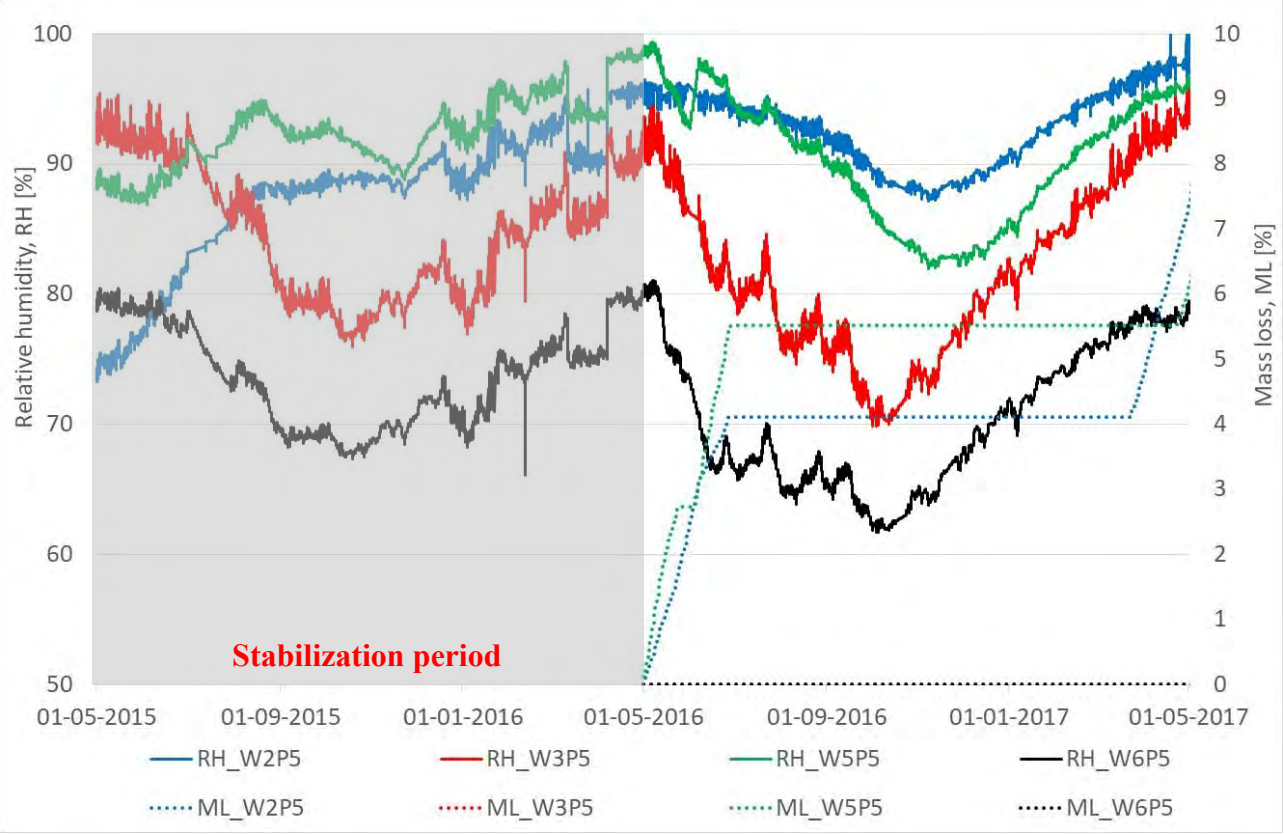

Fig. 63.: Measured relative humidity, RH, calculated wooden decay mass loss, ML, for the sensor in the embedded wooden wall plate, Point 5.

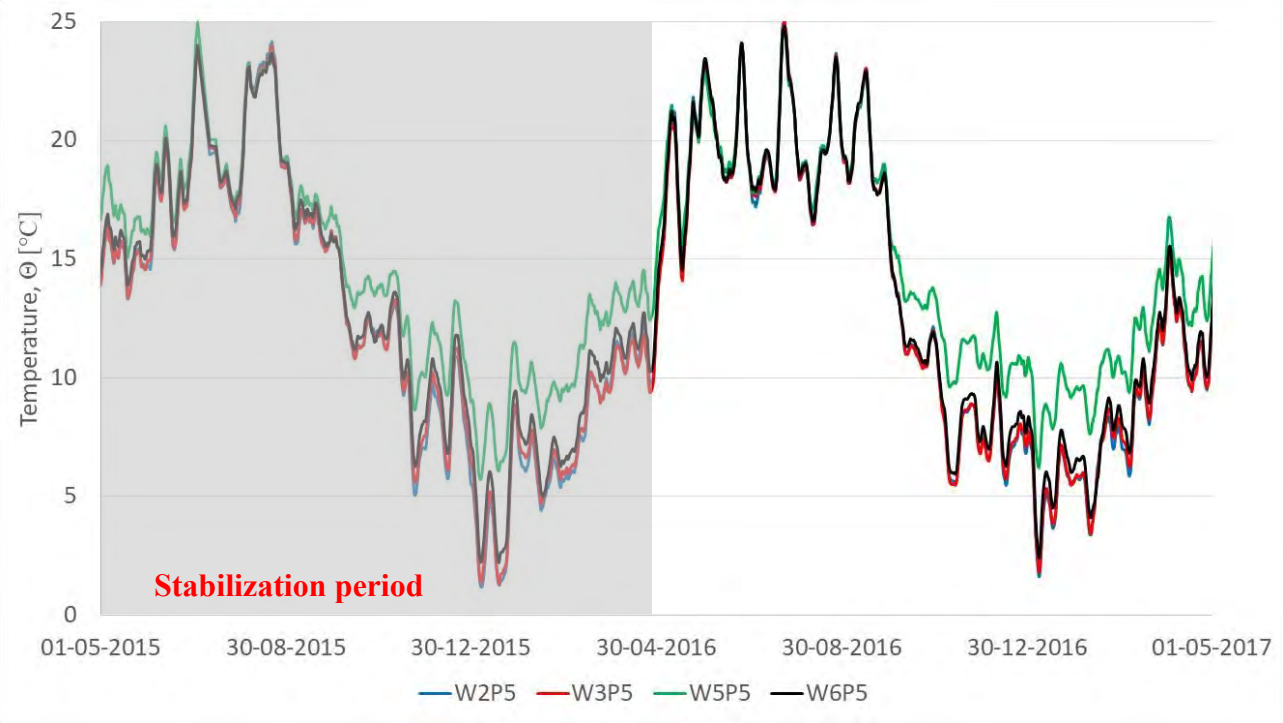

Fig. 64.: Measured temperature, Θ, for the sensor in the embedded wooden wall plate, Point 5.

5.6.4 Hygrothermal conditions in the embedded wooden beam end

Fig. 65 shows the measured relative humidity and theorical predicted risk of wood decay in the embedded wooden beam end, point 6.

In Fig. 65 it is seen that the un-hydrophobized Walls 5 and 2 (with and without insulation respectively) experienced rather similar relative humidity levels during the assessed period; deviating by 2-3% during summer and slightly more during winter. The hydrophobized Walls 3 and 6 on the other hand did not show the same similarities. During the summer period of 2016 until November, the hydrophobization of the exterior surface was seen to reduce the relative humidity in the beam end below 75%. However, in the following winter period from November 2016 until May 2017, the insulated hydrophobized Wall 3 experienced a rapid increase in relative humidity to levels exceeding those of the un-hydrophobized walls. Meanwhile increasing the temperature in the embedded wooden elements by installation of a deliberate thermal bridge (Wall 6) was seen to reduce the increase in relative humidity during winter caused by the hydrophobization, to levels in between those of the two un-hydrophobized walls.

The hygrothermal conditions in the beam end was generally observed to be better than in the embedded wall plate; and opposite to the embedded wooden wall plate, the mathematical model did not predict a risk of wood decay in the embedded wooden beam end within any of the test walls. These results support the findings from previous simulation studies (Morelli & Svendsen, 2012) (Harrestrup & Svendsen, 2016), dealing with internal post insulation for heritage buildings with embedded wooden elements.

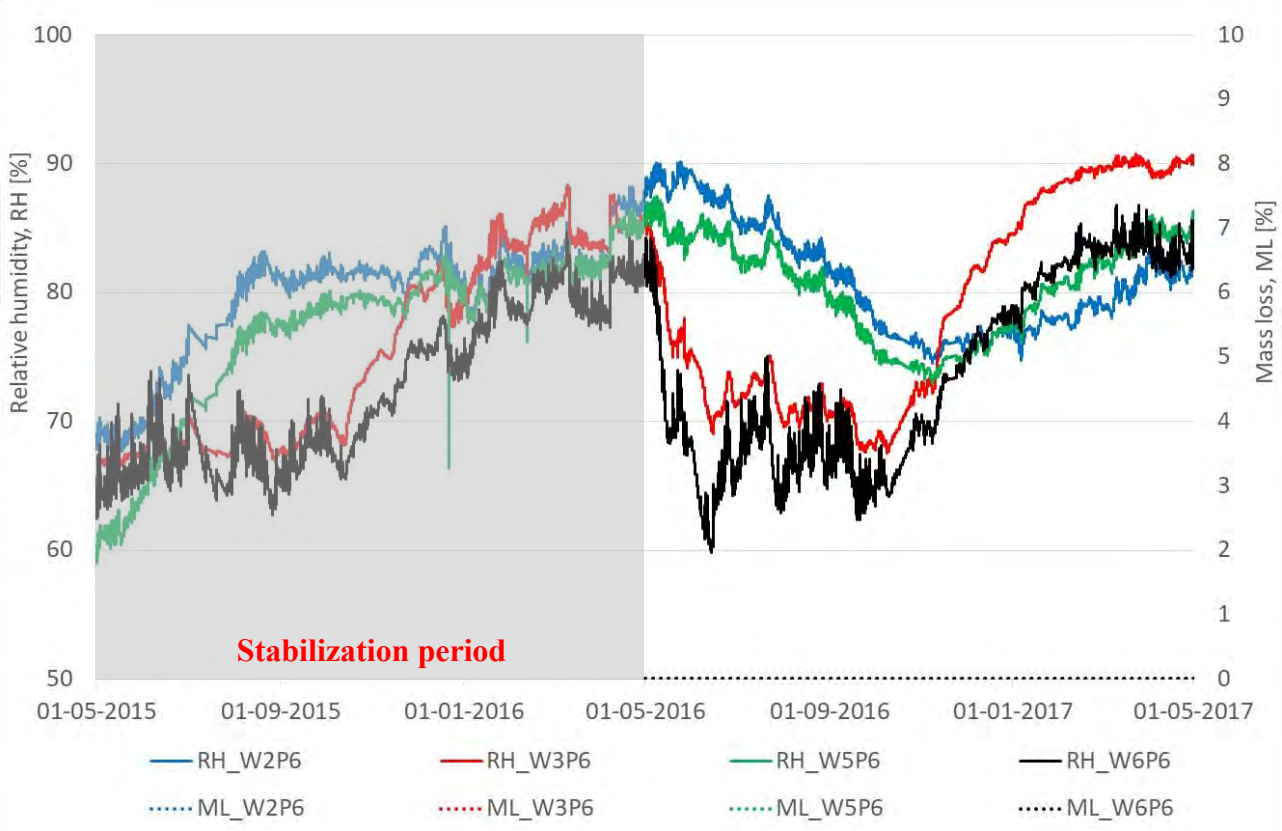

Fig. 65.: Measured relative humidity, RH, calculated wooden decay mass loss, ML, for the sensor in the embedded wooden beam end, Point 6.

5.6.5 Hygrothermal conditions near the exterior surface

Fig. 66 and 67 shows the measured relative humidity and temperature in the existing masonry wall near the exterior surface and in the middle of the wall, points 1 and 2.

In the existing masonry wall it was observed that the temperatures were rather similar in point 1, near the exterior surface, between the un-hydrophobized Walls 2 and 5, and the hydrophobized Walls 3 and 6 during the summer period. During the winter period however, the reference Wall 5 was seen to experience slightly higher temperatures. Meanwhile in the middle of the masonry wall, the reference Wall 5 was seen to experience temperatures 2-3 ºC higher than the hydrophobized insulated Wall 3, which is turn was 1-2 ºC higher than the than the un-hydrophobized insulated Wall 2 and the hydrophobized insulated Wall 6. As for the relative humidity; the four walls showed similar tendencies in the two sensor points, however with a higher measured relative humidity in the un-hydrophobized Walls. Near the exterior surface, the un-hydrophobized Walls 2 and 5 experienced an average of around 85-90% relative humidity during summer and saturation during winter, while the hydrophobized Walls 3 and 6 experienced an average of around 70% in summer and an average of around 85% in winter, with a peak up to around 90%. In the middle of the masonry wall, Wall 2 is rather stable at saturation level through most of the period, with a minor drop to 95% around October-November 2016. Similar, the reference Wall 5 is seen also to be rather stable at saturation level, however with a larger and longer drop during later summer and autumn. The hydrophobized Wall 3 was seen to experience levels around

75-80% during summer and saturation in winter, while Wall 6 an average of around 70% during summer and peak around 93% during winter.

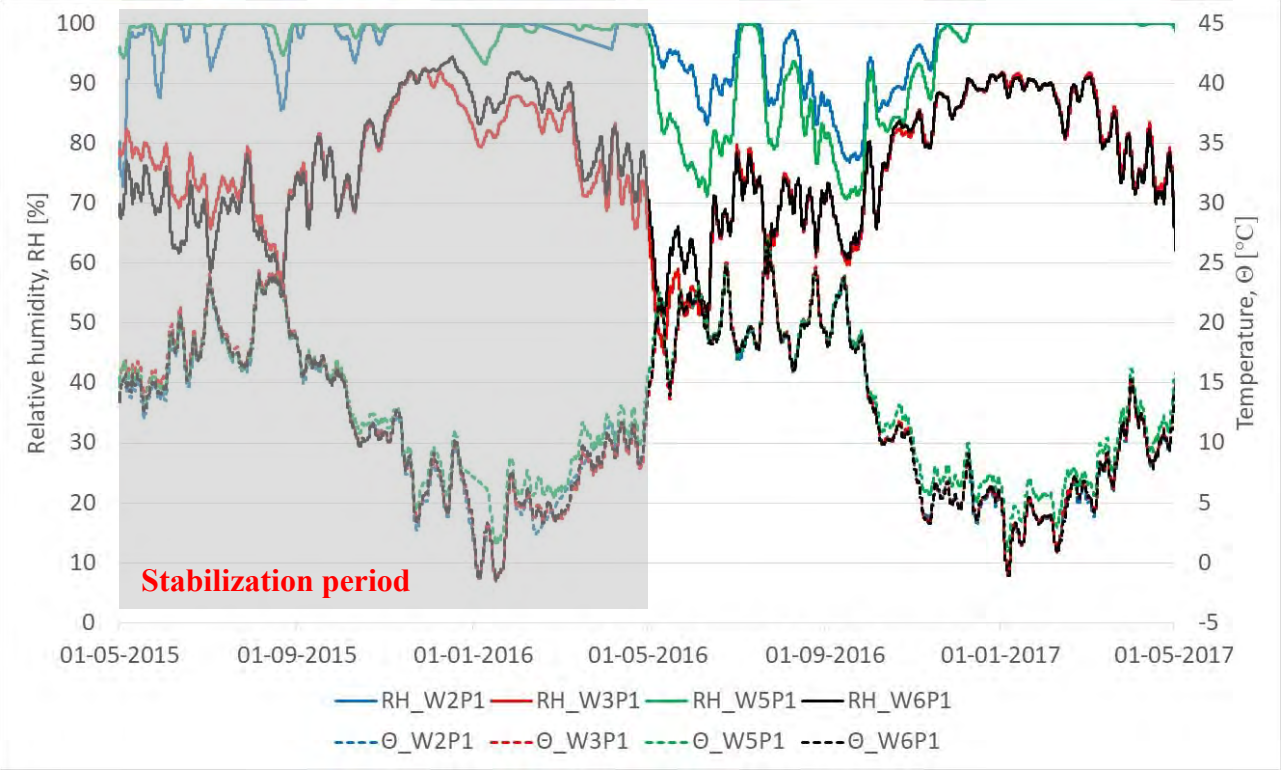

Fig. 66.: Measured relative humidity, RH and temperature, Θ. Sensor point in masonry near the exterior surface: Point 1.

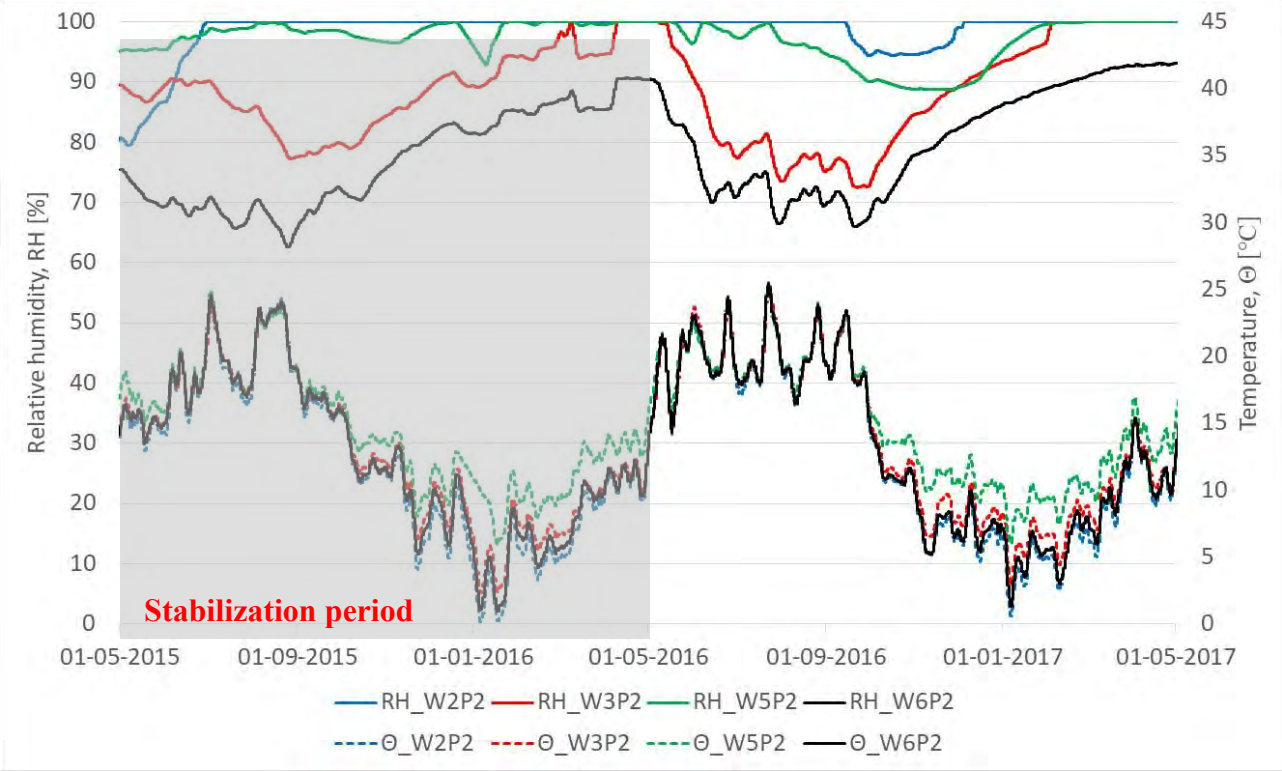

Fig. 67.: Measured relative humidity, RH and temperature, Θ. Sensor point in masonry, middle of the wall: Point 2.

5.6.6 Effect of the hydrophobization

Measurements from the experimental setup indicate that the hydrophobization of the exterior surface has a positive and negative effect on the hygrothermal conditions in the test walls, depending on the season. The hydrophobization lowers the rate of liquid transport through the depth of the hydrophobization layer (e.g. outermost 5-10 mm) toward both the interior and exterior side. During the summer period, the lowered rate of liquid transport by the hydrophobization lowers the rain intrusion resulting in a reduction of the relative humidity within the test wall. However, due to the increased risk of condensation caused by the internal insulation and the lowered rate of liquid transport over the depth of the hydrophobized layer, the hydrophobized test walls experiences a reduced potential for evaporation (drying) to the cold and dry outdoor climate during the winter period. Resulting in increased relative humidity during winter. This effect is seen clearly in Fig. 62, at the interface between the existing masonry wall and new insulation system in the hydrophobized Walls 3 and 6; where the walls were observed to experience relative humidity levels around 70-75% during the summer period, followed by a rapid increase in the following winter period to saturation level. The same tendency was not seen for the un-hydrophobized Wall 2, which however remained rather stable at saturation level. The effect was also seen for the embedded wooden beam end in the insulated hydrophobized Wall 3 (Fig. 65), discussed in section 5.6.4.

5.7 Simulation Studies

5.7.1 Building location

Results and figures presented below are from the master's thesis by former Msc. student at DTU, Peter Otiv (Otiv, 2016). In his thesis, Otiv carried out 1-D hygrothermal simulations with DELPHIN (Nicolai, Grunewald, & Zhang, 2007; Grunewald J. , 1996) for two of the internally insulated masonry assemblies. The masonry assemblies consisted of 348 mm yellow softmolded historical brick, 10mm historical lime plaster, 8mm glue mortar, 100 mm lightweight mineral insulation, and 8mm glue mortar. One of the masonry assemblies had a bare exterior surface, while the other one had a hydrophobized exterior surface (Xella walls X2 and X3 see 5.7.2). The hydrophobization was carried out by reducing the water uptake coefficient, A_w, of the outermost 10mm of the historical brick by a factor of 1000. Note that the materials used for the Delphin simulation were obtained from the DELPHIN material database, with exception of the yellow softmolded historical brick. The material properties for the historical brick were obtained from a previous study carried out by DTU (Dysted & Sandholdt, 2015). Both masonry assemblies were simulated with a cardinal direction towards southwest with a compass angle of 225°.

Initially, the DELPHIN models were validated using measured data, including measured data from sensor location one to four within the two masonry assemblies, as well as for the interior and exterior climates. The model validation by Otiv will not be presented in this report, for more information the reader is referred to (Otiv, 2016). After the model validation, the exterior climate was changed to those of Copenhagen, Esbjerg and Aalborg, in order to investigate how the interior insulated masonry assemblies would perform under different typical Danish climate conditions. For the comparison between the three locations, Design Reference Year (DRY) climate data from the Danish Meteorological Institute was used. Note that the DRY data sets did not include rain data. Rain data for Kgs. Lyngby was therefore used for all three locations. Otiv mentions that this may overestimate the influence of the rain at the other locations, as Kgs. Lyngby generally receives more precipitation in comparison to the other locations.

Regarding the initial conditions of the masonry assemblies, the default settings of 80% relative humidity and 20°C were used. However, note that a two-year initial simulation period using cyclic DRY climate data for Copenhagen was used in order to allow the materials to reach a quasi-steady state before introducing the measured data recorded at the experimental set-up at DTU, Kgs. Lyngby, as recommended in the SUSREF guidelines (Häkkinen, et al., 2012). This process was however only used for the model validation. For the simulations using climate data from other geographical locations (Copenhagen, Esbjerg and Aalborg), the default settings were used and the DRY climate data was simulated for a period of three years. From the three simulated years using DRY data, the last year was taken for further assessment.

As for the boundary conditions, Otiv altered several coefficients under the boundary conditions during the validation process and the values used for the final wall models, for each of the altered coefficients is are shown in table 18. The remaining coefficients were left as default.

Tab. 18.: Boundary conditions

Boundary condition	Coefficient	Position	Value
Rain	Rain exposure coefficient		0.6
Short wave solar radiation	Reflection coefficient of the surrounding ground (albedo)		0.2
Long wave solar radiation	Emission coefficient of the building surface		0.7
Heat conduction	Exchange coefficient for heat flow	External Internal	25 W/m^2K 4 W/m^2K
Vapour diffusion	Exchange coefficient for vapour diffusion	External Internal	2e-7 s/m 3e-8 s/m

Finally, the moisture conditions within the masonry assemblies under the different typical Danish climate conditions were assessed with respect to mould growth at sensor locations 3 and 4 using the VTT mould model (Hukka & Viitanen, 1999) (Ojanen T. , Peuhkuri, Lähdesmäki, Vinha, & Salminen, 2010), wood decay using the VTT wood decay model (Viitanen, et al., 2010), and frost damages using Delphins built-in "Ice volume to pore volume ratio" model (Sontag & Nicolai, 2013). Note that for the evaluation using the damage models, a worst-case scenario was used, with a material sensitivity of sensitive and almost no decline.

For a better understanding of the results section, graphical illustrations of the climatic conditions (temperature, relative humidity, wind direction, wind velocity and rain intensity) are shown below for the DRY data sets for Copenhagen, Esbjerg and Aalborg, as well as the measured data from Kgs. Lyngby.

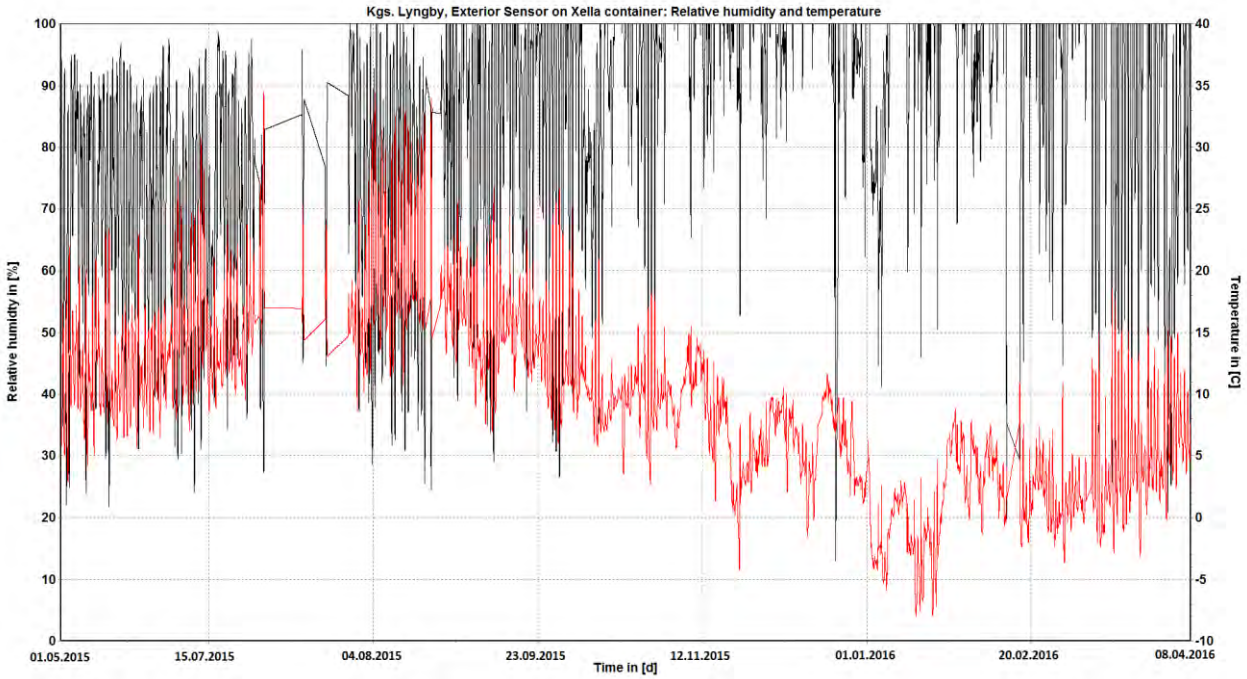

Fig. 68.: Measured data recorded by the exterior sensor on the Xella container, Kgs. Lyngby, showing relative humidity (black) and temperature (red).

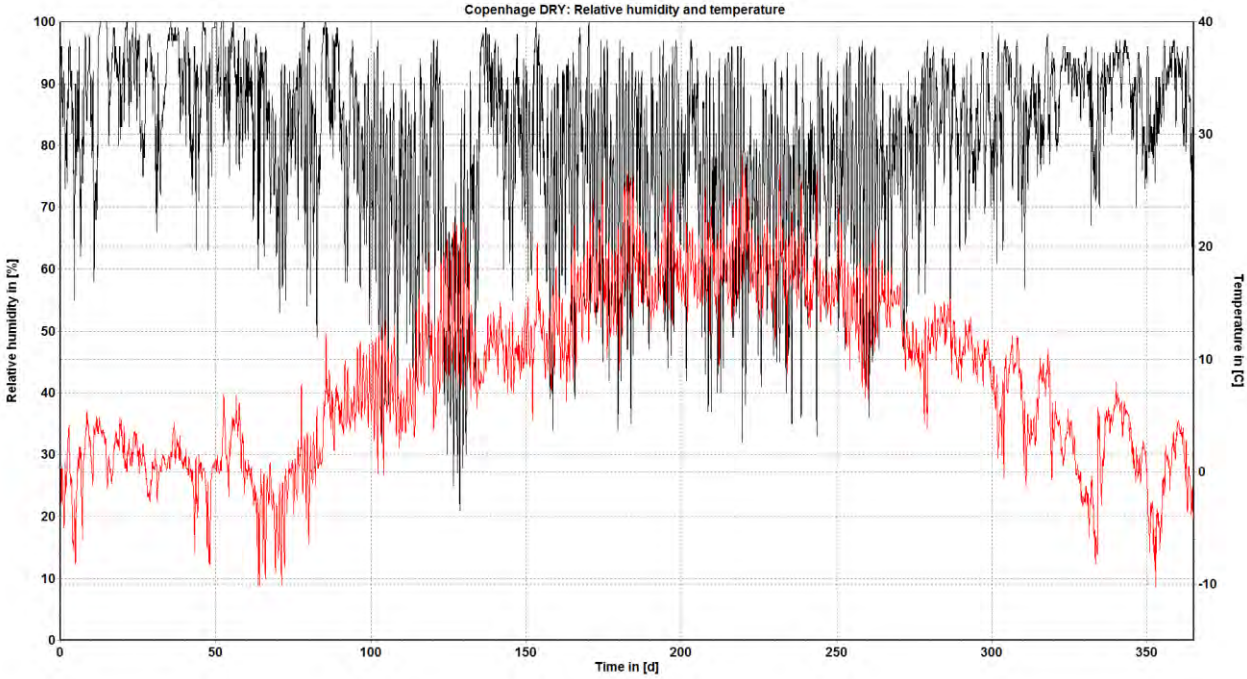

Fig. 69.: Design Reference Year (DRY) climate data for Copenhagen, showing relative humidity (black) and temperature (red).

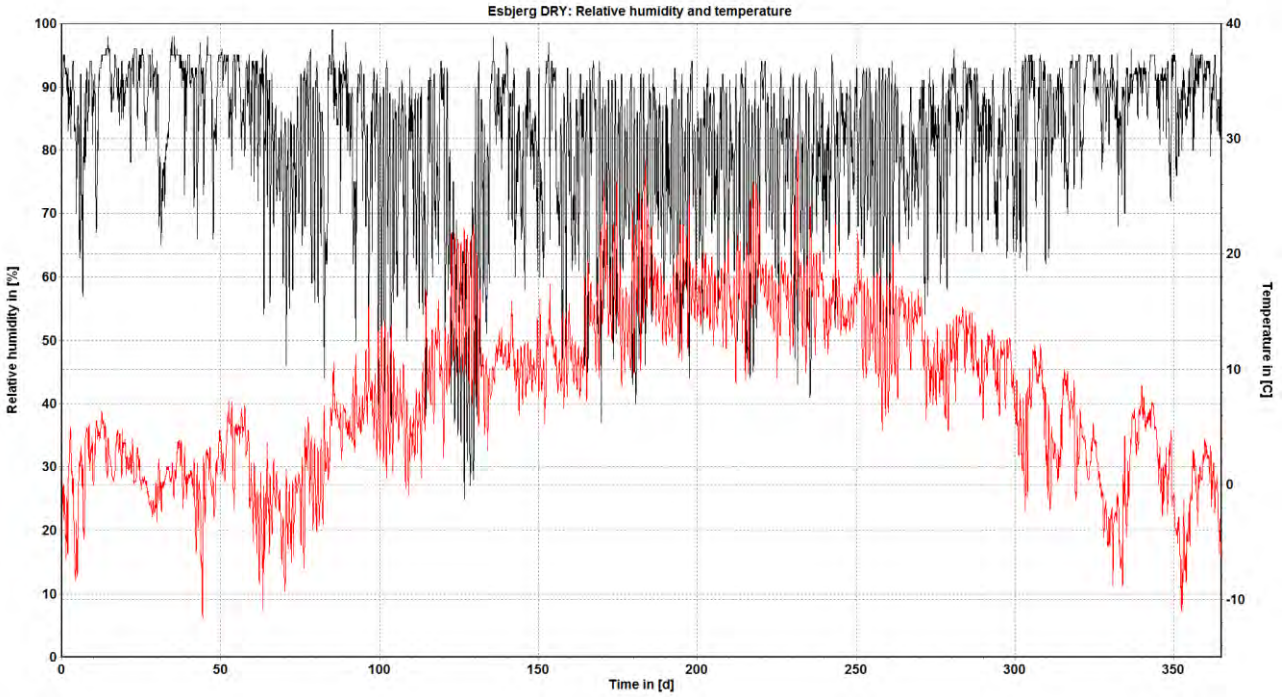

Fig. 70.: Design Reference Year (DRY) climate data for Esbjerg, showing relative humidity (black) and temperature (red).

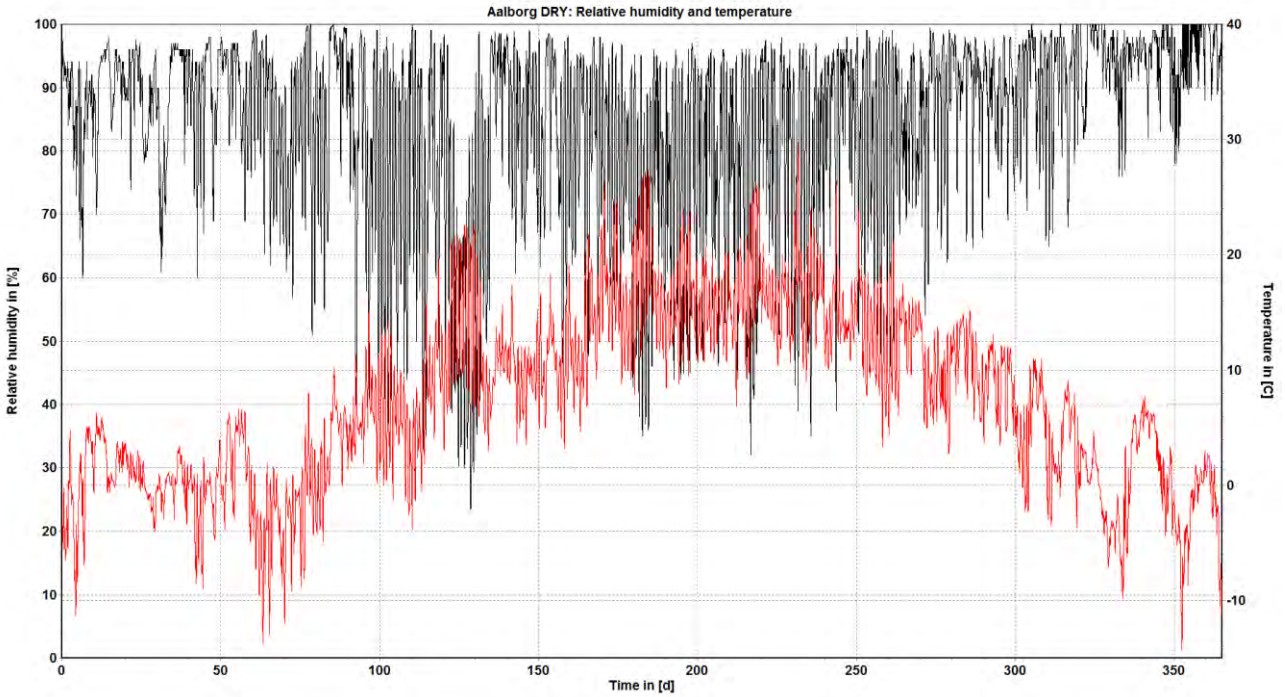

Fig. 71.: Design Reference Year (DRY) climate data for Aalborg, showing relative humidity (black) and temperature (red).

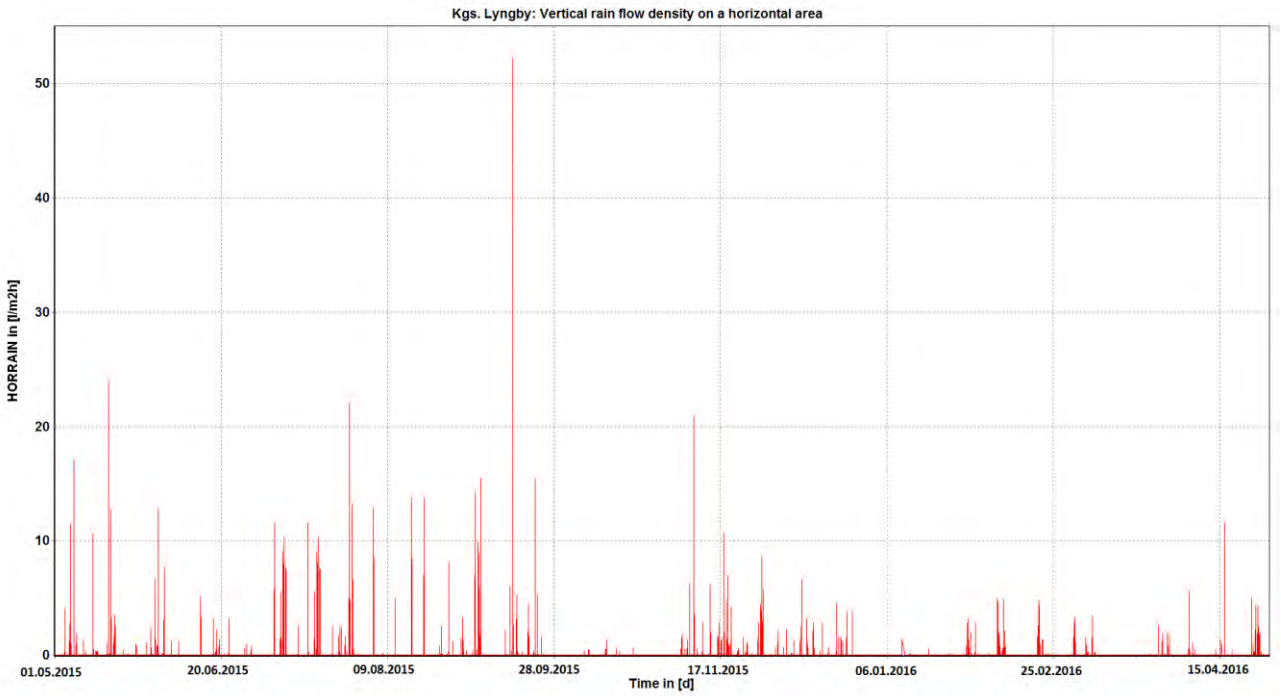

Fig. 72.: Measured data recorded by the DTU weather station, Kgs. Lyngby, showing the vertical rain flow density on a horizontal area (red).

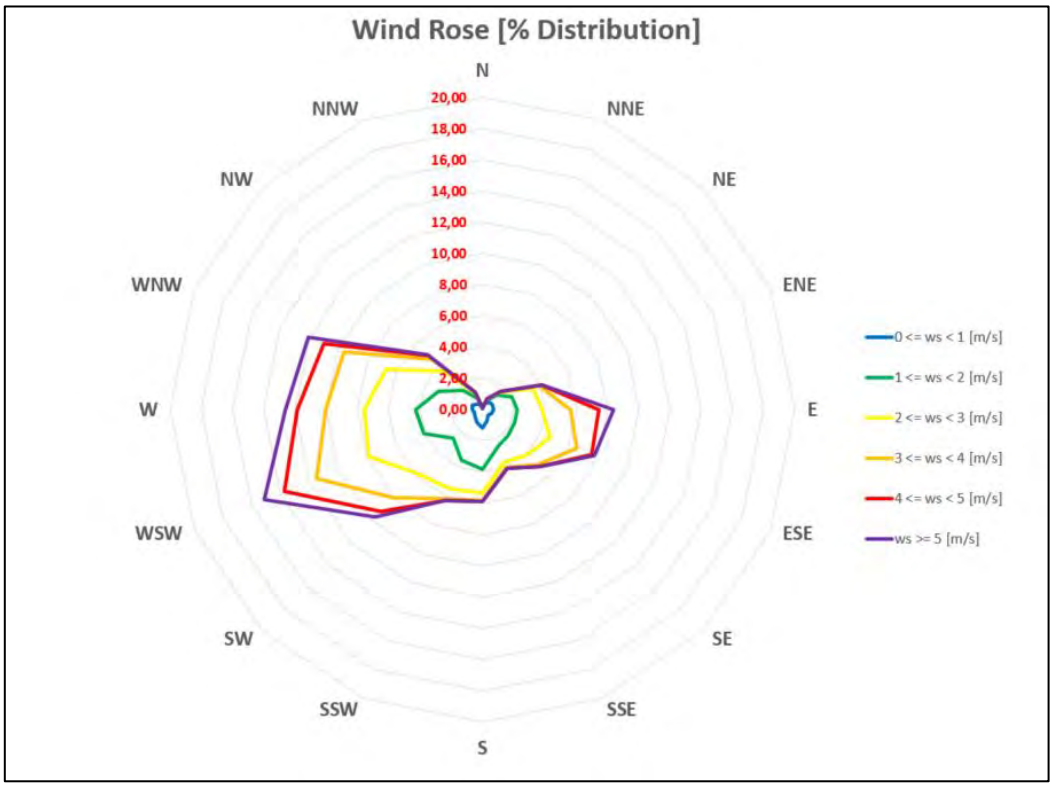

Fig. 73.: Design Reference Year (DRY) climate data for Copenhagen, showing wind direction and velocity (ws). Blue = ws<1 m/s, Green = 1<ws<2 m/s, Yellow = 2<ws<3 m/s, Orange = 3<ws<4 m/s, Red = 4<ws<5 m/s, Purple = ws>5 m/s.

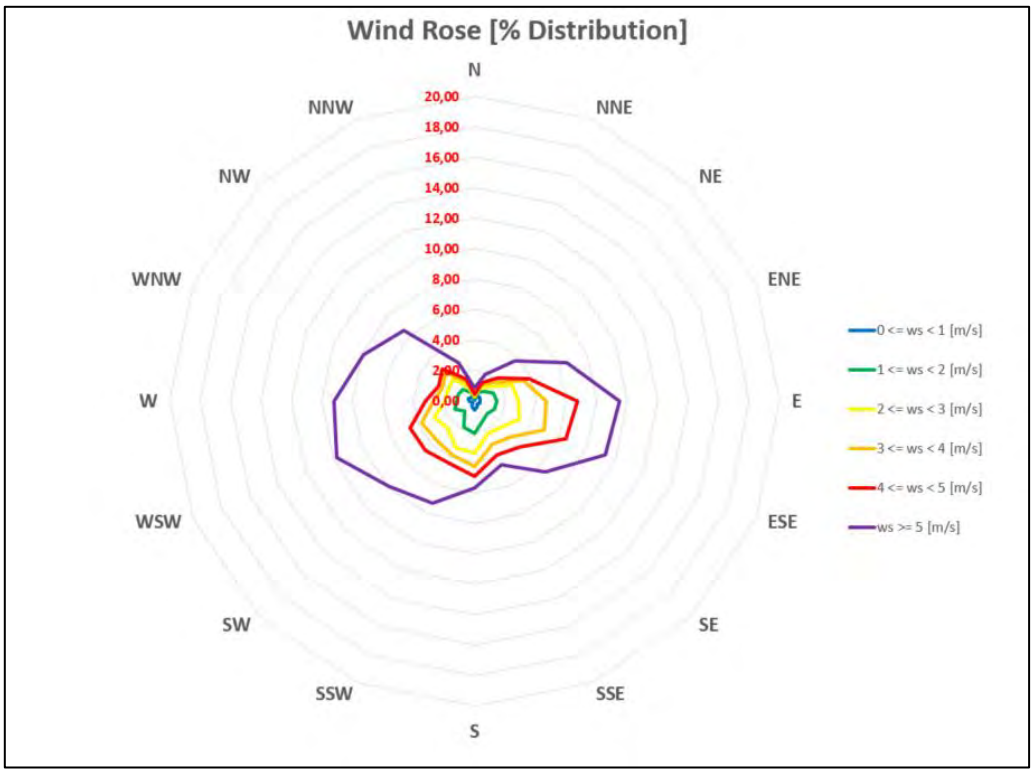

Fig. 74.: Design Reference Year (DRY) climate data for Esbjerg, showing wind direction and velocity (ws). Blue = ws<1 m/s, Green = 1<ws<2 m/s, Yellow = 2<ws<3 m/s, Orange = 3<ws<4 m/s, Red = 4<ws<5 m/s, Purple = ws>5 m/s.

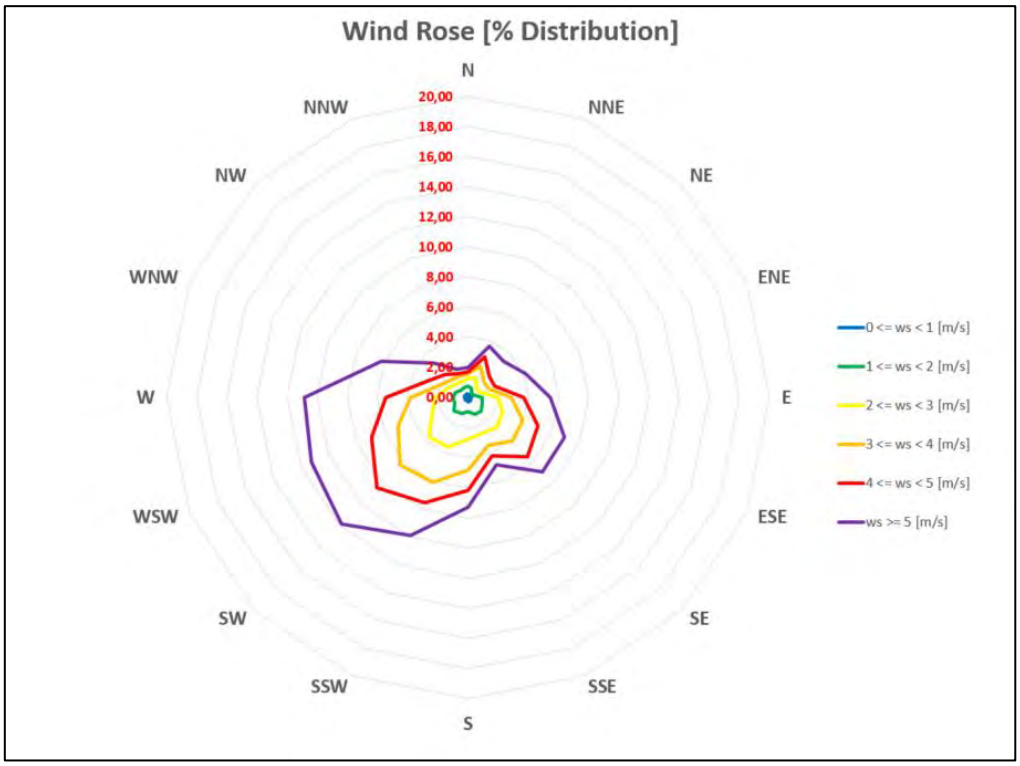

Fig. 75.: Design Reference Year (DRY) climate data for Aalborg, showing wind direction and velocity (ws). Blue = ws<1 m/s, Green = 1<ws<2 m/s, Yellow = 2<ws<3 m/s, Orange = 3<ws<4 m/s, Red = 4<ws<5 m/s, Purple = ws>5 m/s.

The resulting relative humidity for the four sensor locations simulated in Delphin for the two masonry assemblies are shown in figure 76. From the figure it can be seen that the hydrophobization on the exterior surface had a clear effect on the two simulated masonry assemblies, as the relative humidity of the hydrophobized assembly was shown to always be lower than the un-hydrophobized wall, at all four sensor locations. For the un-hydrophobized wall, the relative humidity at sensor locations 1 until 3, were in the range of 90-100% with low peaks at sensor location 1 down just below 80%. While the hydrophobized wall at the same sensor locations reached just under 90% during the winter period, and down to around 50-65% during the summer. These simulation results for sensor locations 1-3 indicate that the hydrophobized wall maintain a low relative humidity levels during the summer period, by limiting moisture from entering the structure from the warm, moist exterior climate, but that the hydrophobized wall has a negative effect during the winter. As the moisture inside the wall is limited from evaporating to the cold, dry exterior climate, thus resulting in the high relative humidity levels during the winter period. These results collaborate with the experimental results found by Jensen et al. (Jensen, Bjarløv, Rode, & Odgaard, 2018). At sensor location 4, at the interior surface, the hydrophobized wall also showed lower relative humidity, with only short peak periods above 70%. While the relative humidity of the un-hydrophobized wall generally lied in the range of 70-80%.

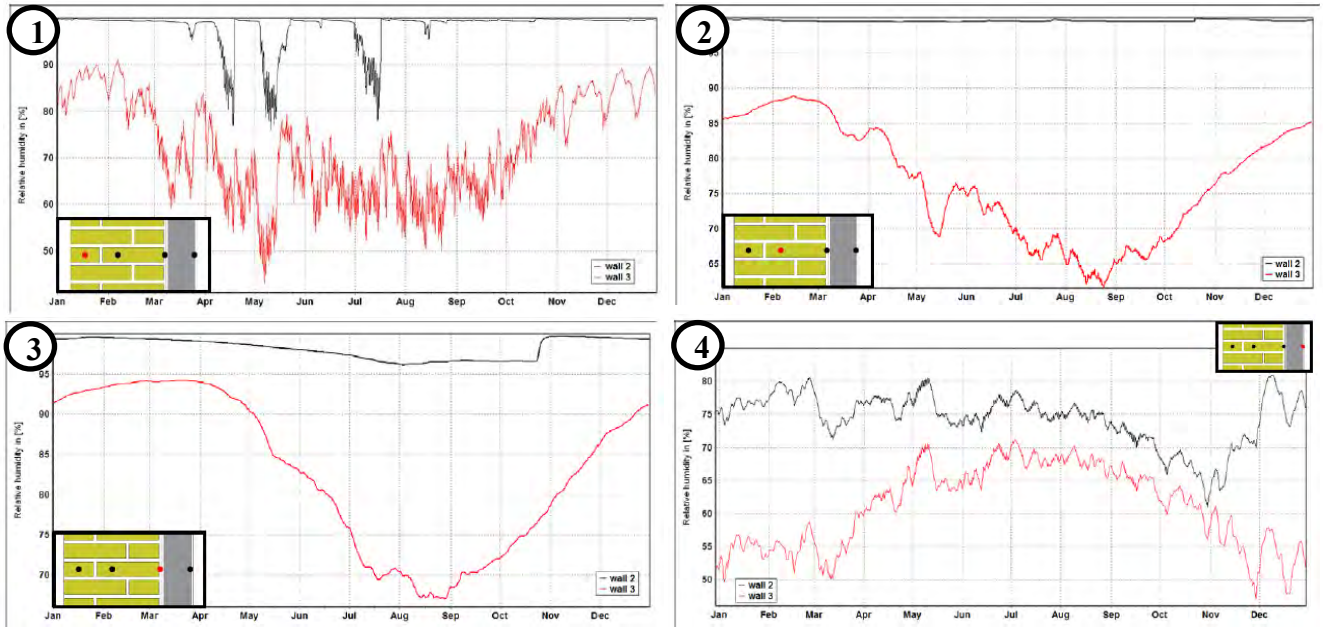

Fig. 76.: Simulation results for Kgs. Lyngby, relative humidity for the hydrophobized wall (Red) and the un-hydrophobized wall (Black). 1) Sensor location 1, near the exterior surface. 2) Sensor location 2, middle of the masonry wall. 3) Sensor location 3, at the interface between the masonry wall and the insulation board. 4) Sensor location 4, behind the interior surface material.

It should be noted when reading the following graphs, that the y-axis is different between the hydrophobized and the un- hydrophobized wall. A comparison between the hydrophobized wall and un-hydrophobized wall at the three locations, showed a generally positive effect from the hydrophobization. Looking at the hydrophobized wall showed relatively similar trends for all three sensor locations, with generally lower relative humidity for the location of Copenhagen (picture 2 of figure 77 and 78). The exception to this being sensor 4, behind the interior surface material, where all three locations were shown to have almost identical relative humidity. The relative humidity for the sensors in the un-hydrophobized wall were on the other hand much more chaotic, for the interior

surface. At the locations Copenhagen and Esbjerg a similar trend was generally seen at all three sensor locations, while the location of Aalborg showed a different trend at all three sensor locations (picture 1 of figure 77 and 78). While only small differences were seen for the relative humidity near the exterior surface, for the location of Aalborg compared to the two other locations (about 0.5% in the middle of the masonry wall). The differences between Aalborg and the two other locations became much larger at the interior surface, where differences of up to 40% were seen during the winter period. As for the differences at the interface between masonry and the insulation, the relative humidity for Aalborg was generally 2-6% lower than Copenhagen and Esbjerg. Otiv concluded on this part that Copenhagen had a higher risk compared to the two other locations, when the masonry assembly was not treated with hydrophobization. While Esbjerg had the highest risk when the wall was treated with hydrophobization, as the wind velocity at the location of Esbjerg were higher than both Copenhagen and Aalborg. Thus making wind-driven rain a bigger issue for building in Esbjerg. However the high wind velocity at the location of Esbjerg was also thought to assist the wall to dry out during the winter period.

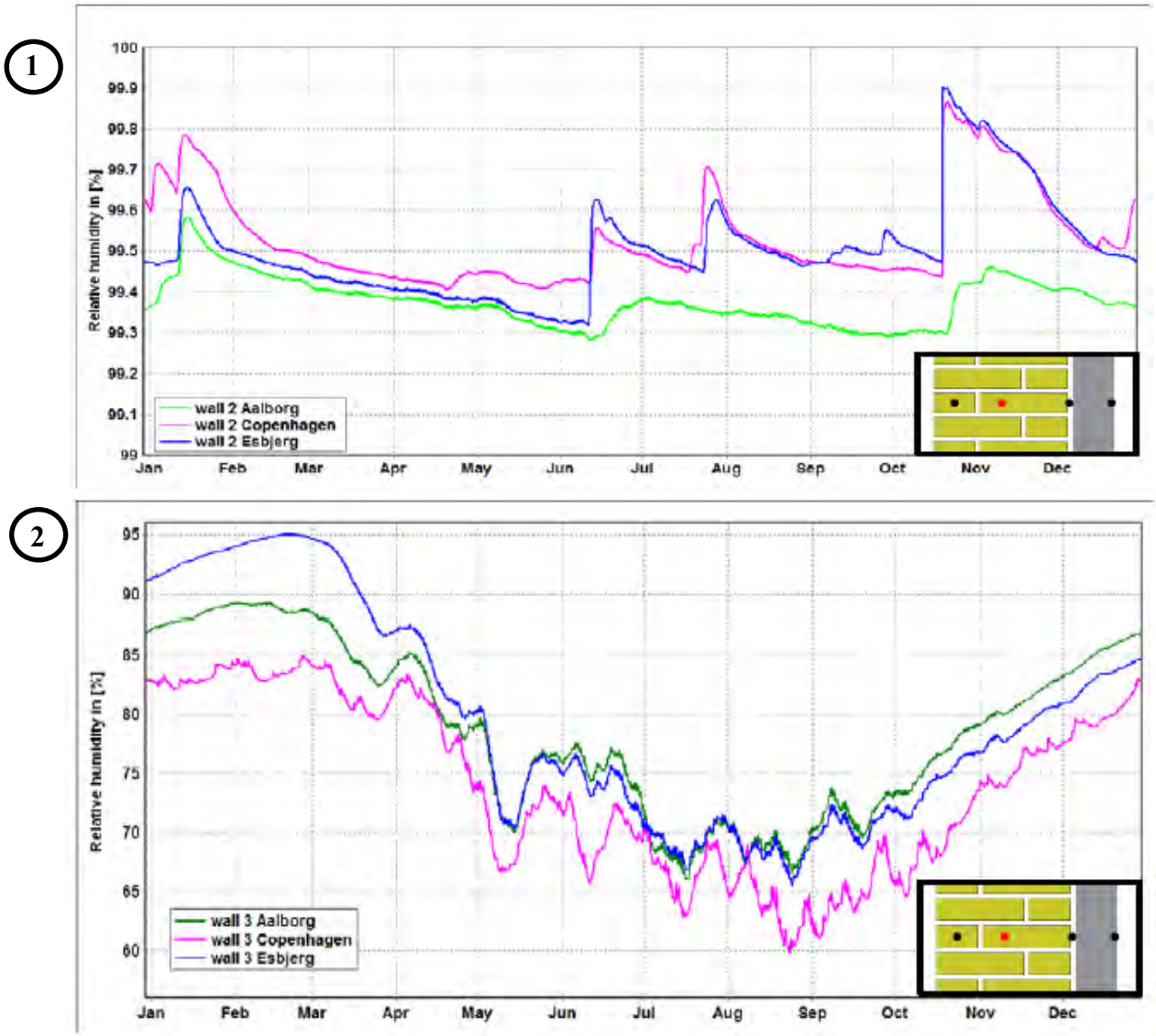

Fig. 77.: Comparison between simulation results for Copenhagen (Pink), Aalborg (Green) and Esbjerg (Blue), relative humidity at sensor location 2, in the middle of the masonry wall. 1) The un-hydrophobized wall. 2) The hydrophobized wall.

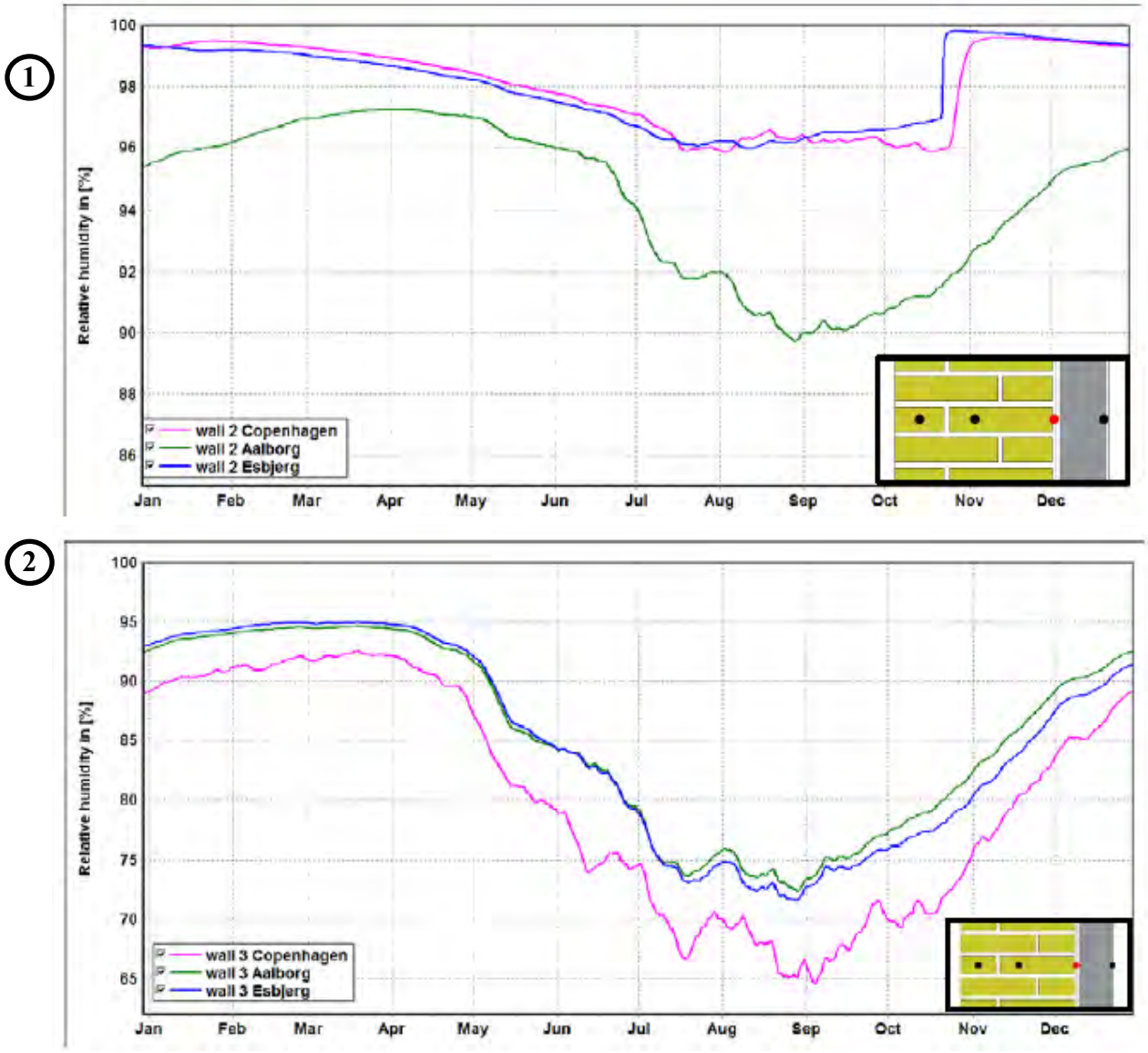

Fig. 78.: Comparison between simulation results for Copenhagen (Pink), Aalborg (Green) and Esbjerg (Blue), relative humidity at sensor location 3, at the interface between the masonry wall and the insulation board. 1) The un-hydrophobized wall. 2) The hydrophobized wall.

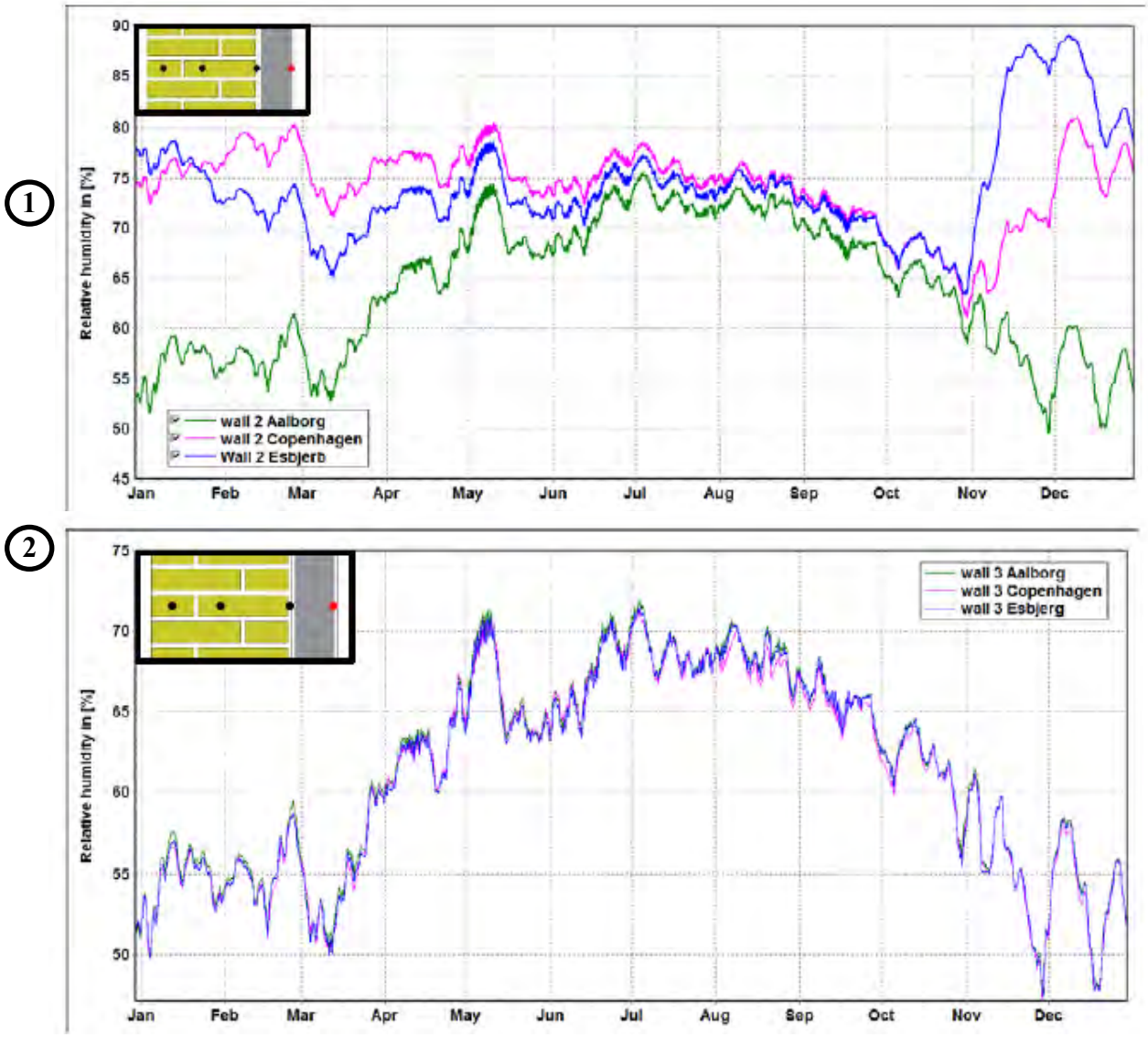

Fig. 79.: Comparison between simulation results for Copenhagen (Pink), Aalborg (Green) and Esbjerg (Blue), relative humidity at sensor location 4, behind the interior surface material. 1) The un-hydrophobized wall. 2) The hydrophobized wall.

The ice volume to pore volume model used for the evaluation of the moisture conditions in the masonry assemblies predicted no risk of frost damages at any of the locations. As none of the two assemblies at any of the locations crossed the critical the ice/pore volume ratio of 30%, set as critical limit. Copenhagen reached 23%, Aalborg 15%, and Esbjerg 8%.

For the wood decay model, Otiv's results showed a large and steady mass loss for both sensor locations 2 and 3 at all three locations of which Copenhagen was predicted to have the highest mass loss, and Aalborg the lowest (picture 1, 3, and 5 of figure 80). Furthermore, the mass loss was predicted to be highest at sensor location 2 (closer to the exterior surface) in comparison to sensor location 3. In addition, Otiv's wood decay results also displayed the positive effect of the hydrophobization on the exterior surface, as the mass loss at both sensor locations for all three locations were greatly reduces (picture 2, 4, and 6 of figure 80). After the hydrophobization the mass loss at sensor location 2 was predicted to be at 0% for both Copenhagen and Aalborg after three years, while at 0.5% for Esbjerg.

While at sensor location 3, the mass loss was predicted to be reduced to around 2-4%, however a 2% mass loss each year do seem to occur for all three locations.

The mould model predicted no mould growth on the interior surface (sensor location 4) for neither the un-hydrophobized- or the hydrophobized assembly for the locations Copenhagen and Aalborg, while in Esbjerg, the un-hydrophobized assembly reached an acceptable mould index of less than 0.5 (picture 1, 2, and 3 of figure 81). Different results were seen for the interface between the masonry wall and the insulation boards (sensor location 3), where the un-hydrophobized assembly reached mould index values between 3 and 3.5 after approximately one year for Copenhagen and Esbjerg, and one and a half year for Aalborg. Corresponding to mould growth beyond the microscopic level at the interface between the masonry wall and the insulation boards. For the hydrophobized assembly the mould model predicted the peak mould index values between 2 and 2.25 for the three locations, with Aalborg slightly higher than the two other locations.

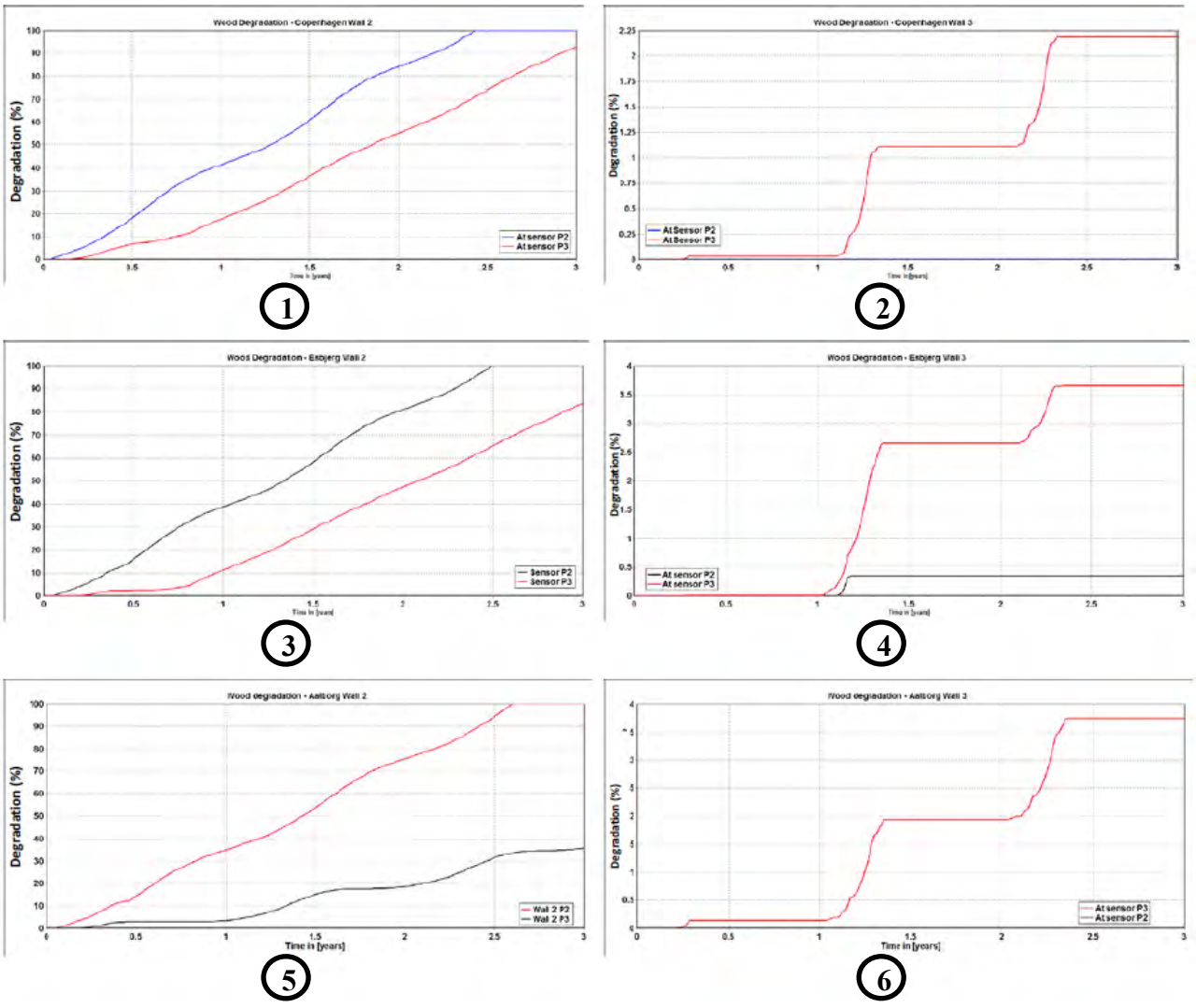

Fig. 80.: Wood decay at sensor locations 2 and 3. 1) Copenhagen, for the un-hydrophobized wall (Blue = sensor 2, Red = sensor 3). 2) Copenhagen, for the hydrophobized wall (Blue = sensor 2, Red = sensor 3). 3) Esbjerg, for the un-hydrophobized wall (Black = sensor 2, Red = sensor 3). 4) Esbjerg, for the hydrophobized wall (Black = sensor 2, Red = sensor 3). 5) Aalborg, for the un-hydrophobized wall (Black = sensor 3, Red = sensor 2). 6) Aalborg, for the hydrophobized wall (Black = sensor 2, Red = sensor 3).

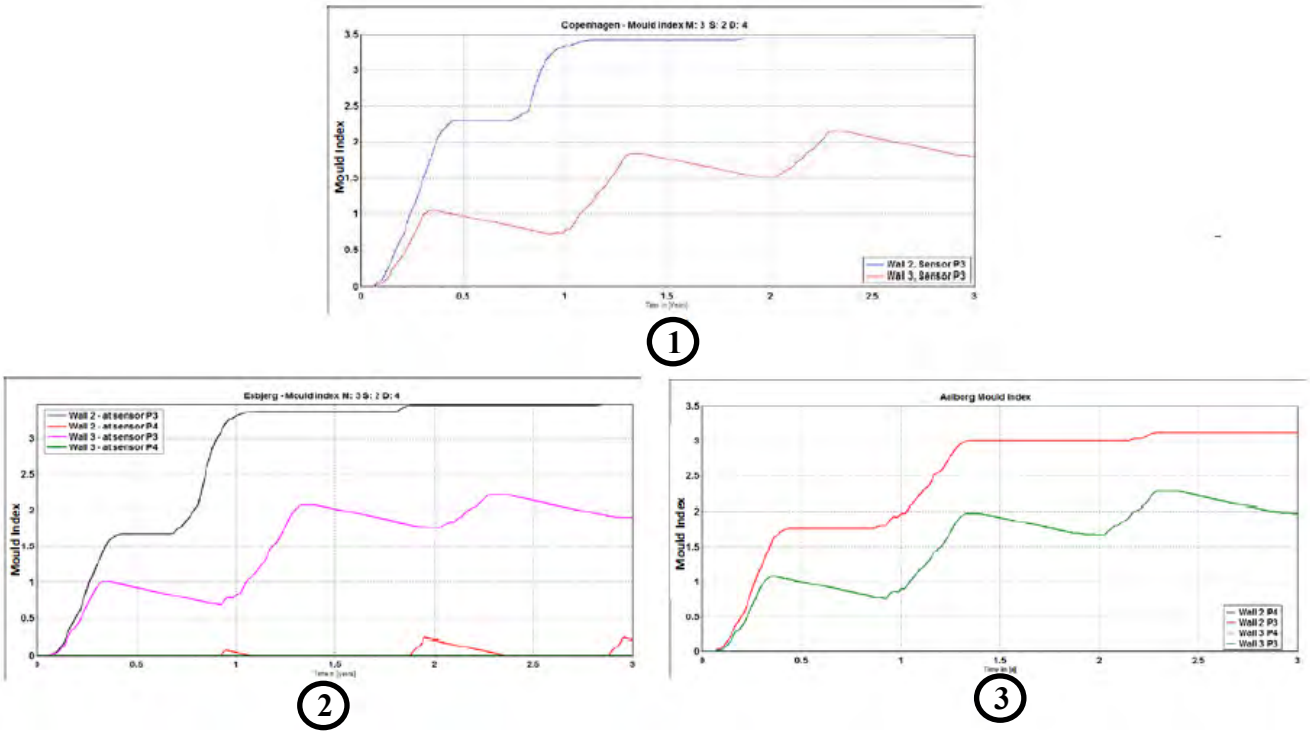

Fig. 81.: Mould index. 1) Copenhagen (Blue = wall 2 sensor 3, Red = wall 3 sensor 3). 2) Esbjerg (Black = wall 2 sensor 3, Red = wall 2 sensor 4, Pink = wall 3 sensor 3, Green = wall 3 sensor 4). 3) Aalborg (Black = wall 2 sensor 4, Red = wall 2 sensor 3, Light-blue = wall 3 sensor 4, Green = wall 3 sensor 3).

From these results Otiv concluded that the insulation system alone without the hydrophobization, would fail to maintain a low relative humidity throughout the simulated period for sensor locations 2 and 3 within the masonry wall. Allowing for favourable conditions for both mould growth as well as wood decay. Although the insulated system with the hydrophobization showed positive results by greatly reducing the relative humidity at these two sensor locations, and thus avoiding wood decay from occurring at sensor location 2 and greatly reducing it at sensor location 3. It was concluded that the hydrophobization would not be able to reduce the relative humidity to a level where mould growth at sensor location 3 would be avoided. With regards to the risk of frost damage, Otiv concluded that neither of the two assemblies showed any risk of frost damages at any of the three locations, as the ice volume to pore volume did not exceed the critical limit.

5.7.2 Effect of controlling the indoor humidity

Present simulation study was carried out in connection with the field study in (Jensen, Bjarløv, Rode, & Odgaard, 2018); as the results from the field study indicated a need to control the indoor humidity already before application of the mineral insulation board. This part of the study investigated the effect of reducing the indoor relative humidity on the hygrothermal performance of an internally insulated solid masonry wall with and without exterior hydrophobization. As discussed earlier in the present report, the indoor relative humidity of 60% is a fitting level according to (Brand, et al., 2013) for summer conditions. For winter conditions however, levels between 30 and 50% are suggested.

The validated Delphin models for Xella walls X2 and X3 (in this study denoted as Wall 2 and Wall 3) by Otiv (Otiv, 2016) were used as a basis and further modified for the purpose of this study. As it was the case for Otivs study, the models were simulated for a period of four years. A two-year initial period using Copenhagen Design Reference Year (DRY) climate data followed by two years of measured outdoor climate data. For each of the two validated models (with and without exterior hydrophobization) two indoor climate scenarios were simulated; 1) using measured indoor climate data from the container experiment, with a set point of 60% relative humidity, and 2) relative humidity fixed to 40% throughout the year. Fixing the indoor relative humidity to 40% throughout the year was based on the normal relative humidity range during winter in Danish residential buildings of 30 to 50% as according to (Brand, et al., 2013).

The VTT model (Hukka & Viitanen, 1999) (Viitanen, et al., 2010) (Viitanen, Krus, Ojanen, Eitner, & Zirkelback, 2015) was used to assess the theoretical prediction of the risk of mould growth at the interface between the existing masonry wall and the internal insulation for the different scenarios. Note that the first year of the data set (the stabilization period) was not used for the assessment using the VTT model, as for the field study.

In addition, the risk of frost damage near the exterior surface was evaluated using the Delphin output type “moisture saturation degree” (the total mouste volume with respect to the total pore volume), and Delphins “Ice volume to pore volume ratio” model (Sontag & Nicolai, 2013). The International Association for Science and Technology of Building Maintenance and Monuments Preservation (WTA Wissenschaftlich- Technische Arbeitsgemeinschaft für Bauwerkserhaltung und Denkmalpflege e.V., 2014) recommend for non-frost resistant material not to exceed a moisture saturation degree of 30% during periods with risk of frost. This threshold was used in this study for evaluating both the moisture saturation degree as well as the Ice volume to pore volume ratio.

At the interface between the existing wall and the internal insulation (Fig. 81), the un-hydrophobized Wall 2 showed little to no difference during the winter periods as an effect of reducing the indoor relative humidity from 60 to 40%. In both scenarios, the wall experienced relative humidity levels near 100% for a period. The reduction of the indoor relative humidity did however shorten the period with 100%, and greatly reduces the levels at interface during summer. For the hydrophobized Wall 3, a lowering of the indoor relative humidity is seen to decrease the levels at the interface throughout the simulated period. The largest reduction occur during summer with around 20% compared to the scenario with 60% indoor relative humidity, while a small reduction occur during winter with around 10%. With regards to the theoretical prediction for the risk of mould growth; the un-hydrophobized Wall 2 with 60% indoor relative humidity showed the highest predicted growth of the four scenarios, with $M = 1.5$ occurring at the end of the period 2016.05.01 - 2017.05.01. While Wall 2 with 60% indoor relative humidity and both Wall 3 scenarios maintained a $M < 0.5$ during the same period. It should be noted that similar to the predicted risk of mould growth in the field study, the un-hydrophobized Wall 2 with 60% indoor relative humidity generally show an increasing tendency, while

the other cases experience a small increase in winter followed by a decrease in summer maintaining an acceptable risk level.

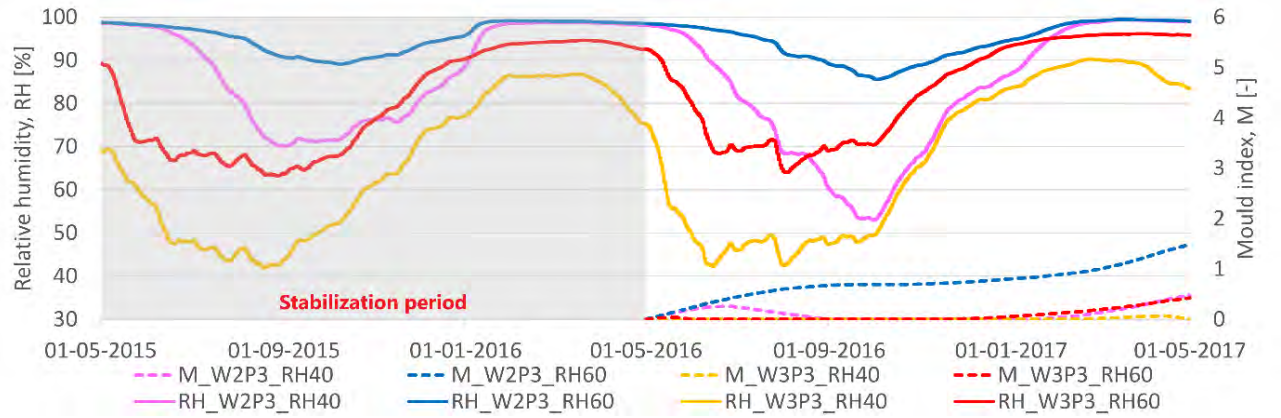

Fig. 82.: Simulated relative humidity, RH and Mould Index, M at the interface: Point 3.

The simulations shows little to no changes near the exterior surface in relation to the risk of frost damage, as a result of reducing the indoor relative humidity. The results for moisture saturation degree and ice volume to pore volume ratio were almost identical between the 60 and 40% wall scenarios. Instead, the risk of frost damage for the un-hydrophobized wall and the hydrophobized wall with 60% relative humidity is presented, as the field study did not address this issues for the test walls in the experimental field study. Fig. 82 show the moisture saturation degree near the exterior surface (point 1), where it is seem that both walls generally stay below the 30% threshold recommended by WTA, with the except of a single occasion within the first half year of the simulation. Similar is seen for the ice volume to pore volume ratio (Fig. 83), where both walls also stay below the 30% threshold through the simulated period. These results suggests that frost damage are likely not to occur in the test walls at the DTU test site. Furthermore, these results correlate with visual inspections of the test walls, which did not show any signs of frost induced damage.

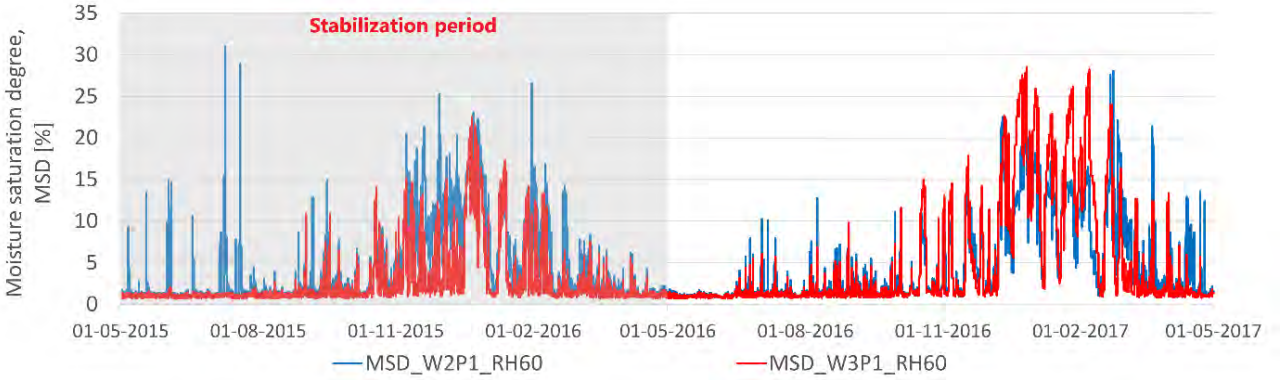

Fig. 83.: Simulated moisture saturation degree at the exterior surface: Point 1.

Comparing the moisture saturation degree for the two walls show several large peaks during the summer of 2015 for the un-hydrophobized Wall 2. This is however not seen for the hydrophobized Wall 3, which may suggest a reduction of the rain intrusion by the hydrophobization do occur. Similar tendencies, however less prominent, occur during winter 2015-16 where the two walls show rather similar moisture saturation degree with the exceptions of several peaks for Wall 2; and again during the summer of 2016. However, during the last winter period 2016-17 a different situation is seen, where Wall 3 show several peaks in moisture saturation degree, which do not occur for Wall 2. Furthermore, this winter period is emphasized in Fig. 83 with the ice volume to pore volume ratio, showing several

occasions where the ratios in Wall 3 are seen to be around twice that seen in Wall 2. This issue is theorized to be related to the issue of the hydrophobization limiting the liquid transport through the outermost part of the masonry wall, resulting in an increased moisture levels during the cold periods as described in section 5.6.6.

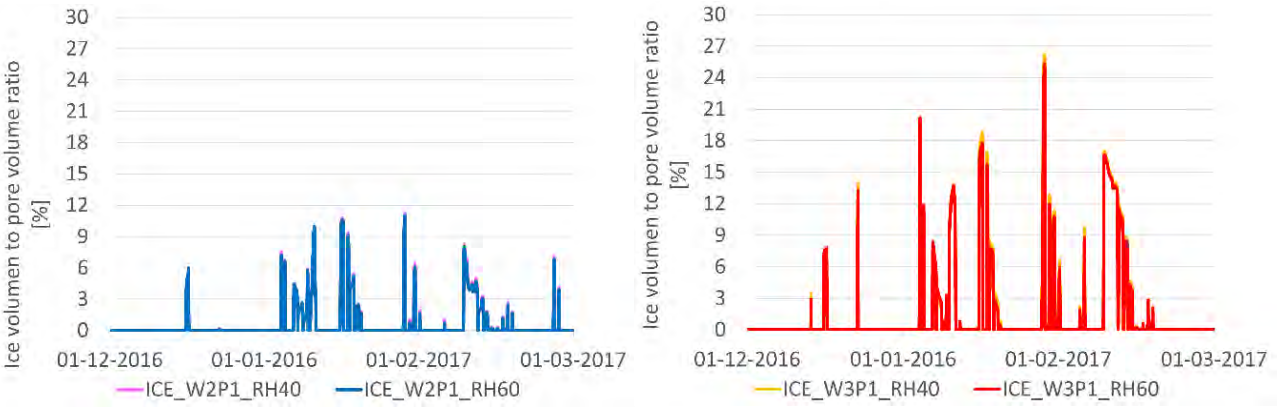

Fig. 84.: Simulated ice volume to pore volume ratio at the exterior surface: Point 1. Left) Un-hydrophobized wall, and Right) Hydrophobized wall.

Simulation results near the interior surface of the wall scenarios are not graphically presented in this report, as the field study did not predict a risk of mould growth on the interior surface of the insulated test wall. A lowering of the indoor relative humidity in the simulation study was seen to reduce the levels near the interior surface (point 4) throughout the simulated period for both wall 2 and 3; thus lowering the risk of mould growth further.

5.8 Indications

Based on the current experimental results and simulations the following indications have been noticed when interior insulation has been applied to solid masonry walls:

- Hydrophobization of the exterior surface reduces the moisture content in the masonry during summer time, but moisture increases during the winter time. This indication is based on the use of an indoor relative humidity of 60%. It could therefore be questioned, if the hydrophobization treatment used in the experiment was too tight, and if the use of a less tight treatment would allow the moisture inside the construction to evaporating to the exterior, resulting in lower relative humidity levels during the cold periods.
- Deliberate thermal bridge installed in front of the embedded wooden elements reduce the moisture content in the wooden elements.
- The combination of hydrophobization of the exterior surface and lower indoor moisture content (e.g. similar to the climate class 2 according to EN ISO 13788, an interior moisture addition of 2-4 g/m^3), more representative for the indoor conditions for Danish historic buildings during winter; could be a solution to lower the risk of mould growth and wood decay to an acceptable level at the critical interface between the masonry and the insulation system.
- The simulation results indicate no risk of frost damage for the test walls at the DTU test site.

6 Test Stand at KUL

6.1 Introduction

At the Building Physics Section of KU Leuven a hot box- cold box experiment has been set-up to investigate the applicability of interior insulation for cases with wooden beam ends embedded in the wall. This is still an active topic of debate, as interior insulation may imply an enlarged risk on wood decay due to two phenomena. Firstly, the moisture content in the masonry wall due to outdoor moisture sources (e.g. wind-driven rain) might be higher as interior insulation reduces the drying potential. Secondly, if warm moist indoor air is able to reach the beam end embedded in the colder masonry wall, condensation can occur.

This study focuses on the latter: the increased risk due to convective moisture transport. To this end, a hot box-cold box experiment simulating steady-state winter conditions is performed. Two vapour transfer reducing systems (EPS and mineral wool with a smart vapour retarder) and one vapour open capillary active (calcium silicate) system are studied, together with a non-insulated reference wall. For each insulation system, two configurations are analysed: one with and one without an airtight sealing between beam and insulation. In a second step, an overpressure is applied to analyse the potential influence of forced exfiltration. The results described below are partly obtained within the IWT-VIS-project 'Renofase', funded by the Flemish Government. They are included here because of their relevance for the RIBuild-project. Furthermore, within RIBuild the same test configuration has been used to set up a second test run, which further investigated the current findings. This second test run focussed on the impact of an air pressure difference across the wall on the moisture risks by convective moisture transport, and will further investigated the most reliable way to achieve an airtight sealing of the wooden beam-ends.

6.2 Test Stand Description

The experiment is performed in a vertical calibrated hot and cold box, constructed to investigate the hygrothermal performances of highly insulated building components. The test setup consists of three major parts; a test frame to install the studied building component enclosed between two climate chambers to simulate indoor and outdoor conditions. To reduce the heat losses through the calibrated hot box to a very minimum, this chamber was insulated with 60 cm polyurethane ($R = 30 Km^2/W$). The hot box has a cubic inner volume with sides of 2.4m and is completely separated from the laboratory conditions without any thermal bridge. The test frame, constructed in the same way, has a measuring area of 2.4m by 2.4m and a depth of 0.6 m. The cold box, on the other hand, was insulated with only 0.1m polyurethane boards. The clamping system, connecting the three parts, consisted of a screw system with 7 bars distributed over the total height of each side of the test setup. In combination with compressible closed cell polyurethane foam with a thickness of 2 cm, this clamping system provides an airtight and insulated connection between the different parts.

A controlled IR-bulb in the middle of the warm chamber creates the desired temperature conditions. Fig. 86.: shows how the IR-bulb is covered with a reflective foil to avoid direct long wave radiation towards the test component. The cold chamber was provided with a liquid-to-air heat exchanger accompanied with a fan system to control and distribute the temperature. The fan system, which can simulate wind effects, allows a steady state air flow along the test wall with velocities between 0.5 - 10 m/s. The humidity in both the warm and cold chamber was conditioned with free evaporation of salt solutions. To create a total air pressure difference across the test section, a small ventilator is installed at

the back of the warm chamber. A detailed description of the vertical hot box – cold box test set-up can be found in Langmans [2013].

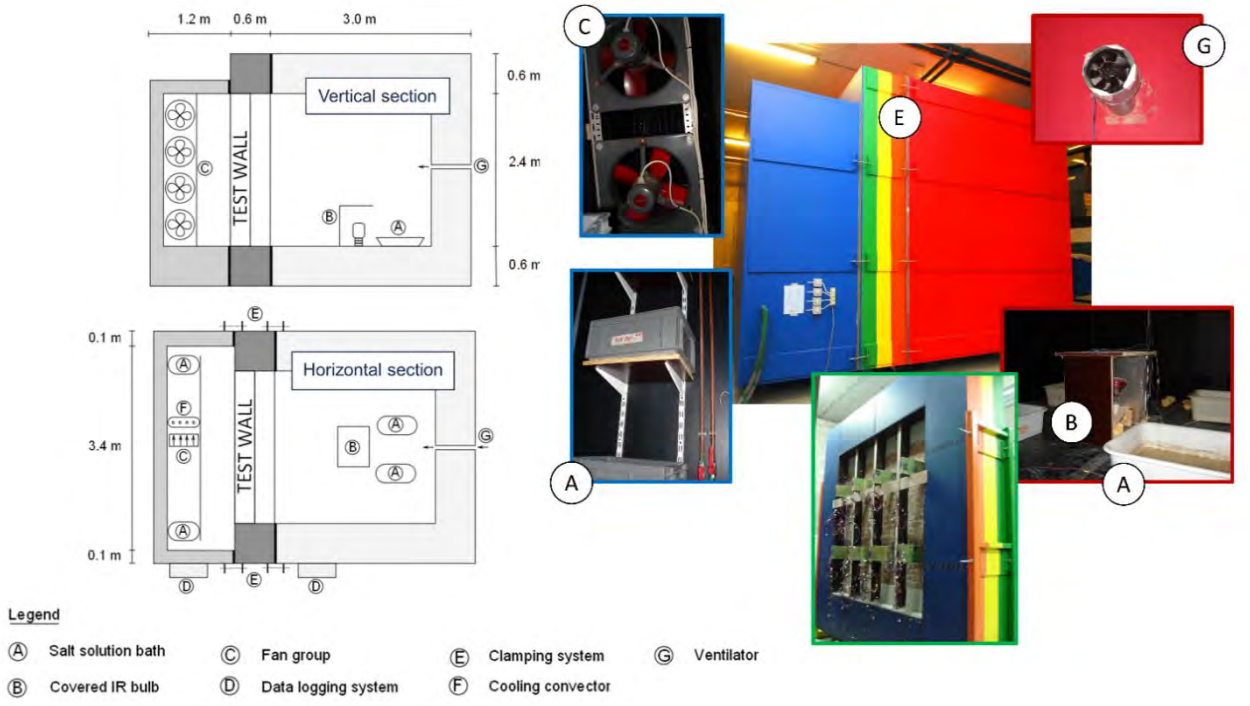

Fig. 85.: Vertical hot box – cold box test set-up used at the Building Physics Section of KU Leuven to investigate the increased risk on decay of wooden beam ends due to convective moisture transport.

6.3 Wall configurations

Four single leaf masonry assemblies of 29.5 cm thick, 55 cm wide and 240 cm high were installed in the test frame and provided with the following insulation systems:

- Wall 'CaSi': 5-10 mm glue mortar + 10 cm calcium silicate + 5-10 mm finishing plaster
- Wall 'MW + SVR': 11.5 cm mineral wool + smart vapour retarder Vario KM Duplex® + 1.25 cm gypsum board
- Wall 'EPS': 5-10 mm glue mortar + 8 cm expanded polystyrene (Doublissimo) + 1.25 cm gypsum board
- Reference wall: no interior insulation system

Both the calcium silicate and the EPS insulation were fully adhered to the masonry (see left picture of Fig. 86.:). The metal studs in the mineral wool system were positioned 4 cm in front of the masonry wall (right picture of Fig. 86.:). Two separate layers of mineral wool were applied; one layer of 7.5 cm between the metal studs and another layer of 4 cm between masonry and metal studs. In this way, the thermal bridge effect induced by the metal stud was reduced.

In each test wall, two beam-ends were embedded in the masonry wall, as shown in Fig. 87.: These beams were embedded at a distance of 15 cm of the exterior surface. Between the wooden beams and the wall, an air gap of approximately 1-1.5 cm was provided. Exception to this forms the connection between both the bottom and the top of the wooden beam and the masonry, where no air gap was foreseen (see Fig. 88.:) though also here after some time small air paths could occur due to shrinkage and dilatation of the construction. For each insulated test wall, the lower wooden beam was provided

with an airtight sealing between beam and insulation while no attention was paid to the airtightness of the connection between the wall and the upper wooden beam. The airtight connections for the lower wooden beams were obtained by a flexible PUR foam in case of the wall with calcium silicate and the wall with EPS. For the wall with the mineral wool, an airtight tape was used to connect the smart vapour retarder with the wooden beam. Additionally, the small gap between gypsum board and wooden beam was filled with a flexible PUR foam. The wooden beam-ends in the reference wall were left unsealed in the first measuring campaign. To check the airtight sealing infrared images have been taken (see Fig. 89.:). In a second measuring campaign, the wooden beam-ends at the top row of the insulated walls have been sealed with an airtight tape (see Fig. 90.:).

Fig. 86.: Left: calcium silicate boards fully adhered to the wall. Right: The metal studs in the mineral wool system were positioned 4 cm in front of the masonry wall to avoid thermal bridges.

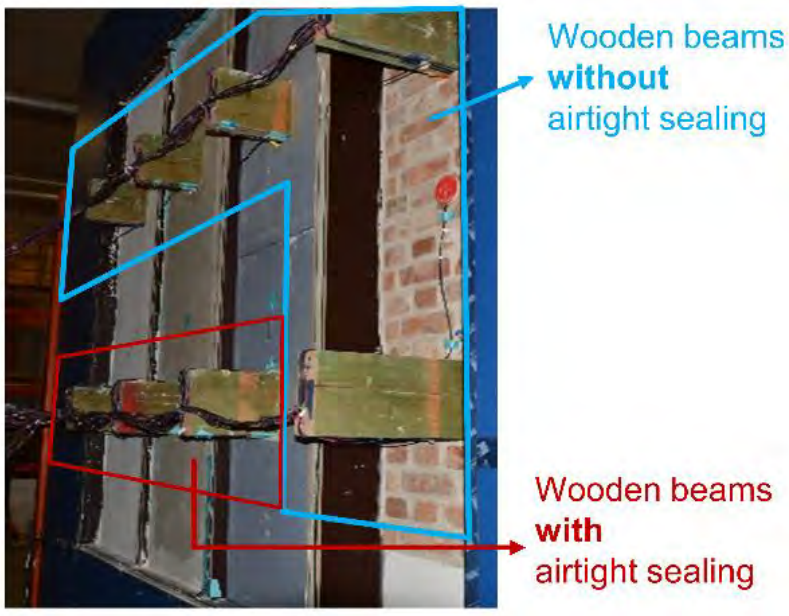

Fig. 87.: Each test walls contains two wooden beam-ends, some airtight sealed, some without airtight sealing.

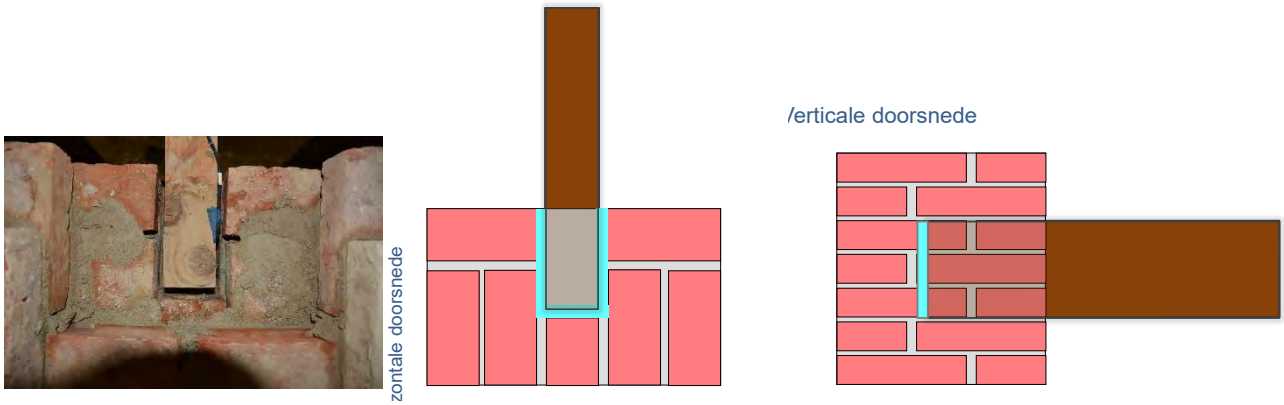

Fig. 88.: Left: top view of the wooden beam end embedded in the masonry. Right: schematic indication of the air gap (light blue) around the wooden beam end (left drawing: top view, right drawing side view).

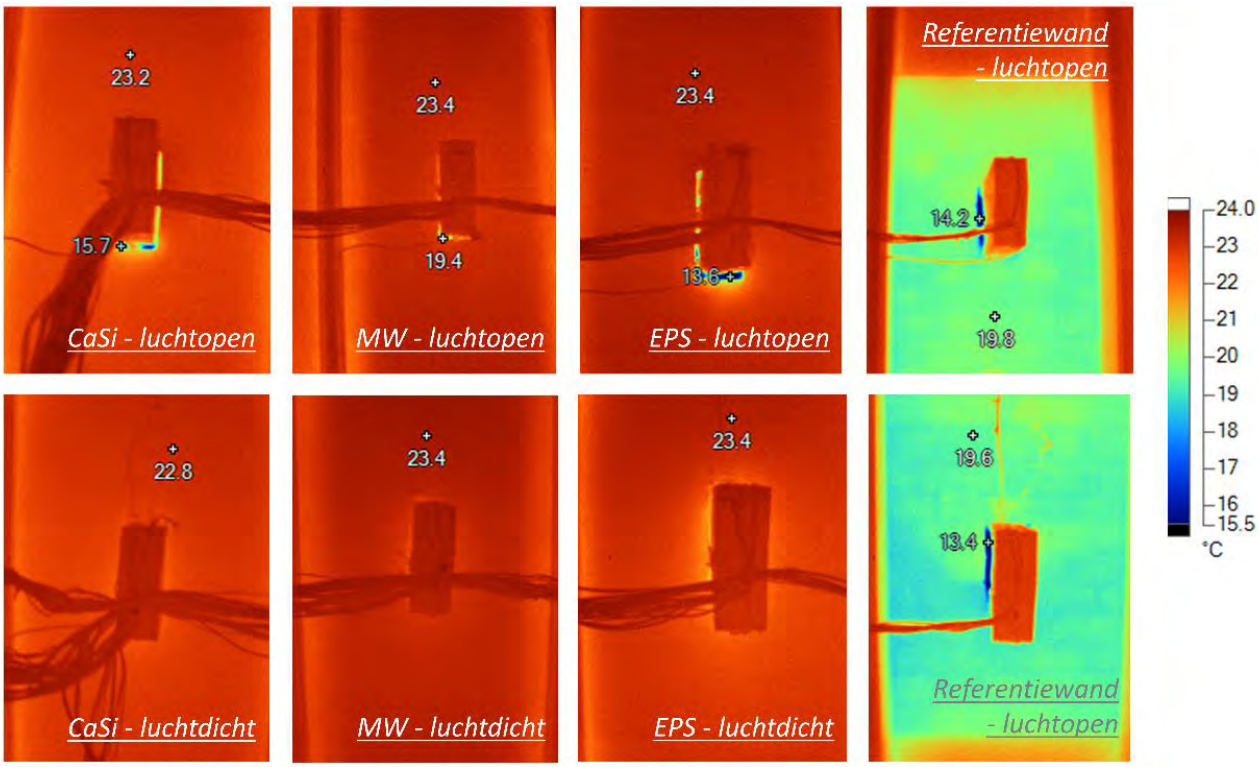

Fig. 89.: IR-images to check the airtightness of the connections. The top row contains the air open connections (from left to right: calcium silicate, mineral wool and EPS-insulated walls and utmost right the reference wall without insulation). The air leakages are clearly visible, though to a less extent for the wall with mineral wool insulation.

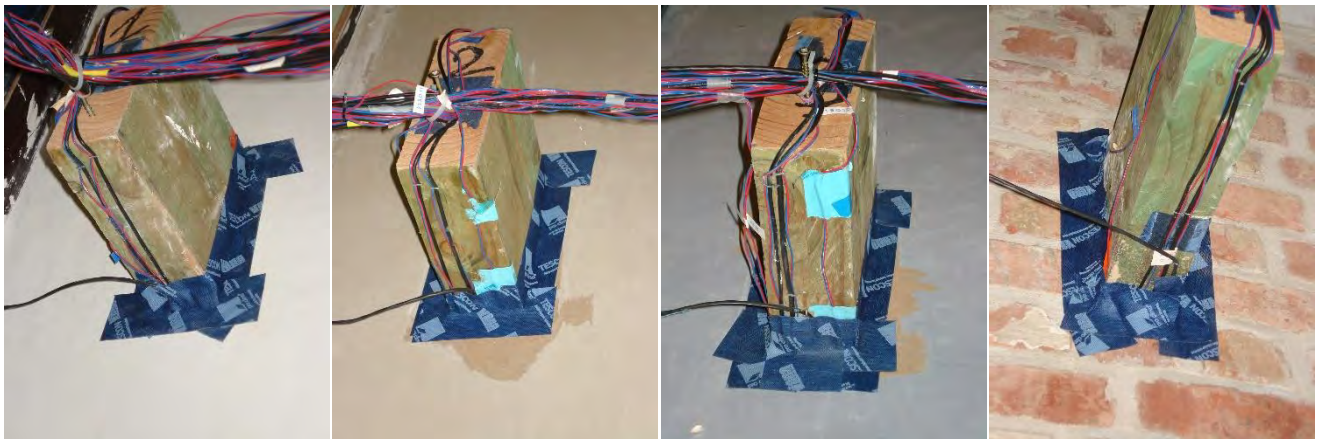

Fig. 90.: Air tight sealing with tape of the top row wooden beam ends in the second measuring campaign.

6.4 Measurement techniques

The temperature and relative humidity in both chambers (hot box and cold box) and within the test walls have been measured by use of Thermo Electric thermocouples and Honeywell RH-sensors. After in-house calibration, they achieve an accuracy of +/- 0.2 °C and +/- 2 % respectively. The positioning of the sensors within the test walls is illustrated in Fig. 91.: The sensors at the wooden beams were fixed to one side of the beams. A set of two moisture pins was positioned at each beam end. As non-insulated moisture pins were used, these pins measured the highest moisture content across the depth of the moisture pins [Dietsch et al. 2015], which is assumed to occur at the surface of the beam end. The moisture pins were calibrated for the type of wood applied in the test setup. At half height of the test walls, in addition to the relative humidity sensors and thermocouples at the interfaces, a heat flux sensor was glued to the warm side of the masonry.

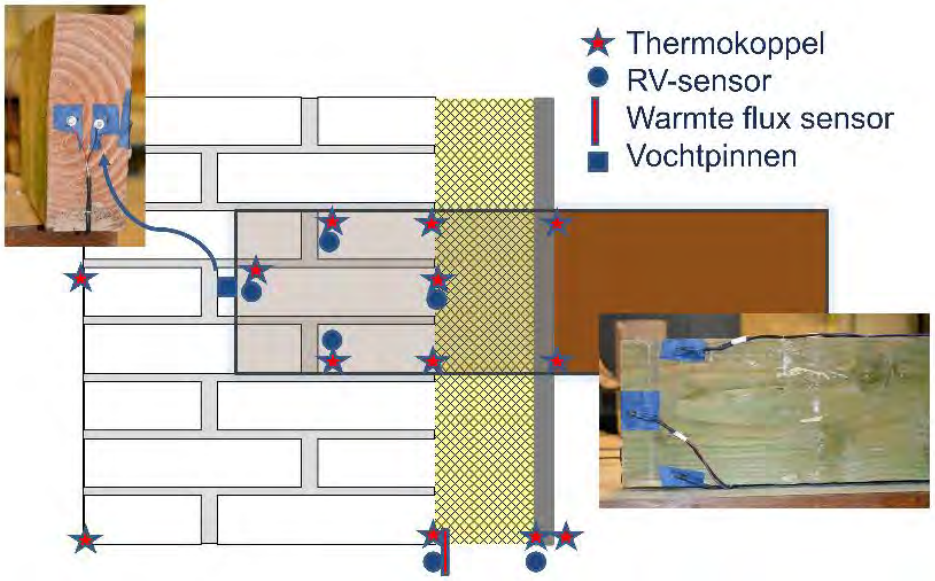

Fig. 91.: Positioning of the thermocouples, RH-sensors, heat flux sensors and moisture pins.

6.5 Initial and boundary conditions

The initial relative humidity (RH) in the masonry walls varied among the different test walls. For the non-insulated wall and the wall with calcium silicate, the RH-sensors in the masonry indicated initial RH's between 60% and 73%. For the initial relative humidity in the walls with the vapour tight systems, values between 65% and 85% were measured due to the lower drying potential during the construction phase. Similarly, the initial relative humidity around the wooden beams with an airtight sealing was higher than for those without a sealing. The initial temperature of the test walls was 20°C.

During the experiment, the temperature and relative humidity in the hot box were approximately 20°C and 54%. In the cold box, a temperature equal to approximately 3°C and a relative humidity equal to approximately 86% were applied. In the experiment, additionally the impact of an air pressure difference across the walls was studied. Thereto, during the first 21 days of the measurement period, no extra air pressure difference across the walls was applied. In a second step the hot box was pressurised by use of the fan at the back of the hot box. The air pressure difference across the walls was measured by air tubes in the two boxes and a DG-500 Pressure Gauge. Two levels of air pressure difference were imposed by adjusting the fan rotation speed. This resulted in three consecutive stages characterised by the level of air pressure difference across the test walls. From day 0 till day 21 no overpressure was imposed resulting in an air pressure difference of -0.7 to 0.5 Pa. In the next step (day 22 till day 28) an overpressure of 1.6 to 2.5 was imposed. Finally, from day 29 till day 34 an overpressure of 6.2 to 7.5 Pa was imposed. The slightly higher air pressure differences correspond to the second test series and might be attributed to a higher level of airtightness for the junctions with the upper wooden beams. . Note that none of the test series included wind-driven rain, making a separate analysis of the convective moisture transport possible.

6.6 Analysis of measurement results

6.6.1 Thermal performance

For each test wall, the thermal performance was determined based on the heat flux q (W/m²) measured through the wall assembly at middle height and the temperatures θ (K) measured by the thermocouples at the same height at exterior and interior surface. At this position heat transfer is assumed to be one-dimensional, simplifying the determination of the thermal resistance R (m²K/W) to:

$$R = \frac{\theta_{se} - \theta_{si}}{\mathrm{q}}$$

Table 19 compares the calculated thermal resistances of the wall assemblies with the measured values. Overall a rather good agreement is observed between measured and design values. Note that the thermal conductivity of the reference wall is tuned to the measured values.

Tab. 19.: Measured versus calculated thermal resistances of the test walls.

	Calculated R-value (W/m²K)	Measured R-value (W/m²K)
Wall 'CaSi'	1.95	1.90
Wall 'MW + SVR'	3.74	3.65
Wall 'EPS'	2.95	3.06
Reference wall	0.39	0.46

6.6.2 Relative humidity

The relative humidity is a key influencing parameter for mould growth and wood decay. As an example, figure 92 shows the relative humidity near the back of the wooden beam (position indicated in figure 91). For both the wall insulated with calcium silicate and with EPS, as well as for the non-insulated reference wall, the highest relative humidity appears when no airtight sealing is provided (thick curve). When providing an airtight tape only (thin curve), the relative humidity is lower for those walls; though, it is still higher than the relative humidity measured when a proper airtight sealing in combination with a sealing by use of flexible PUR (thin dashed curve) is applied. This is especially true for the wall with CaSi. Thus, a proper airtight sealing in combination with an injection of the air gaps is found to be the best option to avoid convective moisture transport and thus to restrain the increase in relative humidity. Also for the wall with mineral wool and a smart vapour retarder, the case with the proper airtight sealing - obtained by a proper junction between the smart vapour retarder and the wooden beam, an injection of the gap between the gypsum board and the wooden beam by flexible PUR and a sealing by use of an airtight tape - shows the lowest relative humidity. However, for the mineral wool system the difference between the airtight sealing provided by an airtight tape only (thin curve) and the air open case (thick curve) is less pronounced. The case with an airtight tape only, shows even a slightly higher relative humidity. However, caution is advised when comparing these results as the initial relative humidity conditions of test series 2 (with the airtight tape only) were slightly higher. Additionally, the vapour pressure difference across the test walls was slightly higher during test series 2 (= test with tape only), which can also result in a slightly higher relative humidity near the wooden beam. Note also that only for the airtight junction with tape and PUR, the smart vapour retarder was connected to the wooden beam. For the other configurations, great care was taken to place the smart vapour retarder, but it was not sealed to the beam, which could have induced a small leakage for vapour diffusion as well.

Apart from the influence of an airtight sealing, the impact of the air pressure difference across the wall can be observed. For most cases, an overpressure induces a more steep increase in relative humidity. Exceptions to this are noticed for, for example, CaSi and EPS without an airtight sealing (especially when a higher overpressure is imposed – indicated as OP (B) in the figure) and for the reference wall. For these cases, the already high relative humidity and/or an increase in the temperature lies at the base of the observed decrease in relative humidity. The vapour pressure (not shown) shows an increase with increasing overpressure. Finally, it is important to note that, during the measurement period with no overpressure, the relative humidity measured for the air open junction in the wall with mineral wool is much lower than found for the air open junctions in the other insulated walls. Especially the less steep increase at the start of the measurement is clearly visible. This can be attributed to the better connection of the soft insulation material to the wooden beam. Also for the properly airtight cases, the wall with mineral wool performs better than the other walls, with inclusion of the non-insulated reference wall, and this while the wall with mineral wool (1) starts at a higher initial relative humidity and (2) has the largest thermal resistance and thus the lowest temperature in the masonry. When an overpressure is applied, the more steep increase in relative humidity is more pronounced for the wall with mineral wool; though it starts from a lower relative humidity. This more steep increase could be explained by the smaller impact of the overpressure on the temperature near the wooden beam embedded in the wall with mineral wool. In this way, the relative humidity in case of the wall with mineral wool can exceed the relative humidity measured for the other walls.

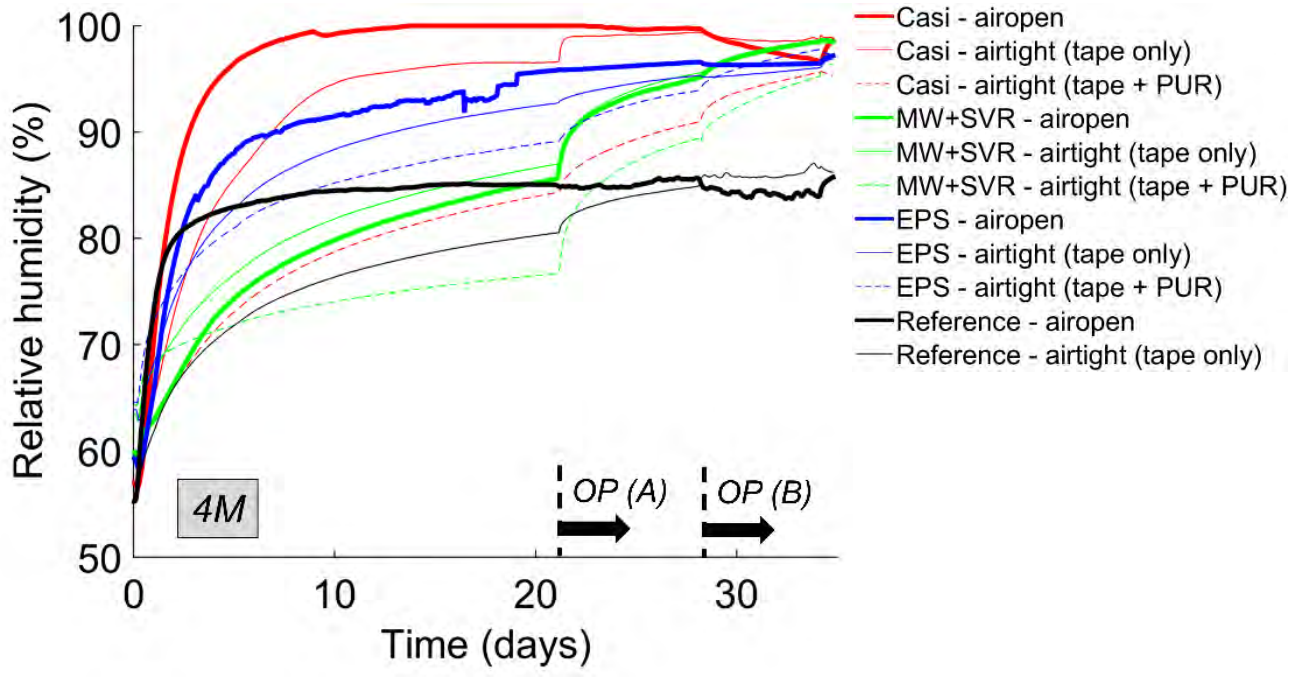

Fig. 92.: Relative humidity as a function of time at the back of the wooden beam ends. The arrows (OP(A) and OP(B) refer to the two steps of air overpressure.

6.6.3 Moisture content

Figure 83 shows for the two test series the moisture content measured at the back of the wooden beam end. A comparison between the air open and airtight configurations studied in test series 1 (left figure) shows the higher increase in moisture content when no airtight sealing is provided. The largest moisture content is obtained for the wall with EPS and the wall with CaSi. As with the relative humidity, the lowest moisture content is obtained for the airtight junction in the wall with mineral wool. In none of the cases the moisture content does exceed 20%, which is often indicated as the critical threshold for wood decay [Carl and Highley, 1999].

A comparison between the properly airtight sealed configurations and the configurations sealed with an airtight tape only as measured in test series 2 is shown in the right figure. For the wall with CaSi, a (slightly) higher increase in moisture content is obtained if the junction is sealed with an airtight tape only. The other insulated walls seem to be less sensitive to the way of sealing the junction; if the airtight sealing is combined with a sealing based on flexible PUR than the moisture content is lower, though, the increase in moisture content is substantially equal. Finally, figure 93 shows the (increase in) moisture content of the wooden beams embedded in some of the insulated walls to be lower than found for the non-insulated wall.

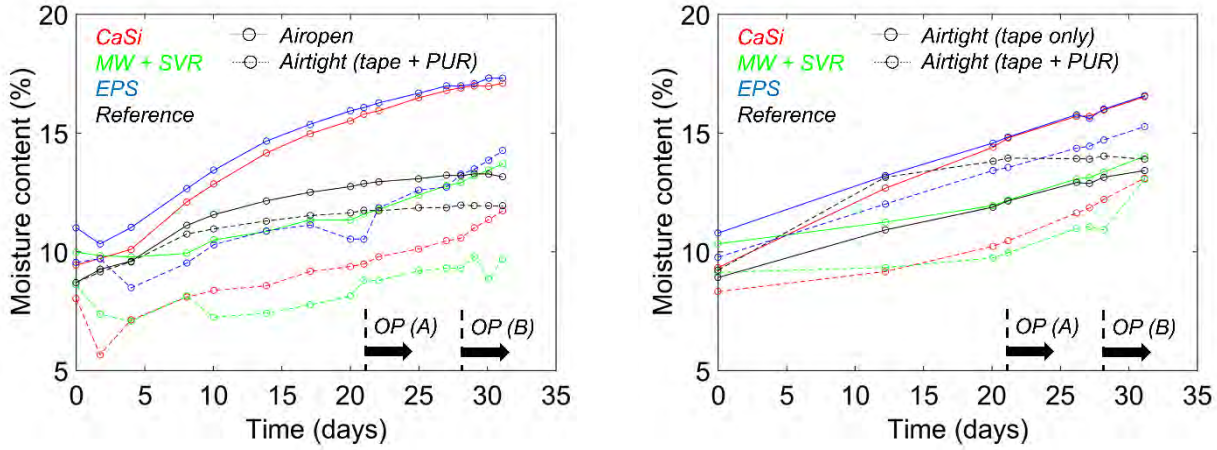

Fig. 93.: Moisture content at the back of the wooden beam end.

6.6.4 Mould growth evaluation

The risk on wood rot decay depends on the moisture content and was briefly discussed in the previous section. Mould growth, on the other hand, is influenced by the relative humidity and the temperature and act as a precursor for wood decay. Therefore, this section discusses the relative humidity in combination with the temperature. To assess the risk on mould growth different prediction models which reckon the temperature and relative humidity are available. In the current study, Sedlbauer's isopleth model will be used to get an indication of the mould growth risk. Sedlbauer's germination isopleths indicate the number of days at specified RH-/T-combinations resulting in the start of mould spore germination.

Figure 94 shows the scatter plots for the RH-/T-combinations near the back of the wooden beam together with Sedlbauer's germination isopleths, and this for the conditions measured till the end of the 5th (Figure 94a,b), the 21st (Figure 94c,d) and the 30th day (Figure 94e,f). The conditions measured at the start of the experiment are located in the right lower corner (around 20°C). While the experiment proceed, the conditions move toward the left upper corner. If no airtight sealing is provided (Figure 94a,c,e), the scatter plots show a steep increase for the wall with calcium silicate and - in less extend - for the wall with EPS. Also the curve for the non-insulated reference wall shows a steep increase. The curves for the latter three walls end up above the germination isopleths, and thus in the critical range for mould growth. On the other hand, for the wall with mineral wool a much flatter course is observed. For the latter case, the steep increase starts later and at a lower temperature. The lowest isopleth for mould germination (LIM) is exceeded after applying an overpressure (i.e. after day 21).

If an airtight sealing is provided (Figure 94b,d,f), all walls show a much flatter curve. The moment lower temperature is reached (Figure 94d,f), the increase in relative humidity is more pronounced. This increase in relative humidity occurs starting from a slightly higher temperature if the airtightness is obtained by an airtight tape only. The difference between the conditions measured for the junction sealed with a tape only and those for the junction also injected with flexible PUR before sealing it with a tape is again most pronounced for the wall with calcium silicate. If an overpressure is applied (Figure 94e,f), the temperature increases due to the air exfiltration through the wall, which can accelerate the mould growth..

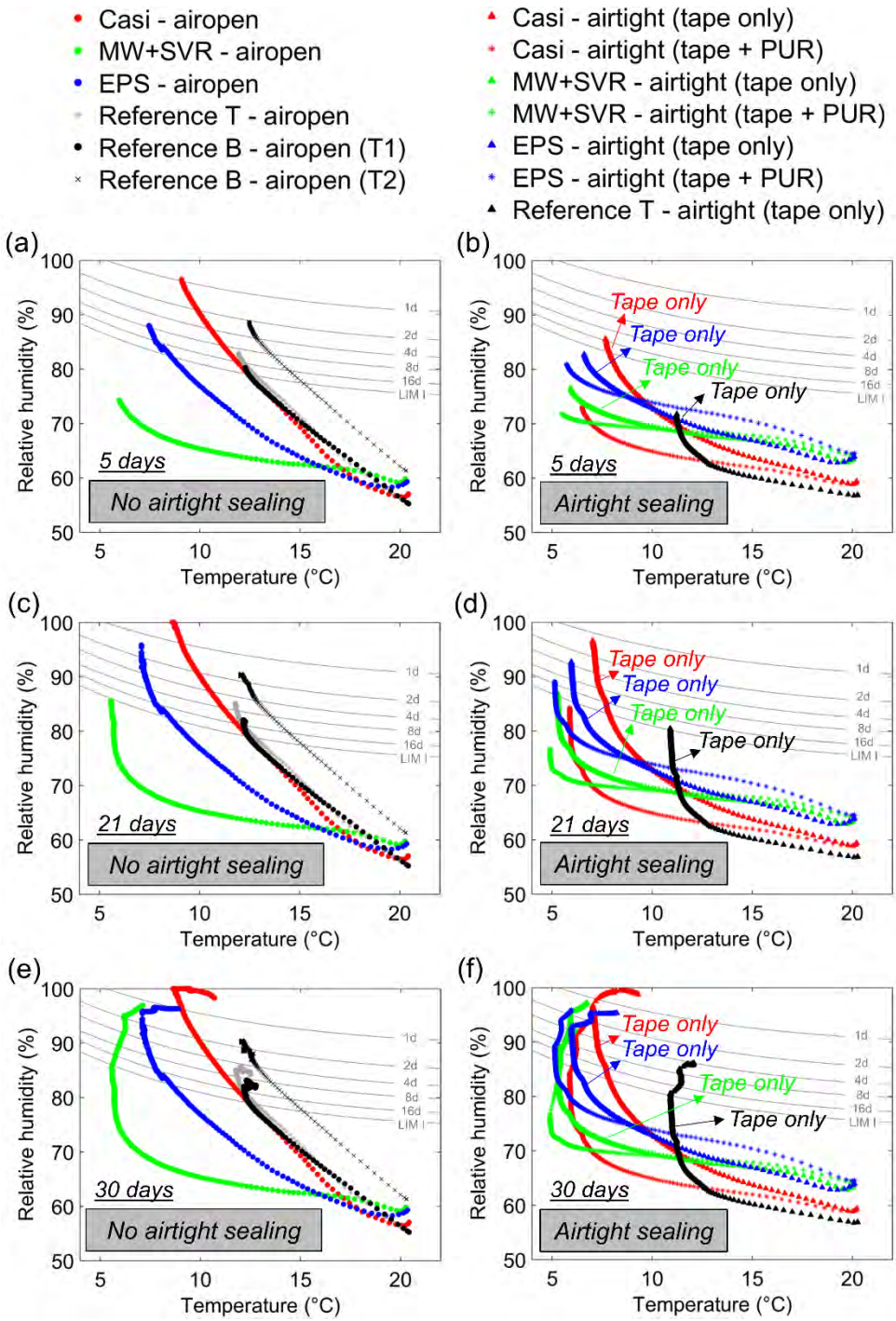

Fig. 94.: Scatter plots for the temperature and relative humidity combinations measured near the back of the wooden beams after 5 days (a,b), 21 days (c,d) and 30 days (e,f) together with Sedlbauer's isopleths for germination. (a,c,e) show the cases without an airtight sealing, (b,d,f) show the cases with an airtight sealing.

6.6.5 Temperature and air flow pattern

Based on the temperatures measured at the wooden beams, a view on the air flow pattern can be obtained. As an example, Figure 94 shows the temperature measured in the wall with calcium silicate. For the case with no airtight sealing and no overpressure (left part in Figure 94a), a comparison of the

temperatures shows that the temperature measured near the top of the wooden beam is significantly higher than the temperature measured near the bottom of the wooden beam (1T versus 1B, 2T versus 2B, 3T versus 3B). Convective air flow is clearly visible based on the difference in temperature. Air at room temperature seems to infiltrate in the wall via the top of the wooden beam, cools down behind the insulation and flows back toward the room via the lower part of the wooden beam. An overpressure across the wall makes that the temperatures at the lower part of the wooden beam (slightly) increase, resulting in a smaller difference with the temperatures at the beam's upper positions close to the hot box (room side), see 1T versus 1B and 2T versus 2B. For an overpressure of 6.2 - 6.5 Pa ('Overpressure B') almost no temperature difference between upper and lower position can be observed anymore at these positions. For the positions deeper in the wall (3T versus 3B), a temperature difference is still visible and is even slightly larger than without overpressure. Due to the overpressure, a rather one-dimensional air exfiltration seems to occur near the zone of the insulation system. Deeper in the wall, convection loops are still found to occur, as indicated by the higher temperature difference. When the junction with the wooden beam is made airtight by a tape only (Figure 95b) or by a tape and injecting the gap with flexible PUR (Figure 95c), the temperatures at the lower part of the wooden beam are globally in closer agreement with the upper temperature at the same depth in the wall (as indicated by the grey arrows between the curves). The top and bottom temperature measured near the interior surface are substantially the same if an airtight sealing is provided. Deeper in the wall, convection loops are still visible. These convection loops could, for instance, transport moisture buffered in the glue mortar and hence can explain the higher moisture conditions in the wall when no flexible PUR is applied. For the airtight junction, the steps in overpressure are less pronounced.

Based on the temperature measured near the wooden beams embedded in the wall with EPS, similar phenomena were found (not shown). On the other hand, for the wall with mineral wool (not shown), a much smaller temperature difference was found between the top and bottom positions, and this for both the air open (Figure 96) and airtight junctions. This points out the better connection between the soft mineral wool and the wooden beam and again explains the lower moisture conditions for the mineral wool system shown in the previous sections. A larger temperature difference indicating convection loops deeper in the wall, only became visible after applying an overpressure to the air open junction.

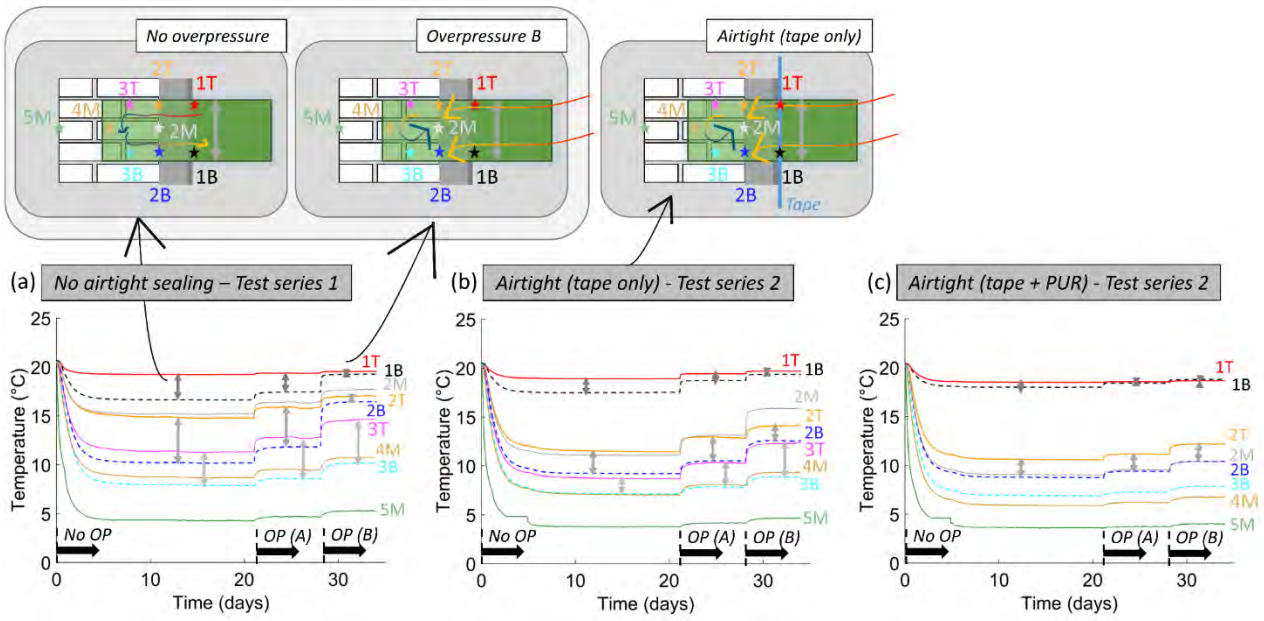

Fig. 95.: Impact of the airtight sealing and of the air pressure across the wall on the temperature at the wooden beams embedded in the wall with calcium silicate.

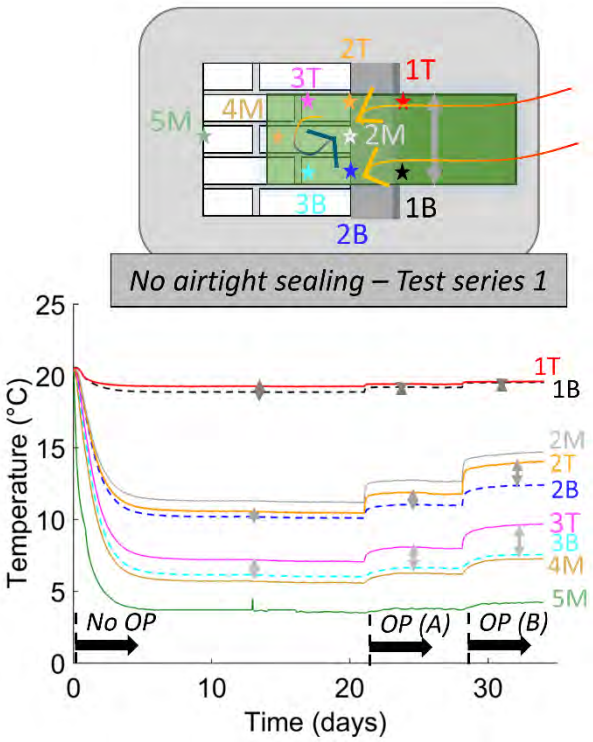

Fig. 96.: Temperature at the wooden beam embedded in the wall with mineral wool for the case without an airtight sealing.

6.6.6 Discussion and conclusions

The test series performed at the Building Physics Section of KU Leuven explored the air convection and infiltration at wooden beam ends embedded in an insulated masonry wall. A hot box-cold box experiment was performed in which three internally insulated masonry walls and one non-insulated masonry wall, each with embedded wooden beams, were exposed to a steady-state winter condition. Cases with as well as without an airtight sealing of the junction between wooden beam and wall surface were investigated to analyse the impact of convective moisture transport.

If no airtight sealing was provided, the (increase in) relative humidity at the wooden beam ends was higher than found for the wooden beams with an airtight junction. This was especially true for the wall insulated with calcium silicate. If no airtight sealing was provided, of all walls, the wall with calcium silicate showed the highest relative humidity at the wooden beam end. A prevention of air exfiltration by an airtight sealing at the indoor wall surface only was however found to be insufficient to avoid a steep increase in relative humidity. Based on the temperatures measured at the wooden beam, internal convection loops next to the embedded wooden beam were observed if an air gap next to the wooden beam was present. This internal convective air flow can transport air to a colder area where this air can cool down and hence induces a higher relative humidity. Additionally, interstitial condensation or moisture buffered in the glue mortar layer could be transported in this way. When, apart from an airtight sealing of the junction with the indoor surface, the junction between wooden beam and the calcium silicate system was injected with flexible PUR and thus an internal air flow was avoided, a much lower relative humidity near the wooden beam end was observed. In general, the behaviour found for the wall with EPS showed similarities. Though, in the latter case no moisture can be buffered in the insulation system and thus there is no extra moisture that can be transported in the wall via the convection loops, which may explain the lower moisture conditions.

For the wall with mineral wool and a smart vapour retarder, a minor risk on (internal) convective air flow is found. Also the impact of the airtight sealing of the junction between the beam and the indoor surface is found to be less. This can be attributed to the softer insulation material that allows a better contact with the beam. At short notice, the wall insulated with mineral wool performed even better than the non-insulated wall. It is however important to note that the non-insulated wall was not provided with an interior finishing layer, while the other walls had an airtight finishing. In this way, additional air flow paths via the masonry could have occurred. Furthermore, if the boundary conditions persist, the wooden beams embedded in the internally insulated walls are at higher relative humidity, and thus at higher mould growth risk, than the wooden beams embedded in the non-insulated walls, for which the relative humidity apparently reached equilibrium.

An overpressure across the walls was shown to influence both the relative humidity and the temperature in the wall, even when an airtight sealing was provided, and this while most numerical risk assessment do not reckon a potential overpressure. An overpressure results in a higher exfiltration rate of the warm moist indoor air, which possibly elevates the relative humidity. From this point of view, it is recommended to be cautious when imposing an overpressure e.g. when applying a ventilation strategy. On the other hand, exfiltration can elevate the temperature, which in its turn can reduce the relative humidity.

In conclusion, a well-installed mineral wool system is found to be less sensitive to the airtightness of the junction between wooden beam and indoor surface, while the calcium silicate system is most sensitive. In the latter case it is recommended to avoid air exfiltration as well as air circulation near the wooden beam. The results found for the calcium silicate may however not be extrapolated to other vapour open (capillary active) interior insulation systems, as they can have widely varying properties.

Finally, it should be stressed that the current study was limited to a steady-state winter condition without wind-driven rain; this in order to get a better view on the convective moisture transport phenomenon.

7 Inverse Modelling Approach

The following approach of inverse modelling is adopting a generic optimization tool, GenOpt, in order to improve the correspondence between measured and simulated hygrothermal performance of a construction. This calibration[3] approach for hygrothermal modelling has been published on the Nordic Building Symposium in Trondheim in June 2017 (Freudenberg, Ruisinger, & Stöcker, 2017)

A meaningful calibration assumes a verification[4] and a validation[5] of the applied software. In other words, verification is the very basic level, which ensures plausibility of the computational model. It does not include a comparison of model outcomes with reference values. Validation is performed at a higher level and includes an assessment of results via comparison of computational model results with reference values (from measurements or other sources). This validity has been proved and published for

[3] "Calibration is the process of adjusting physical modeling parameters in the computational model to improve agreement with experimental data." (Oberkampf & Roy, 2010)
[4] "Verification is the process of determining that the model implementation accurately represents the developer's conceptual description of the model." (Oberkampf & Roy, 2010)
[5] "Validation is the quantification of the accuracy of the computational model results by comparing the computed system response quantities of interest with experimentally measured system response quantities." (Oberkampf & Roy, 2010)

a number reference cases (Sonntag, Nicolai, & Vogelsang, 2013). On top level, presuming a successful verification and validation of the computational model, the calibration process aims to minimize the difference between model outputs and reference values by the help of parameter adjustment (not via modification of the computational model). It allows a reverse identification of parameters, which are not reliably known from the measurements.

7.1 Problem Description

Hygrothermal simulation software such as DELPHIN is an appropriate tool to evaluate complex engineering problems concerning heat and moisture transport through the envelope of a building. The initialization of such projects requires a number of input variables and functions. Some of them, e.g. the sorption curves for the moisture storage, are based on values, which are measured in a lab and converted into material functions as part of a systematic calibration procedure. These values are assumed to have a low uncertainty range, which is depending on the exactness of the lab measurements and the procedure itself. Further variables of the hygrothermal simulation project, such as surface transfer coefficients, are defined pragmatically on the base of national standards or the individual engineer's experience. This is a feasible method for typical engineering projects, where detailed information about initial conditions, boundary conditions etc. is often not available. It is less constructive for the simulation of laboratory tests where the accordance between measured and simulated data series is crucial for the results interpretation.

The main challenge of this application field for hygrothermal simulations is a systematic and reproducible identification of uncertainly known input variables. Typically, only one parameter is varied and optimized, while the other values remain fixed. This is continued for the next input variable(s) and therefore a time-consuming procedure. Because a variation of the first input variable yields a non-optimal constellation for the other variables which have to be adjusted as well in an iterative way. The achieved accordance is thus only a partial one that is strongly depending on the start values, the intuition of the user etc. Despite this, congruency of measured and simulated data series is mostly not rated numerically, with defined statistic key values, but either visually, with subjectively selected data series and accordance criteria.

7.2 Systematic Procedure with a Generic Optimization Algorithm

The systematic procedure is based on the application of a generic optimization program, GenOpt [7]. This software comprises a number of optimization algorithms, which allow the minimization of a defined cost-function that is laborious to be evaluated and whose analytical properties are not available. GenOpt has been developed for the application in the field of building energy use, namely the cost resp. energy demand minimization. A general procedure description for this case is part of the manual. A modified procedure as shown in the graph below was necessary for the mentioned application case of hygrothermal modelling calibration with DELPHIN.

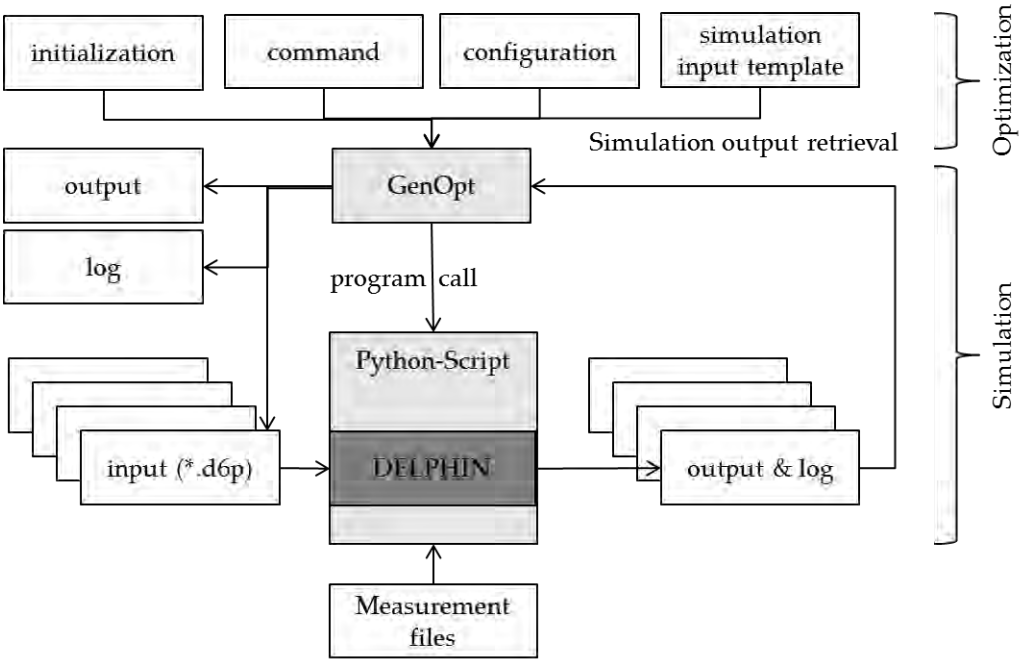

Fig. 97.: Modified interface scheme and file references for GenOpt with DELPHIN.

GenOpt is set up with four constituent parts that describe the specific problem. The configuration part describes the syntax of the simulation software call. The initialization part describes the project-specific input files, namely the directly executable project file and a template file based on it, which includes the placeholders for the parameters to be varied, the log files carrying the error messages and an output file, which defines the target parameter to be minimized. The command part specifies all variation parameters and the optimization algorithm that is used. Based on this information

GenOpt manages the input for the simulation tool, in this case .d6p-files for DELPHIN 5.8. This file is submitted to the executing software, a Python-script, the tool response (log-file) is checked and the output (target value to be minimized) is evaluated. The Python script is used to wrap the problem due to the fact, that the result of interest, the accordance between measured and simulated data series, is not a direct output of the simulation software. Therefore, the script functionality calls the software, checks the execution response, reads the simulated files, compares each of them with the corresponding measurement file and creates an output file with all required statistical results of this comparison. The target value is a statistic value, which represents the accordance between measured and simulated data series. Different approaches are possible, e.g. range-independent values like the correlation or range-dependent values like the average of the absolute difference.

7.3 Application

An application of the procedure is demonstrated for a simple two-dimensional detail. The construction is part of a test stand, which designed to evaluate joist ends in internally insulated masonry and calibrate simulation results with the measured data series. A proper calibration was essential to interpret the deviations between measurements and simulations. It was performed for different levels of complexity. The final case was the evaluation of three-dimensional details of the anisotropic joist ends for the validation of the three-dimensional extension of the simulation software DELPHIN. This has successfully been demonstrated for the isolated joist end itself by Vogelsang et al. [4] and furthermore for the installed case by Ruisinger et al. [5].

An overview of the measurement track in this given in the following graph. Sensors location was close to the warm-side surface of the test stand to record heat flux (WFP3) and surface temperature (TIDO3) and close to the cold-side surface to record relative humidity (HWA3) and temperature (TWA3). Measurements within the construction capture relative humidity and temperature of both, the potential condensation layer (TIDE3, HIDE3) and the middle of the masonry (HWM3, TWM3).

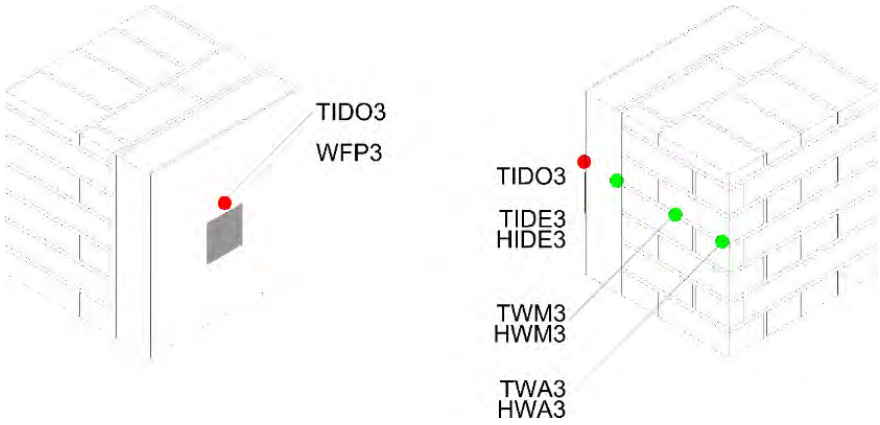

Fig. 98.: Location of the sensors within the 2D-construction. Left figure shows the view from the warm-side of the test stand (right surface is the warm side). Right hand figure shows the view from the cold side of the test stand (right surface is the cold side). Red points illustrate pure temperature sensors, green points illustrate combined temperature and relative humidity sensors and grey area illustrates the heat flux plate.

Cold-side chamber and warm-side chamber were both equipped with specific HVAC-systems for the simulation of different scenarios of indoor and outdoor climate (temperature and relative humidity). The period used in this application case started with homogeneous conditions on both sides of the test stand (20°C, 55%) and continued with an abrupt reduction of the cold-side temperature from 19°C to -10°C, 45% while the warm-side conditions remained as before. An initial hygrothermal simulation model was set up with calibrated material functions for the moisture storage and (liquid and vapour) transport as well as single measurement values for the thermal properties. Boundary conditions were defined and applied as measured curves in the model. The initial conditions were known for the measured points and defined over a self-chosen area. Uncertain input values of the initial hygrothermal model were the thermal (radiative and convective) and hygric surface transfer coefficients, the initial conditions of the areas between the measurement points and the thermal conductivity of the insulation material. The last parameter is underlying a bigger measurement uncertainty due to the measurement technique of the applied heat flow meter, which is sensitive to radiative effects for low-density materials that could cause a deviation of up to 10% additional to the usual uncertainty of this measurement technique. Transfer coefficients are normally determined with simplified calculations and were therefore not exactly quantifiable. Assuming standard values gives the following results for the sensors.

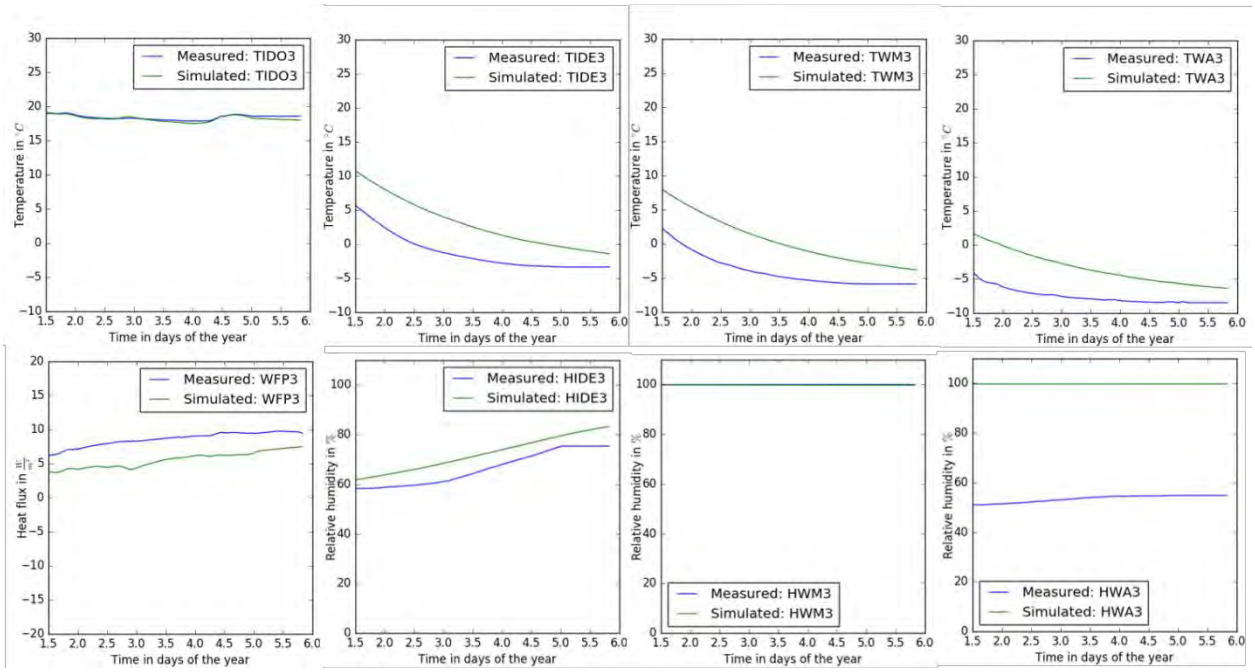

Fig. 99.: Graph summary of all sensors of both, the simulated (green curves) and the measured (blue curves) case in the initial simulation model. Only some days of the entire simulation period are shown in these graphs.

The initial simulation model shows diverse results for the different sensors and partially high deviations to the measurement results. Especially the cold-side relative humidity sensor (HWA3) is far below the simulation curve and shows an average difference to the measured curve of 22.5% for the whole simulation phase. Temperature sensors deviate between 0.22 (TIDO3) and 3.34 (TIDE3) °C, heat flux about 1.97 W/m² (WFP3) and relative humidity sensors between 0.09 (HWM3) and 22.46% (HWA3). The summarized linear correlation (Bravais & Pearson) of all sensors is about 0.69, the non-linear correlation (Spearman) about 0.66.

7.3.1 Test Case Description: Uncertain simulation model parameters

Uncertain model parameters are the hygric and thermal transfer coefficients of both surfaces, the thermal conductivity of the insulation and the distribution of the initial conditions.

For standard calculations, EN ISO 6946 suggests values around 6 to 10 W/m²K for the combined (convective and radiative) inside heat exchange coefficients and 25 W/m²K for exterior coefficients. The included convective part is assumed to be 20 W/m²K. The radiative part is given with 5 W/m²K for both, interior and exterior surface. [1].

Realistic surface coefficients can be identified with measurements of the air velocity and the temperature conditions in the adjacent chambers of the test wall. Air velocity in the cold side chamber is relevant to allow an approximation of the convective heat and moisture transfer from the wall surface to the air. The chamber was equipped with three smaller vents and one bigger vent. Measurement of the air velocity directly in front of the vents resulted in 2.3 to 2.5 m/s for the small vents and 4.5 m/s for the single vent. Measurements at the wall surface resulted in a spatial distribution of 0.1 to 0.4 m/s. An estimation of the corresponding convective heat transfer with an empiric approach [2, p 805, equation G4-6] yielded values of about 2 W/m²K.

The same estimation as for the convective heat transfer was done for the radiative part. The chamber surface temperature was measured at three different points and yielded (short-time) temperature differences between the masonry surface and the chamber walls of up to 8.3 K. Computation of the corresponding heat flux, simplified as exchange between two parallel surfaces ([1], S. 83) with realistic emission coefficients, resulted an average value of 4-5 W/m²K. The standard value of 5 W/m² is consequently very close to reality for the cold side of this test stand.

According to this, an approximation for the warm side of the chamber was made and resulted in a convective heat transfer coefficient of below 1 W/m²K and a radiative part of 2.5 W/m²K. Hygric transfer coefficients were derived from the convective thermal transfer coefficients via Lewis-Relation with 1 to $2 \cdot 10^{-8}$ s/m. The uncertainty of the insulation thermal conductivity was estimated with 20%.

7.4 Results of the optimization problem

In summary, the five selected variation parameters of the simulation model are the combined thermal transfer coefficient at the cold side α_e and at the warm side α_i, the cold- (β_e) and warm-side (β_i) hygric transfer coefficients and the thermal conductivity of the insulation (λ_{ins}). They were defined as variables in the optimization case with a corresponding start value (see previous paragraph), variation step and value range (min, max). Furthermore, a cost function was required in form of a statistic representation of the accordance between measured and simulated curves. Three approaches were tested, the average difference between simulated and measured curve, the linear correlation according to Bravais & Pearson and the non-linear correlation according to Spearman. Simulation series of all three target values for the same optimization case with the appropriate GenOpt algorithm (GPSPSOOCCHJ) produced the following outcome.

Tab. 20.: Results for three different target values of the optimization problem

Target value	Achieved target value	No. of simulations	Identified values				
			α_e	α_i	β_e	β_i	λ_{ins}
			W/m²K	W/m²K	s/m	s/m	W/mK
Absolute average difference between eight simulated and measured curves (regardless of the value range)	x_{abs}= 1.32	235	12.0	5.5	5e-7	5e-8	0.046
Average linear correlation between eight simulated and measured curves (range- independent value)	σ_{Lin}= 0.84	306	12.0	7.2	5e-7	5e-8	0.053
Average non-linear correlation between eight simulated and measured curves (range- independent value)	σ_{NonLin}= 0.81	252	12.0	6.6	5e-7	5e-8	0.043

A comparison of the three target value runs shows equal results for the hygric transfer coefficients. On the contrary, the identified inner thermal transfer coefficient and thermal conductivity differ among the three runs. Furthermore, the number of required simulations is the highest for the linear correlation and the lowest for the absolute average difference.

It seemed suspicious that some variation parameters are identified as minimum or maximum values. This is the case for the cold-side hygric and thermal transfer coefficients. Further extensions of the limits for these coefficients showed a highly increased number of required simulations and the same result (maximum values). It seemed to approximate unrealistic values. A reduction of the step size for these parameters did also raise the simulation quantity intensely but not change the identification of defined maximum values. This was seen as a hint of inaccuracies in the initial hygrothermal simulation model. Due to the unknown distribution of initial conditions between the measured points, a correction of this setting seemed promising to eliminate the unrealistic convergence. The high humidity level in

the middle of the masonry was limited to the inner part of the jointing. A reduced humidity level was defined for the adjacent areas and smooth temperature gradients for the whole construction.

The impact of this correction was remarkable. An analysis of the identified best-case variation values from the previous three runs yielded an average difference of about 0.48, an average linear correlation of about 0.93 and non-linear correlation of about 0.88. A summary of this optimization and correction result is given below for all eight sensors in the construction.

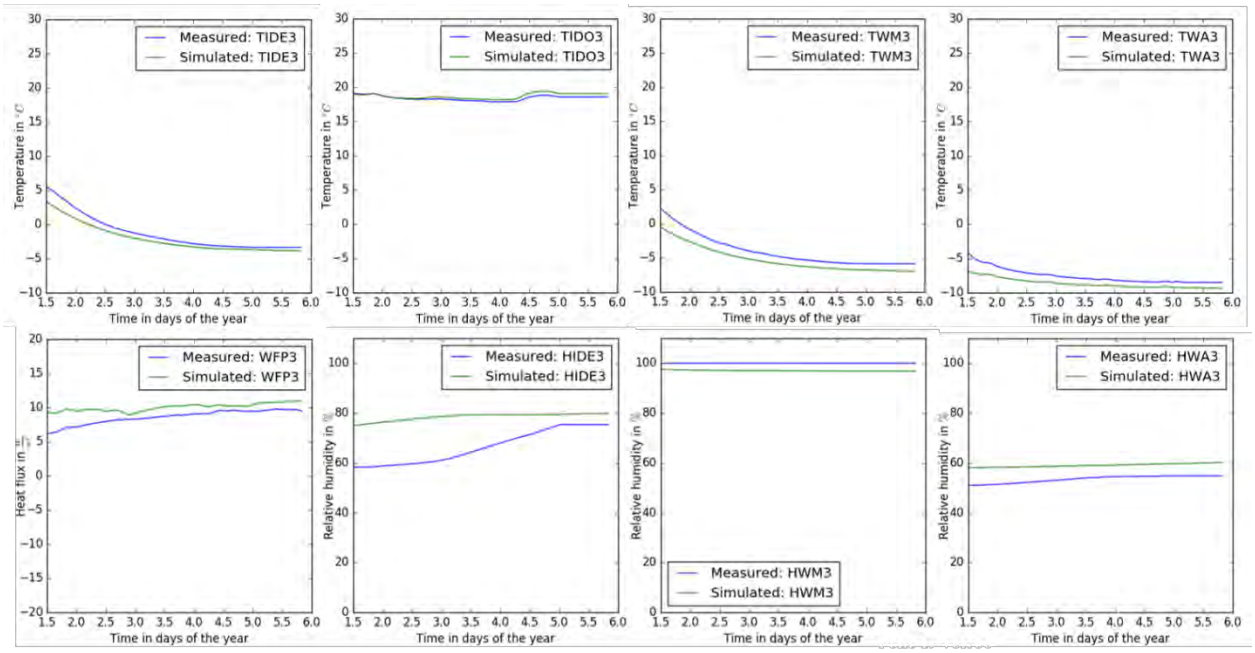

Fig. 100.: Graph summary of all sensors of both, the simulated (green curves) and the measured (blue curves) case in the final simulation model.

7.5 Summary

The application of a generic optimization algorithm in the field of hygrothermal simulation model calibration has successfully been demonstrated for the example of a masonry test wall with interior insulation. Three different target values (difference, linear and non-linear correlation) were set up with five variation parameters (hygric and thermal transfer coefficients on both sides, thermal conductivity of insulation material) and yielded a remarkable improvement of the accordance between measured and simulated curves.

8 References

VDI (Verein Deutscher Ingenieure). (2013). *VDI-Wärmeatlas, 11., bearb. und erw. Aufl.* Berlin, Heidelberg: Springer Vieweg.

Alev, Ü., Uus, A., Teder, M., Miljan, M.-J., & Kalamees, T. (2014). Air leakage and hygrothermal performance of an internally insulated log house. *Proceedings of the NSB 2014*, (pp. 55-61). Lund.

Arbeiter, K. (2014). *Innendämmung - Auswahl, Konstruktion, Ausführung.* Köln: Rudolf Müller Publishing.

Baehr, H. D. (2016). *Wärme- und Stoffübertragung, 9., aktualisierte Auflage.* Berlin, Heidelberg: Springer Vieweg.

Bichlmair, S., Krus, M., & Kilian, R. (2014). Testing a new method for VIP interior insulation for heritage buildings. *Proceedings of the NSB 2014*, (pp. 1349-1355). Lund.

Bishara, A., Meissner, F., & Plagge, R. (2014). *3EnCult (Efficient Energy for EU Cultural Heritage) - Documentation of each study case.* Brussels: European Commission DG Research and Innovation.

Borsch-Laaks, R. (2005). Innendämmung - Risikokonstruktion oder Stand der Technik. *6. Leipziger Bauschadenstag*, (pp. 1-17). Leipzig.

Brand, E., Bunch-Nielsen, T., Christensen, G., Gudum, C., Hansen, M. H., & Møller, E. B. (2013). *SBi-Anvisning 224 - Fugt i Bygninger 2nd Edition (Danish).* Copenhagen, Denmark: Statens Byggeforskningsinstitut, SBI.

Cattarin, G., Causone, F., Kindinis, A., & Pagliano, L. (2016, 11 11). Outdoor test cells for building envelope experimental characterisation – A literature review. *Renewable and Sustainable Energy Reviews*, pp. 606-625.

COND, IBK, TUD. (n.d.). *Software des Instituts für Bauklimatik*. Retrieved 10 23, 2015, from http://www.bauklimatik-dresden.de/

Conrad, C., Häupl, P., Petzold, H., & Löber, H. (2007). Energetisch und bauphysikalisch optimierte Sanierung eines Baudenkmals in Görlitz. *Bauphysik*, pp. 221-230.

Delphin, IBK, TUD. (n.d.). *Software des Instituts für Bauklimatik*. Retrieved 10 2015, 10, from bauklimatik-dresden.de

DIN 4108-2 Deutsches Insitut für Normung e.V. (2013). *Wärmeschutz und Energieeinsparung in Gebäuden - Teil 2: Mindestanforderungen an den Wärmeschutz.* Berlin: Beuth Verlag.

DIN 4108-3 Deutsches Insitut für Normung e.V. (2014). *Wärmeschutz und Energieeinsparung in Gebäuden - Teil 3: Klimabedingter Feuchteschutz.* Berlin: Beuth Verlag.

Dysted, D., & Sandholdt, H. (2015). *Experimental and theoretical investigation of Interior insulation of solid brick walls with foam concrete and another silicate based material.* Kgs. Lyngby, Denmark: Technical University of Denmark.

EN 13501 Deutsches Institut für Normung e.V. (2010). *Fire classification of construction products and building elements - Part 1 Classification using data from reaction to fire tests (German version).* Berlin: Beuth Verlag.

Fisher, D. E., & Pedersen, C. O. (1997). *Convective Heat Transfer in Building Energy and Thermal Load Calculations in ASHRAE Transactions 1997 Vol. 103, Part2, 4065 (RP-664).* American Society of Heating, Refrigerating and Air-Conditioning Engineers, Inc.

Freudenberg, P., Ruisinger, U., & Stöcker, E. (2017, Oct). Calibration of Hygrothermal Simulations by the Help of a Generic Optimization Tool. *Energy Procedia 132 (2017), Elsevier* , pp. 405-410.

Geburtig, G. (2009). Innendämmung nach WTA. In A. Worch, *Innendämmung im Bestand.* Stuttgart: Fraunhofer IRB Verlag.

Grunewald, J. (1996). *Diffusiver und konvektiver Stoff- und Energietransport in kapillarporösen Baustoffen.* Dresden: Fakultät Bauingenieurwesen, Technische Universität Dresden.

Grunewald, J., Häupl, P., & Bomberg, M. (2003, April). Towards an Engineering Model of Material characteristics for Input to Ham Transport Simulations - Part 1: An Approach. *Journal of Thermal Envelope and Building Science Vol. 26*, pp. 343-366.

Guizzardi, M., Derome, D., Vonbank, R., & Carmeliet, J. (2015, Feb). Hygrothermal behaviour of a massive wall with interior insulation during wetting. *Building and Environment*, pp. 59-71.

Hansen, E. J., Stang, B. F., Ginnerup, S., Kirkeby, I. M., Buch-Hansen, T. C., Aagaard, N.-J., . . . Brandt, E. (2010). *SBi-Anvisning 230 - Anvisning om Bygningsreglement 2010 (in Danish).* Hørsholm, Denmark: Statens Byggeforskningsinstitut, Aalborg University.

Hasper, W., Kaufmann, B., Pfluger, R., & Feist, W. (2010). *Energetische Sanierung eines denkmalgeschützten Speichergebäudes mit aufgesprühter Zellulose-Innendämmung.* Darmstadt: Passivhaus- Institut .

Hasper, W., Kaufmann, B., Pfluger, R., Feist, W., & Aust, H. (2010). *Energetische Sanierung eines denkmalgeschützten Speichergebäudes mit aufgesprühter Zellulose- Innendämmung.* Darmstadt: Passivhausinstitut.

Häupl, P. (2008). *Bauphysik - Klima Wärme Feuchte Schall: Grundlagen, Anwendungen, Beispiele, Aktiv in Mathcad.* Berlin: Ernst & Sohn Verlag für Architektur und Technische Wissenschaften GmbH & Co. KG.

Häupl, P., Grunewald, J., & Petzold, H. (2004, Heft 1). Energetische Sanierung des Herrenschießhauses in Nürnberg mit kapillaraktiver Innendämmung. *Bauphysik - Wärme, Feuchte, Schall, Brand, Licht, Energie, Klima*, pp. 43-48.

Häupl, P., Jurk, K., & Petzold, H. (2003). Inside thermal insulation for historical facades. *In Proc. Of the 2nd International Conference on Building Physics*, (pp. 463-469). Rotterdam.

Häupl, P., Löber, H., Conrad, C., Grunewald, J., Schmidt, M., & Bolsius, J. (2010). *Energetisch und bauphysikalisch optimierte Sanierung eines Baudenkmals in Görlitz (Abschlussbericht AZ 21216).* Osnabrück: Deutsche Bundesstiftung Umwelt (DBU).

Hong, T., Feng, W., Lu, A., Xia, J., Yang, L., Shen, Q., . . . Bhandari, M. (2013). *Building Energy Monitoring and Analysis.* Berkeley: Ernes Orlando Lawrence Berkeley National Laboratory.

IQ-Lator, IBK TUD (i.A. Remmers). (n.d.). *Software im Auftrag v. Remmers*. Retrieved 11 16, 2015, from http://www.remmers.de/9349.0.html

ISO 13788 Deutsches Insitut für Normung e.V. (2013). *Wärme- und feuchtetechnisches Verhalten von Bauteilen und Bauelementen - Raumseitige Oberflächentemperatur zur Vermeidung kritischer Oberflächenfeuchte und Tauwasserbildung im Bauteilinneren - Berechnungsverfahren.* Berlin: Beuth Verlag.

ISO 6946 Deutsches Insitut für Normung e.V. (2003). *DIN EN ISO 6946: Wärmedurchlasswiderstand und Wärmedurchgangskoeffizient, Berechnungsverfahren.* Berlin: Beuth Verlag.

IST. (2014). *Data sheet Humidity HYT 221.* Retrieved 12 13, 2017, from INNOVATIVE SENSOR TECHNOLOGY IST AG: https://www.ist-ag.com/sites/default/files/DHHYT221_E.pdf

Jenisch, R. (1996). *Schadenfreies Bauen, Band 16 - Tauwasserschäden.* Stuttgart: Fraunhofer IRB Verlag.

Kautsch, P., Häupl, P., Hengsberger, H., & Streicher, W. (2005). *Zellulose-Innendämmung ohne Dampfsperre.* Wien: Berichte aus Energie-und Umweltforschung.

Kilian, R., Bichlmair, S., Krus, M., & Thiel, A. (2014). *Vakuumdämmung mit Klebematte im Altbau.* Stuttgart: Fraunhofer IRB Verlag.

Kopecky, P., Kamil, S., Bures, M., & Tywoniak, J. (2017, Oktober). Experimental investigations of wooden beam ends in masonry with internal insulation. *Energy Procedia 132*, pp. 682-687.

Korjenic, A., & Dreyer, J. (2003). Untersuchungen zur thermisch-hygrischen Eignung von Vakuumdämmplatten zur Sanierung von Gebäuden der Wiener Gründerzeit. *Bauphysik*, pp. 344-349.

Loga, T., Feldmann, R., Diefenbach, N., Großklos, M., & Born, R. (2003). *Wiesbaden - Lehrstraße 2, Energetische Modernisierung eines Gründerzeithauses.* Darmstadt: Insitut für Wohnen und Umwelt (IWU).

Marincioni, V., Altamirano-Midina, H., & Ridley, I. (2014). Performance of internal wall insulation systems - experimental test for the validation of a hygrothermal simulation tool. *NSB*, (pp. 119-126). Lund.

Nicolai, A., Grunewald, J., & Zhang, J. (2007). Recent improvements in HAM simulation tools: Delphin 5 / CHAMPS-BES. *Conference Proceedings of 12th Symposium of Building Physics*, pp. 866-876.

Oberkampf, W. L., & Roy, C. J. (2010). *Verification and Validation in Scientific Computing.* Cambridge: Cambridge University Press.

Odgaard, T., Bjarløv, S. P., & Rode, C. (n.d.). Influence of hydrophobation and deliberate thermal bridge on hygrothermal conditions of internally insulated historic solid masonry walls with built-in wood (Unpublished results/In press). *Energy Build*.

Ojanen, T., Peuhkuri, R., Viitanen, H., Lähdesmäki, K., Vinha, J., & Salminen, K. (2011). Classification of material sensitivity – New approach for mould growth modeling. *Nordic Symposium on Building Physics* (pp. 867-874). Tampere, Finland: NSB.

Oswald, R., Zöllner, M., Liebert, G., & Sous, S. (2011). *Baupraktische Detaillösungen für Innendämmungen (nach EnEV 2009).* Stuttgart: Fraunhofer IRB Verlag.

Oswald, R., Zöllner, M., Liebert, G., & Sous, S. (2011). *Energetisch optimierte Gründerzeithäuser - Baupraktische Detaillösungen für Innendämmngen unter besonderer Berücksichtigung der Anforderungen der EnEV von April 2009.* Stuttgart: Fraunhofer IRB Verlag.

Otiv, P. (2016). *Hygrothermal modelling of internal insulation to solid masonry walls.* Kgs. Lyngby, Denmark: Technical University of Denmark.

Peuhkuri, R., Holøs, S., Geving, S., Holme, J., Tweed, C., & Gandhi , K. (2011). *SUSREF: Guidelines for the use of building physical modelling methods and tools in the development of sustainable refurbishment technologies for external walls.*

Ruisinger, U., & Grunewald, J. (2009). *Feuchteatlas zur Vermeidung planungsbedingter Feuchteschäden (Abschlussbericht).* Dresden: Institut für Bauklimatik.

Ruisinger, U., Petzold, H., Grunewald, J., & Häupl, P. (2004). Energetische Bewertung von Gebäuden mit raumseitiger Wärmedämmung aus Calciumsilikat. Energiefachtagung der Landesregierung Thüringen.

Sanders, C., Baker, P., & Hermann, C. (2014). Hygrothermal assessment of wind-driven rain as a risk for internal insulation retrofit of traditional buildings. *Proceedings of NSB 2014*, (pp. 1053-1060). Lund.

Scheffler, G. A. (2008). *Validation of hygrothermal material modelling under consideration of the hysteresis of moisture storage.* Dresden: Technische Universität Dresden, Fakultät Bauingenieurwesen, Institut für Bauklimatik.

Scheffler, G. A., Grunewald, J., & Häupl, P. (2004). Calibration of an Engineering Model of Hygrothermal Material Characteristics. *IEA-EXCO Energy Conservation in Buildings and Community Systems*, (pp. 1-18). Glasgow.

Sedlbauer, K., & Krus, M. (2003). Experimentelle und rechnerische Untersuchungen an Holzfachwerk mit nachträglicher Innendämmung. *Bauphysik*, pp. 137-145.

Sonntag, L., Nicolai, A., & Vogelsang, S. (2013). *Validierung der Solverimplementierung des hygrothermischen Simulationsprogramms DELPHIN.* Institut für Bauklimatik, Bauphysik. Dresden: Qucosa Sachsen. Retrieved from urn:nbn:de:bsz:14-qucosa-128968

Sontag, L., & Nicolai, A. (2013). Implementation of an efficient numerical solution method to simulate freezing processes in porous media. *Central European Symposium on Building Physics.* Vienna, Austria.

Spitler, J., Pedersen, C., & Fisher, D. (1991). *Interior Convective Heat Transfer in Buildings, ASHRAE Transactions. 97, part 1: 505-515.* American Society of Heating, Refrigerating and Air-Conditioning Engineers, Inc.

Strangfeld, P., Staar, A., & Stopp, H. (2012). Das hygrothermische Verhalten von Holzbalkenköpfen im innengedämmten Mauerwerk. *Bausubstanz (Hefte 2 und 3)*, pp. 49-55.

Straube, J. (2010). Simplified Prediction of Driving Rain on Buildings: ASHRAE 160P and WUFI 4.0. *Building Science Digest*, 1-16.

VDI. (2016). *VDI- Wärmeatlas, 11.Auflage.* (G. V. Hrsg., Ed.) Berlin, Heidelberg: Springer-Verlag.

Vereecken, E., & Roels, S. (2014). A comparison of the gygric performance of interior insulation systems: A hot box-cold box experiment. *Energy and Buildings*, 37-44.

Viitanen, H., Toratti, T., Makkonen, L., Peuhkuri, R., Ojanen, T., Ruokolainen, L., & Räisänen, J. (2010). Towards modelling of decay risk of wooden materials. *European Journal of Wood and Wood Products,*, 303-313.

Wagner, A., Voss, K., Grunewald, J., Petzold, H., Wenning, M., Reiß, J., & Kratz, M. (2008). *EnSan - Hamburg, Kleine Freiheit 46-52 (Abschlussbericht).* Jülich, Wuppertal, Karlsruhe, Freiburg, Aachen, Würzburg: EnOB - Forschung für Energieoptimiertes Bauen.

WTA 6-5-1. (2014). *Innendämmung nach WTA I - Merkblatt 6-5-1: Nachweis von Innendämmsystemen mittels numerischer Berechnungsverfahren.* WTA Publications (Wissenschaftlich- Technische Arbeitsgemeinschaft für Bauwerkserhaltung und Denkmalpflege e.V.).

WTA Wissenschaftlich- Technische Arbeitsgemeinschaft für Bauwerkserhaltung und Denkmalpflege e.V. (2009). *Innendämmung nach WTA I - Merkblatt 6-4: Planungsleitfaden.* WTA Publications.

WTA Wissenschaftlich- Technische Arbeitsgemeinschaft für Bauwerkserhaltung und Denkmalpflege e.V. (2014). *Innendämmung nach WTA II - Merkblatt 6-4: Planungsleitfaden.* WTA Publications.

WTA Wissenschaftlich- Technische Arbeitsgemeinschaft für Bauwerkserhaltung und Denkmalpflege e.V. (2014). *Innendämmung nach WTA II - Merkblatt 6-5-2: Nachweis von Innendämmsystemen mittels numerischer Berechnungsverfahren.* WTA Publications.

WUFI, IBP. (n.d.). *Fraunhofer Institut für Bauphysik, Software "Wärme Und Feuchte Instationär" (WUFI)*. Retrieved 11 16, 2015, from https://wufi.de/de/

Wulf, R. (2009). *Wärmeleitfähigkeit von hitzebeständigen und feuerfesten Dämmstoffen - Untersuchungen zu Ursachen für unterschiedliche Messergebnisse bei verwendung verschiedener Messverfahren.* Freiberg: Dissertation an der Technischen Universität Bergakademie Freiberg.

Brand, Erik; Bunch-Nielsen, Tommy; Christensen, Georg; Gudum, Charlotte; Hansen, Morten Hjortslev; Møller, Eva B. 2013. SBi-Anvisning 224 - Fugt i Bygninger 2nd Edition (Danish). Statens Byggeforskningsinstitut, Aalborg University, Copenhagen, Denmark.

Brand, E.; Bunch-Nielsen, T.; Christensen, G.; Gudum, C.; Hansen, M.H.; Møller, E.B. 2013. SBi-Anvisning 224 - Fugt i Bygninger 2nd Edition (Danish). Statens Byggeforskningsinstitut, Aalborg University, Copenhagen, Denmark.

Carl CG, Highley TL. Decay of wood and wood-based products above ground in buildings. J Test Eval 1999;27(2):150-158

Dietsch P, Franke S, Franke B. Methods to determine wood moisture content and their applicability in monitoring concepts. J Civil Struct Health Monit 2015;5:115-127

Dysted, D., & Sandholdt, H., 2015, Experimental and theoretical investigation of Interior insulation of solid brick walls with foam concrete and another silicate based material, MSc. Thesis, Technical University of Denmark, Kgs. Lyngby, Denmark.

Hansen, Ernst Jan de Place; Stang, Birgitte Friis Dela; Ginnerup, Søren; Kirkeby, Inge Mette; Buch-Hansen, Thomas Cornelius; Aagaard, Niels-Jørgen; Sørensen, Lars Schiøtt; Bergsøe, Niels Christian; Hoffmeyer, Dan; Aggerholm, Søren; Brandt, Erik. 2010. SBi-Anvisning 230 - Anvisning om Bygningsreglement 2010 (in Danish). Statens Byggeforskningsinstitut, Aalborg University, Hørsholm, Denmark.

Hansen, E.J.d.P.; Stang, B.F.D.; Ginnerup, S.; Kirkeby, I.M.; Buch-Hansen, T.C.; Aagaard, N.; Sørensen, L.S.; Bergsøe, N.C.; Hoffmeyer, D.; Aggerholm, S.; Brandt, E.. 2010. SBi-Anvisning 230 - Anvisning om Bygningsreglement 2010 (in Danish). Statens Byggeforskningsinstitut, Aalborg University, Hørsholm, Denmark.

IST, 2014, Data Sheet Humidity HYT 221, Online document, https://www.ist-ag.com/sites/default/files/DHHYT221_E.pdf

Odgaard, T.; S.P. Bjarløv, C. Rode, Influence of hydrophobation and deliberate thermal bridge on hygrothermal conditions of internally insulated historic solid masonry walls with built-in wood (Unpublished results/In press)., Energy Build. (n.d.).

Ojanen, T.; Peuhkuri, R.; Viitanen, H.; Lähdesmäki, K.; Vinha, J.; Salminen, K., 2011, Classification of material sensitivity – New approach for mould growth modeling, 9th Nordic Symposium on Building Physics, pp. 867-874.

Otiv, Peter. 2016. Hygrothermal modelling of internal insulation to solid masonry walls. MSc. Thesis, Technical University of Denmark, Kgs. Lyngby, Denmark.

Peuhkuri, R. et al., 2011, SUSREF: Guidelines for the use of building physical modelling methods and tools in the development of sustainable refurbishment technologies for external walls.

Sedlbauer K. Beurteilung von Schimmelpilzbildung auf und in Bauteilen. 2001. Dissertation Universität Stuttgart

Sontag, L.; Nicolai, A., 2013, Implementation of an efficient numerical solution method to simulate freezing processes in porous media, In Proceedings of 2nd Central European Symposium on Building Physics.

Straube, John. 2010. Simplified Prediction of Driving Rain on Buildings: ASHRAE 160P and WUFI 4.0. Build. Sci. Dig. Vol. 148:1–16.

Viitanen, H.; Toratti, T.; Makkonen, L.; Peuhkuri, R.; Ojanen, T.; Ruokolainen, L.; Räisänen, J., 2010, Towards modelling of decay risk of wooden materials, European Journal of Wood and Wood Products, Vol. 68, pp. 303-313.

9 Appendix

Tab. 21.: TUD test stand: list of sensors which were used in the project with their measurement range and uncertainty

Sensor type (type reference)	Specification	Measurement Range	Uncertainty	Comment
Temperature sensor (T_NTC)	NTC Sensor (Thermistor)	-20 – 100 °C	-20 – 0 °C: ±0,4 K 0 – 70 °C: ±0,1 K > 70 °C: ±0,6 K	Ahlborn NTC FN 0001K
Combined temperature and relative humidity sensor (TH_D)	Digital, CMOSSens	5 – 98 % RH -20 – 60 °C	10 – 90 % RH: 1,8 % bei 25 °C 10 – 40 °C: ±0,4 K -20 – 80 °C: ±1,3 K	Ahlborn FHAD 46, Raumklimasensoren
Combined temperature and relative humidity sensor (TH_NTC)	Capacitive sensor resp. NTC (type N)	-30 – 100 °C 0 – 100 % RH	-20 – 0 °C: ±0,4 K 0 – 70 °C: ±0,1 K > 70 °C: ±0,6 K < 90 % RH: ±2 %	Ahlborn FHA 646 R, eingebaute Sensoren
Combined temperature and air velocity (TV_D)	Thermoanemo-meter	-20 – 70 °C 0,08 – 2 m/s 700 – 1100 mbar	0 – 50 °C: ±0,7 K ±0,04 m/s + 1 % v MW 0 – 65 °C: ±2,5 mbar	Ahlborn FVAD 35 TH4
Heat flux board and temperature (TF_D)		-40 – 80 °C	5 % (23 °C)	Ahlborn FQA 118
Material moisture content (MC_D)	Capacitive sensor	5 – 50 M.-% (23 °C) 0 – 80 °C 0 – 90 % RH	Auflösung von 0,1 % und Reproduzierbarkeit von 1 %	Ahlborn FHA 636 MFS1, Temperaturkorrektur erforderlich

Tab. 22.: TUD test stand: list of sensors in the cold-side and warm-side chamber

Sensor- ID	Specification	Sensor type reference
TRaO, HRaO	Air conditions in the upper zone of the chamber	TH_D
TRaM, HRaM	Air conditions in the middle zone of the chamber	TH_D
TRaU, HRaU	Air conditions in the lower zone of the chamber	TH_D
TRaD	Surface temperature of the ceiling	T_NTC
TRaSW	Surface temperature of the side wall	T_NTC
TRaRW	Surface temperature of the back wall	T_NTC
TRiO, HRiO	Air conditions in the upper zone of the chamber	TH_D
TRiM, HRiM	Air conditions in the middle zone of the chamber	TH_D
TRiU, HRiU	Air conditions in the lower zone of the chamber	TH_D

Tab. 23.: TUD test stand: list of sensors sorted by test field in test strip 1 (iQ-Therm)

Sensor- ID	Specification	Sensor type reference
Upper joist end test field (double sealing tape and plaster connection collar) in test strip 1 (iQ-Therm)		
TWA1O	Temperature in the bed joint of the masonry, about 5 mm behind the cold-side directed surface of the masonry	T_NTC
TBKT1O, HBKT1O	Temperature and relative humidity in the bed joint of the	TH_NTC

	masonry, located close to the cavity-directed masonry surface	
TBK1O	Surface temperature of the wood at the cavity-directed front face of the joist end.	T_NTC
TBKSH1O, HBKSH1O	Temperature and relative humidity 5 mm behind the cavity-directed front face of the beam end.	TH_NTC
Middle field (wall segment) in test strip 1 (iQ-Therm)		
TWM1, HWM1	Temperature and relative humidity in the middle of the masonry (bed joint)	TH_NTC
TIDE1, HIDE1	Temperature and relative humidity at the interface between insulation system and basic construction (adhesive mortar layer)	TH_NTC
WFP1	Heat flux at the warm-side surface on top of the insulation system	TF_D
TIDO1	Surface temperature at the warm-side surface on top of the insulation system	T_NTC
Lower joist end test field (double sealing tape and plaster connection collar) in test strip 1 (iQ-Therm)		
TWA1U	Temperature in the bed joint of the masonry, about 5 mm behind the cold-side directed surface of the masonry	T_NTC
TBKT1U, HBKT1U	Temperature and relative humidity in the bed joint of the masonry, located close to the cavity-directed masonry surface	TH_NTC
TBK1U	Surface temperature of the wood at the cavity-directed front face of the joist end.	T_NTC
TBKSH1U, HBKSH1U	Temperature and relative humidity 5 mm behind the cavity-directed front face of the beam end.	TH_NTC

Tab. 24.: TUD test stand: list of sensors sorted by test field in test strip 2 (Calsitherm)

Sensor- ID	Specification	Sensor type reference
Upper joist end test field (single sealing tape and plaster connection collar) in test strip 2 (Calsitherm)		
TWA2O	Temperature in the bed joint of the masonry, about 5 mm behind the cold-side directed surface of the masonry	T_NTC
TBKT2O, HBKT2O	Temperature and relative humidity in the bed joint of the masonry, located close to the cavity-directed masonry surface	TH_NTC
TBK2O	Surface temperature of the wood at the cavity-directed front face of the joist end.	T_NTC
TBKSH2O, HBKSH2O	Temperature and relative humidity 5 mm behind the cavity-directed front face of the beam end.	TH_NTC
HFBK2O*	Mass-related moisture content of the beam end wood, about 2 cm behind beam front end	MC_D
TIDEBU2O, HIDEBU2O*	Temperature and relative humidity in the wall part below the joist end (about 5 cm below) at the interface between insulation system and basic construction (adhesive mortar layer)	TH_NTC
TIDOBU2O*	Surface temperature in the wall part below the joist end (about 5 cm below) on the warm side surface (finishing plaster)	T_NTC
Middle field (wall segment) in test strip 2 (Calsitherm)		
TWM2, HWM2	Temperature and relative humidity in the middle of the masonry (bed joint)	TH_NTC

TIDE2, HIDE2	Temperature and relative humidity at the interface between insulation system and basic construction (adhesive mortar layer)	TH_NTC
WFP2	Heat flux at the warm-side surface on top of the insulation system	TF_D
TIDO2	Surface temperature at the warm-side surface on top of the insulation system	T_NTC
TWA2, HWA2*	Temperature and relative humidity in the bed joint of the masonry, about 2 cm behind cold side surface	TH_NTC
Lower joist end test field (plaster connection collar) in test strip 2 (Calsitherm)		
TWA2U	Temperature in the bed joint of the masonry, about 5 mm behind the cold-side directed surface of the masonry	T_NTC
TBKT2U, HBKT2U	Temperature and relative humidity in the bed joint of the masonry, located close to the cavity-directed masonry surface	TH_NTC
TBK2U	Surface temperature of the wood at the cavity-directed front face of the joist end.	T_NTC
TBKSH2U, HBKSH2U	Temperature and relative humidity 5 mm behind the cavity-directed front face of the beam end.	TH_NTC
HFBK2U*	Mass-related moisture content of the beam end wood, about 2 cm behind beam front end	MC_D
TIDEBO2U, HIDEBO2U*	Temperature and relative humidity in the wall part below the joist end (about 7 cm below) at the interface between insulation system and basic construction (adhesive mortar layer)	TH_NTC
TIDOBO2U, HIDOBO2U*	Surface temperature in the wall part below the joist end (about 7 cm below) on the warm side surface (finishing plaster)	T_NTC

Tab. 25.: TUD test stand: list of sensors sorted by test field in test strip 3 (Multipor)

Sensor- ID	Specification	Sensor type reference
Upper joist end test field (open joist end) in test strip 3 (Multipor)		
TWA3O	Temperature in the bed joint of the masonry, about 5 mm behind the cold-side directed surface of the masonry	T_NTC
TBKT3O, HBKT3O	Temperature and relative humidity in the bed joint of the masonry, located close to the cavity-directed masonry surface	TH_NTC
TBK3O	Surface temperature of the wood at the cavity-directed front face of the joist end.	T_NTC
TBKSH3O, HBKSH3O	Temperature and relative humidity 5 mm behind the cavity-directed front face of the beam end.	TH_NTC
HFBK3O*	Mass-related moisture content of the beam end wood, about 2 cm behind beam front end	MC_D
TAMLS3O, VAMLS3O*	Temperature and air velocity in the cavity of the joist end (sidelong the beam end)	TV_D
TBO3O, HBO3O*	Temperature and relative humidity in the perpend joint of the masonry above the joist end.	TH_NTC
TMB3O, HMB3O*	Temperature and relative humidity in the contact are of the beam end (mortar layer)	TH_NTC
TLS3O, HLS3O*	Temperature and relative humidity in the joist end cavity (sidelong the joist end)	TH_NTC
TBIDE3O, HBIDE3O*	Temperature and relative humidity in the joist end (insulation layer level)	TH_NTC
Middle field (wall segment) in test strip 3 (Multipor)		

TWM3, HWM3	Temperature and relative humidity in the middle of the masonry (bed joint)	TH_NTC
TIDE3, HIDE3	Temperature and relative humidity at the interface between insulation system and basic construction (adhesive mortar layer)	TH_NTC
WFP3	Heat flux at the warm-side surface on top of the insulation system	TF_D
TIDO3	Surface temperature at the warm-side surface on top of the insulation system	T_NTC
TWA3, HWA3*	Temperature and relative humidity in the bed joint of the masonry, about 2 cm behind cold side surface	TH_NTC
Lower joist end test field (hemp band) in test strip 3 (Multipor)		
TWA3U	Temperature in the bed joint of the masonry, about 5 mm behind the cold-side directed surface of the masonry	T_NTC
TBKT3U, HBKT3U	Temperature and relative humidity in the bed joint of the masonry, located close to the cavity-directed masonry surface	TH_NTC
TBK3U	Surface temperature of the wood at the cavity-directed front face of the joist end.	T_NTC
TBKSH3U, HBKSH3U	Temperature and relative humidity 5 mm behind the cavity-directed front face of the beam end.	TH_NTC
HFBK3U*	Mass-related moisture content of the beam end wood, about 2 cm behind beam front end	MC_D
TAMLS3U, VAMLS3U*	Temperature and air velocity in the cavity of the joist end (sidelong the beam end)	TV_D
TBO3U, HBO3U*	Temperature and relative humidity in the perpend joint of the masonry above the joist end	TH_NTC
TMB3U, HMB3U*	Temperature and relative humidity in the contact are of the beam end (mortar layer)	TH_NTC
TLS3U, HLS3U*	Temperature and relative humidity in the joist end cavity (sidelong the joist end)	TH_NTC
TBIDE3U, HBIDE3U*	Temperature and relative humidity in the joist end (insulation layer level)	TH_NTC